



Numerical Improvements for Large-Scale Flood Simulation

Yueling Wang

Thesis submitted in partial fulfilment of the requirements
of the regulations for the degree of Doctor of Philosophy

Newcastle University

Faculty of Science, Agriculture & Engineering

School of Civil Engineering & Geosciences

July / 2011

Numerical Improvements for Large-Scale Flood Simulation

A thesis submitted in partial fulfilment for the degree of Doctor of Philosophy at the
Newcastle University.

By Yueling Wang, School of Civil Engineering & Geosciences, July 2011

ABSTRACT

This work assesses two numerical approaches that are most commonly used nowadays for large-scale flood simulation. For this purpose, two different numerical models are developed, i.e. a finite volume Godunov-type model that solves the fully 2D shallow water equations and a simplified model that is based on the zero-inertia formula.

The fully 2D model employs an explicit finite volume Godunov-type scheme to solve a pre-balanced formulation of the 2D shallow water equations (SWEs). The interface fluxes are calculated by an HLLC approximate Riemann solver with the local Riemann problems defined by the Riemann states that are reconstructed using a depth-positivity-preserving approach. The second order accuracy is achieved using a Runge-Kutta integrated method in time and a slope limited linear reconstruction (MUSCL) scheme in space. For the explicit scheme, the adaptive time step controlled by the Courant-Friedrichs-Lewy (CFL) criterion is implemented to maintain the computational stability. After being validated against several theoretical benchmark tests, this fully 2D model is applied to simulate different types of flood waves, including rapidly-varying dam breaks, slow-evolving inundations and coastal applications. In all of the tests, the numerical results are found to agree well with the analytical solutions, laboratory measurements, previously published predictions and field data whenever available. Closely related to the reliability of the numerical solutions, the effects of the mesh resolution and the numerical accuracy are also investigated in this work. The flood extent, water depth and arrival time are found to be sensitive to the change of the mesh resolution. However, the sensitive response of the numerical accuracy is only restricted to those simple analytical tests but not found in any of the realistic simulations.

A new zero-inertia model is developed for predicting slow-varying flood inundations, where the governing equation is solved by an explicit finite volume scheme implemented with a depth-positivity-preserving condition. The new zero-inertia model is validated against analytical tests and a realistic flood inundation event in Thamesmead, England. The numerical results present good agreement with the analytical solutions and predictions produced by the aforementioned fully 2D shallow flow model. The mass conservation is strictly maintained throughout the computations. However, the computational cost is found to be much more expensive than the fully 2D model due to the use of much smaller time step in maintaining numerical stability.

Acknowledgements

First of all, I would like to express my deep and sincere thanks to my supervisor Dr. Qihua Liang. It is my honour to be his first PhD student. I appreciate all his contributions of time, support, patience and encouragement. He taught me not only in research and writing but also an attitude of research. He let me know I will succeed if I work hard and never give up. I also wish to thank my second supervisor Prof. Jim Hall for all his novel suggestions, creative ideas and kind help on my work. I could not finish this thesis without their guidance and encouragement.

I want to express my deepest gratitude to my parents. Without their unchanging support and encouragement, I could not be able to start and finish my PhD study. They give me all their loves and help me to make my dream come true. They are the most important persons to me in the world. I would dedicate this thesis to them as a gift.

I also want to thank the Henry Lester Trust Limited and the Great Britain-China Educational Trust. Without their financial support, I could not afford the living expenses for my PhD study in Newcastle. To repay their kindness, I will return to China and continue my research at a university or research institution. I will devote my whole life to solve the Chinese flooding problem.

I would like to thank my colleagues for providing a stimulating and enjoyable environment for learning and researching. I would like to particularly thank Georges Kesserwani, Lucy Manning, Nor Azlina Alias, Miao Wang and Hongbin Zhang. I also want to thank my dear friends for their endless support and encouragement. They are Na Xu, Ping Wang, Lei Zhang, Mo Xu and Minglei Ren.

Lastly, I am grateful to the secretaries and technicians in the school of Civil Engineering and Geosciences and the SAgE Graduate School, and also the librarians in Robinson Library, for their hard work to provide an excellent research and work environment, and also kind help to assist me in many different ways. Here I especially thank Melissa Ware, Sonia Wilson, Lynn Patterson and Graham Patterson.

Contents

Chapter 1 Introduction and Background	1
1.1 Introduction	1
1.2 Objectives.....	3
1.3 Outline.....	4
Chapter 2 Literature Review	6
2.1 Fully 2D Shallow Flow Model.....	7
2.2 Zero-inertia Model	15
2.3 Conclusions	18
Chapter 3 Development of a Fully 2D Shallow Flow Model	20
3.1 Fully 2D Shallow Water Equations	21
3.2 Numerical Scheme	25
3.2.1 <i>Godunov-type finite volume scheme</i>	25
3.2.2 <i>Calculation of the flux terms</i>	25
3.2.3 <i>Calculation of the source terms</i>	31
3.2.4 <i>CFL criterion</i>	33
3.2.5 <i>Boundary condition</i>	33
3.3 Case Studies	35
3.3.1 <i>Tidal wave flow</i>	35
3.3.2 <i>Oblique hydraulic jump</i>	38
3.3.3 <i>Shock reflection by a circular cylinder</i>	43
3.3.4 <i>Shock diffraction in an hourglass channel</i>	51
3.3.5 <i>Steady transcritical flow over a hump</i>	55
3.3.6 <i>Frictional flow in a parabolic bowl</i>	58
3.4 Conclusions	61
Chapter 4 Dam Break Flood Simulation.....	63
4.1 Results	64
4.1.1 <i>Laboratory dam break over a triangular hump</i>	64
4.1.2 <i>Toce river dam break</i>	69
4.1.3 <i>Malpasset dam break</i>	75
4.2 Conclusions	81
Chapter 5 Coastal Wave Run-up Applications	83
5.1 Non-reflective Boundary Condition.....	83
5.2 Results	85

5.2.1	<i>Sinusoidal wave reflected against a vertical wall</i>	85
5.2.2	<i>Surge reflection</i>	87
5.2.3	<i>Tidal flow in a channel with non-uniform topography</i>	89
5.2.4	<i>Shallow flow oscillation in a parabolic bowl</i>	91
5.2.5	<i>Solitary wave run-up along a sloping beach</i>	96
5.2.6	<i>Experimental tsunami run-up with realistic domain features</i>	103
5.3	Conclusions	111
Chapter 6	Effect of Spatial Resolution and Numerical Accuracy.....	112
6.1	Mathematical Methods.....	113
6.2	Case Studies and Discussions	115
6.2.1	<i>Dam-break flow over a triangular bump</i>	115
6.2.2	<i>Frictional flow in a parabolic bowl with planar surface</i>	120
6.2.3	<i>Malpasset dam break</i>	127
6.3	Conclusions	136
Chapter 7	Zero-inertia Model.....	138
7.1	Zero-inertial Model	139
7.1.1	<i>Depth-positivity-preserving condition</i>	140
7.1.2	<i>Flux calculation</i>	141
7.1.3	<i>Time stepping and boundary conditions</i>	141
7.2	Results	142
7.2.1	<i>Open channel flow with flat bed</i>	142
7.2.2	<i>Tidal flow over a beach with varying slope</i>	145
7.2.3	<i>Thamesmead flood inundation</i>	148
Chapter 8	Conclusion and Future Work	157
8.1	Conclusions	157
8.1.1	<i>Fully 2D shallow flow model</i>	157
8.1.2	<i>Dam-break simulation</i>	158
8.1.3	<i>Coastal wave run-up simulation</i>	158
8.1.4	<i>Effect of grid scale and numerical order</i>	159
8.1.5	<i>Zero-inertia model</i>	159
8.2	Future Work and Recommendation	160
8.2.1	<i>Fully 2D shallow flow model</i>	160
8.2.2	<i>Zero-inertia model</i>	161
References	163

List of figures and tables

Figure 3.1 Deriving the pre-balanced SWEs: the control volume.

Figure 3.2 Sketch of the bed topography for the shallow water equations.

Figure 3.3 Three possible dry-bed configurations in numerical computation.

Figure 3.4 Well-balanced scheme for dry-bed applications: local bed modification.

Figure 3.5 The HLLC Riemann solver structure.

Figure 3.6 Sketch of the local boundary modification method.

Figure 3.7 Tidal wave flow: the bed topography of the irregular bed.

Figure 3.8 Tidal wave flow: comparison of water surface elevation and the analytical solution at $t = 10800$ s.

Figure 3.9 Tidal wave flow: comparison of velocity and the analytical solution at $t = 10800$ s.

Figure 3.10 Oblique hydraulic jump: the sample computational grid (80×60).

Figure 3.11 Oblique hydraulic jump: water depth contours.

Figure 3.12 Oblique hydraulic jump: the convergence history (LBMM – local boundary modification method).

Figure 3.13 Oblique hydraulic jump: velocity field near to the inclined wall.

Figure 3.14 Oblique hydraulic jump: the 3D view of water.

Figure 3.15 Shock reflection by a circular cylinder: the 3D surface view at different times: at (a) $t = 0.05$ s; (b) $t = 0.1$ s; (c) $t = 0.15$ s; (d) $t = 0.2$ s; (e) $t = 0.25$ s; (f) $t = 0.3$ s; (g) $t = 0.35$ s.

Figure 3.16 Shock reflection by a circular cylinder: the shock wave depth contours at different times: (a) at $t = 0.025$ s; (b) $t = 0.05$ s; (c) $t = 0.1$ s; (d) $t = 0.15$ s; (e) $t = 0.2$ s; (f) $t = 0.25$ s; (g) $t = 0.3$ s; (h) $t = 0.35$ s.

Figure 3.17 Shock diffraction in an hourglass channel: geometry of the contraction-expansion channel.

Figure 3.18 Shock diffraction in an hourglass channel: the depth contours of the bore diffraction in a contraction-expansion channel at a sequence of moments: at $t = 0.067$ s; $t = 0.11$ s; $t = 0.125$ s; $t = 0.15$ s; $t = 0.19$ s; $t = 0.31$ s; $t = 0.36$ s; $t = 0.4$ s.

Figure 3.19 Steady transcritical flow over a hump: time history of relative error.

Figure 3.20 Steady transcritical flow over a hump: water surface elevation profile.

Figure 3.21 Steady transcritical flow over a hump: discharge comparison.

Figure 3.22 Steady transcritical flow over a hump: Froude number comparison.

Figure 3.23 Time histories of the velocity components at gauging point (1000, 0) for four-period simulations: (a) frictionless flow; (b) frictional flow.

Figure 3.24 Water surface profile along the x -direction centreline after half of a period and four periods: (a) frictionless flow; (b) frictional flow.

Figure 4.1 Dam break over a hump: experimental set up.

Figure 4.2 Dam break over a hump: time histories of predicted water depth by the present shallow flow model (Northwest), simulated by Kesserwani and Liang (2010) (Northeast) and velocity (Southwest) at different gauges.

Figure 4.3 Toce River dam break: floodplain and location of gauge points.

Figure 4.4 Toce River dam break: time history of the adaptive time step in 180 s.

Figure 4.5 Toce River dam break: flood routing.

Figure 4.6 Toce River dam break: velocity field at $t = 180$ s (a) in the whole domain; (b) zoom-in view near the outlet.

Figure 4.7 Toce River dam break: time history of water depth at different gauge points.

Figure 4.8 Malpasset dam break: floodplain and location of gauges (G) and police survey points (P).

Figure 4.9 Malpasset dam break: time history of the adaptive time step in 1800 s.

Figure 4.10 Malpasset dam break: numerical inundation map at different output times.

Figure 4.11 Malpasset dam break: velocity field at $t = 30$ min: (a) the whole domain; (b) zoom-in view near the flood front.

Figure 4.12 Malpasset dam break: comparison of numerical and surveyed maximum water depth (left – by the present model; right – by Liang *et al.* (2007)).

Figure 4.13 Malpasset dam break: comparison of numerical and measured arrival time at different gauge points (left – by the present model; right – by Alcrudo and Gil (1999)).

Figure 4.14 Malpasset dam break: comparison of numerical and experimental maximum water depth at different gauge points (left – by the present model; right – by Liang *et al.* (2007)).

Figure 5.1 Non-reflective boundary conditions.

Figure 5.2 Sinusoidal wave reflected against a vertical wall: reflective waves at $t = 1993.95$ s and $t = 2004.05$ s.

Figure 5.3 Sinusoidal wave reflected against a vertical wall: time history of water depth at $x = 500$ m.

Figure 5.4 Surge reflection: comparison of the analytical and predicted water depth at $t = 200$ s.

Figure 5.5 Surge reflection: comparison of the predicted and analytical water depth at $t = 1000$ s.

Figure 5.6 Surge reflection: time history of the water depth at $x = 5000$ m.

Figure 5.7 Surge reflection: time history of the flow velocity at $x = 5000$ m.

Figure 5.8 Tidal flow: comparing analytical and prediction water level at $t = 7552.13$ s.

Figure 5.9 Tidal flow: comparing analytical and predicted velocity at $t = 7552.13$ s.

Figure 5.10 Shallow flow oscillation in a parabolic bowl: the bed profile and the initial water surface elevation.

Figure 5.11 Shallow flow oscillation in a parabolic bowl: time histories of the water surface elevation (a) at $x = 0$ and (b) at $x = 500$ m.

Figure 5.12 Shallow flow oscillation in a parabolic bowl: water surface profile at different output times.

Figure 5.13 Analytical solitary wave run-up: definition of solitary wave and bed profile.

Figure 5.14 Analytical solitary wave run-up: time history of the water level at (a) $\zeta = 0.25$ m and (b) $\zeta = 9.95$ m.

Figure 5.15 Analytical solitary wave run-up: wave profiles at (a) $t(g/h)^{1/2}=30$; (b) $t(g/h)^{1/2}=50$; (c) $t(g/h)^{1/2}=70$.

Figure 5.16 Experimental solitary wave run-up: wave profiles at different output times, (up – by the present model, where \circ (red) stands for experimental data, — (blue) represents numerical results and — (black) denotes sea bed; down – by Yamazaki *et al.* (2009), where \circ (black) stands for experimental data, — (blue and red) represents numerical results and — (black) denotes sea bed).

Figure 5.17 Tsunami run-up: domain topography.

Figure 5.18 Tsunami run-up: contour lines of the bed topography of (a) the whole computational domain; (b) the pocket beach and two small valleys.

Figure 5.19 Tsunami run-up: the 22.5 s incident wave.

Figure 5.20 Tsunami run-up: flood maps (left) and water surface contours (right) at different output times.

Figure 5.21 Tsunami run-up: predicted velocity field (a) in the whole domain; (b) near the two valleys; (c) around the Muen Island.

Figure 5.22 Tsunami run-up: time histories of water level at three gauge points (left – by the present model; right – by Franchello (2010)).

Figure 6.1 Dam-break flow over a triangular bump: bed profile.

Figure 6.2 Dam-break flow over a triangular bump: time history of the water depth at different gauges.

Figure 6.3 Dam-break flow over a triangular bump: time histories of Fit statistics ($F1$) for 90 s.

Figure 6.4 Dam-break flow over a triangular bump: time histories of fit statistics ($F2$) for 90 s.

Figure 6.5 Dam-break flow over a triangular bump: time histories of the root mean square errors (RMSE) calculated against water depth for 90 s.

Figure 6.6 Frictional flow in a parabolic bowl with planar surface: central profiles of water surface along the x -axis at different times.

Figure 6.7 Frictional flow in a parabolic bowl with planar surface: time histories of the water surface elevation in 7200 s at (a) G1 ($x = 500$ m); (b) G2 ($x = 1000$ m); (c) G3 ($x = 1500$ m).

Figure 6.8 Frictional flow in a parabolic bowl with planar surface: time history of fit statistics ($F1$) for 7200 s.

Figure 6.9 Frictional flow in a parabolic bowl with planar surface: time history of fit statistics ($F2$) for 7200 s.

Figure 6.10 Frictional flow in a parabolic bowl with planar surface: time histories of RMSE in terms of water depth for 7200 s: (a) use the 2nd order prediction as the benchmark; (b) use the analytical solution as the benchmark.

Figure 6.11 Malpasset dam break: plane view of the floodplain and location of Gauge points (G) and Police survey points (P).

Figure 6.12 Malpasset dam break: the arrival time at different gauge points predicted on grids with different resolutions.

Figure 6.13 Malpasset dam break: the maximum water level at different gauge points predicted by grids with different resolutions.

Figure 6.14 Malpasset dam break: the maximum water level predicted on different grid scales at the Police survey locations.

Figure 6.15 Malpasset dam break: the snapshots of flood map at different times predicted on different resolutions: $\Delta x = 200$ m (Northwest), $\Delta x = 80$ m (Northeast), $\Delta x = 40$ m (Southwest) and $\Delta x = 20$ m (Southeast).

Figure 6.16 Malpasset dam break: Fit statistics ($F1$) history in 5000 s based on different grid scales.

Figure 6.17 Malpasset dam break: Fit statistics ($F2$) history in 5000 s based on different grid scales.

Figure 6.18 Malpasset dam break: Root Mean Square Error (RMSE) history of the water depth in 5000 s based on different grid scales.

Figure 6.19 Malpasset dam break: Root Mean Square Error (RMSE) history of the water depth in 5000 s.

Figure 7.1 Open channel flow with flat bed: (a) initial flow condition and the final free-surface profile predicted by the ZIM; (b) a zoomed part of the solution.

Figure 7.2 Open channel flow with flat bed: the time history of the RMSE.

Figure 7.3 Open channel flow with flat bed: a grid convergence study for the ZIM model: (a) the final free-surface; (b) the associated time histories of the RMSE.

Figure 7.4 Tidal flow over a beach with varying slope: free-surface profiles predicted by the ZIM and fully 2D shallow flow model (using a fixed time step of 0.0075 s) at different output times.

Figure 7.5 Tidal flow over a beach with varying slope: the time history of the RMSE.

Figure 7.6 Thamesmead flood inundation: floodplain (also being illustrated are the locations of the breach and 8 gauge points for recording time history of water surface elevation).

Figure 7.7 Thamesmead flood inundation: inflow hydrograph.

Figure 7.8 Thamesmead flood inundation: flood maps of the Thamesmead flood inundation predicted by the ZIM model (left) and the fully 2D model (right): (a) $t = 1.5$ hrs; (b) $t = 10$ hrs.

Figure 7.9 Thamesmead flood inundation: time histories of water depth at eight different gauge points.

Figure 7.10 Thamesmead flood inundation: time history of RMSE calculated against the fully 2D solution.

Figure 7.11 Thamesmead flood inundation: mass conservation.

Figure 7.12 Thamesmead flood inundation: Fit-statistic ($F1$).

Figure 7.13 Thamesmead flood inundation: Fit-statistic ($F2$).

Table 3.1 Bed elevation at point x for irregular bed.

Table 3.2: L^2 -error and order of accuracy evaluated against numerical water level after half a period ($t = 672.8$ s).

Table 6.1 The corresponding RMSE and computational time to different grid scales.

Chapter 1 Introduction and Background

1.1 Introduction

The birthplaces of humanity are mostly near to rivers. Rivers and alluvial plain are an important part of the ecosystem and provide several essential functions for human use. Rivers provide not only drinking water but also water for irrigation, livestock farming, fishing, hydropower, traffic and industry. Furthermore, they play a significant role in sediment transportation, flora and fauna habitat, and influence the stability of ecosystem. However, rivers can also bring flood disasters to humanity. The possible reason of flood disasters can be sustained rainfalls, rapid snow melt, suddenly collapsed flooding defence (e.g. dam/dyke), tsunami, hurricane and severe storm in the coastal area, etc. These flood events could cost heavy casualties and huge economic and environment losses.

Human activities have brought significant changes and pressures to the natural environment causing increases of natural disasters. Increased population density brings pressure on the supply of clean drinking water and food. And the spatial distribution of water resources is changed by humanity. Moreover, deforestation and urbanization are increasing, especially in the developing countries, in order to obtain economic and agriculture development. These changes of land-use lead to degradation of land cover and reduce the storage capacity of water. Therefore, these man-made influence factors lead to climate change causing a series of increasing problems, e.g. alternation of precipitation and evaporation, snowmelt and ice-melt, severe storm, hurricane and tsunami. All these problems may increase flooding disasters.

Amongst the natural disasters like landslides, volcanic eruptions, drought, tsunami and earthquakes, the risk of flooding has evidently increased in the world wide in the recent year (e.g. Milly *et al.* 2002; Brissette *et al.* 2003; Kundzewicz *et al.* 2005; Teng *et al.* 2006; Chang *et al.* 2009). In 1998, China experienced a devastating flood event in the Yangtze River basin from June to August, in which over 4,100 people died, over 10 million acres of farmland were inundated, more than 4.3 million buildings were destroyed and 20 million people were made homeless. The total economic

loss was over 150 billion Yuan. In October 2000, the south east England was attacked by extremely heavy rainfalls which consequently led to the worst flooding inundation in 40 years. The consequences of this flood disaster involved destroyed structures and roads, traffic and power interruption, damaged farmland, crops and livestock, with a total economic loss of more than 100 million pounds. In July 2005, a devastating flood happened in Maharashtra and Mumbai, India. It took away over 1000 lives of people and caused more than 3.5 million US dollars of economic losses. In 2007, the southern and central China was hit by a severe flood that caused 700 people died and more than \$ 7 million damages. An extreme flooding inundation attacked England and Wales in June and July 2007 resulting in 13 people dead and about 48,000 houses damaged, which also caused the local resources to the limit. After that, Sir Michael Pitt reviewed the 2007 flood event and reported the causes and consequences of flood events in Pitt (2007), in which Sir Michael Pitt made recommendations on the flood risk management to minimise the effect of floods on the individual and communities. In 2008, a 1-in-115 year flood event happened in Morpeth, UK, affecting approximately 1,000 properties. Due to the heavy precipitation, a 1-in-100 year flood attacked America's Midwest in June 2008 affecting seven states and causing over \$ 20 billion damages. Last year (2010) also saw severe flood disasters in several countries and regions, e.g. northeast and southwest of China, Madeira, central European, north eastern Brazil, etc. The risk based analysis has been undertaken to reduce the huge casualties, physical damages and economic losses related to these flood events.

Flood risk management has been established to provide a well designed plan to warn, prevent, monitor and control flood risks, which in turn needs a reliable flood risk assessment. In a flood risk assessment framework, an efficient and reliable hydraulic model is an essential component to provide the hydraulic characteristics, especially for the complex floodplain topography. The hydraulic model can be adopted to simulate potential flood events, in order to provide important flood information, e.g. flood extent, water depth, velocity and arriving time. The predicted information can be used for flood mapping, land use planning, flood defence designing and evacuation planning in order to reduce flood damages in the frequently flooding area.

Compared with the physical model, the computer model presents advantages in lower cost, flexibility, efficiency and accuracy. Many hydraulic modellers and other relevant scientists have contributed on the development of the hydraulic modelling. With the

rapid development of computer technology and computational techniques, now this is generally achieved by numerical simulation. The majority of flood flow can be considered as shallow flow, including the floods happening in the river, near-shore floods in the coastal area and dam-break induced floods. The feature of shallow flow is the horizontal length scale is much greater than the vertical length scale. In this case, the vertical flow acceleration can be neglected. The shallow water equations are implemented to solve the shallow flow hydrodynamics, based on the principles of mass and momentum conservation. The basic assumption of the shallow water equations is that the vertical velocity is very small, compared with the horizontal velocity. Consequently, the vertical pressure field can be considered as hydrostatic. The shallow flow model has been widely used for flood simulation (e.g. Zhao *et al.* 1996; Mingham and Causon 1998; Caleffi *et al.* 2003; Liang *et al.* 2004; Mignot *et al.* 2006; Liang *et al.* 2007; Delis *et al.* 2008; Liang and Borthwick 2009). In this study, a novel numerical solver of shallow water equations is developed to simulate the complex hydrodynamics over the natural domain topography. And a new but simple numerical model is developed to solve the flow hydrodynamics over slow-varying floodplain, based on the simplified shallow water equation. These two numerical models are compared and validated against the realistic flood event. In the future, the proposed models can be implemented for the flood risk assessment of the real-world flood disasters.

1.2 Objectives

This thesis aims to implement a robust numerical scheme for solving the fully 2D shallow water equations for modelling complicated hydraulic phenomena and test it for different types of flood simulations. It is also intended to compare its performance with alternative flood modelling approaches. For this purpose, a new finite volume zero-inertia model is developed and validated. Hence this work needs to achieve the following objectives,

- Develop a fully 2D shallow flow model to solve the flux term and the source term well-balanced shallow water equations using a finite volume Godunov-type scheme and implement a non-negative depth preserving method to deal with the wet-dry fronts over complex topography;

- Validate and apply the fully 2D shallow flow model for different types of flood modelling including dam-break and coastal flood inundation;
- Investigate the effects of the grid scale and the numerical accuracy on flood modelling;
- Develop an explicit finite volume free-limited numerical scheme for solving the simplified shallow water equation (zero-inertia equation) and test it for flood modelling;
- Compare the performance of the two models in flood simulations.

The proposed fully 2D shallow flow model is expected to be able to accurately solve complicated hydrodynamic problems in different flow regimes including subcritical flow, transcritical flow, supercritical flow and shock-like flow discontinuities, and effectively resolve the repeating wetting-drying problem over complex domain topography. Therefore, the proposed numerical model can be employed in the realistic applications, which could provide useful information for the flood prevention and defence design and also offer a guide for evacuation in a flood event. The zero-inertia model is proposed to be efficient and capable of reproducing reliably the slow varying flood flows happening over gentle-sloped floodplains. In this work, the efficiency of the zero-inertia model is examined and compared with the fully 2D shallow flow model.

1.3 Outline

The next chapter presents a literature review of the numerical approaches to solve fully 2D shallow water equations and zero-inertia equation. Chapter 3 describes a finite volume Godunov-type scheme for solving the well-balanced 2D shallow water equations, incorporating a non-negative reconstruction method and a local bed elevation modification approach to resolve the wet-dry front problem. The HLLC approximate Riemann solver is employed to evaluate the interface fluxes. The higher order accuracy is achieved by implementing the Runge-Kutta time integration method in time and the MUSCL scheme in space. The numerical model is validated and applied to dam-break flooding simulation on the realistic and experimental cases in Chapter 4. Chapter 5 validates the fully 2D shallow flow model against coastal wave run-up simulation in the analytical and experimental cases. The investigation of the scale effect and numerical

accuracy is carried out based on the analytical and realistic cases in Chapter 6. The zero-inertia equation is derived from fully 2D shallow water equations and then solved by an explicit finite volume method in Chapter 7. An effective non-negative approach (in term of water depth) is implemented to capture the wet-dry interface over complex domain topography. The zero-inertia model is validated against the idealised flooding inundation event at Thamesmead area. The numerical results and computational cost are compared with the fully 2D simulation. Chapter 8 presents the conclusion, the recommendation and the possible future research.

Chapter 2 Literature Review

This chapter reviews the development of researches on the numerical solutions of fully 2D shallow water equations and zero-inertia equation in the last several decades. Fully 2D shallow water equations (SWEs) have been widely used to solve shallow flow hydrodynamic problems of complex flood flows (e.g. Alcrudo and Garcia-Navarro 1993; Zhao *et al.* 1996; Anastasiou and Chan 1997; Hu *et al.* 1998; Zhou and Stansby 1999; Hubbard and Dodd 2002; Caleffi *et al.* 2003; Haider *et al.* 2003; Pan *et al.* 2006; Liang *et al.* 2007; Zhang *et al.* 2007; Gallegos *et al.* 2009; Liang 2010). The most challenging issues in the numerical solutions of shallow flow problems can be described as follows,

- Accurately solve subcritical, supercritical and transcritical flows;
- Accurately simulate the shock-like flow discontinuities;
- Accurately simulate the steady and the unsteady flow;
- Capability to deal with the complex domain topography;
- Effectively handle the repeat wetting and drying problems;
- Represent high roughness value along the flood route.

Herein the review studies different methods solving these most challenging flow hydrodynamic problems in the real-world application of 2D shallow flow model, and presents the advantages and the disadvantages of these numerical approaches. Then a new fully 2D shallow flow model will be proposed to solve all the most challenging issues in a single code based on this review.

The zero-inertia equation (ZIE) is simplified from fully 2D shallow water equations by eliminating the dynamic terms of momentum equations. The assumption is based on the balance of the friction and gravity forces. Due to the mathematical simplicity, the zero-inertia model is popular for the urban flooding simulation in recent years (e.g. Bates and de Roo 2000; Bradbrook *et al.* 2004; Yu and Lane 2006a). The review presents the developments and the achievements of zero-inertia model, and also shows the encountered problems in the research in recent several decades. Then a new numerical scheme is proposed to solve the zero-inertia equation.

2.1 Fully 2D Shallow Flow Model

The research on seeking solutions of fully 2D shallow water equations has lasted for more than one century. The first instance was done by deriving analytical solutions of certain simple idealised cases (e.g. Ritter 1892; Dressler 1952; Whitham 1955). With the fast development of electronic computers in the latter half of the 20th century, numerical solutions have been intensively sought for different types of shallow flow simulations (e.g. Kutija 1993; Tchamen and Kahawita 1998; Zoppou and Roberts 2003; Rogers *et al.* 2001; Zhou *et al.* 2001; Liang *et al.* 2004; Horritt 2004; Sanders 2008; Wright *et al.* 2008; Liang and Borthwick 2009; Lee and Wright 2010). In general, the numerical models based on the 2D shallow water equations have been widely used in simulating flood inundation (e.g. Jha *et al.* 2000; Zoppou and Roberts 2000; Sheu and Fang 2001; Yoon and Kang 2004; Mignot *et al.* 2006; Marche *et al.* 2007; Liang *et al.* 2008; Liang and Marche 2009; Franchello 2010).

Numerical models based on different numerical approaches have been widely reported for flood inundation simulations, e.g. finite difference method (FDM) (e.g. Miyata 1986; Casulli 1990; Fennema and Chaudhry 1990; Wang *et al.* 2000; Liang *et al.* 2007), finite volume method (FVM) (e.g. Bellos *et al.* 1991; Alcrudo and García-Navarro 1993; Zhao *et al.* 1996; Anastasiou and Chan 1997; Hu *et al.* 1998; Caleffi *et al.* 2003; Wang *et al.* 2003; Horritt 2004; Lai *et al.* 2005; Nguyen *et al.* 2006) and finite element method (FEM) (e.g. Akanbi and Katopodes 1988; Leclerc *et al.* 1990; Tisdale *et al.* 1998; Tucciarelli and Termini 2000; Burg *et al.* 2001; Schwanenberg and Harms 2004).

Compared with FDM and FEM, the finite volume method presents attractive advantages and merits, which have been discussed by Tan (1992), Zhao *et al.* (1994), Zhao *et al.* (1996) and Ferziger and Peric (1999).

- The finite volume method is a discretization method based on the integral form of the conservation laws. Hence, the mass and momentum can be maintained strictly;
- The finite volume method is the simplest method to be operated maintaining the conservation laws in the numerical simulation, especially for the hyperbolic

conservation laws of the 2D shallow water equations. In the finite volume method, the local conservation is achieved in each discretized cells;

- The finite volume method and the finite element method can be easily formulated for the unstructured grid system for the arbitrary geometries. However, the computational cost of the finite volume method is much less than the finite element method because the size of matrix in the finite element method consumes lot of computational time at every time step;
- Shock-capturing schemes can be easily constructed in conservative form, due to the application of the integral form of conservation equation.

In the application of dam-break flow, the shock wave happens and generates the Riemann problem. The Riemann problem is a special initial value problem, which consists of piecewise constant states with a single jump discontinuity. It naturally occurs in finite volume method due to the discreteness of the grid. Armed with automatic shock-capturing, a Godunov-type scheme can be easily implemented with the finite volume method to solve the Riemann problem because the finite volume method is based on the conservative form of shallow water equations. In the original Godunov-type scheme, the wave propagation information at the discontinuity can be solved to give the local exact solution, which is considered as the exact Riemann solver (Godunov 1959). However, the exact Riemann solver consumes much computational cost due to the mathematical complexity. In contrast, the approximate Riemann solver provides a simpler and more efficient solution of the Riemann problem, such as, Roe's scheme (Roe 1981), Osher's scheme (Osher 1981), HLL scheme (Harten *et al.* 1983), and HLLC scheme (Toro *et al.* 1994).

Toro (2001) presented the approximate Riemann solver in the application of shallow flow models. A linear Riemann solver is attractive to be used due to its simplicity and efficiency. However, it is also limited by some shortcomings. First, the linearized Riemann solver may give spurious oscillation when dealing with the transcritical flow. Second, the negative water depth could be calculated in the strong rarefaction waves. Furthermore, the linear Riemann solver has difficulty to deal with the strong wave interaction. However, the Roe's Riemann solver (Roe 1981), known as sophisticated linear Riemann solver, presents satisfactory performance on solving the Riemann problem.

The non-linear Riemann solvers present advantages on solving the aforementioned problems in the linear Riemann solvers. However, it also appears some drawbacks due to the simplification. In this case, the number of wave families in the exact Riemann solver may be decreased in the solution of Riemann problems in order to gain the simplification. And the simplification may cost much numerical dissipation. The HLL Riemann solver developed by Harten *et al.* (1983) belongs to this category, in which only two wave families are involved in the wave structure. Hence the HLL Riemann solver can only be implemented for 1D case for accurate simulations. The HLLC Riemann solver (Toro *et al.* 1994) was developed to complete the missing wave families in the HLL Riemann solver, in order to overcome the drawback of the simplification. The HLLC Riemann solver has been successfully adopted to solve the Riemann problems for 2D shallow flow modelling (e.g. Fraccarollo and Toro 1995; Liang *et al.* 2004). Erduran *et al.* (2002) investigated and compared the accuracy, applicability, efficiency and stability of different Riemann solvers in the finite volume shallow flow model, i.e. Osher, HLL, HLLC, flux difference scheme (i.e. Roe) and flux vector splitting. This study recommended that the HLLC Riemann solver is suitable for all kinds of applications.

With the application of the HLLC Riemann solver to solve the interface fluxes, the Godunov-type finite volume scheme can be applied to handle different flow regimes (e.g. transcritical flow, subcritical flow and supercritical flow), steady and unsteady flow, as well as shock-like discontinuities. In the last two decades, research has been focused on developing Godunov-type schemes with capability to cope with complex domain topography and track moving wet-dry interface.

For flow over complex topography, the aim is to have a Godunov-type scheme that preserves the solution of lake at rest. Such a scheme is defined as well-balanced (Greenberg and Leroux 1996) or satisfying *C*-property (Bermúdez and Vázquez 1994). Numerous well-balanced shallow flow models have been reported and it is impossible to give a complete account. Among those most notable techniques for obtaining well-balanced solutions are the upwind discretization of bed slope source terms (e.g. Bermúdez and Vázquez 1994; García-Navarro and Vázquez-Cendón 2000), surface gradient method (Zhou *et al.* 2001), mathematical balancing (Rogers *et al.* 2003; Liang and Borthwick 2009) and hydrostatic reconstruction (Audusse *et al.* 2004).

Bermúdez and Vázquez (1994) developed the upwind scheme of the bed slope source term discretization for the hyperbolic system of shallow water equations to solve the 1D unsteady flow problems. Compared with point-wise methods, the upwind scheme presents more efficient and better performance on dealing with the channel flow with constant rectangular cross-section (Vázquez-Cendón 1994). Later, the upwind scheme was extended to maintain the conservation property in the hyperbolic 2D shallow water equations by Bermúdez *et al.* (1998). The upwind scheme was improved by Vázquez-Cendón (1999) and García-Navarro and Vázquez-Cendón (2000) to solve a wider range of the flow problems. However, the improved upwind scheme is complex for implementation.

Toro (1997) introduced a simple and straightforward method, i.e. fractional step method. It is performed on the inhomogeneous form of the SWEs, which is split into a homogenous equation and a set of ordinary differential equations. These equations are individually solved by a series of term-by-term splitting computation. However, the fraction step method shows poor performance in dealing with the quasi-steady or steady flow problems. LeVeque (1998) developed a new approach to balance the bed gradient terms with the flux terms, in which a Riemann problem is introduced at the centre of cells to address the source terms into the wave propagation algorithm. Compared the fractional step method, this method was successfully implemented to predict quasi-steady flow. However, it met difficulties when dealing with the steady transcritical flow with a shock.

An attempt of simple and accurate solution was carried out by Zhou *et al.* (2001) for the development of well-balanced scheme. Zhou *et al.* (2001) developed the surface gradient method (SGM) to solve the source terms by reconstructing the conservative variables at cell interfaces in MUSCL-type schemes. Several merits of the surface gradient method were mentioned by Zhou *et al.* (2001). First, all the source terms can be discretized by the simple centred method without special treatment. Second, the surface gradient method is suitable to solve the homogeneous form of the equations. Third, the water surface elevation can be accurately calculated for data reconstruction instead of water depth. Finally, the surface gradient method has been successfully implemented to solve the steady and unsteady flow. However, the surface gradient method has difficulty to solve the flow problems over a vertical step. Hence, an improved method called surface gradient method for steps (SGMs) was developed by

Zhou *et al.* (2002) by extending the surface gradient method to solve the shallow water equations, especially for complex bed topography with a vertical step. Then the SGM/SGMs were successfully implemented by Zhou *et al.* (2004) to solve the dam-break cases in CADAM project.

Hydrostatic reconstruction method (HRM) was developed by Audusse *et al.* (2004) to prevent the imbalance between flux and bed slope source terms, i.e. to reconstruct the interface variables according to the balance relationship between the hydrostatic pressure and the pressure caused by bed topographic gradient in the steady flow. Later, Audusse and Bristeau (2005) adopted the hydrostatic reconstruction method to reproduce complex hydrodynamics phenomena in the idealized and realistic cases with good performance. HRM was extended to higher order by Noelle *et al.* (2006), in order to study arbitrary order of accuracy in the finite volume scheme, in which the fourth and fifth order numerical results predicted by the new scheme presented expected convergence rates and high resolution of discontinuities. The hydrostatic reconstruction method (HRM) was compared with the surface gradient method (SGM) by Lai *et al.* (2010). The comparisons of the predictions demonstrate that both of HRM and SGM can be implemented to solve the steady flow problems. The SGM generates unphysical velocity in dealing with the 2D still flow over a symmetric hump. The spurious velocity field is induced by the central bed-slope discretization in the SGM. And the unphysical velocity can be decreased by increasing the mesh resolution. In contrast, HRM maintains the steady state without spurious velocity. Compared with SGM, HRM shows better computational stability, accuracy and efficiency in dealing with the shallow flow problems over irregular bed topography. However, the HRM was first developed to preserve the conservation property based on the kinetic homogeneous solver.

A simple and efficient method was introduced by Lee and Wright (2010), in which the homogenous form of one-dimensional shallow water equations was modified to enable the source terms combined with the flux term. Then the combined flux terms can be directly solved by the same structure of numerical scheme. Several advantages of this simple method were demonstrated by the computational results in Lee and Wright (2010). First, this effective scheme maintains the balance of the flux and source terms in dealing with flow problems over irregular bed topography. Second, the physical hydrodynamics features are exactly represented in the computation. Third, higher-order

scheme can be developed straightforwardly without special treatment. Finally, this approach can be widely applied to different conservative numerical schemes.

The aforementioned numerical methods use numerical reconstruction/modification to treat the imbalance between the flux and bed slope source terms. Another strategy to preserve the well-balanced property is the algebraic approach, i.e. mathematically rearranging the shallow water equations to achieve the equilibrium conditions (Roger *et al.* 2001; Roger *et al.* 2003). This mathematical balancing method was straightforwardly operated without implementing a reconstructed method. Hence, the computational cost can be saved. And the complex combination of the numerical schemes can be avoided. This reformulated shallow water equations can be called as *pre-balanced* shallow water equations. Liang and Marche (2009) and Liang and Borthwick (2009) demonstrated that the numerical scheme automatically maintains the conservation property by using the *pre-balanced* shallow water equations, without implementing special numerical approach to balance the source term. Hence, the merit of algebraic approach (Roger *et al.* 2003) is the strong capability to provide well balance between the flux and source terms without complicate numerical treatment.

For applications involving wetting and drying, well-balanced and non-negative (in terms of water depth) scheme are desirable. It is not a trivial task to design a numerical model to reproduce the wetting and drying process as it is essentially a moving boundary problem where the wet-dry interface continuously and repeatedly evolves inside the computational domain. Negative water depth and unphysical high velocities are easily predicted near the wet-dry fronts and causes numerical instability.

A traditional way to deal with this is to add small water depth in the dry cells to avoid direct calculation of wetting and drying (e.g. Wang 1987; Vincent *et al.* 2001; Lin *et al.* 2003). Although this might be practically feasible, Toro (2001) pointed out that adding water mass, even though it is small, in dry-bed calculations is physically incorrect and may significantly influence the accuracy of the flow solution near the wet-dry front.

In the framework of finite volume method, Zhao *et al.* (1994) developed a solution for the wetting and drying cycles between the shallow flow elements in the river basin, according to the hydraulic conditions. The cell faces are classed as *land boundary* and *wet boundary*. Three types of flow elements are classed as *entirely dry element*,

partially dry element and *wet element*, respectively for three different states (Zhao *et al.* 1994) by considering two levels of the water depth tolerance (*threshold depth*) and two types of cell faces. With four land boundaries of a cell element, the entirely dry element is not considered in the computation for the present time step. The partially dry element is calculated only considering the mass flux calculation and neglecting the momentum exchange. When the flow element is wet, the mass and momentum fluxes are both calculated by the Riemann solver. The wet-dry solution is proved to be suitable for handling the wetting and drying processes in the river basin with complicated bed topography.

A similar approach was presented by Sleigh *et al.* (1998) based on the contribution of Zhao *et al.* (1994), which mentioned the limitation of Zhao *et al.* (1994) approach is not easy to be quantified. The improved approach employs the same monitoring system to define the wet-dry state in the grid cells (*entirely dry element*, *partially dry element* and *wet element*). However, Sleigh *et al.* (1998) achieved the same results as Zhao *et al.* (1994) by modifying the fluxes at the cell face instead of removing dry cells from the updating calculation. The improved method is validated against a wide range of 1D and 2D shallow flow problems, in which the wetting and drying procedure is accurately predicted. Hubbard and Dodd (2002) implement a similar method of Sleigh *et al.* (1998) to successfully reproduce the wetting and drying procedure and track the shoreline based on a hierarchical Cartesian Adaptive Mesh Refinement (AMR) algorithm. However, with different criteria, the simulations could show big differences in wetting and drying process. This kind of approach is developed based on the professional experience and the numerical results depend on the setting of the threshold parameters.

Numerical models that directly solve the wet-dry interfaces have been reported in the family of the finite volume Godunov-type methods. The *modified wave speed* approach is introduced by Toro (1994), in which the wave speed estimates in the HLL approximate Riemann solver are modified for the dry front at the cell interface. This method has been implemented by Fraccarollo and Toro (1995) to reproduce an experimental dam-break case with an initial dry bed downstream of the dam. The numerical scheme is found to be able to provide satisfactory simulation of the main hydrodynamics features of the dam-break flow. Hu *et al.* (2000) introduced a simpler approach named *minimum wet depth* approach and compare it with the *modified wave*

speed approach. The new approach redefines the dry state as the water depth is below a water depth tolerance equalling to 10^{-6} m. In this case, the modification of the wave speed estimates can be avoided. This method is successfully implemented for the simulation of wave overtopping of coastal structures.

Brufau *et al.* (2002) and (2004) introduced a local bed modification technique to handle wetting and drying for both steady (Brufau *et al.* 2002) and unsteady flows (Brufau *et al.* 2004). Based on the physical law at the advancing front, the technique was implemented with the upwind discretization of bed slope terms for well-balancing. However, the model predicts negative water depth and an approach for controlling negative depth was implemented in Brufau *et al.* (2004) to eliminate the mass error. The method locally modifies the flow variables and may cause violation of the momentum conservation.

Based on a well-balanced hydrostatic reconstruction technique, Audusse *et al.* (2004) presented a model properly simulates the wetting and drying and preserves the non-negativity of water depth, in which there is no artificially setting of zero water depth and velocity. Marche *et al.* (2007) implemented the hydrostatic reconstruction method to deal with the wetting and drying processes over varying slope. The numerical simulations are validated against the analytical solutions with good agreement. Motivated by Audusse *et al.* (2004), Liang and Marche (2009) developed a non-negative water depth method to reconstruction the flow variables at the wet-dry interface, in order to maintain the numerical stability. This method is proved to be effective and robust for a wide range of application, including moving shoreline over varying bed slope and dam-break over irregular bed topography.

Another new wetting and drying algorithms is recently reported by Casulli (2009), which is derived from the governing differential equations to discrete the water surface elevation in order to maintain mass balance and produce wetting/drying process. The induced mildly nonlinear system provides rigorous mass conservation and maintains non-negative water depth even for the coarse mesh. The accurate wetting and drying process can be achieved for the dry area with exact zero water depth even with the large time step.

Inclusion of friction source terms to account for high value of roughness in the flow path is also essential in practical flooding simulations. The problem is normally

associated with wetting and drying. In the vicinity of wet-dry front, the vanishing water depth may exaggerate the friction force and cause the flow to reverse. This is physically meaningless and results in unstable solutions. Explicit numerical scheme for the friction term will cause instability in terms of vanishing water depth near the wet-dry front (Burguete *et al.* 2007; Burguete *et al.* 2008; Murillo *et al.* 2009).

Implicit discretization of the friction source terms has been recognised to give more stable simulation with infinitesimal water depth (Brufau *et al.* 2002). Yoon and Kang (2004) and Burguete *et al.* (2008) suggest a fully implicit approach with a simple splitting technique to discretize the friction source term. However, Burguete *et al.* (2008) and Liang and Marche (2009) realised that an implicit discretization is not adequate to maintain stability of a numerical scheme when the frictional flow takes place in an initially dry domain with irregular bed profile. They suggested that the friction force should be bounded to prevent unphysical behaviour of the flow.

2.2 Zero-inertia Model

Due to the high computational cost associated with the fully 2D simulations, substantial efforts have been made to develop computationally more efficient flood models. One of the strategies is to simplify the governing equations, whilst endeavouring meanwhile to maintain a reasonable physical representation of flood waves. The zero-inertia models (ZIM) or diffusion-wave models (DWM) fall in this category. In the realistic application, a special case is that the flood flow happens over a gentle sloping floodplain with slow flow speed. In this case, the temporal and convective effect can be neglected. The fully 2D shallow water equations can be simplified by neglecting the momentum dynamic terms to derive the zero-inertia equation. The researchers have developed several flooding flow models based on this concept (e.g., Bates and de Roo 2000; Bradbrook *et al.* 2004; Yu and Lane 2006a). The simplified governing equation and hydrodynamic feature leads to a simpler numerical solution of the zero-inertia equation that could potentially provide further computational efficiency.

After it was introduced by Cunge *et al.* (1976), the diffusion-wave or zero-inertia concept has been used by many researchers to develop over-land flow models and a number of successful ZIMs or DWMs for flood simulations have also been reported and

become popular in literature. Extended from the LISFLOOD catchment model (De Roo *et al.* 1999), Bates and De Roo (2000) adopted the zero-inertia approach to develop their raster-based flood model (LISFLOOD-FP), in order to provide an accurate numerical tool for simulation of flooding extent, without considering the process of the flooding event. This explicit finite difference model implements a 1D kinematic wave approximation to represent the channel flow and a 2D diffusion wave approximation for the floodplain flow. The flux across each cell face is estimated by the analytical flow formulae Manning equation. Compared with the satellite-derived data and the air photo, the numerical simulation presented an obvious uncertainty on capturing realistic flooding extent. The best prediction matched less than 90 percentages of the real inundated area. However, the error may be caused in the segmentation of the satellite image. Further studies need to be carried out to improve the capability of capturing more accurate inundation extent. And the effect of the data resolution on the numerical accuracy should be investigated for the raster-based model.

Later, the effect of the spatial resolution of 1D LISFLOOD-FP was studied by Horritt and Bates (2001b), in which the near channel floodplain storage (NCFS) scheme is implemented to deal with the problems at the conjunction of the narrow channel and the floodplain pixel. The research shows that the constant response to the changing scales is observed on the predicted inundation extent. While the NCFS-model presents more stable response to the flood wave travel time than the original LISFLOOD-FP. Hence, the near channel storage effect plays an important role of the model response to the changing scale, for which the shoreline location and flooding route can be seriously influenced. And the acceptable travel time and flooding area cannot be achieved at the same time.

Later on, the computational performance of LISFLOOD-FP has been compared with a 1D model (HEC-RAS) by Horritt and Bates (2002) and a 2D finite element shallow flow model (TELEMAC-2D) by Horritt and Bates (2001a) and Horritt and Bates (2002). HEC-RAS is developed by the US Army Corps of Engineers, based on the fully 1D St Venant equations for unsteady open channel flow. TELEMAC-2D (Galland *et al.* 1991; Hervouet and Van Haren 1996) employs a 2D finite element method to solve the fluvial flooding problems based on fully 2D shallow water equations. Horritt and Bates (2001a, 2002) demonstrated that LISFLOOD-FP can reproduce a similar accuracy level of flood extent and flood wave travelling times, compared with the other two models, despite the

use of highly simplified equation and simple numerical method. And the lack of the inertia and advection terms may cause the differences between the predictions and the different responses to the friction parameterisations.

To further improve the present LISFLOOD-FP model, Hunter *et al.* (2005) developed two methods to maintain the computational stability and improve the numerical efficiency for this explicit storage cell code. One is a user-free-parameter adaptive time step (ATS) method, which is mainly estimated by the water depth gradient. Then the ATS scheme is tested by the analytical solutions of the wave propagation over flat and complex topography. The comparison with the fixed-time-step code shows the ATS method significantly improves the computational accuracy and stability. The code is found to be sensitive to the floodplain friction for the application over the complex domain topography. An alternative approach of a flow limiter was also introduced by Hunter *et al.* (2005) to limit the maximum flux across the cell interface by considering the water depth difference, in order to maintain the stability at the cell interface. And the flow limiter is found to be sensitive to the time step and grid size. The grid size and the time step are controlled by the artificial factor. The selection of grid size and time step could significantly influence the flow limiter. Hence, the effect of the flow limiter is questioned and needs to be further investigated.

Later, Hunter *et al.* (2006) realised the disadvantages of the flow limiter and suggest the ATS approach is a better solution to maintain the computational accuracy. Further studies are carried out to validate the ATS-based model for the realistic application. The ATS-based model provides better predictions than the original LISFLOOD-FP with fixed time step, however, it consumes much more computational time. Hunter *et al.* (2008) also revealed that the storage cell model is markedly more computational expensive, compared with the fully shallow flow model. Hence, a solution is recommended by Hunter *et al.* (2008) to improve the computational efficiency by including inertia terms and the important flow physical elements for particular case. According to this concept, Bates *et al.* (2010) introduced a new storage cell model with an inertia formulation to achieve the computational efficiency and stability, and reiterated that the reason of using a small time step is the lack of mass and dynamic terms. However, the core concept of zero-inertia model may be broken by the inertia formula in this new model.

Bradbrook *et al.* (2004) introduced another explicit model (JFLOW) based on the diffusion-wave concept for the flood inundation simulations. With a similar basic concept of LISFLOOD-FP, JFLOW shows two main differences with LISFLOOD-FP model (Bates and de Roo 2000), i.e. representation of channel and implementation of the wetting parameter. The wetting parameter is only operated in JFLOW to control the propagation of the wet front while LISFLOOD-FP only uses the drying parameter to trace the dry front. Furthermore, the transfer of flow between the channel and floodplain cells only happens where there is excess flow from the channel cells in JFLOW. However, LISFLOOD-FP enable the transfer happens to any floodplain cells where the channel passes by, by adopting a kinematic wave treatment of flow in the channel.

Application of ZIMs/DWMs (Bradbrook *et al.* 2004) in urban flood prediction was also explored by Yu and Lane (2006a), in which the effect of mesh resolution was also investigated. The performance of predicted flood wave travel time and inundation extent is proved to be quite sensitive to the mesh resolution. The wet-dry treatment (i.e. wetting parameter) is found to reduce the model dependence of the roughness parameter, which can partly compensate for a coarser mesh resolution. However, the coarser resolution will weaken the effect of the roughness parameter on the flooding process. Hence, for the urban flood event modelling, a sub-grid-scale treatment is developed by Yu and Lane (2006b) for an explicit representation of small scale topographic variation to provide more effective effect of the structure element.

2.3 Conclusions

This chapter has reviewed the recent progress of researches on the numerical methods to solve the shallow flow hydrodynamics over complex domain topography and the zero-inertia equation applied with a gentle-sloping floodplain. For the fully 2D shallow water model, much effort has been devoted to tackle the aforementioned challenges in the practical numerical flooding inundation model. But there is still a scope for further research in this area, especially in developing a single model that can resolve all the problems. Presented in 1D, the numerical scheme presented by Liang and Marche (2009) is such an attempt. The model solved the pre-balanced shallow water equation due to Liang and Borthwick (2009) using a non-negative (in terms of water depth) finite volume Godunov-type scheme for dry-bed applications over complex domain,

incorporated with the HLLC Riemann solver to calculate the interface flux. The friction source term was evaluated using a limited implicit scheme. Therefore this work aims to extend the Liang and Marche's model into 2D and improve it for practical flooding inundation model.

Zero-inertia model or diffusion-wave model has been intensively investigated for the realistic flooding simulation over slow-varying floodplain for the last decades. In this work, concerning the merit of the finite volume method, i.e. mass conservation, the zero-inertia equation is going to be solved by using an explicit finite volume method, incorporated with a positive water depth method to deal with the wetting and drying problems. With this non-negative water depth method, the flux could be automatically controlled. This model seems to be able to provide a limiter-free solution of the zero-inertia equation.

In the next chapter, the fully 2D shallow flow model is presented to solve the complex hydrodynamics phenomena over irregular boundary geometry and bed topography, including tidal wave flow, hydraulic jump, shock-like discontinuous problems and steady transcritical flow. Further investigation and application of the presented fully 2D shallow flow model will be carried out in the later chapters. In the following chapter, the new positivity-preserving zero-inertia model will be represented and validated against an idealistic flooding event at Thamesmead, UK.

Chapter 3 Development of a Fully 2D Shallow Flow Model

Objectives

- Develop a novel well-balanced fully 2D shallow flow model to solve different flow regimes and shock-like discontinuities over non-uniform domain topographies;
- Validate the model against different benchmark tests.

Introduction

In recent years, research on shallow flow modelling has been mainly focused on developing models for simulating real-world problems. This in turns requires a model to be able to capture complex flow hydrodynamics such as shock-like discontinuities, achieve well-balanced solution and handle wetting and drying over complex domain topographies. In this chapter, these challenging issues are resolved in a single code. A pre-balanced formulation of shallow water equations (SWEs) is first derived, which automatically maintains well-balanced solution for wet-bed applications. The pre-balanced SWEs are then solved by using a finite volume Godunov-type scheme implemented with an HLLC approximate Riemann solver for flux calculation. The higher order accuracy is achieved using a second-order Runge-Kutta time integration method together with the slope limited linear reconstruction (MUSCL) scheme in space. For wetting and drying over complex domain topography, a depth-positivity-preserving approach is devised to reconstruct the flow variables at the cell interfaces for flux calculation. The friction source term is evaluated using a splitting point-implicit scheme. The proposed model is validated against several analytical test cases, including tidal wave over an irregular bed profile, oblique hydraulic jump, shock reflection against a circle cylinder, shock diffraction at the throat of the hourglass channel, steady transcritical flows over a hump and oscillation flow in a frictional/frictionless parabolic bowl.

3.1 Fully 2D Shallow Water Equations

The 2D SWEs have been used in simulating different types of shallow flow hydrodynamics for a long time (e.g. see Toro (2001) for a review). In a matrix form, the hyperbolic SWEs are generally written as

$$\frac{\partial \mathbf{q}}{\partial t} + \frac{\partial \mathbf{f}}{\partial x} + \frac{\partial \mathbf{g}}{\partial y} = \mathbf{s}, \quad (3.1)$$

where \mathbf{q} is the vector containing the conserved flow variables, \mathbf{f} and \mathbf{g} denotes the flux vectors in the x and y -direction, respectively, \mathbf{s} is the source term vector, t is the time and x and y are the Cartesian coordinates. The vectors are given by

$$\mathbf{q} = \begin{bmatrix} h \\ uh \\ vh \end{bmatrix}, \quad \mathbf{f} = \begin{bmatrix} uh \\ u^2h + \frac{1}{2}gh^2 \\ uvh \end{bmatrix}, \quad \mathbf{g} = \begin{bmatrix} vh \\ uvh \\ v^2h + \frac{1}{2}gh^2 \end{bmatrix}, \quad \mathbf{s} = \begin{bmatrix} 0 \\ -\frac{\tau_{bx}}{\rho} - gh \frac{\partial z_b}{\partial x} \\ -\frac{\tau_{by}}{\rho} - gh \frac{\partial z_b}{\partial y} \end{bmatrix}, \quad (3.2)$$

where z_b is the bed elevation above datum, h is the water depth, u and v are the depth-averaged velocity components in the x and y -direction, g is the acceleration due to gravity, ρ is the water density, $-\frac{\partial z_b}{\partial x}$ and $-\frac{\partial z_b}{\partial y}$ are the bed slope in the Cartesian directions and τ_{bx} and τ_{by} denote the bed friction stresses, which can be calculated by the following formulae

$$\tau_{bx} = \rho C_f u \sqrt{u^2 + v^2} \quad \text{and} \quad \tau_{by} = \rho C_f v \sqrt{u^2 + v^2}, \quad (3.3)$$

in which the bed roughness coefficient C_f can be evaluated by $C_f = gn^2/h^{1/3}$ and n is the Manning coefficient. When $h < 1.0 \times 10^{-6}$, C_f is directly set to zero (a cell is assumed to be dry when $h < 1.0 \times 10^{-6}$).

The above formulation of shallow water equations has been widely used. In the x -direction, the pressure difference and the force induced by the bed gradient can be

represented by the terms $-\frac{g}{2} \frac{\partial h^2}{\partial x} - gh \frac{\partial z_b}{\partial x}$. In a control volume as shown in Figure 3.1, the pressure forces and the effect of bed slope are expressed as

$$P_1 - P_2 - F_b = \frac{1}{2} \rho g h_1^2 - \frac{1}{2} \rho g h_2^2 - \rho g \bar{h} \Delta z_b, \quad (3.4)$$

where P_1 and P_2 are the pressure force, F_b is the force acting on the fluid by the sloping bed, h_1 and h_2 are the water depth at the west and east faces of the control volume; ρ is the constant water density; \bar{h} is the mean water depth across the control volume; Δz_b is the difference of bed elevation at the west and east faces of the control volume. After being divided by Δx and ρ and assuming that Δx is infinitely close to 0, the above expression can be rewritten as

$$\bar{F} = -\frac{g}{2} \frac{\partial h^2}{\partial x} - gh \frac{\partial z_b}{\partial x}, \quad (3.5)$$

which is the same as the aforementioned pressure terms in the SWEs (3.1) – (3.2).

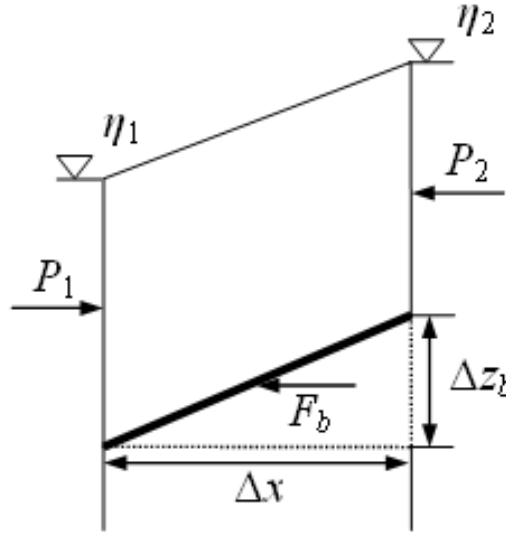


Figure 3.1 Deriving the pre-balanced SWEs: the control volume.

In a motionless lake with $h \neq 0$, $u = 0$ and $v = 0$, the pressure related expression (3.5) should equal to zero, i.e. $-\frac{g}{2} \frac{\partial h^2}{\partial x} - gh \frac{\partial z_b}{\partial x} = 0$. However, directly discretizing the above SWEs cannot maintain the solution of lake at rest at the discrete level (e.g. Roger *et al.* 2003), i.e. the discretized formulation of (3.5) does not equal zero. The imbalance may numerically drive the original motionless lake into motion if no special numerical technique is implemented (Rogers *et al.* 2003), which is physically incorrect. Herein the

aim is to derive a new set of SWEs that can automatically balance the flux and source terms and give zero value to (3.5) at the discrete level so that well-balanced solution can be achieved regardless of the numerical method being used. In equation (3.5), replacing the water depth h by $h = \eta - z_b$ leads to

$$\bar{F} = -\frac{g}{2} \frac{\partial(\eta^2 - 2\eta z_b)}{\partial x} - g\eta \frac{\partial z_b}{\partial x}, \quad (3.6)$$

where η is defined as the water level as shown in Figure 3.2. The vector terms of the SWEs (3.2) can now be rewritten as

$$\mathbf{q} = \begin{bmatrix} \eta \\ uh \\ vh \end{bmatrix}, \quad \mathbf{f} = \begin{bmatrix} uh \\ u^2h + \frac{1}{2}g(\eta^2 - 2\eta z_b) \\ uvh \end{bmatrix}, \quad (3.7)$$

$$\mathbf{g} = \begin{bmatrix} vh \\ uvh \\ v^2h + \frac{1}{2}g(\eta^2 - 2\eta z_b) \end{bmatrix}, \quad \mathbf{s} = \begin{bmatrix} 0 \\ -\frac{\tau_{bx}}{\rho} - g\eta \frac{\partial z_b}{\partial x} \\ -\frac{\tau_{by}}{\rho} - g\eta \frac{\partial z_b}{\partial y} \end{bmatrix},$$

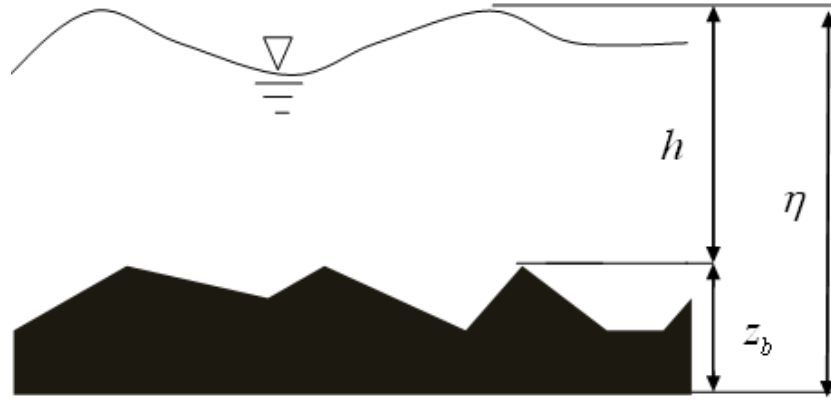


Figure 3.2 Sketch of the bed topography for the shallow water equations.

In a still lake, η is a constant for the whole domain and $\bar{F} = 0$, $\frac{\partial \eta}{\partial x} \equiv 0$, $u = 0$, $v = 0$. The momentum in x -direction in equation (3.7) leads to

$$\frac{g}{2} \frac{\partial(\eta^2 - 2\eta z_b)}{\partial x} = -g\eta \frac{\partial z_b}{\partial x}, \quad (3.8)$$

In this work, a Godunov-type scheme is implemented to solve the shallow water equations, incorporated with the HLLC approximate Riemann solver to estimate the

interface fluxes. Herein, the left term of (3.8) ($\frac{g}{2} \frac{\partial(\eta^2 - 2\eta z_b)}{\partial x}$) can be approximated by fluxes through the east (f_E) and west (f_W) cell faces of the current cell as $\frac{(f_E - f_W)}{\Delta x}$, in which f_E and f_W can be calculated by

$$f_E = \frac{g}{2} (\eta^2 - 2\eta z_{bE}) \text{ and } f_W = \frac{g}{2} (\eta^2 - 2\eta z_{bW}), \quad (3.9)$$

Hence, $\frac{(f_E - f_W)}{\Delta x} = -g\eta \frac{(z_{bE} - z_{bW})}{\Delta x}$. And the discretized form of the right side term in (3.8) is $-g\eta \frac{(z_{bE} - z_{bW})}{\Delta x}$. Therefore, (3.8) can be automatically balanced in the motionless steady state. The momentum in y -direction of (3.7) can be derived in a similar way. Therefore, the set of shallow water equations in (3.1) and (3.7) can provide mathematically well-balanced flux and source terms in the numerical computation. The present shallow water equations can be called *pre-balanced* shallow water equations.

The hyperbolic property of the pre-balanced shallow water equations (3.1) and (3.7) can be confirmed by finding the eigenstructure of the flux Jacobian. The flux Jacobian is obtained by

$$\mathbf{J} = \frac{\partial \mathbf{F}}{\partial \mathbf{q}} = \begin{bmatrix} 0 & n_x & n_y \\ (c^2 - u^2)n_x - uvn_y & 2un_x + vn_y & un_y \\ -uvn_x + (c^2 - v^2)n_y & vn_x & un_x + 2vn_y \end{bmatrix}, \quad (3.10)$$

in which \mathbf{F} ($=\mathbf{f}n_x + \mathbf{g}n_y$) is the combined flux vector; n_x and n_y are the unit vector components in the x and y -direction; c ($=\sqrt{gh}$) is the wave celerity. The eigenvalues associated with (3.8) are given by

$$\lambda_1 = un_x + vn_y, \quad \lambda_2 = un_x + vn_y - c, \quad \lambda_3 = un_x + vn_y + c, \quad (3.11)$$

The eigenvalues are real and distinct for wet-bed application ($h \neq 0$), which proves the hyperbolic property of the present SWEs. More details about this new formulation of shallow water equations and its property can be found in Liang and Borthwick (2009).

3.2 Numerical Scheme

3.2.1 Godunov-type finite volume scheme

In the context of a finite volume scheme, the following time-marching formula may be used to discretized equation (3.1) and update the flow variables to a new time step:

$$\mathbf{q}_{i,j}^{k+1} = \mathbf{q}_{i,j}^k - \frac{\Delta t}{\Delta x} (\mathbf{f}_{i+1/2,j} - \mathbf{f}_{i-1/2,j}) - \frac{\Delta t}{\Delta y} (\mathbf{g}_{i,j+1/2} - \mathbf{g}_{i,j-1/2}) + \Delta t \mathbf{s}_{i,j}, \quad (3.12)$$

where the superscript k represents the present time level, subscripts i and j are the cell indices and Δt , Δx and Δy are the time step and cell size in the x and y -directions, respectively. Combined with a second-order Runge-Kutta method, (3.12) may be rewritten as

$$\mathbf{q}_{i,j}^{k+1} = \mathbf{q}_{i,j}^k - \frac{1}{2} \Delta t (\mathbf{K}_{i,j}(\mathbf{q}_{i,j}^k) + \mathbf{K}_{i,j}(\mathbf{q}_{i,j}^*)), \quad (3.13)$$

where $\mathbf{K}_{i,j}$ is the Runge-Kutta coefficient defined as

$$\mathbf{K}_{i,j} = \frac{\mathbf{f}_{i+1/2,j} - \mathbf{f}_{i-1/2,j}}{\Delta x} + \frac{\mathbf{g}_{i,j+1/2} - \mathbf{g}_{i,j-1/2}}{\Delta y} - \mathbf{s}_{i,j}, \quad (3.14)$$

and the intermediate flow variables $\mathbf{q}_{i,j}^*$ is calculated by

$$\mathbf{q}_{i,j}^* = \mathbf{q}_{i,j}^k + \Delta t \mathbf{K}_{i,j}(\mathbf{q}_{i,j}^k), \quad (3.15)$$

$\mathbf{K}_{i,j}(\mathbf{q}_{i,j}^k)$ and $\mathbf{K}_{i,j}(\mathbf{q}_{i,j}^*)$ must be calculated in two consecutive steps, which in turn requires correct evaluation of the interface fluxes ($\mathbf{f}_{i+1/2,j}$, $\mathbf{f}_{i-1/2,j}$, $\mathbf{g}_{i,j+1/2}$ and $\mathbf{g}_{i,j-1/2}$) and source terms ($\mathbf{s}_{i,j}$) in each step. The interface fluxes are calculated by HLLC approximate Riemann solver that is introduced in the following section.

3.2.2 Calculation of the flux terms

In a Godunov-type framework, the interface fluxes are obtained by solving local Riemann problems defined at cell interfaces. Taking $\mathbf{f}_{i+1/2,j}$ as an example, the fluxes may be expressed as $\mathbf{f}_{i+1/2,j} = \mathbf{F}(\mathbf{q}_{i+1/2,j}^L, \mathbf{q}_{i+1/2,j}^R)$, i.e. the solutions to the local Riemann problem defined by the left and right Riemann states ($\mathbf{q}_{i+1/2,j}^L$ and $\mathbf{q}_{i+1/2,j}^R$) on either side of the cell interface $(i + 1/2, j)$. The Riemann states are obtained from the face values

that are reconstructed from the cell-centred flow variables. Herein the MUSCL (Monotone Upstream-centred Schemes for Conservation Laws) slope limited linear reconstruction (van Leer, 1979) is adopted to rebuild the face values in order to achieve 2nd-order accuracy in space. At the left hand side of the cell interface $(i + 1/2, j)$,

$$\begin{aligned}\bar{\eta}_{i+1/2,j}^{-L} &= \eta_{i,j} + \frac{\psi}{2}(\eta_{i,j} - \eta_{i-1,j}), \quad \bar{h}_{i+1/2,j}^{-L} = h_{i,j} + \frac{\psi}{2}(h_{i,j} - h_{i-1,j}), \\ \bar{q}_{xi+1/2,j}^{-L} &= q_{xi,j} + \frac{\psi}{2}(q_{xi,j} - q_{xi-1,j}), \quad \bar{q}_{yi+1/2,j}^{-L} = q_{yi,j} + \frac{\psi}{2}(q_{yi,j} - q_{yi-1,j}), \\ \bar{z}_{bi+1/2,j}^{-L} &= \bar{\eta}_{i+1/2,j}^{-L} - \bar{h}_{i+1/2,j}^{-L},\end{aligned}\quad (3.16)$$

where ψ is a slope limited function calculated at cell (i, j) for the specific flow variable under consideration. In order to evaluate ψ , flow data are required at the considering cell and its upwind and downwind neighbours. The minmod limiter is used in this work for better numerical stability (e.g. Hirsch 1990; Liang *et al.* 2004; Liang and Borthwick 2009). The face values at the right hand side of the cell interface $(i + 1/2, j)$ are calculated by

$$\begin{aligned}\bar{\eta}_{i+1/2,j}^{-R} &= \eta_{i+1,j} - \frac{\psi}{2}(\eta_{i+1,j} - \eta_{i,j}), \\ \bar{h}_{i+1/2,j}^{-R} &= h_{i+1,j} - \frac{\psi}{2}(h_{i+1,j} - h_{i,j}), \\ \bar{q}_{xi+1/2,j}^{-R} &= q_{xi+1,j} - \frac{\psi}{2}(q_{xi+1,j} - q_{xi,j}), \\ \bar{q}_{yi+1/2,j}^{-R} &= q_{yi+1,j} - \frac{\psi}{2}(q_{yi+1,j} - q_{yi,j}), \\ \bar{z}_{bi+1/2,j}^{-R} &= \bar{\eta}_{i+1/2,j}^{-R} - \bar{h}_{i+1/2,j}^{-R},\end{aligned}\quad (3.17)$$

Herein ψ is evaluated based on the flow information in cell $(i + 1, j)$ and its two direct neighbours. The corresponding velocity components are then obtained by:

$$\begin{aligned}\bar{u}_{i+1/2,j}^{-L} &= \bar{q}_{xi+1/2,j}^{-L} / \bar{h}_{i+1/2,j}^{-L}, \quad \bar{v}_{i+1/2,j}^{-L} = \bar{q}_{yi+1/2,j}^{-L} / \bar{h}_{i+1/2,j}^{-L}, \\ \bar{u}_{i+1/2,j}^{-R} &= \bar{q}_{xi+1/2,j}^{-R} / \bar{h}_{i+1/2,j}^{-R}, \quad \bar{v}_{i+1/2,j}^{-R} = \bar{q}_{yi+1/2,j}^{-R} / \bar{h}_{i+1/2,j}^{-R},\end{aligned}\quad (3.18)$$

Instead of calculating by the above formulae, the velocity components directly equal zero when $h < 1.0 \times 10^{-6}$. It should be noted that the above slope limited linear reconstruction applies only to those wet cells away from the wet-dry interface. In a dry cell or a wet cell next to a dry cell, face values are assumed to be piece-wise constant,

i.e. the same as those at the cell centre. This essentially reduces the second-order accurate scheme to become first-order, which is as expected because, near to flow discontinuity (e.g. wet-dry interface, shock), the accuracy of the high-order scheme automatically reduces to first-order due to the slope limiting process.

Riemann states are then obtained from the above linear reconstructed face values to define the local Riemann problems. The first but important step is to define a single bed elevation at the cell interface $(i + 1/2, j)$:

$$z_{bi+1/2,j} = \max(z_{bi+1/2,j}^{-L}, z_{bi+1/2,j}^{-R}), \quad (3.19)$$

This is also used by Audusse *et al.* (2004) in the context of hydrostatic reconstruction. The Riemann states of water depth are then defined as:

$$h_{i+1/2,j}^L = \max(0, \eta_{i+1/2,j}^{-L} - z_{bi+1/2,j}), \quad h_{i+1/2,j}^R = \max(0, \eta_{i+1/2,j}^{-R} - z_{bi+1/2,j}), \quad (3.20)$$

The Riemann states of the other flow variables are evaluated as follows:

$$\begin{aligned} \eta_{i+1/2,j}^L &= h_{i+1/2,j}^L + z_{bi+1/2,j}, & \eta_{i+1/2,j}^R &= h_{i+1/2,j}^R + z_{bi+1/2,j}, \\ q_{xi+1/2,j}^L &= \bar{u}_{i+1/2,j}^{-L} h_{i+1/2,j}^L, & q_{xi+1/2,j}^R &= \bar{u}_{i+1/2,j}^{-R} h_{i+1/2,j}^R, \\ q_{yi+1/2,j}^L &= \bar{v}_{i+1/2,j}^{-L} h_{i+1/2,j}^L, & q_{yi+1/2,j}^R &= \bar{v}_{i+1/2,j}^{-R} h_{i+1/2,j}^R, \end{aligned} \quad (3.21)$$

Obviously, the above reconstruction gives non-negative water depth and the Riemann problem is locally defined on a horizontal bed. By carefully selecting a Riemann solver, the above numerical treatment leads to an overall numerical scheme preserving non-negative (water depth) solutions (Marche *et al.* 2007).

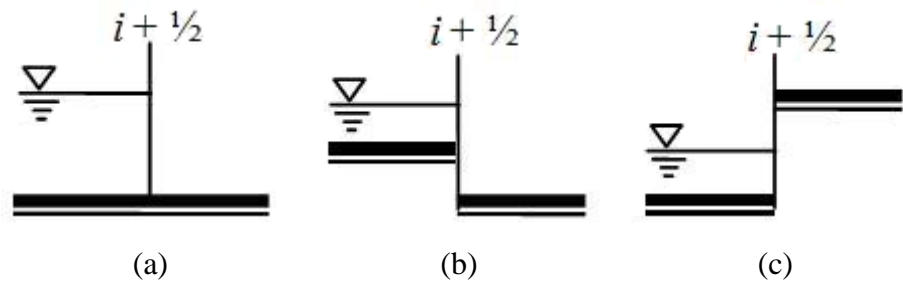


Figure 3.3 Three possible dry-bed configurations in numerical computation.

It is obvious that the above reconstruction of Riemann states does not affect the well-balanced property of the pre-balanced shallow water equations when applying to a wet-bed case. Dry-bed calculation may be generalised into the three cases as illustrated in

water level $\eta \equiv \text{constant}$). The flux cannot be balanced by that across the cell interface $(i - \frac{1}{2}, j)$, calculated against the actual water level $\eta \equiv \text{constant}$. This creates a spurious net momentum flux into cell (i, j) and thus drive the still water into motion, which leads to the violation of the well-balancing property. In order to cure this, a simple local bed modification method is implemented. The difference between the actual and *fake* water surfaces may be calculated at cell interface $(i + \frac{1}{2}, j)$ by

$$\Delta z = \max\left(0, (z_{bi+1/2,j} - \bar{\eta}_{i+1/2,j}^{-L})\right), \quad (3.22)$$

as indicated in Figure 3.4. Then the bed elevation and the stage component of Riemann states are locally and instantaneously modified by subtracting Δz from the original values

$$\begin{aligned} z_{bi+1/2,j} &\leftarrow z_{bi+1/2,j} - \Delta z, \\ \eta_{i+1/2,j}^L &\leftarrow \eta_{i+1/2,j}^L - \Delta z, \\ \eta_{i+1/2,j}^R &\leftarrow \eta_{i+1/2,j}^R - \Delta z, \end{aligned} \quad (3.23)$$

Now we have $\eta_{i+1/2,j}^L = \eta_{i+1/2,j}^R = z_{bi+1/2,j} = \eta$ and no spurious flux is calculated for the case of lake at rest, which brings back the well-balancing.

Now the Riemann states obtained in (3.21) and (3.23) can be employed by a proper Riemann solver to calculate the interface fluxes $(\mathbf{f}_{i+1/2, j})$. The HLLC approximate Riemann solver is chosen in this work because it is easy to implement for applications involving wetting and drying and automatically satisfies entropy conditions (Toro 2001). The structure of the HLLC Riemann solver is shown in Figure 3.5.

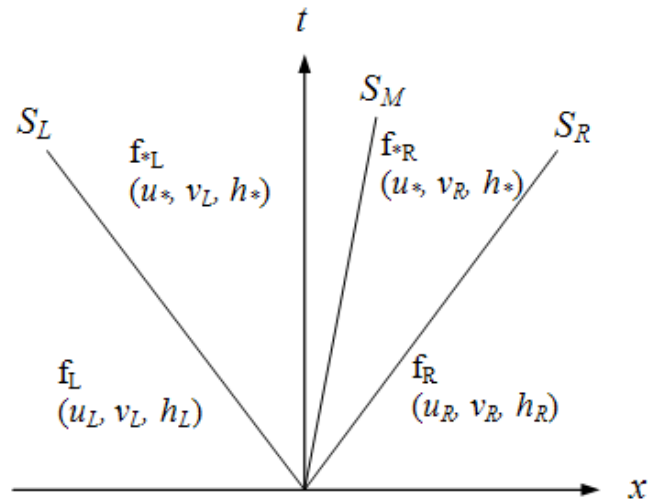


Figure 3.5 The HLLC Riemann solver structure.

Taking the east interface flux as an example, $\mathbf{f}_{i+1/2,j}$ can be calculated by the following formula:

$$\mathbf{f}_{i+1/2,j} = \begin{cases} \mathbf{f}_L & \text{if } 0 \leq S_L \\ \mathbf{f}_{*L} & \text{if } S_L \leq 0 \leq S_M \\ \mathbf{f}_{*R} & \text{if } S_M \leq 0 \leq S_R \\ \mathbf{f}_R & \text{if } 0 \geq S_R \end{cases}, \quad (3.24)$$

where \mathbf{f}_L and \mathbf{f}_R are the left and right flux vectors and \mathbf{f}_{*L} and \mathbf{f}_{*R} are the left and right part flux vectors at the middle region in a local Riemann problem. \mathbf{f}_{*L} and \mathbf{f}_{*R} can be evaluated as follows

$$\mathbf{f}_{*L} = \begin{bmatrix} \mathbf{f}_{1*} \\ \mathbf{f}_{2*} \\ \mathbf{f}_{1*} \cdot \nu_L \end{bmatrix}, \quad \mathbf{f}_{*R} = \begin{bmatrix} \mathbf{f}_{1*} \\ \mathbf{f}_{2*} \\ \mathbf{f}_{1*} \cdot \nu_R \end{bmatrix}, \quad (3.25)$$

in which ν_L and ν_R are the left and right tangential velocity components in a local Riemann problem, \mathbf{f}_{1*} and \mathbf{f}_{2*} are the first and second entries of the flux vector \mathbf{f} in the middle region that are evaluated by the following HLL formula proposed by Harten *et al.* (1983)

$$\mathbf{f}_* = \frac{S_R \mathbf{f}_L - S_L \mathbf{f}_R + S_L S_R (\mathbf{u}_R - \mathbf{u}_L)}{S_R - S_L}, \quad (3.26)$$

In equation (3.26), S_L , S_M and S_R are the estimates of the left, middle and right wave speeds. Suggested by Fraccarollo and Toro (1995), S_L and S_R can be computed by the following formulae:

$$S_L = \begin{cases} u_R - 2\sqrt{gh_R} & \text{if } h_L = 0 \\ \min(u_L - \sqrt{gh_L}, u_* - \sqrt{gh_*}) & \text{if } h_L > 0 \end{cases}, \quad (3.27)$$

$$S_R = \begin{cases} u_L + 2\sqrt{gh_L} & \text{if } h_R = 0 \\ \max(u_R + \sqrt{gh_R}, u_* + \sqrt{gh_*}) & \text{if } h_R > 0 \end{cases}, \quad (3.28)$$

$$u_* = \frac{1}{2}(u_L + u_R) + \sqrt{gh_L} - \sqrt{gh_R}, \quad (3.29)$$

$$h_* = \frac{1}{g} \left[\frac{1}{2}(\sqrt{gh_L} + \sqrt{gh_R}) + \frac{1}{4}(u_L - u_R) \right]^2, \quad (3.30)$$

As Toro (2001) suggested, the middle wave speed S_M can be calculated by

$$S_M = \frac{S_L h_R (u_R - S_R) - S_R h_L (u_L - S_L)}{h_R (u_R - S_R) - h_L (u_L - S_L)}, \quad (3.31)$$

Then the fluxes across the east interface of cell (i, j) can be calculated by (3.24). The Riemann states and the corresponding fluxes $(\mathbf{f}_{i-1/2, j}, \mathbf{g}_{i, j+1/2}, \mathbf{g}_{i, j-1/2})$ on the other cell interfaces are computed in an identical way.

3.2.3 Calculation of the source terms

In order to update the flow variables to a new time step, the source terms must also be evaluated in a compatible way in order to maintain the well-balanced solutions with non-negative water depth. Due to the use of the pre-balanced shallow water equations (3.1) and (3.7), the bed slope source terms can be simply calculated by a central-differencing scheme at the cell centre. The x -direction slope source term is discretized as

$$-g\eta \frac{\partial z_b}{\partial x} = -g\bar{\eta} \left(\frac{z_{b_{i+1/2, j}} - z_{b_{i-1/2, j}}}{\Delta x} \right), \quad (3.32)$$

where $\bar{\eta} = (\eta_{i-1/2, j}^R + \eta_{i+1/2, j}^L)/2$. Herein the stage Riemann states and face value of bed elevation are those obtained after considering the local bed modification in (3.23). The y -direction slope source term is discretized in a similar way. It should be emphasised that, based on the pre-balanced shallow water equations (3.1) and (3.7), this simple slope term discretization combining with the aforementioned non-negative reconstructing technique provides a robust well-balanced scheme for different types of shallow flow hydrodynamics over complex topography. An important advantage of the current numerical scheme is that there is no need of any clipping tricks, like those used by Brufau *et al.* (2004) and Liang and Borthwick (2009), to modify the flow variables when a wet-dry interface is present. As a consequence, the absolute mass conservation is guaranteed and this is one of the most important features a flood modelling tool should have.

When modelling realistic flood events, bed friction is an important force influencing the flow evolution. It is also a main parameter for calibrating a flood model. Therefore it should be included explicitly in the numerical model. However, inclusion of the bed friction terms in a numerical scheme is not a trivial task, especially when the application

is involving wetting and drying. Due to the presence of water depth in the denominator of the friction terms, the friction force could be exaggerated and become large enough to reverse the flow when the water depth is vanishing near the wet-dry front. This is physically incorrect and causes numerical instability. For better stability, this work uses a splitting point-implicit scheme (Bussing and Murman 1988; Fiedler and Ramirez 2000) to evaluate the friction component of the source terms and the following ordinary differential equation (ODE) is solved:

$$\frac{d\mathbf{q}}{dt} = \mathbf{S}_f, \quad (3.33)$$

where $\mathbf{S}_f = [0 \quad S_{fx} \quad S_{fy}]^T$ with $S_{fx} = -\tau_{bx}/\rho$ and $S_{fy} = -\tau_{by}/\rho$. In the x -direction, the friction term may be isolated and expanded using a Taylor series as (Fiedler and Ramirez 2000):

$$S_{fx}^{k+1} = S_{fx}^k + \left(\frac{\partial S_{fx}}{\partial q_x} \right)^k \Delta q_x + o(\Delta q_x^2), \quad (3.34)$$

where $\Delta q_x = q_x^{k+1} - q_x^k$. Ignoring the higher-order terms and substituting it into the x -direction entry of (3.33), the following time marching formula can be obtained for q_x :

$$q_x^{k+1} = q_x^k + \Delta t \left(\frac{S_{fx}}{D_x} \right)^k = q_x^k + \Delta t F_x, \quad (3.35)$$

where $D_x = 1 - \Delta t \left(\partial S_{fx} / \partial q_x \right)^k$ is the coefficient derived for a point implicit scheme in the x -direction and F_x is the friction source term including the implicit coefficient.

As mentioned previously, inclusion of friction terms may affect the stability of the numerical scheme when flow computation is performed near to the wet-dry front with disappearing water depth. Liang and Marche (2009) derived a limiting value for F_x by considering $q_x^{k+1} q_x^k \geq 0$, i.e. the maximum effect of friction force is to stop the fluid:

$$F_x = \begin{cases} -q_x^k / \Delta t & \text{if } q_x^k \geq 0 \text{ and } F_x < -q_x^k / \Delta t \\ -q_x^k / \Delta t & \text{if } q_x^k \leq 0 \text{ and } F_x > -q_x^k / \Delta t \end{cases}, \quad (3.36)$$

In implementing this, the value of F_x is replaced by the above critical one when it is computed beyond the limit. Similar treatment can be applied to the y -direction equation.

3.2.4 CFL criterion

The current second-order finite volume scheme is overall explicit and its numerical stability is controlled by the Courant-Friedrichs-Lewy (CFL) criterion. A proper time step (Δt) can be decided by the following formula:

$$\Delta t = C \cdot \min \left[\frac{\Delta x_{i,j}}{|u_{i,j}| + \sqrt{gh_{i,j}}}, \frac{\Delta y_{i,j}}{|v_{i,j}| + \sqrt{gh_{i,j}}} \right], \quad (3.37)$$

where $\Delta x_{i,j}$ and $\Delta y_{i,j}$ are the dimensions of cell (i, j) in the x - and y -direction; $u_{i,j}$ and $v_{i,j}$ are the depth-averaged velocity components at the cell centre and C is the Courant number ($0 < C \leq 1$). In the computation, the Courant number is normally set to be 0.5.

3.2.5 Boundary condition

In this work, slip and transmissive open boundary conditions are applied to the test cases. In the context of a Cartesian grid, the boundary conditions can be imposed in the x -direction as follows.

1) slip boundary

$$h_B = h_I, \quad u_B = -u_I, \quad v_B = v_I, \quad (3.38)$$

2) open boundary

$$h_B = h_I, \quad u_B = u_I, \quad v_B = v_I, \quad (3.39)$$

where u and v are the depth-averaged velocity components in normal and tangential directions to the boundary; subscripts B and I denote the positions at the boundary (ghost) and inner boundary cells, respectively.

In practice, the geometry of the computational domain is complicated and the boundary curves may not be aligned with the edges of a Cartesian cell. Liang and Borthwick (2008) recommend a new simple local boundary modification method to cope with this kind of non-aligned boundaries.

The Cartesian grid is separated by the non-aligned boundary into two different areas, which are defined as the solid area and the fluid area. The cells with the centre in the

solid area are defined as the solid cell, which are not included in the computation. The other cells in the computational domain are the fluid cells. And the fluid cells with at least one solid neighbour are called boundary fluid cells. The values of flow variables in a ghost cell can be calculated from those in the neighbouring boundary fluid cells, using the local boundary modification method. Herein, the local boundary modification method is presented by an example shown in Figure 3.6, in which the shadow part is the solid area; the green line is the curved boundary; C is the boundary fluid cell under consideration; G is the ghost cell; O' is the midpoint at the interface of C and G , i.e. the boundary point without using a special boundary treatment.

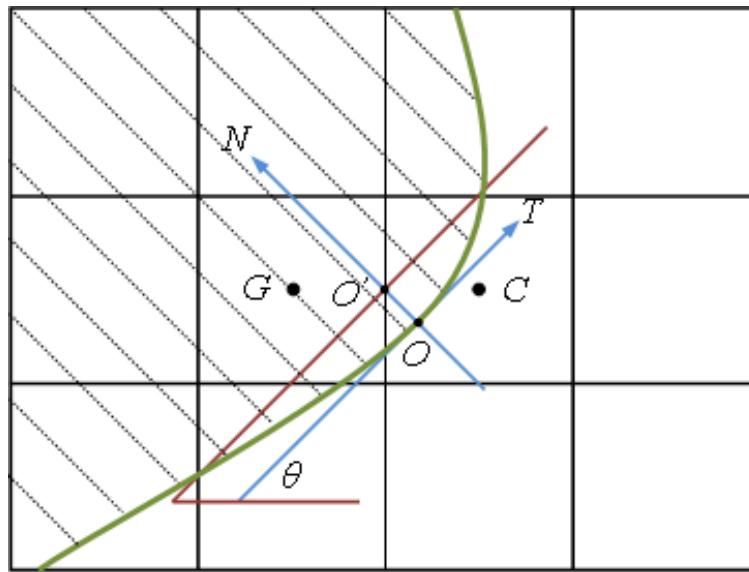


Figure 3.6 Sketch of the local boundary modification method.

The first step is to find the new boundary point O , which is the nearest seeding point to O' along the curved boundary. θ is the angel between the tangential direction at point O and the x -direction. Then the boundary point O' is assumed to be moved to O . This shift produces small error, which has no influence on the overall computational accuracy (Liang and Borthwick 2008). The tangential and normal directions of O' are assumed to be the same as those of O . Then the velocity is decompounded at the tangential and normal directions. For the slip boundary condition in equation (3.38), the velocity components can be described as

$$\begin{aligned} \text{Normal direction:} & \quad -u_c \sin \theta + v_c \cos \theta = -(-u_G \sin \theta + v_G \cos \theta) \\ \text{Tangential direction:} & \quad u_c \cos \theta + v_c \sin \theta = u_G \cos \theta + v_G \sin \theta \end{aligned}, \quad (3.40)$$

The above equations can be rearranged as

$$\begin{aligned} u_G &= u_C - 2(u_C \sin \theta - v_C \cos \theta) \sin \theta \\ v_G &= v_C + 2(u_C \sin \theta - v_C \cos \theta) \cos \theta \end{aligned} \quad (3.41)$$

where u_G , u_C , v_G and v_C are the velocity components in x - and y -directions at the ghost cell and the boundary fluid cell, respectively. θ can be estimated analytically.

First, a series of seeding points is generated to represent the curved boundary. This step is carried out after the Cartesian grid generation. Then the local tangential and normal direction of O can be determined from two neighbour seeding points. Therefore, θ can be calculated by

$$\theta = \arctan\left(\frac{y_s(i+1) - y_s(i-1)}{x_s(i+1) - x_s(i-1)}\right), \quad (3.42)$$

in which x_s and y_s are the coordinates of the seeding points; i is the index of O . Fine resolution of seeding points is required for good representation of the boundary curve and accurate calculation of θ . Then the values of θ are stored for the computation. Hence, the computational expense can be decreased during the entire simulation.

3.3 Case Studies

3.3.1 Tidal wave flow

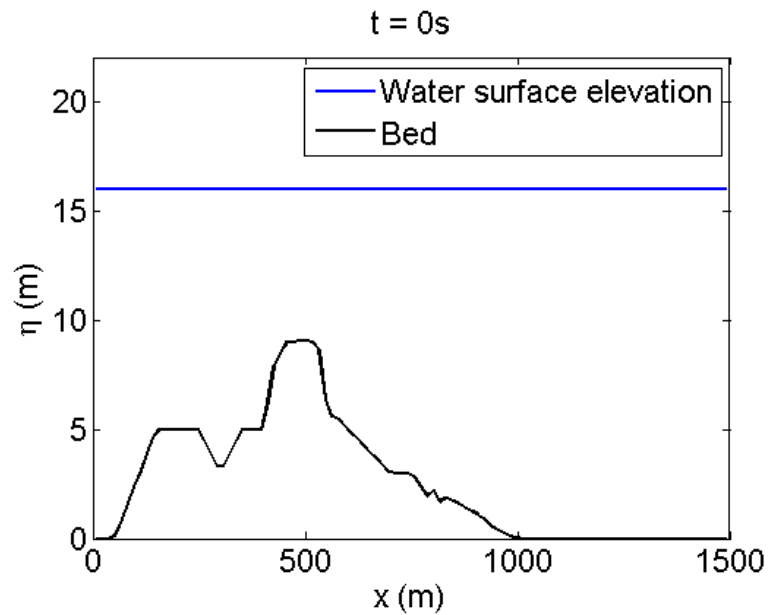


Figure 3.7 Tidal wave flow: the bed topography of the irregular bed.

The first test is to reproduce a tidal wave flow over an irregular bed topography, which was presented at a workshop on dam-break simulations (Goutal and Maurel 1997). The same test problem is also studied by Zhou *et al.* (2001). Here it is used to validate the capability of the present model on dealing with the complex bed topography. This is a one-dimensional problem with bed topography shown in Figure 3.7 and bed elevation defined $z_b(x)$ in Table 3.1. For this 2D model, the channel is 1500 m long and horizontal in y -direction with 150 m width. The channel is assumed to be frictionless.

x	0	50	100	150	250	300	350	400	425	435	450	475	500	505
z_b	0	0	2.5	5	5	3	5	5	7.5	8	9	9	9.1	9
x	530	550	565	575	600	650	700	750	800	820	900	950	1000	1500
z_b	9	6	5.5	5.5	5	4	3	3	2.3	2	1.2	0.4	0	0

Table 3.1 Bed elevation at point x for irregular bed

The analytical solution of the water depth and the velocity component in x -direction is given as below:

$$h(x,t) = H(x) + 4 - 4 \sin \left[\pi \left(\frac{4t}{86400} + \frac{1}{2} \right) \right], \quad (3.43)$$

$$u(x,t) = \frac{(x-L)\pi}{5400h(x,t)} \cos \left[\pi \left(\frac{4t}{86400} + \frac{1}{2} \right) \right], \quad (3.44)$$

The initial and boundary conditions are given as follows,

$$\eta(0) = 16 \text{ m}, \quad (3.45)$$

$$H(x) = \eta(0) - z_b(x), \quad (3.46)$$

$$h(x,0) = H(x), \quad (3.47)$$

$$u(x,0) = 0, \quad (3.48)$$

$$h(0,t) = \eta(0) + 4 - 4 \sin \left[\pi \left(\frac{4t}{86400} \right) + \frac{1}{2} \right], \quad (3.49)$$

$$u(L,t) = 0, \quad (3.50)$$

A uniform grid of 150×15 cells is implemented with $\Delta x = 10$ m, $\Delta y = 10$ m. Initially, it has still water surface with 16 m high. Slip boundary conditions are imposed at the northern and southern boundary walls. The eastern and western ends of this channel are supposed to be inflow and outflow boundaries, respectively. $h(0,t)$ and $u(0,t)$ are given as the inflow boundary conditions while $u(L,t)$ is used to define the outflow boundary. This work is proposed to predict the evolution of the tidal wave for 10800 s.

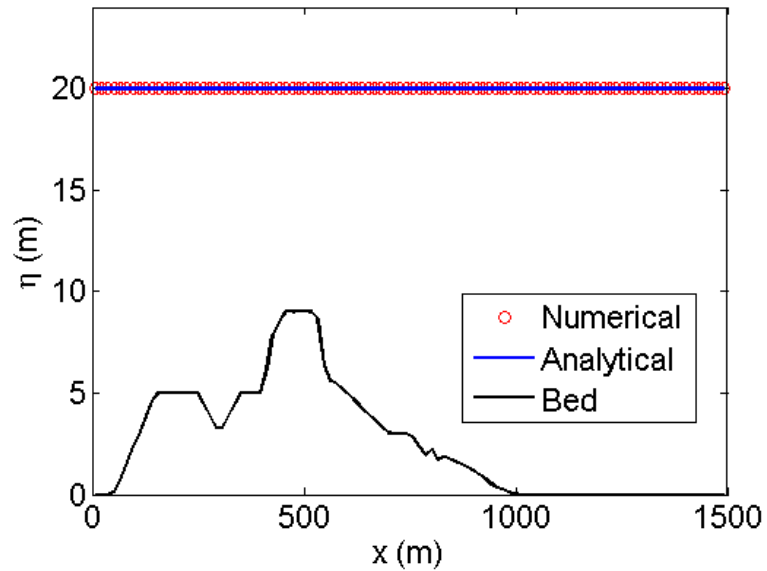


Figure 3.8 Tidal wave flow: comparison of water surface elevation and the analytical solution at $t = 10800$ s.

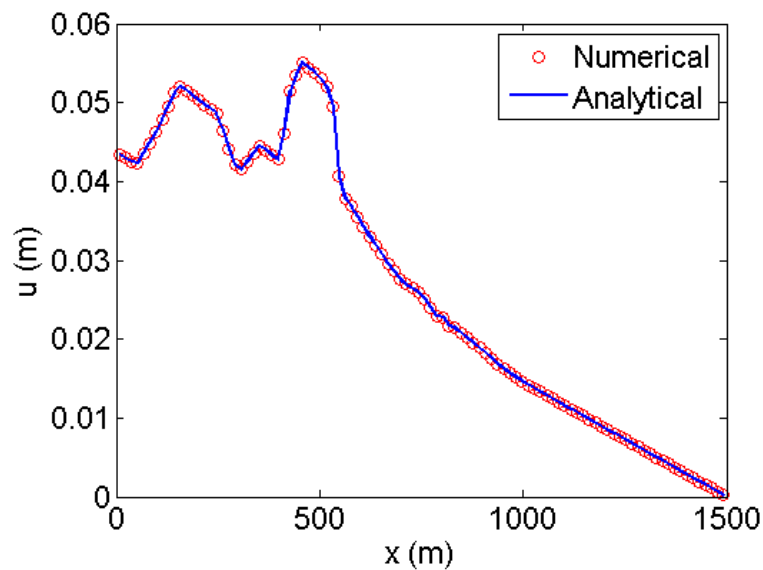


Figure 3.9 Tidal wave flow: comparison of velocity and the analytical solution at $t = 10800$ s.

The comparison of the numerical prediction of water surface elevation with the analytical solution at $t = 10800$ s is shown in Figure 3.8. Close agreement is achieved. Figure 3.9 illustrates the predicted velocity, which also agrees well with the theoretical solution. These results indicate that the present fully 2D shallow flow model has the capability to handle complex bed topography.

3.3.2 Oblique hydraulic jump

In this case, an oblique hydraulic jump happens in an open channel when a supercritical flow interacts with an inclined contraction wall. The computational domain is a $40\text{ m} \times 30\text{ m}$ frictionless floodplain with a flat bed. The supercritical flow comes into the computational domain from the western boundary, which is the inflow boundary. The inflow water depth and velocity component in x -direction are set to be 1 m and 8.57 m/s respectively. At the southern end of the channel, there is an inward deflection of 8.95° to the x -direction, starting at $x = 10\text{ m}$. Theoretically, the jump should occur from $x = 10\text{ m}$, covering a domain with an inward angle of 30° to the x -direction. Then the water depth increases from 1 m to 1.5 m across the jump.

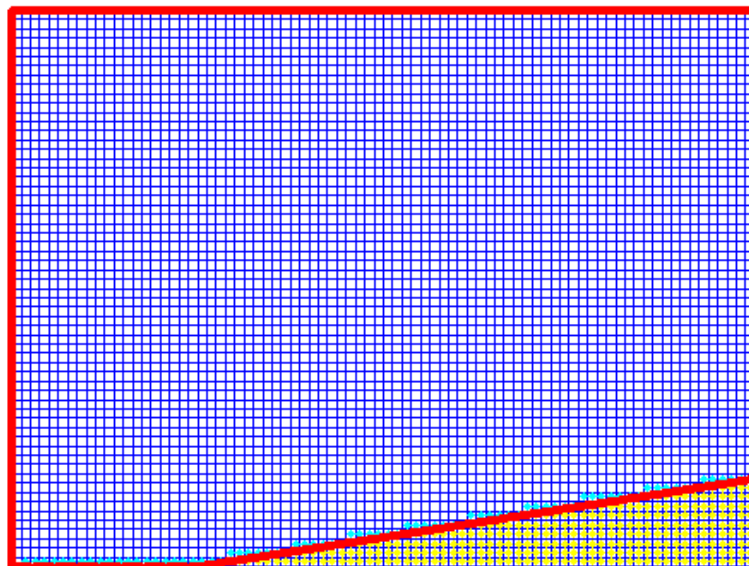


Figure 3.10 Oblique hydraulic jump: the sample computational grid (80×60).

In this case, the local boundary modification method (Liang and Borthwick 2008) is implemented here to deal with the southern non-aligned boundary. And the numerical predictions with/without modification are compared. An example of computational

mesh consists of 80×60 cells shown in Figure 3.10, in which the modified boundary is shown as red line. And the blue grid defines the inner part of the computational domain while the yellow cells are the solid part behind the oblique wall. The southern and northern boundary walls are assumed to be slip boundaries. The eastern boundary is set to be open boundary. The west end of the domain is set to be inflow boundary with a fixed velocity $u = 8.57$ m/s and a fixed water depth $h = 1$ m.

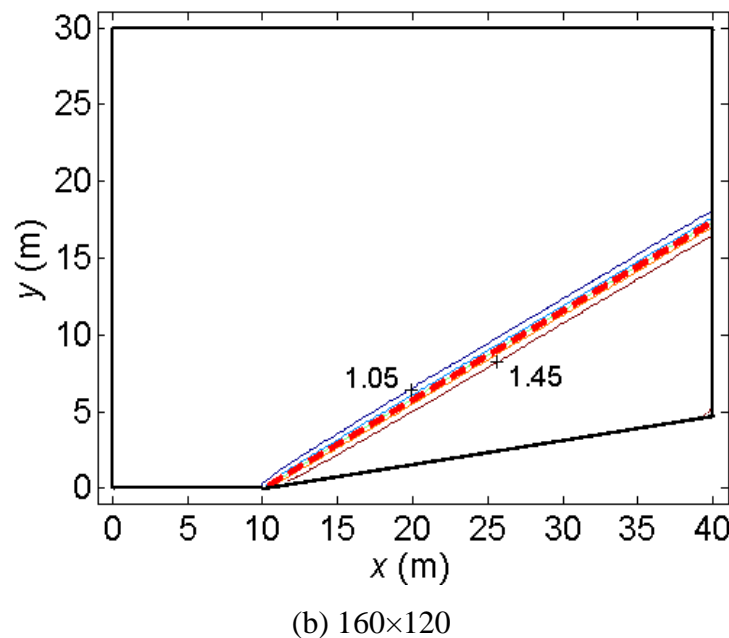
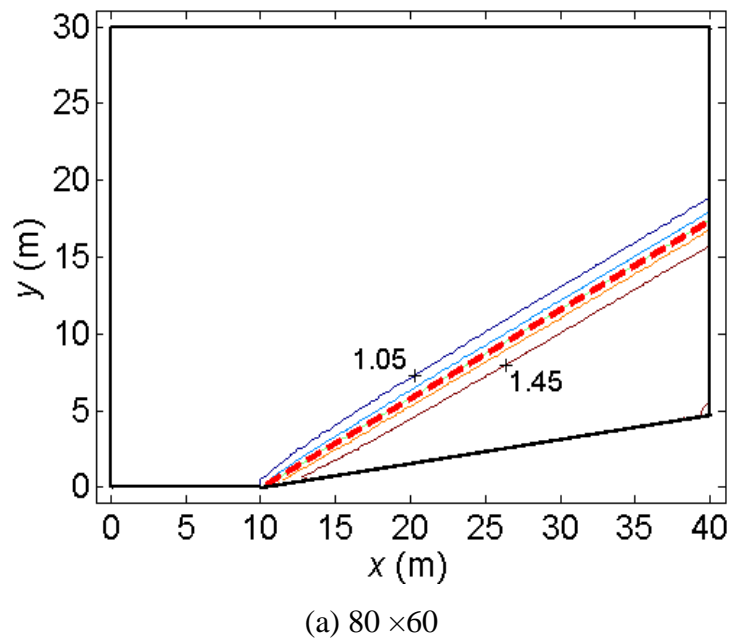


Figure 3.11 Oblique hydraulic jump: water depth contours.

Simulations are first carried out on two different meshes (80×60 , 160×120) with the local boundary modification method activated. Figure 3.11 shows the contour lines of

water depth, where the analytical position of jump is indicated the red dash line. Obviously, the position of jump is accurately predicted and Figure 3.11 (b) gives better converged solution as the result of using higher-resolution grid. Hence, the mesh of 160×120 cells is employed for the following simulations and comparisons.

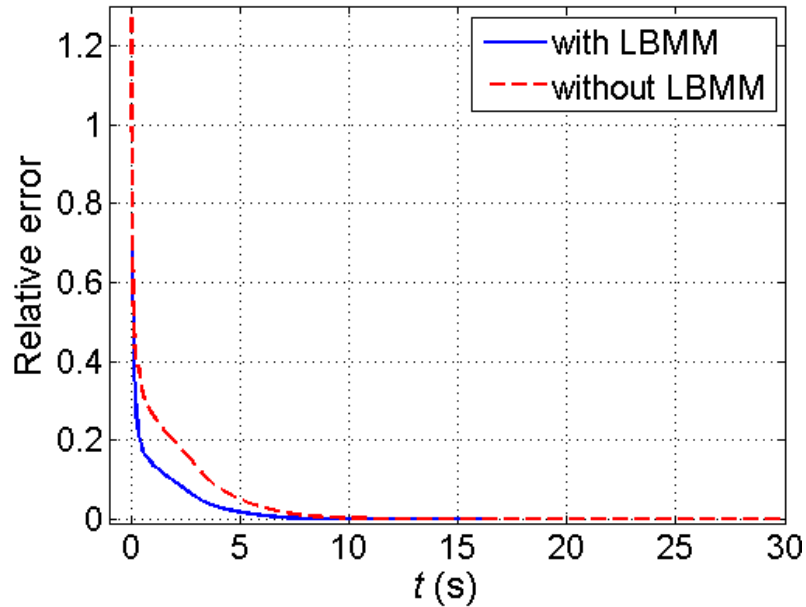
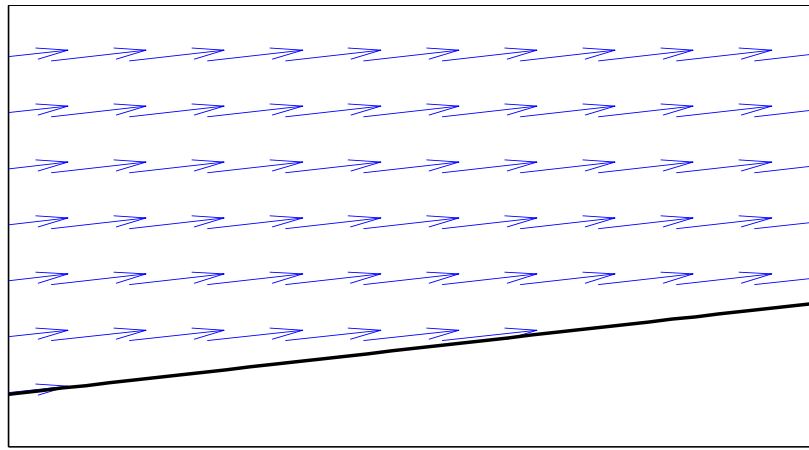


Figure 3.12 Oblique hydraulic jump: the convergence history (LBMM – local boundary modification method).

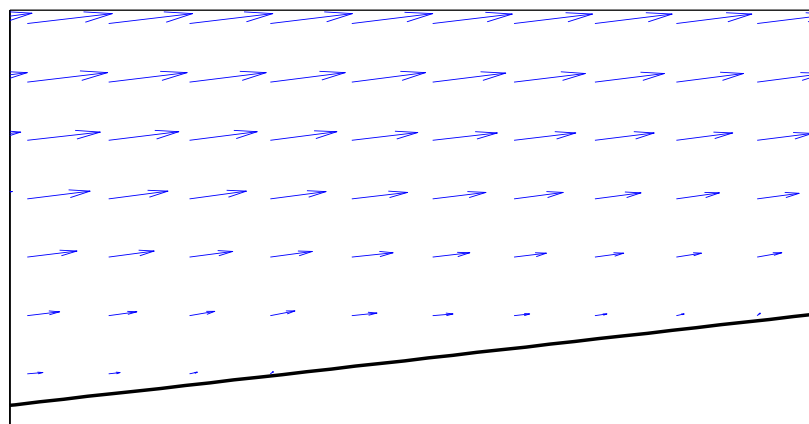
A global relative error (er) of water depth of the current and previous time steps is defined, in order to evaluate the influence of the local boundary modification method on the convergence time of this steady flow, as below,

$$er = \sqrt{\sum_{i,j} \left(\frac{h_{i,j}^k - h_{i,j}^{k-1}}{h_{i,j}^k} \right)^2}, \quad (3.51)$$

where $h_{i,j}^k$ and $h_{i,j}^{k-1}$ are water depth at cell (i, j) calculated in the present and previous time step, respectively. When $er < 1.0 \times 10^{-8}$, the state is assumed to be steady. The converged time is predicted approximate 14 s by the numerical scheme with the local boundary modification. A much longer converged time is produced as 27.5 s without using the local boundary modification method approach illustrated in Figure 3.12. Obviously, the local boundary modification presents computational efficiency in the application with non-aligned boundary.



(a) With the local boundary modification method



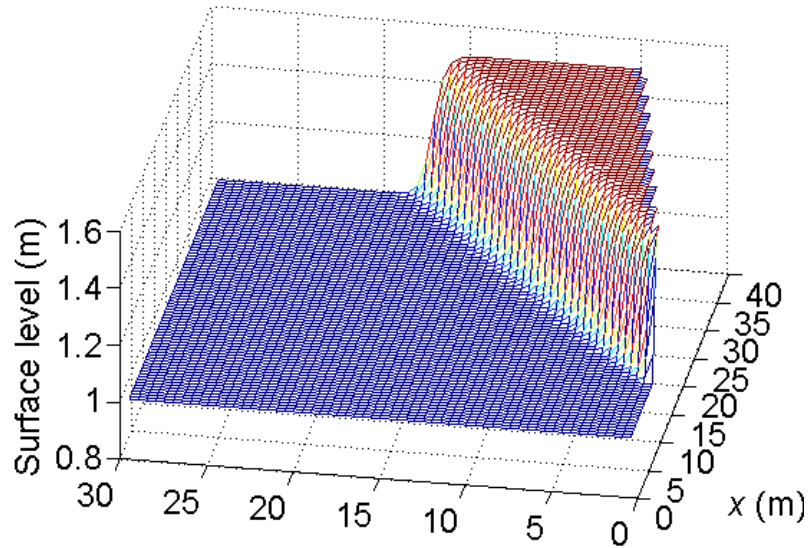
(b) Without using the local boundary modification method

Figure 3.13 Oblique hydraulic jump: velocity field near to the inclined wall.

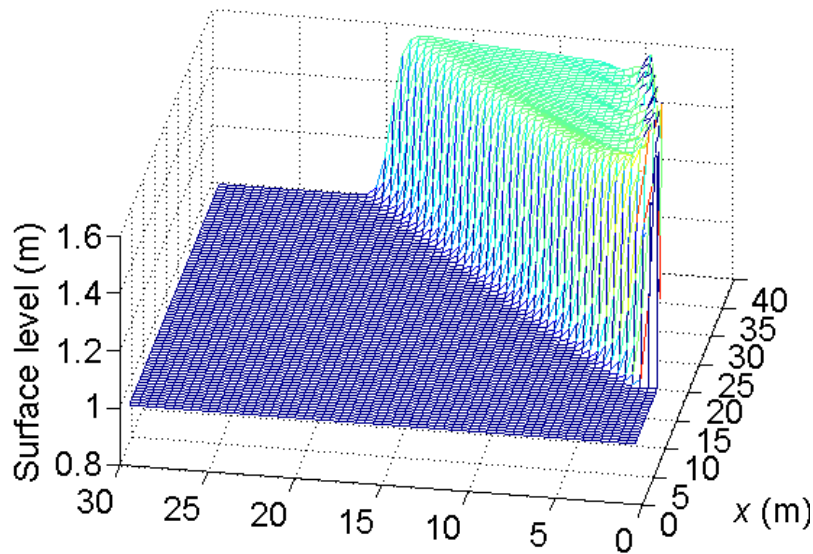
The velocity vectors corresponding to the simulation in Figure 3.11 (b) are presented in Figure 3.13 ((a) prediction with the local boundary modification method; (b) prediction without the local boundary modification method) near to the inclined wall. Due to the application of the local boundary modification method, the predicted velocity vectors are parallel to the inclined boundary without decreasing in magnitude, which is physically correct as shown in Figure 3.13 (a). Compared with the predictions in Figure 3.13 (b), the effectiveness of the local boundary modification method has been proved in predicting the velocity vectors along the inclined boundary.

Figure 3.14 (a) presents the 3D view of water surface which describes the accurate water depth of 1.5 m near to the inclined wall with smooth and steady edge, contributed by the simple local boundary modification method. In Figure 3.14 (b), the unphysical behaviour happens near to the boundary caused by the staircase approximation, which is

adopted for the non-aligned boundary in the Cartesian grid system. A related discussion based on the oblique hydraulic jump case is operated by Roger *et al.* (2001) on the spurious behaviour near to the irregular boundary.



(a) With the local boundary modification method



(b) Without the local boundary modification method

Figure 3.14 Oblique hydraulic jump: the 3D view of water.

Overall, the oblique hydraulic jump has been accurately reproduced by the present Cartesian grid based finite volume Godunov-type scheme. The local boundary modification method (Liang and Borthwick 2008) is implemented to avoid the spurious behaviours near to the non-aligned boundary, which are caused by the staircase

approximation for the non-aligned boundary in Cartesian grid system. Furthermore, the comparison of the numerical simulations demonstrates that the local boundary modification method contributes to the computational efficiency as well.

3.3.3 Shock reflection by a circular cylinder

In this test, a shock reflection by a circular cylinder is reproduced, which is also studied by Causon *et al.* (2000) and Liang *et al.* (2007). The 5 m × 5 m horizontal and frictionless computational domain is approximated by a uniform grid with 200 × 200 cells. A circular cylinder with a radius of $R = 0.5$ m is located at the centre of the domain. The Cartesian coordinate system originates at the domain centre. Four boundaries are all open. The local boundary modification method (Liang and Borthwick 2008) is activated to represent the circular boundary of the cylinder.

The shock evolution starts from the left edge of the circular cylinder travelling to the right, which are recognized as the left side (l) and the right side (r) respectively. The relationship of the two sides are given by Causon *et al.* (2000) in the following equations,

$$h_r = Lh_l, \quad (3.52)$$

$$u_r = c + (u_l - c)/L, \quad (3.53)$$

$$v_r = v_l, \quad (3.54)$$

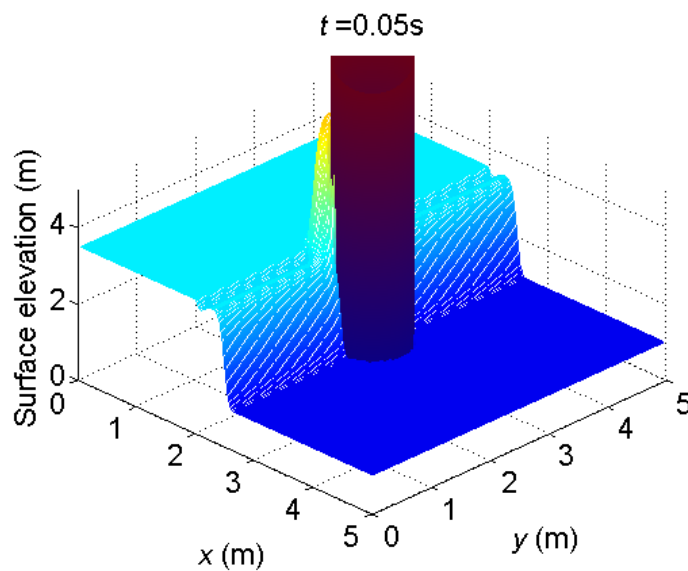
In the above equation, $c (= Fr_s \sqrt{gh_l})$ defines the speed of the shock wave. Herein L is calculated by

$$L = \frac{1}{2} \left(\sqrt{1 + 8(Fr_l - Fr_s)^2} - 1 \right), \quad (3.55)$$

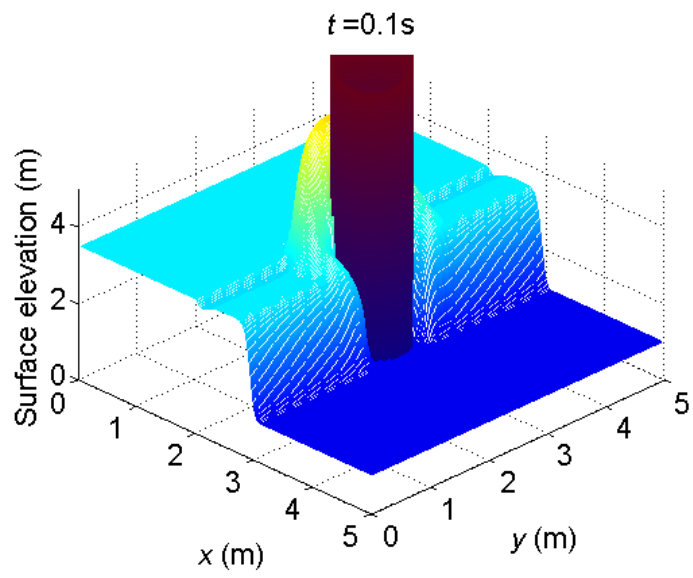
in which $Fr_l = u_l / \sqrt{gh_l}$ is the Froude number of the flow before bore, $Fr_s = 2.81$ is the Froude number of the shock. Before the shock occurs, the still water depth is $h_l = 1.0$ m.

The case of shock reflection by the circular cylinder is investigated by Yang *et al.* (1987), which express the complex phenomena of the shock-shock interaction and the shock wave propagation after reflected by the circular cylinder. The evolution of the shock reflection is described here related to the 3D views of the shock interaction event

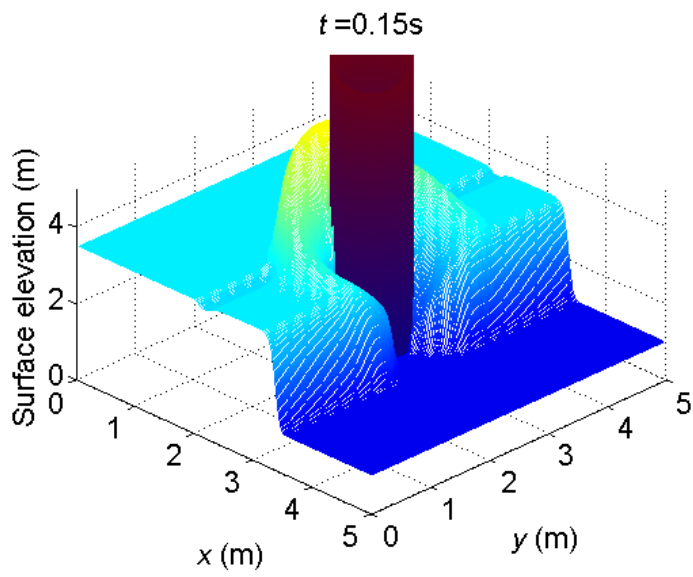
shown in Figure 3.15 and the contour lines presented in Figure 3.16. Theoretically, the bore occurs when the flow encounters the left edge of the circular cylinder from left to right. As shown in Figure 3.15 (a) - (c) and Figure 3.16 (a) - (d), the regular reflection happens as a two-shock system caused by the circular cylinder. The collision front propagates along the surface of the circular cylinder. The two-shock system is symmetric related to the x -axis in this case. As illustrated in Figure 3.15 (d) and Figure 3.16 (e), the two-shock system changes into three-shock system after the two separated collision fronts hit each other. In other words, the regular reflection is transferred to the Mach reflection. The confluence point is changed from the cylinder surface to the triple point of the three shocks, where a slipstream arises. A vortex is forming due to the dynamic effect of the slipstream, which is accurately predicted and presented in Figure 3.15 (f) and Figure 3.16 (g). The interacted shock wave propagates away from the circular cylinder to the right end of the computational domain. Some complex interactions occur in this stage shown in Figure 3.15 (g) and Figure 3.16 (h). The capability of the present shock-capturing Godunov-type scheme on capturing the complex shock interaction has been verified by the accurate numerical simulation of the shock reflection by the circular cylinder.



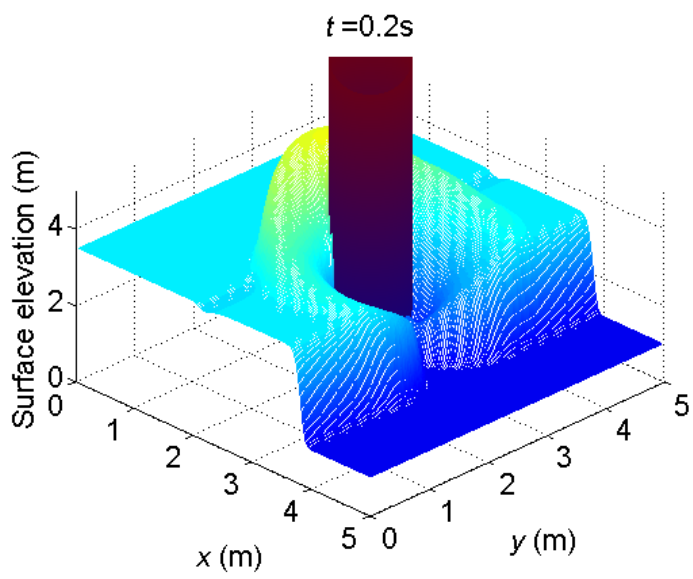
(a)



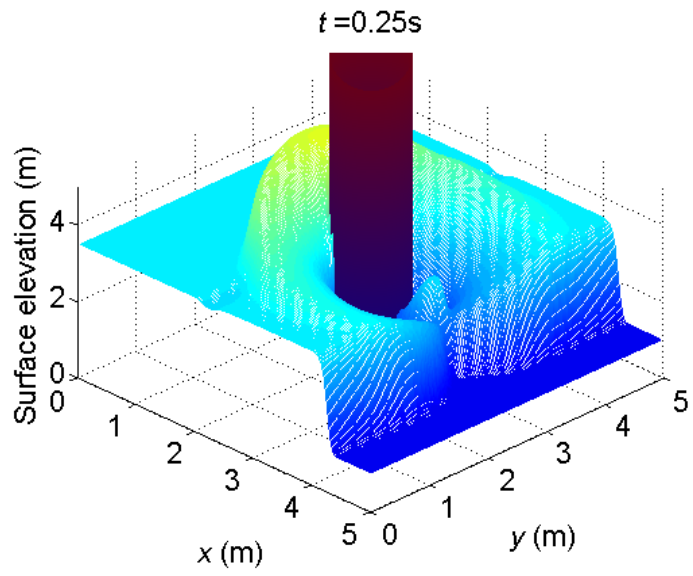
(b)



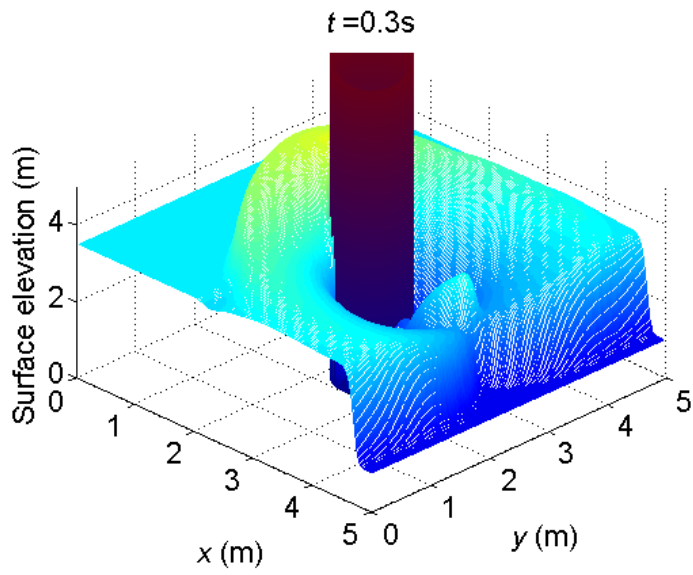
(c)



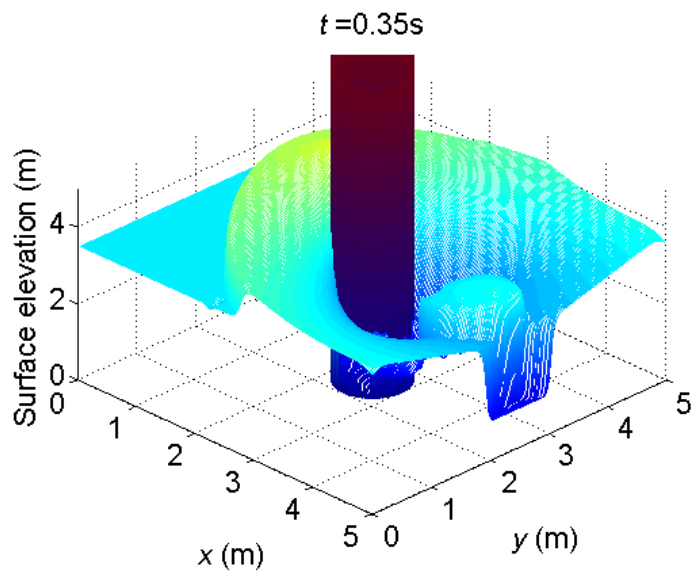
(d)



(e)

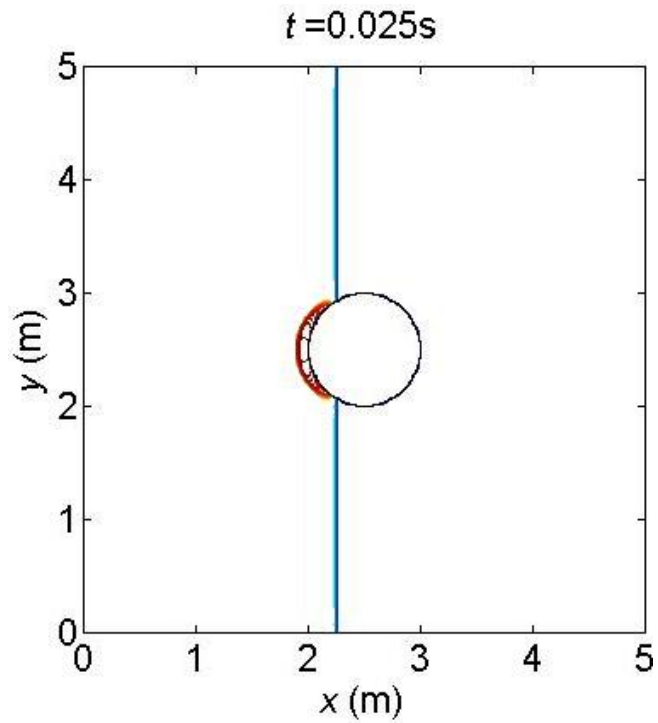


(f)

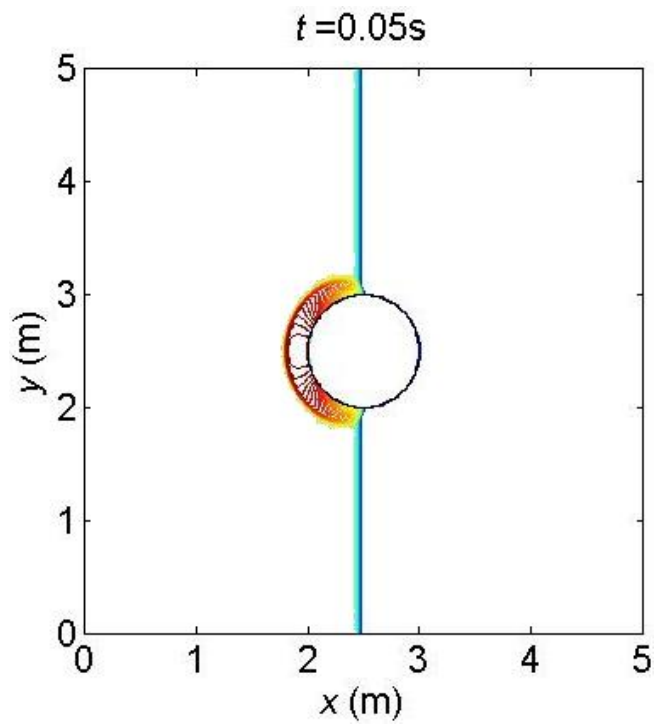


(g)

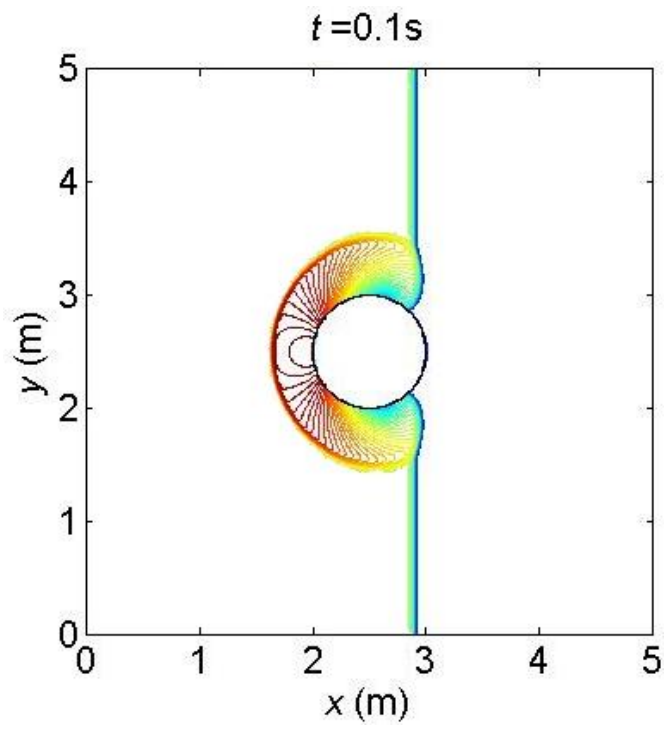
Figure 3.15 Shock reflection by a circular cylinder: the 3D surface view at different times: at (a) $t = 0.05$ s; (b) $t = 0.1$ s; (c) $t = 0.15$ s; (d) $t = 0.2$ s; (e) $t = 0.25$ s; (f) $t = 0.3$ s; (g) $t = 0.35$ s.



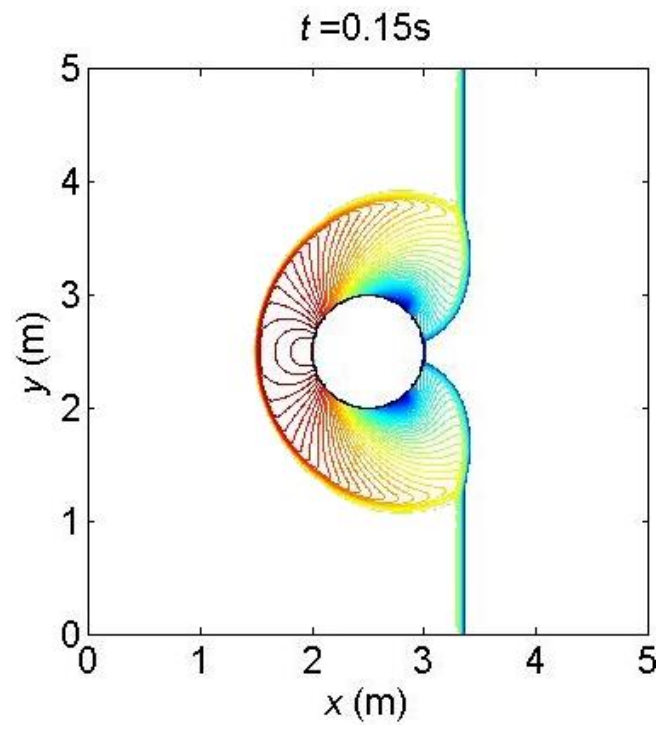
(a)



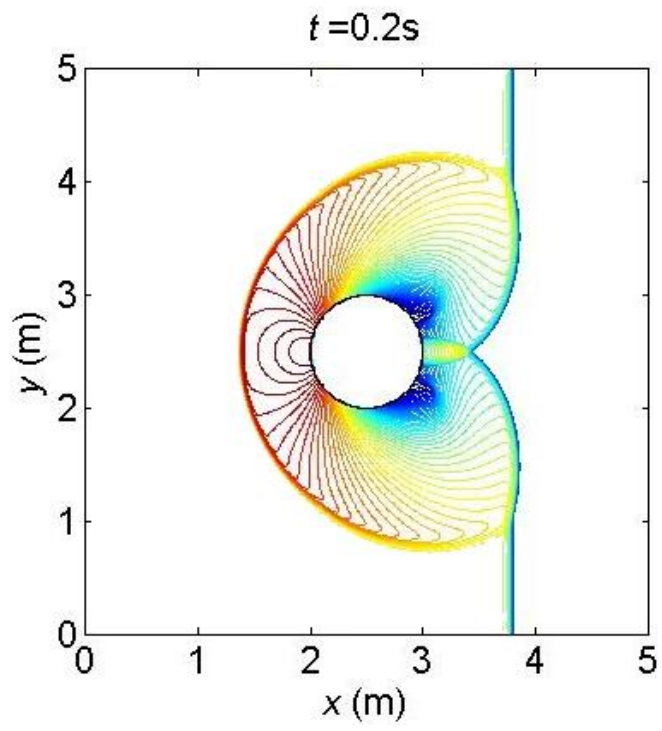
(b)



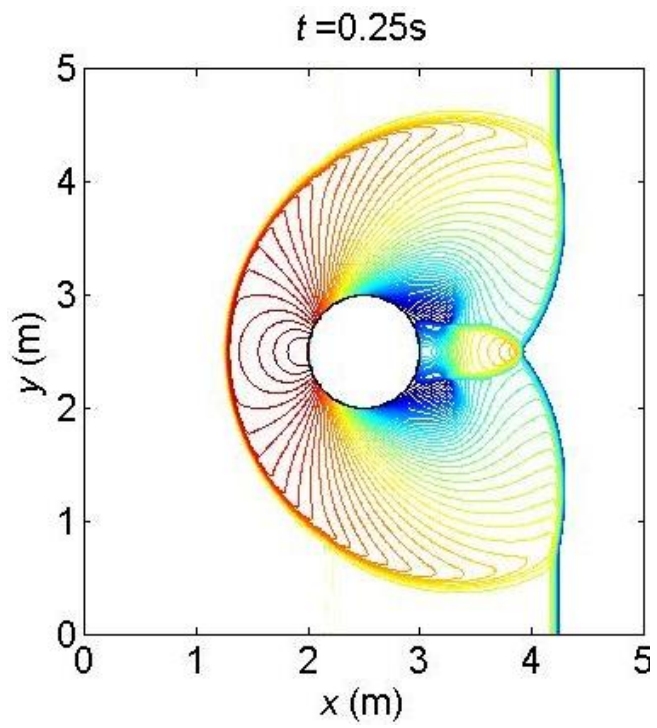
(c)



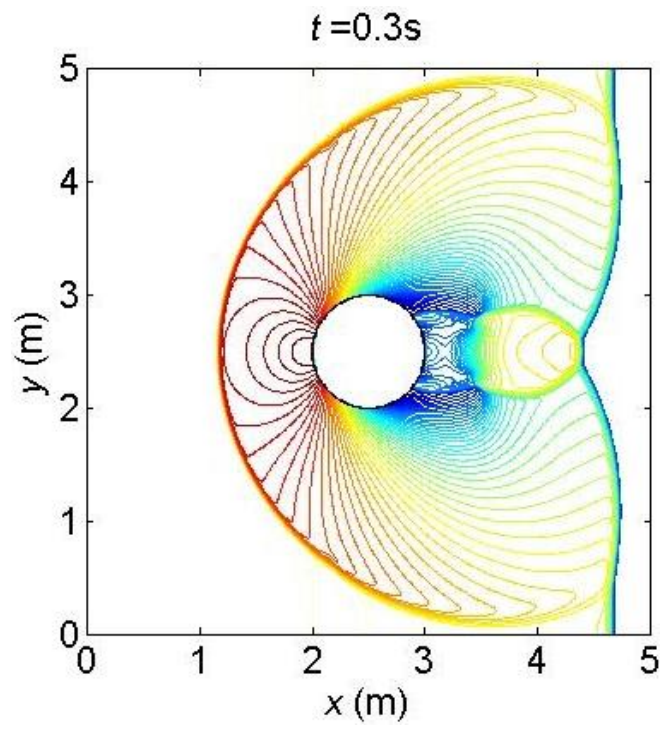
(d)



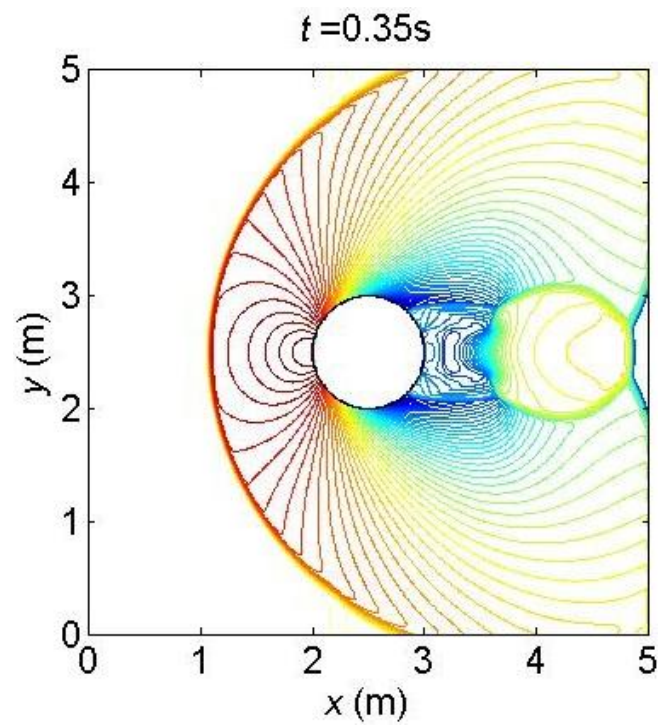
(e)



(f)



(f)



(h)

Figure 3.16 Shock reflection by a circular cylinder: the shock wave depth contours at different times: (a) at $t = 0.025\text{ s}$; (b) $t = 0.05\text{ s}$; (c) $t = 0.1\text{ s}$; (d) $t = 0.15\text{ s}$; (e) $t = 0.2\text{ s}$; (f) $t = 0.25\text{ s}$; (g) $t = 0.3\text{ s}$; (h) $t = 0.35\text{ s}$.

3.3.4 Shock diffraction in an hourglass channel

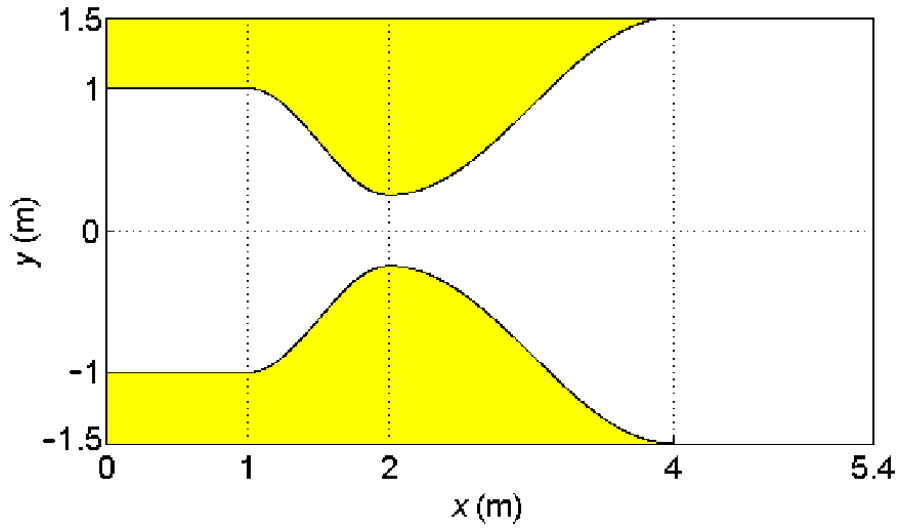


Figure 3.17 Shock diffraction in an hourglass channel: geometry of the contraction-expansion channel.

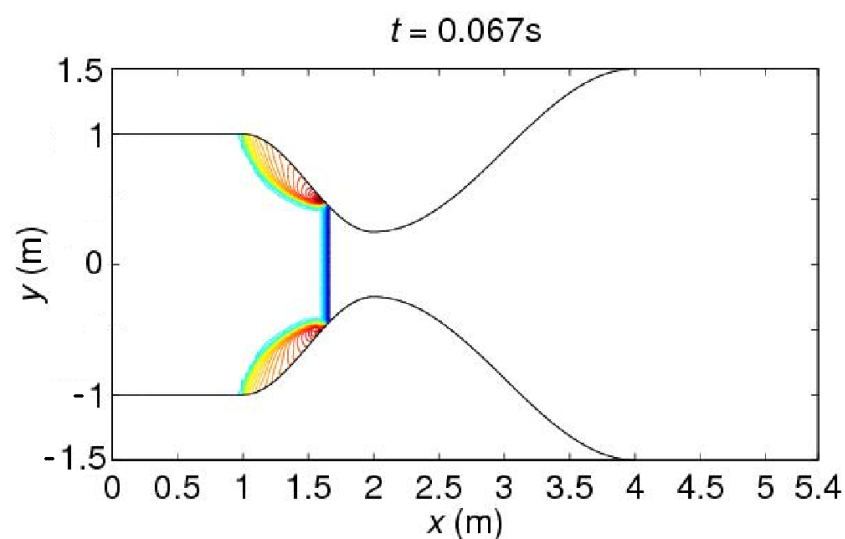
This case is employed to verify the performance of the present model on reproducing the shock propagation at river estuary. The channel is flat and frictionless shown in Figure 3.17. The whole computational domain is $5.4 \times 3.0 \text{ m}^2$, with a 0.5 m wide throat part. The origin of the coordinate system is located at the starting point of the centre line in the x -direction. The hourglass channel is symmetrical against the x -axis. The northern wall of the channel begins with a 1 m straight line, followed by two connected cosine curves at the throat part, and ends with a 1.4 m straight line. Herein the irregular boundary of the computational domain can be calculated by

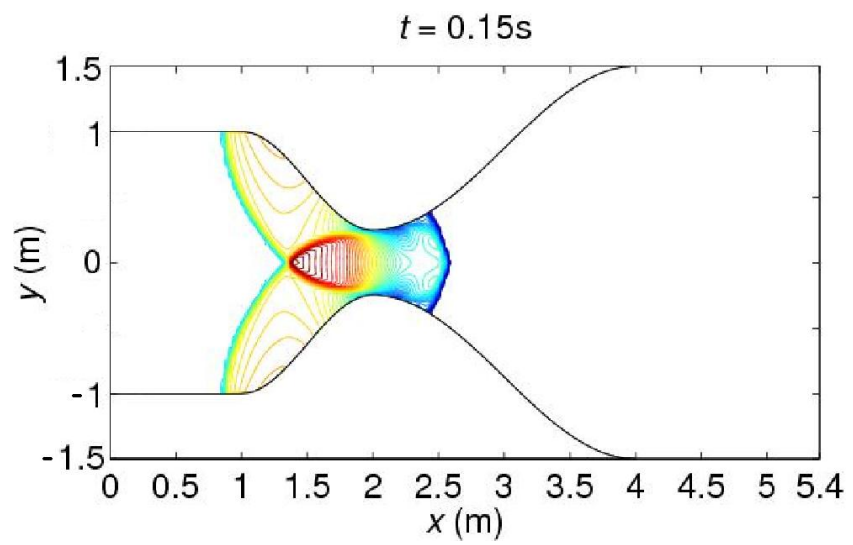
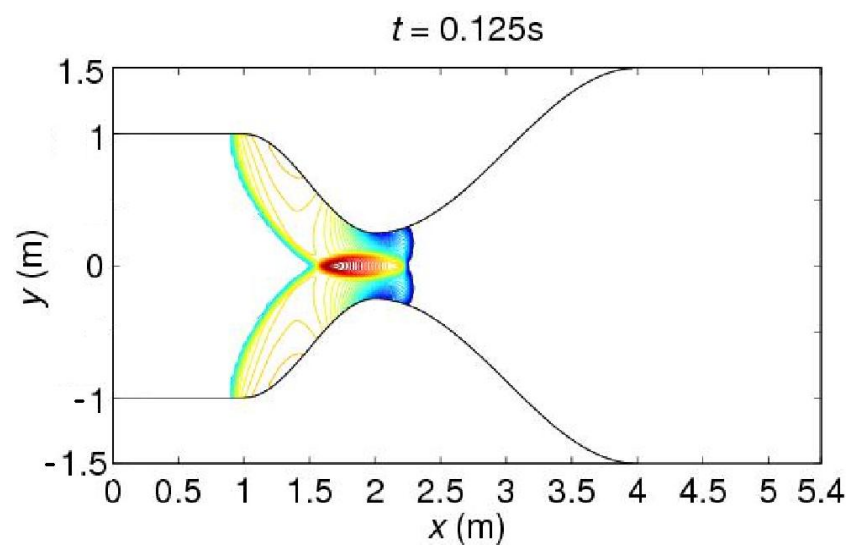
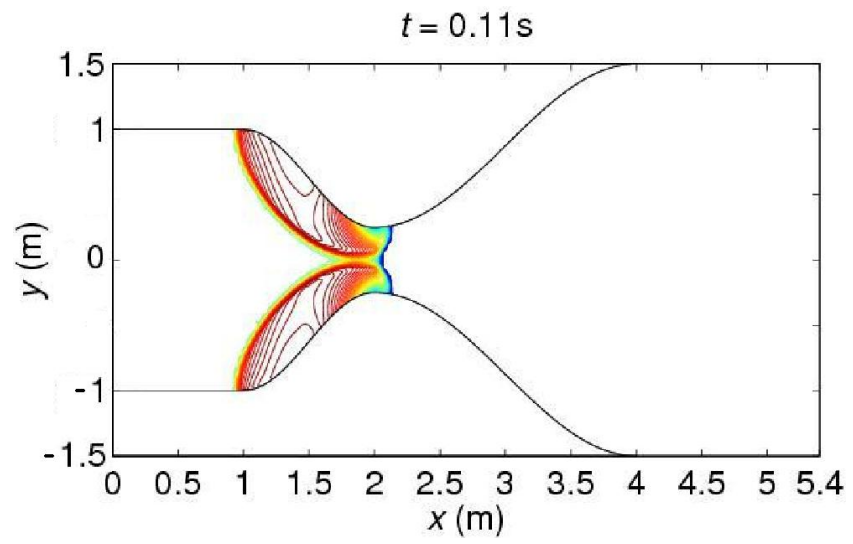
$$y = \begin{cases} 1.0 & 0 \leq x \leq 1 \\ -0.375 \cos(\pi(x-2)) + 0.625 & 1 < x \leq 2 \\ -0.625 \cos\left(\frac{\pi}{2}(x-2)\right) + 0.875 & 2 < x \leq 4 \\ 1.5 & 4 < x \leq 5.4 \end{cases}, \quad (3.56)$$

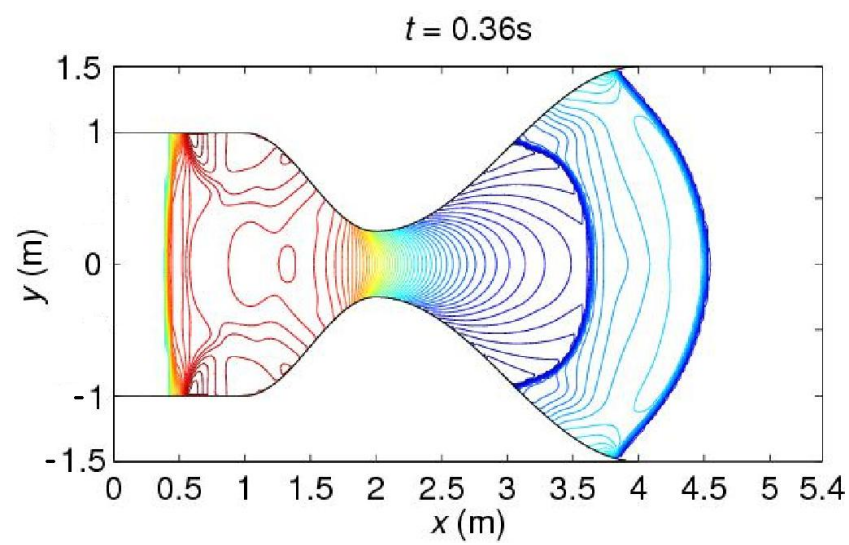
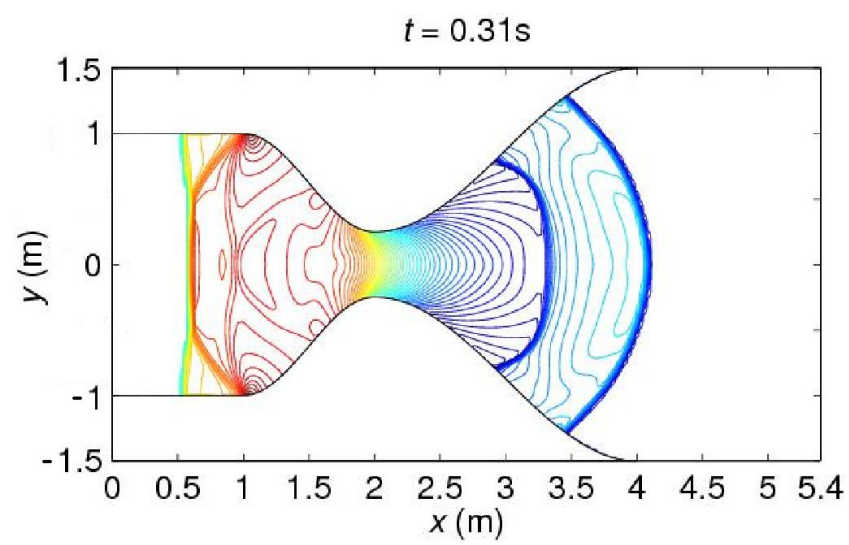
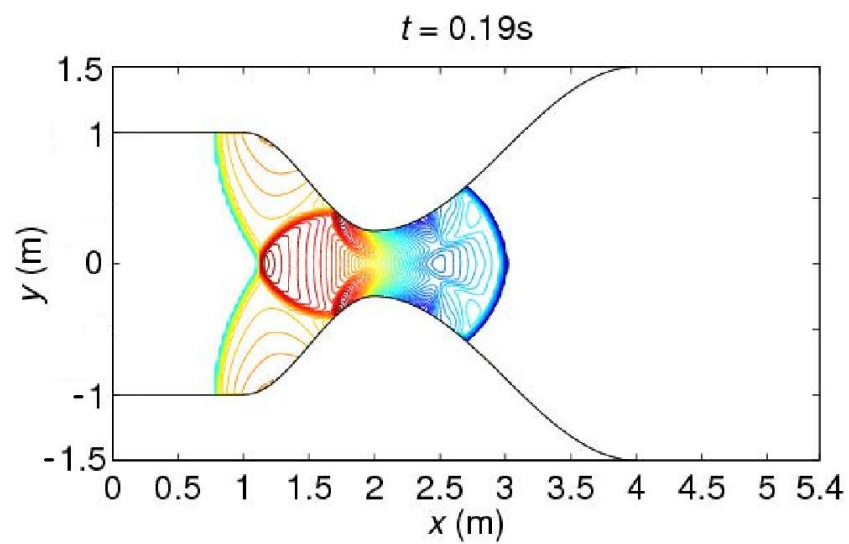
Initially, the flow in the hourglass channel is separated into two parts defined by a vertical line $x = 1 \text{ m}$, which can be recognized as pre-bore part ($x < 1 \text{ m}$) and post-bore part ($x > 1 \text{ m}$). The initial flow variables in the pre-bore part is $h = 1 \text{ m}$; $u = 0 \text{ m/s}$; $v = 0 \text{ m/s}$. The initial flow variables in the post-bore part can be calculated using the bore wave relations described in (3.52)-(3.55). Herein, $Fr_s = 3$. In this model, the northern

and southern walls are set to be slip boundaries while the western and eastern walls are assumed to be transmissive boundaries. The local bed modification method is used to define the hourglass channel wall. A mesh of 540×300 grid cells is implemented here for computation.

Figure 3.18 illustrates the water depth contours of the bore diffraction in an hourglass channel at $t = 0.067$ s, $t = 0.11$ s, $t = 0.125$ s, $t = 0.15$ s, $t = 0.19$ s, $t = 0.31$ s, $t = 0.36$ s and $t = 0.4$ s. Theoretically, the evolution of the shock wave interaction can be described as follows, corresponding to Figure 3.18, The incident flow begins from left to right, i.e. from pre-bore part to post-bores part. Firstly, the incident flow is reflected by the contractive part of the hourglass channel as the regular reflection system including two shocks. And then the two-shock system is changed into three-shock system as Mach reflection system when the shock wave arrives at the throat of the hourglass channel. After that, the Mach reflection travels to the right side of throat, which leads to the Mach stems. Then a secondary shock wave is raised by the Mach stems travelling to the expanding part of the hourglass channel. A repeated reflection of the shock wave happens in the channel against the wall. Two Mach discs encounter and interact at the throat part. The incident shock wave is reflected and then the reflected shock wave travels to upstream and changes into a planar shock wave. In this study, the computational results accurately present the bore wave generation, propagation and interaction.







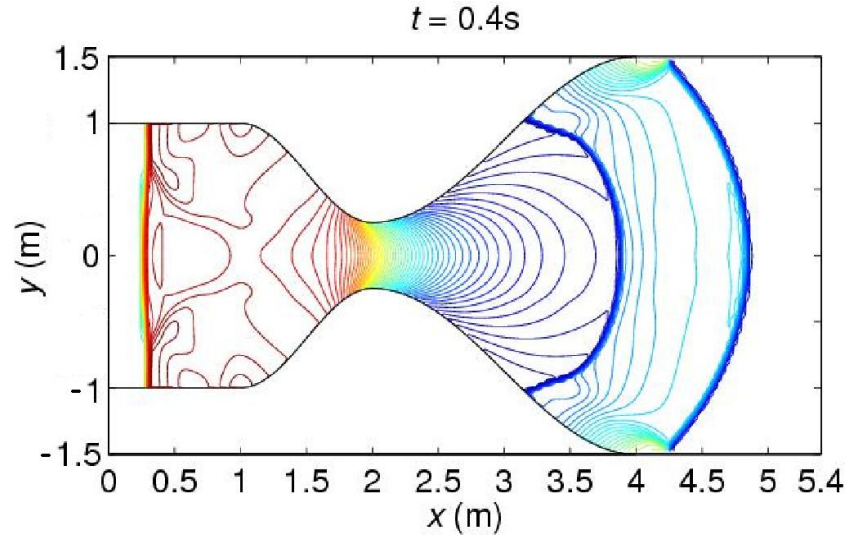


Figure 3.18 Shock diffraction in an hourglass channel: the depth contours of the bore diffraction in a contraction-expansion channel at a sequence of moments: at $t = 0.067$ s; $t = 0.11$ s; $t = 0.125$ s; $t = 0.15$ s; $t = 0.19$ s; $t = 0.31$ s; $t = 0.36$ s; $t = 0.4$ s.

3.3.5 Steady transcritical flow over a hump

This case is considered to test the performance of the current model in reproducing a steady transcritical flow over non-uniform topography. In a 25 m long frictionless channel, the bed topography is defined by

$$z_b = \begin{cases} 0.2 - 0.05(x - 10)^2 & \text{if } 8 < x < 12 \\ 0 & \text{otherwise} \end{cases}, \quad (3.57)$$

The analytical solution is provided by Goutal and Maurel (1997). For a 2D simulation, the channel is assumed to be 5 m wide. The 25 m \times 5 m computational domain is then decomposed by a 400 \times 10 uniform grid. Initially, $\eta = 0.33$ m, $q_x = 0.18$ m²/s and $q_y = 0$ are assumed throughout the domain. During the simulation, a constant unit discharge of 0.18 m²/s is imposed at upstream end while the water depth is fixed to be 0.33 m at the downstream end as an outflow condition. Slip boundary conditions are used at the northern and southern boundary walls.

A global of relative error (er) of water depth is employed here to investigate the convergence time as in equation (3.51).

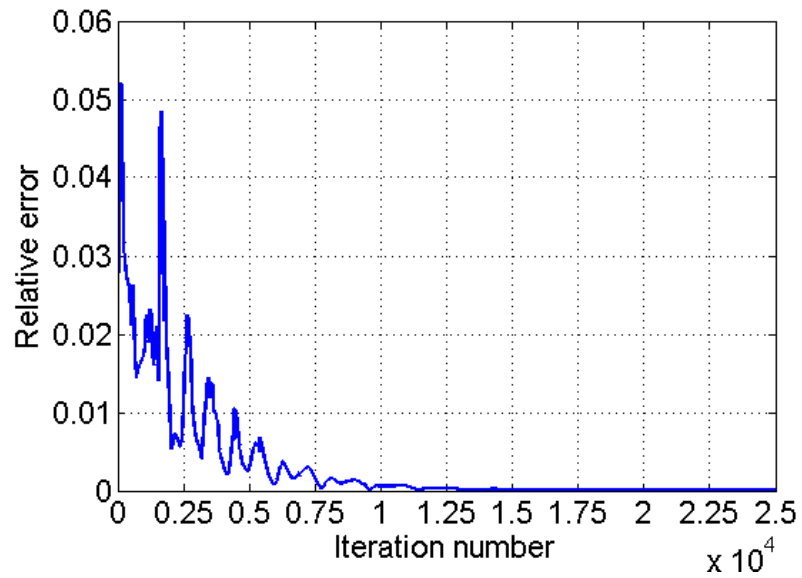


Figure 3.19 Steady transcritical flow over a hump: time history of relative error.

The time history of the convergence is illustrated in Figure 3.19. The maximum relative error happens at the beginning of computation around 0.052. And then it goes to steady state. The steady state of the transcritical flow is converged after 15,000 iterations.

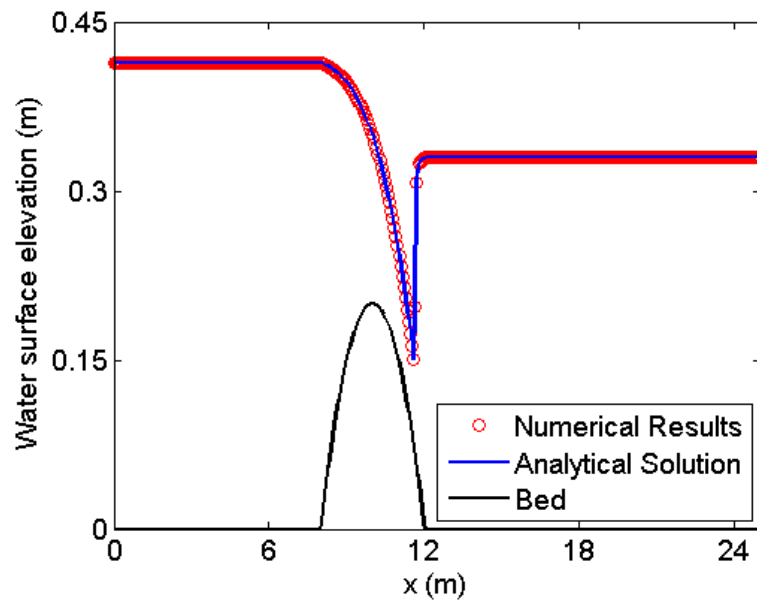


Figure 3.20 Steady transcritical flow over a hump: water surface elevation profile.

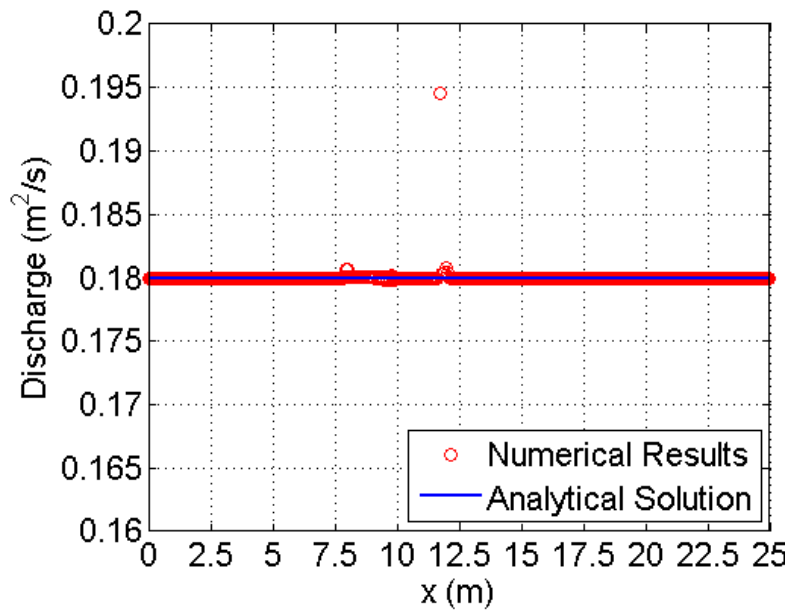


Figure 3.21 Steady transcritical flow over a hump: discharge comparison.

Figure 3.20 presents the predicted water surface profile along the flow direction, compared with the analytical solution. A hydraulic jump is developed right after the hump, which is correctly captured by the numerical solution. Figure 3.21 illustrates the corresponding profile of discharge, where the constant discharge is preserved nicely apart from a small disturbance caused by the presence of hydraulic jump.

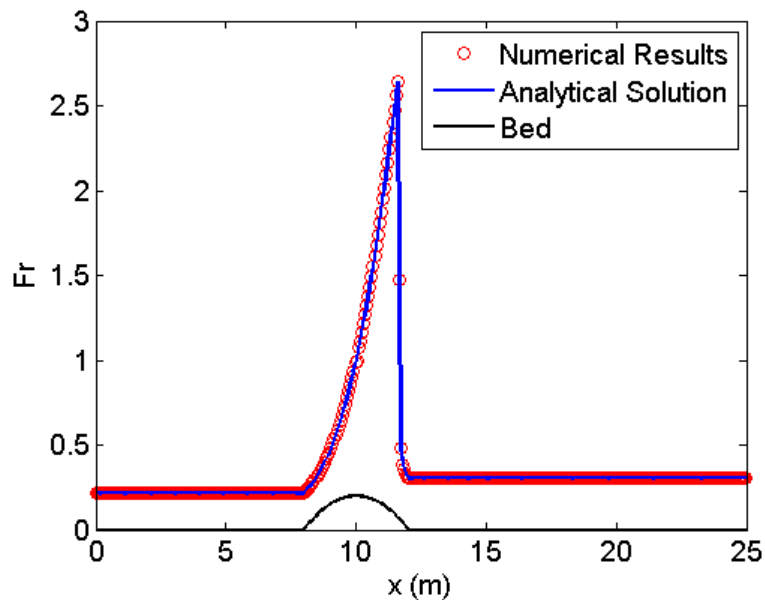


Figure 3.22 Steady transcritical flow over a hump: Froude number comparison.

The Froude number is calculated along the centre line of the channel. The predicted Froude number close agree with the analytical solution shown in Figure 3.22, which increases from approximate 0.23 to about 2.78 because of the hydraulic jump. This test case demonstrates the good performance of the present shallow flow model in reproducing the steady transcritical flow with a hydraulic jump.

3.3.6 Frictional flow in a parabolic bowl

The classic analytical test of oscillatory flow in a parabolic bowl due to Thacker (1981) has been extended to include friction effect in a 1D manner by Sampson *et al.* (2006). Herein the analytical frictional flow is re-derived and extended to 2D in order to test the current model in dealing with bed roughness and repeatedly wetting and drying over non-uniform topography. Assuming that the origin of the Cartesian coordinate system is located at the domain centre, the 2D parabolic bed topography is defined by,

$$z_b(x, y) = h_0(x^2 + y^2)/a^2, \quad (3.58)$$

where h_0 and a are both constants. In such a container, the analytical solution of the frictional flow depends on the relationship between the bed friction parameter τ and a peak amplitude parameter $p = \sqrt{8gh_0/a^2}$. For $\tau < p$, the 2D theoretical solution of the flow is derived to be

$$\begin{aligned} \eta(x, y, t) = & h_0 - \frac{1}{2g} B^2 e^{-\pi} - \frac{1}{g} B e^{-\pi/2} \left(\frac{\tau}{2} \sin st + s \cos st \right) x \\ & - \frac{1}{g} B e^{-\pi/2} \left(\frac{\tau}{2} \cos st - s \sin st \right) y \end{aligned}, \quad (3.59)$$

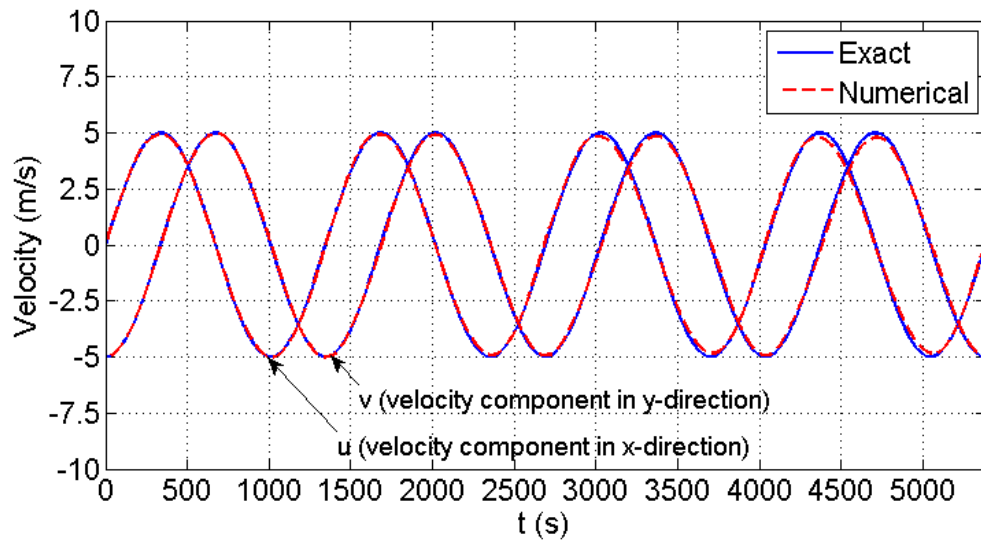
and

$$\begin{aligned} u(t) &= B e^{-\pi/2} \sin st \\ v(t) &= -B e^{-\pi/2} \cos st \end{aligned}, \quad (3.60)$$

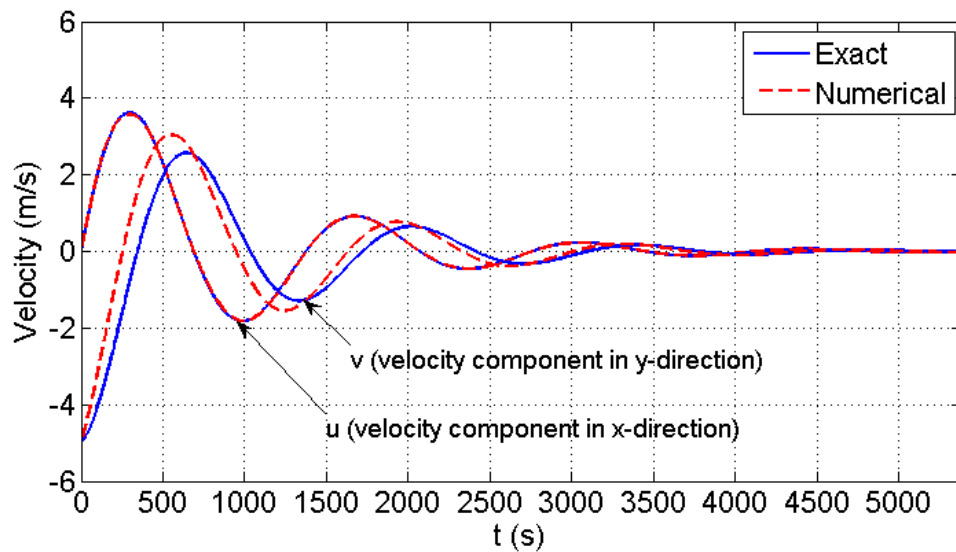
where B is a constant and $s = \sqrt{p^2 - \tau^2}/2$.

The computational domain is assumed to be 10000 m \times 10000 m and discretized by a 200 \times 200 uniform grid. The constants are set to be $h_0 = 10$ m, $a = 3000$ m, and $B = 5$ m/s. At first, the friction parameter is set to zero ($\tau = 0$) and the flow is expected to

indefinitely oscillate inside the bowl with a half-period equal to 672.8 s. For the frictional flow, $\tau = 0.002 \text{ s}^{-1}$ is assumed. The bed friction parameter is related to the roughness coefficient via $C_f = h\tau/\sqrt{u^2 + v^2}$. Simulations are run for four periods until $t = 5382.4 \text{ s}$ for both cases, under the transmissive boundary conditions.



(a)

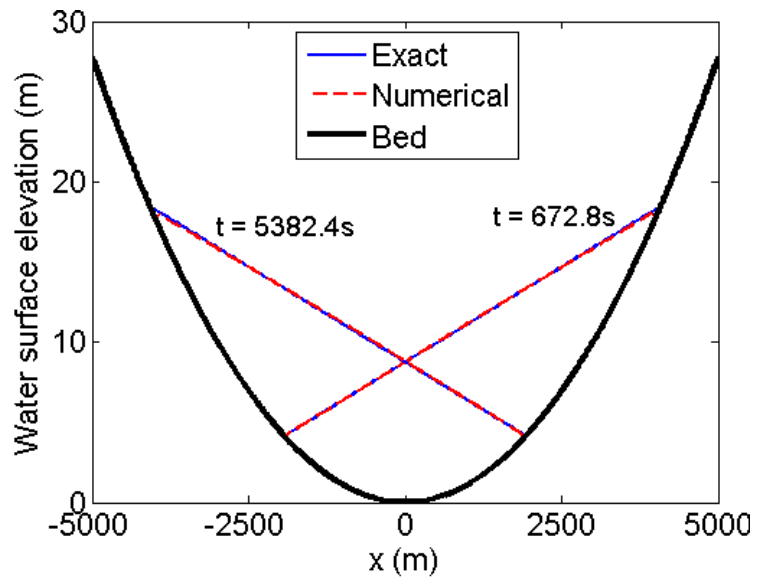


(b)

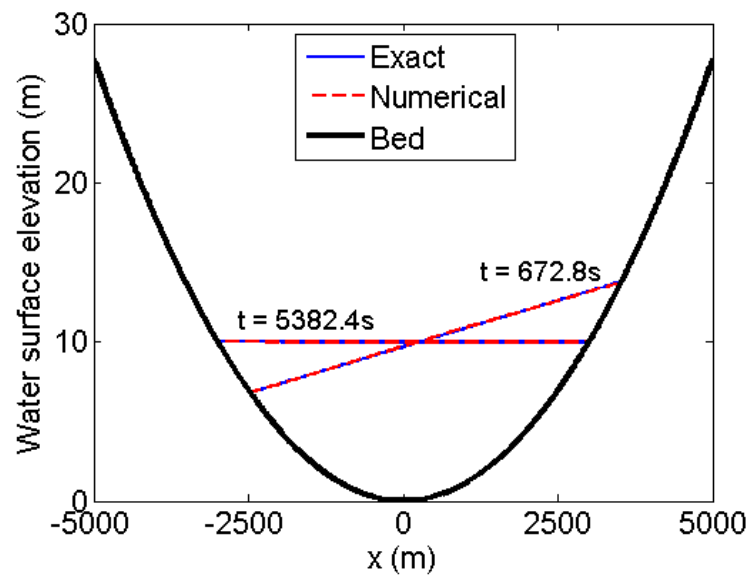
Figure 3.23 Time histories of the velocity components at gauging point (1000, 0) for four-period simulations: (a) frictionless flow; (b) frictional flow.

Numerical results are presented in Figure 3.23 and Figure 3.24 in terms of time histories of velocities at a (1000, 0) and water surface profile along the x -direction centreline at two different output times ($t = 672.8 \text{ s}$ and 5382.4 s). The numerical results are observed

to agree closely with the reference solutions. Compared with the frictionless flow, the friction effect on the flow is evident and causes the amplitude of flow oscillation to decrease throughout the simulation. The constantly moving wet-dry fronts are accurately trailed. A convergence study has been carried out according to the mesh setup in Table 3.2, showing the overall second-order accuracy for the smooth solutions with wetting and drying and with/without friction effect.



(a)



(b)

Figure 3.24 Water surface profile along the x -direction centreline after half of a period and four periods: (a) frictionless flow; (b) frictional flow.

$M \times N$	<i>Frictionless</i>		<i>Frictional</i>	
	<i>Error</i>	<i>Order</i>	<i>Error</i>	<i>Order</i>
20×20	5.1E-3	--	1.2E-3	--
40×40	1.2E-3	1.9	4.9E-4	1.9
80×80	3.0E-4	2.0	3.0E-4	2.0
160×160	7.3E-5	2.0	7.3E-5	2.0
320×320	1.7E-5	2.1	1.6E-5	2.1

Table 3.2: L^2 -error and order of accuracy evaluated against numerical water level after half a period ($t = 672.8$ s).

The above numerical predictions are observed to agree closely with the reference solutions. The effect of friction on the flow is evident and causes the amplitude of flow oscillation to decrease throughout the simulation. The wet-dry fronts are accurately and smoothly captured and no distortion of water surface is detected near the moving shoreline. Therefore, this test case is successfully simulated and essentially proves the robustness of the current model in handling complex shallow flow problems involving simultaneously non-uniform domain topography, moving wet-dry front and bed roughness, which in turn implies that it is readily applicable to real-world simulations.

3.4 Conclusions

This chapter has presented a novel fully 2D pre-balanced shallow flow model based on a uniform Cartesian grid. The pre-balanced fully 2D shallow water equations are solved using an explicit finite volume Godunov-type scheme, with the interface fluxes evaluated by the HLLC approximate Riemann solver. A non-negative water depth reconstruction approach, incorporated with a local bed modified method is adopted to treat the problems of wet-dry interface over the complex bed topography. The second-order Runge-Kutta integrating method was applied to update the flow variables for the next time step, in order to achieve second order accuracy. The second order accuracy in space is achieved by implementing the MUSCL slope limiter. The friction source term is implicitly discretized and controlled by a limiter to maintain the computational stability.

The present numerical model has been validated against several benchmark cases to test the performance on handling the complex shallow flow problems. The case of tidal wave over irregular bed topography is used to verify the capability of the fully 2D shallow flow model on dealing with the irregular bed profile. Compared with the analytical solutions, close agreements are achieved. Then the numerical scheme is tested on a series of analytical cases, in which the shock-capturing Godunov-type scheme present excellent performance on capturing the shock-like continuities and reproducing different flow regimes, e.g. oblique hydraulic jump, shock reflection, shock diffraction and steady transcritical flow over a hump. The numerical predictions are found to agree well with analytical solutions. Then a moving shoreline problem of frictional flow in a parabolic bowl is investigated to verify the good performance of the present model in dealing with wet-dry problems, non-uniform domain topography and bed roughness. The smooth evolution of wetting and drying is accurately captured and traced without spurious oscillation and negative water depth at the wet-dry front. Overall, the present shallow flow model is proved to be a robust and reliable tool for handling the most challenging issues in the shallow flow modelling, i.e. handling different flow regimes, shock-like discontinuity, repeatedly wetting and drying problems over non-uniform domain topography and representing bed roughness.

Chapter 4 Dam Break Flood Simulation

Objectives

- Implement the fully 2D shallow flow model for simulating rapidly-varying dam-break flows and verify its capability for capturing shock-like flow discontinuities and handling wetting and drying over complex domain topographies;
- Demonstrate the accurate prediction of the water depth, flow velocity, flood route and arrival time in the experimental and real world examples of dam-break.

Introduction

Dams/dykes can serve as barriers to prevent water flow into a particular area or domain such as a city, village and farmland and provide protection from flooding for human communities. However, these hydraulic structures also pose a great threat to human's lives and properties. A dam-break event can lead to a devastating flood disaster that induces huge economic and human costs. For example, the Malpasset dam, located in the Reyran river valley in France, burst in December 1959 and caused more than 400 casualties. Most recently, a dam failed near Piaui, a rural Brazilian city, in May 2009 killed four people and affected thousands. In March 2009, a dam break occurred near Jakarta in Indonesia. 77 people died and more than 100 people went missing from the event. Therefore, it is essential to assess and manage the flood risk associated with dam breaks. This in turn requires us to reliably model the possible flooding events caused by dam breaks. Basically, a successful dam-break model should be able to

1. Provide accurate solutions for different flow regimes including subcritical, supercritical, trans-critical flows as well as shock-like flow discontinuities;
2. Effectively handle flow over complex domain topography with repeatedly wetting and drying;
3. Represent high and variable roughness values along the flood route.

This chapter presents the application of the fully 2D shallow flow model described in Chapter 3 in modelling dam break induced flood inundation. Three test cases recommended by the European Commission funded Concerted Action on Dam Break Modelling (CADAM) project are considered, which are respectively the 1D dam-break flow over a triangular hump, laboratory-scale TOCE river dam break and the realistic Malpasset dam-break event through the Reyran river valley.

4.1 Results

4.1.1 Laboratory dam break over a triangular hump

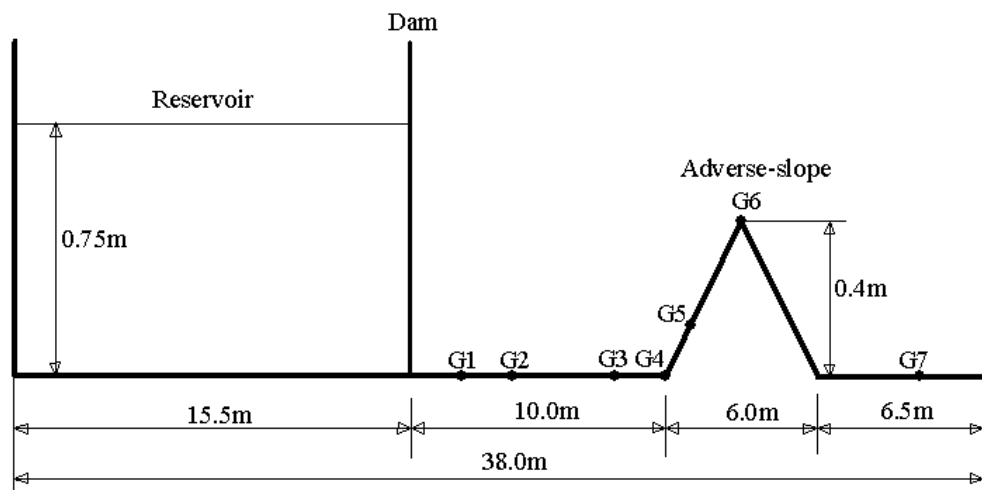
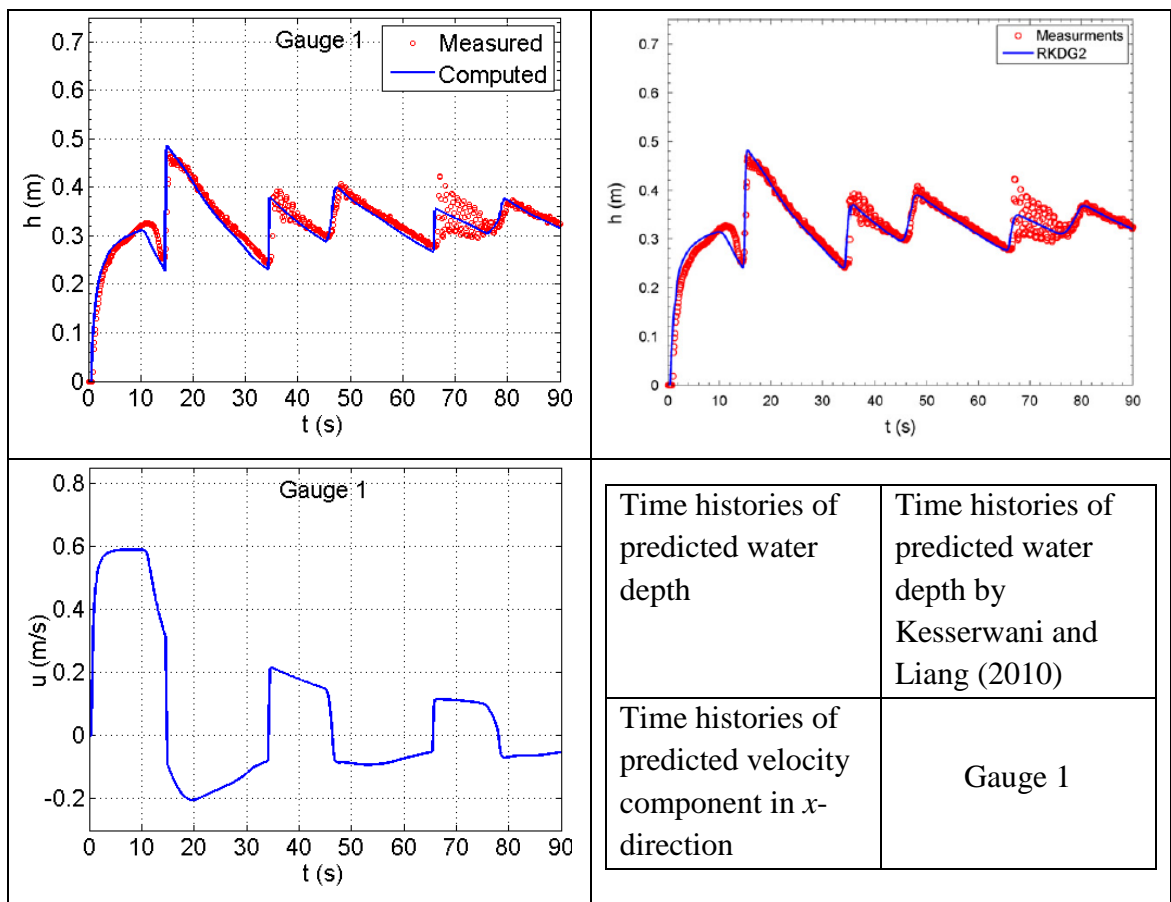


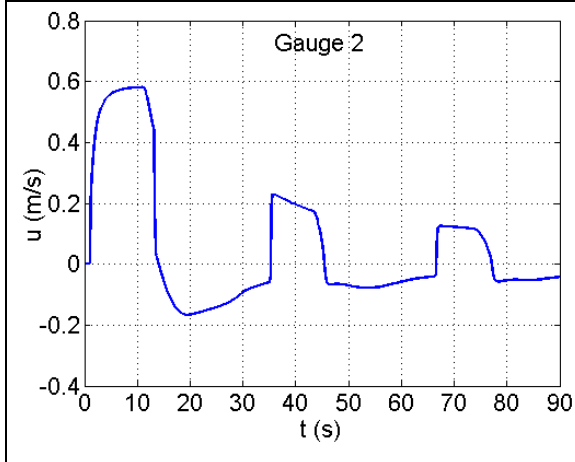
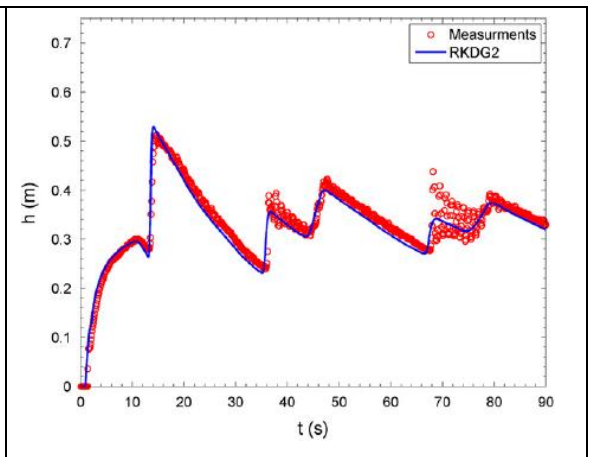
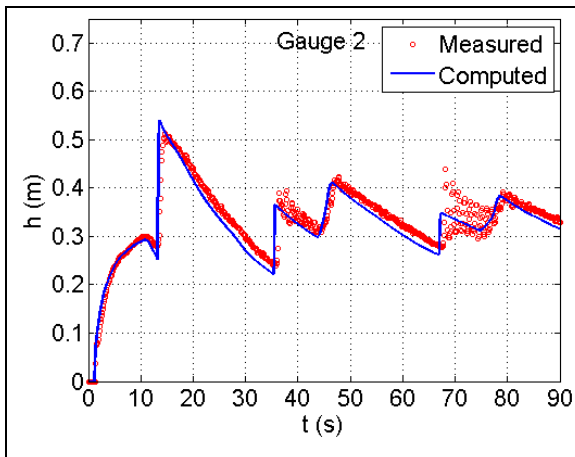
Figure 4.1 Dam break over a hump: experimental set up.

The experimental setup for this dam-break test is sketched in Figure 4.1. In a 38 m long horizontal flume, the dam is located 15.5 m away from the upstream end. Behind the dam is a reservoir with a still water surface elevation of 0.75 m above the channel bed. In the downstream floodplain, a topographic structure featured as a symmetric triangular hump is installed with its top located 13 m away from the dam. The hump is 0.4 m high and has 3 m long normal and adverse slopes on both sides. A similar experiment was also carried out by the European Commission funded IMPACT project (Soares-Frazão 2007). During the simulation, the computational domain is approximated by a uniform grid of 25 cm resolution. For the 2D simulation, the flume is assumed to be 5 m wide but this value has no influence on the results as this is essentially a 1D test. A constant Manning coefficient $n = 0.0125 \text{ s/m}^{1/3}$ is used in the entire domain, as recommended by

CADAM. Reflective boundary conditions are used at the upstream end of the domain while a free outlet is imposed at the downstream end. The simulation lasts for 90 s. The adaptive time steps are kept as a constant during the simulation throughout the dam-break flow progress in 90 s. The CPU time of the simulation is 42.84 s.

The dam fails suddenly at $t = 0$ and a wall of the initial still water starts to rush onto the downstream dry floodplain driven by the unbalanced pressure. The dam-break flow propagates to the obstacle and arrives at the hump about $t = 3$ s. Meanwhile, a rarefaction wave is induced and propagates upstream from the initial location of the dam. After reaching the hump, the flood front runs up the sloping obstacle and overtops its peak. A reflected wave is formed on the upstream side of the hump and starts to travel upstream. After hitting the upstream solid, another reflected shock wave is developed and propagates towards the hump. This wave-structure interaction leads to the change of the water depth and velocity at gauges and the repeat wetting-drying interface at the slope of the hump. The overtopping wave floods the dry bed downstream of the obstacle and then flows out of the domain from the downstream end.



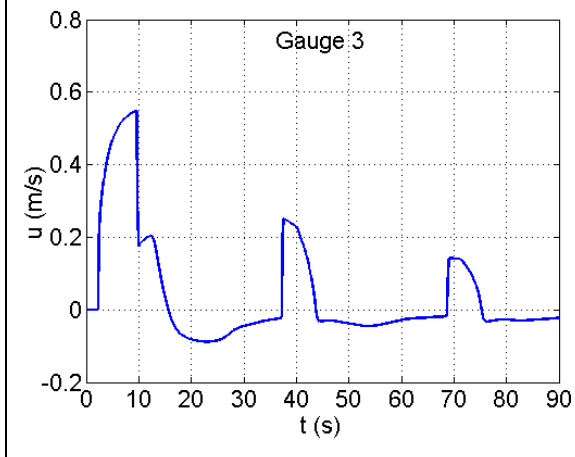
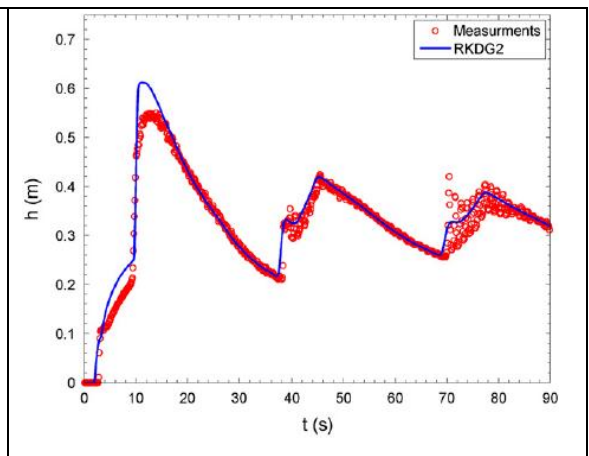
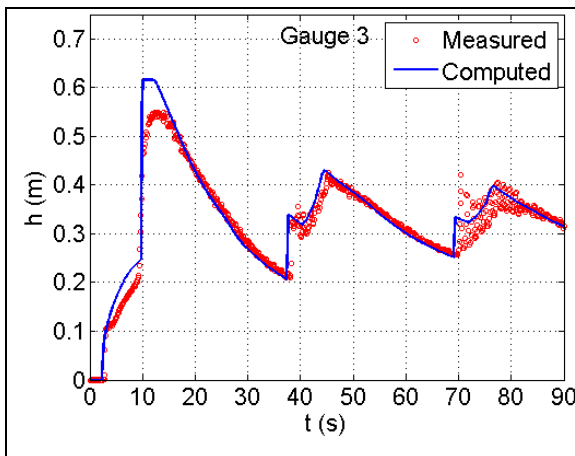


Time histories of predicted water depth

Time histories of predicted water depth by Kesserwani and Liang (2010)

Time histories of predicted velocity component in x -direction

Gauge 2

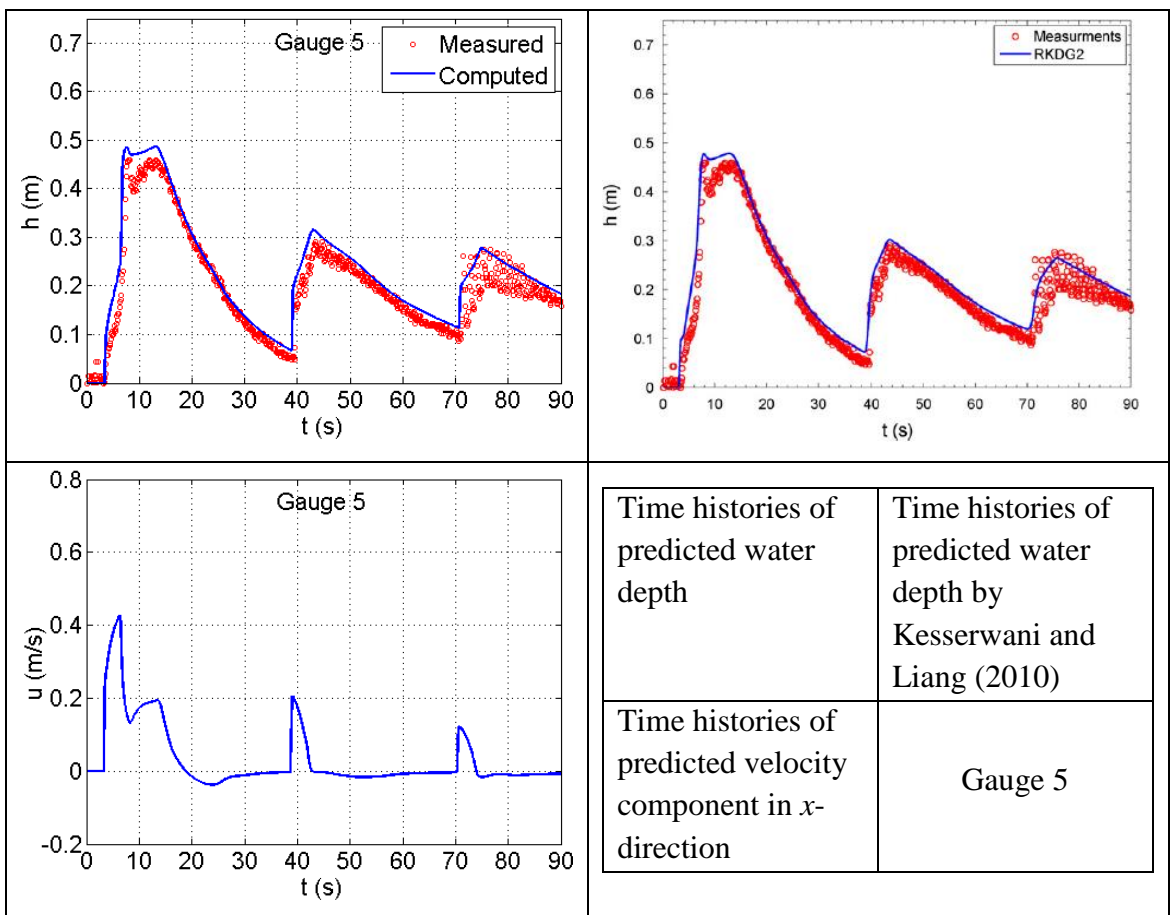
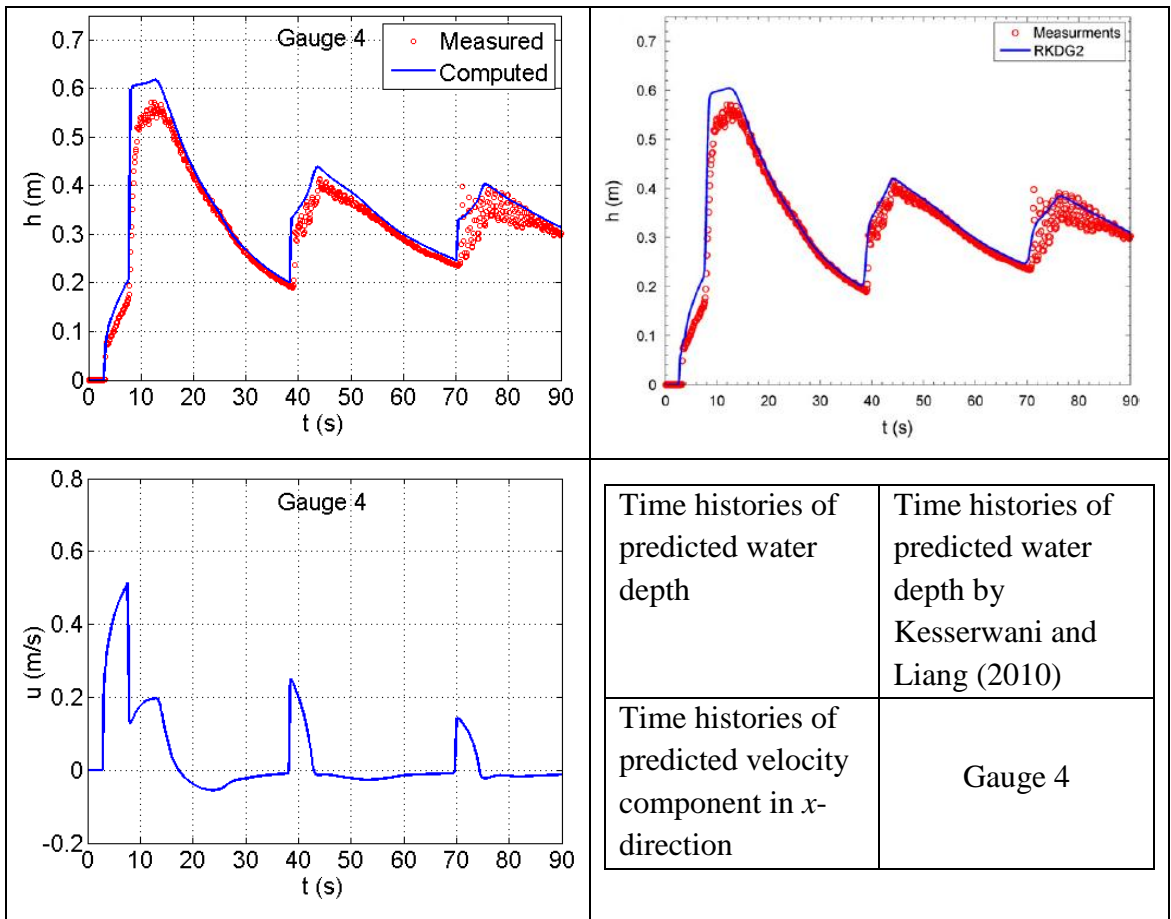


Time histories of predicted water depth

Time histories of predicted water depth by Kesserwani and Liang (2010)

Time histories of predicted velocity component in x -direction

Gauge 3



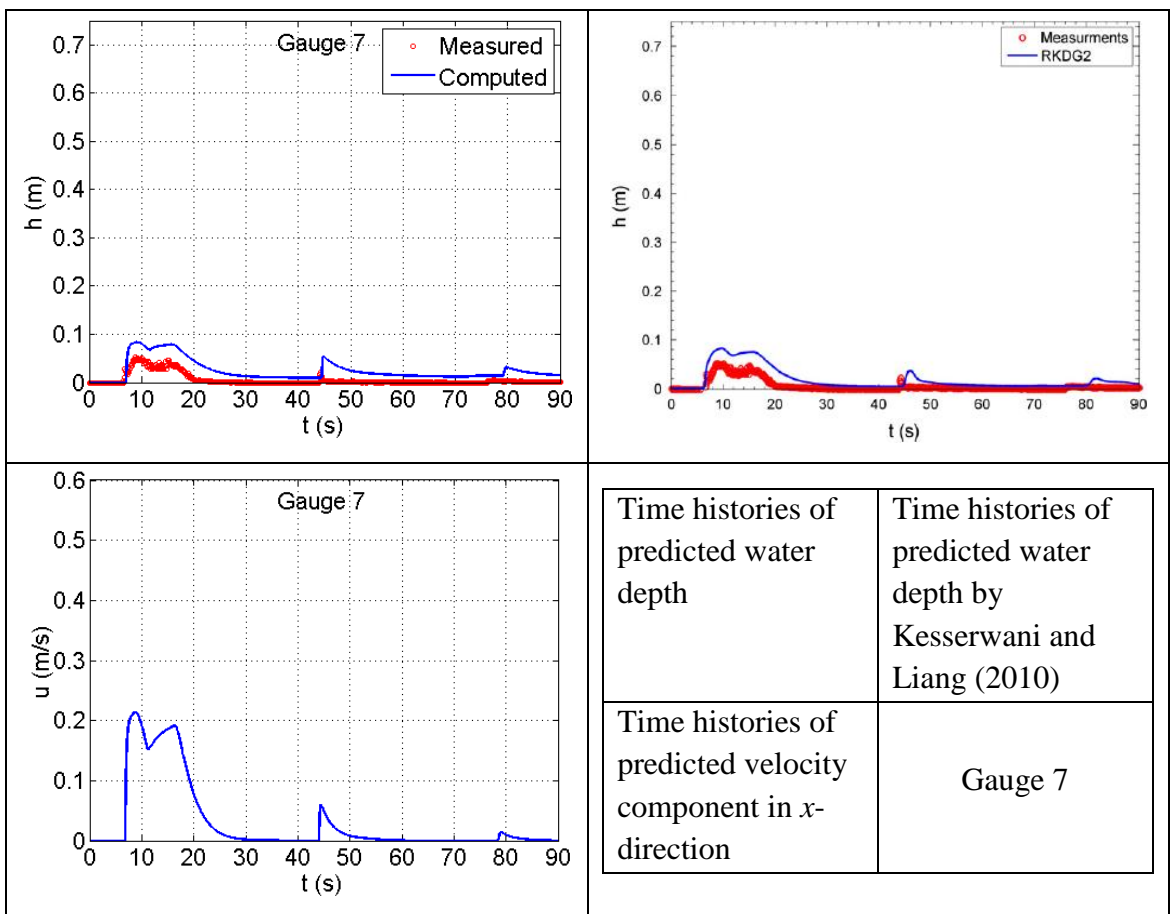
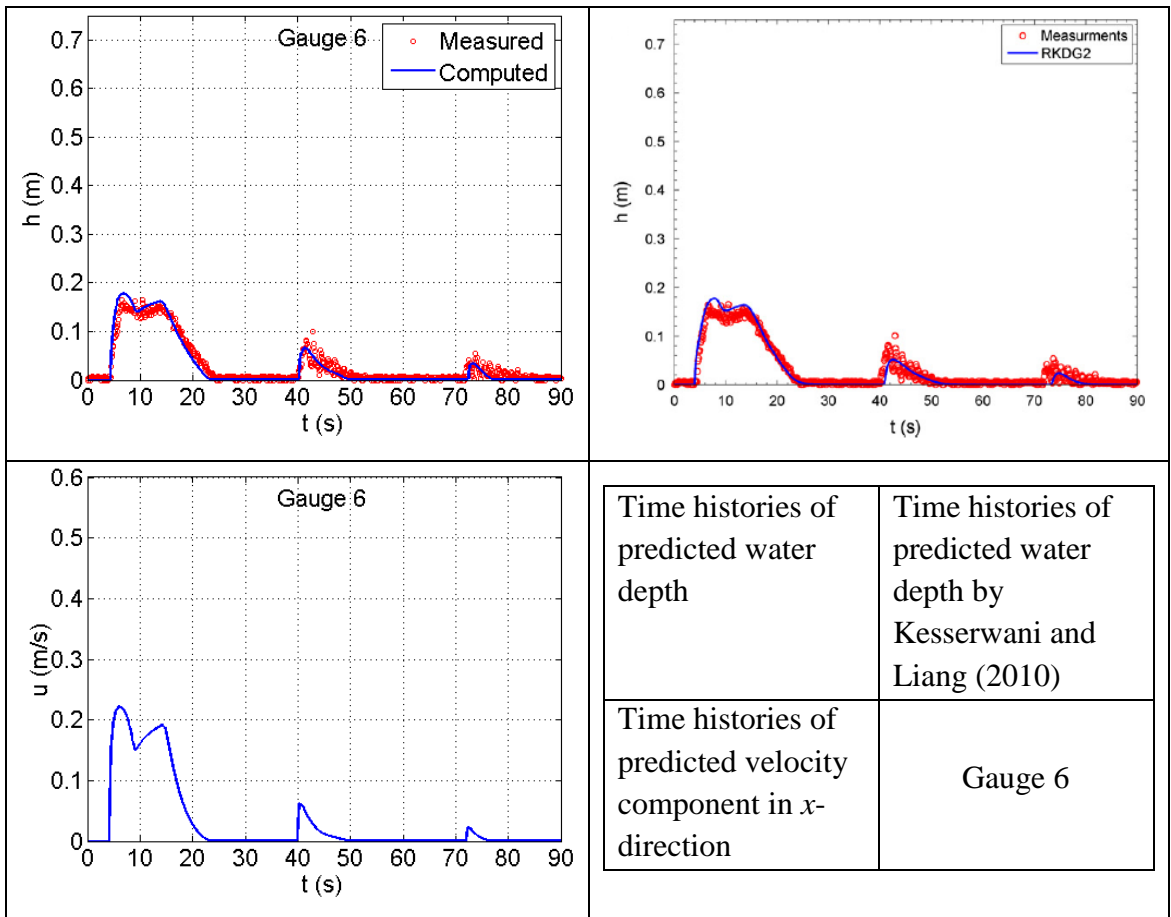


Figure 4.2 Dam break over a hump: time histories of predicted water depth by the present shallow flow model (Northwest), simulated by Kesserwani and Liang (2010) (Northeast) and velocity (Southwest) at different gauges.

Figure 4.2 (Northwest) compares the measured and predicted time histories of water depth recorded at the 7 gauges, which are located at 2 m, 4 m, 8 m, 10 m, 11 m, 13 m and 20 m downstream of the dam as shown in Figure 4.1. Compared with measured data, the arriving time and water depth are both reasonably well predicted at those gauges before and on the hump. The corresponding time histories of velocity are also presented in Figure 4.2 (Southwest). The velocity evolves according to changing trend of velocity at gauging point is predicted well matching the development of water depth, which indicates that the velocity of the flood wave is also correctly predicted. At the gauge after the hump (Gauge 7), the numerical water depth is observed to deviate from the experimental measurement, which is also reported by other researchers using different numerical schemes (e.g. Kesserwani and Liang 2010; Brufau *et al.* 2002). Herein, Figure 4.2 (Northeast) presents the predicted time history of water depth at gauges by Kesserwani and Liang (2010). The discrepancy is probably because the flow after the hump is highly complex and fully 3D and so the 2D hydrostatic shallow water equations are no longer valid for this situation. However, the current numerical model accurately predicts the arriving time which is a more important factor in dam-break simulation. Generally, the numerical predictions are satisfactory. The repeating wetting-drying process over the triangular hump is precisely captured. This essentially confirms the effectiveness of the current numerical scheme on handling wetting and drying, balancing the flux and source term gradients and reproducing the friction effects.

4.1.2 Toce river dam break

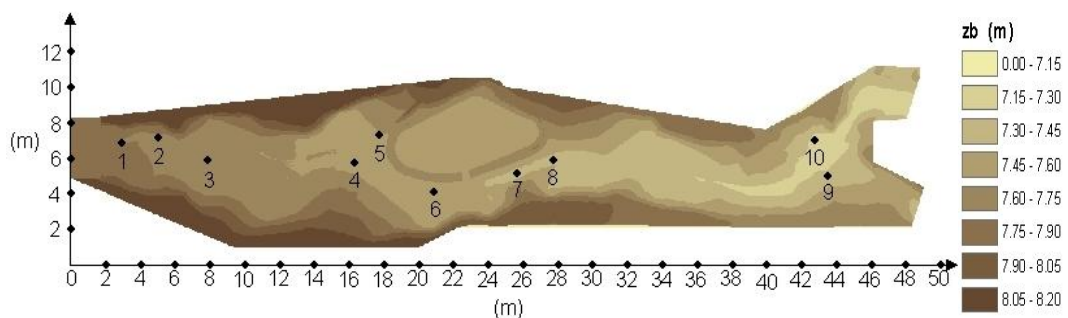


Figure 4.3 Toce River dam break: floodplain and location of gauge points.

The Toce River dam break has been simulated to validate the current numerical scheme on reproducing rapidly-varying flood wave propagating over a highly complex domain including natural features. The physical model was set up in ENEL (Italy) to reproduce in the laboratory the 5 km Toce River reach in the Northern Alps in Italy. As indicated in Figure 4.3, the 55 m × 13 m experimental facility scaled down the site at a ratio of 1:100 reproduced many details of the real topography, including river bed and an empty reservoir located roughly in the middle of the domain. The dam-break flow into the initial dry river reach is driven by a hydrograph provided from an upstream inflow tank. Therefore, the upstream boundary conditions are imposed according to the inflow hydrograph provided by CADAM and free outlet is assumed at the downstream end. A constant Manning coefficient of $n = 0.0162 \text{ s/m}^{1/3}$ is applied throughout whole computation domain. In order to verify the model predictions, gauges as indicated in Figure 4.3 were used to record time histories of the water surface elevation.

The simulation was run for 180 s on a uniform grid of 5 cm resolution as provided by the original DEM. The computing time is 8555.84 s. Figure 4.4 illustrates the change of the adaptive time steps throughout the simulation in 180 s. Figure 4.5 presents the time evolution of the flood waves at different output times. Driven by the inflow hydrograph, the dam-break wave travels rapidly along the river to downstream. At $t = 35 \text{ s}$, the flood wave has already reached the empty reservoir, which becomes a main obstacle in the way of flood. The water depth starts to increase in the upstream of the reservoir and a small amount of water overtops the surrounding dam and enters the reservoir. Due to the blocking effect, the main stream of the flood wave bends around the reservoir and continues to propagate downstream. At $t = 65 \text{ s}$, the reservoir has been entirely flooded and the flood front has just reached the downstream end of the domain. Figure 4.5 (d) shows the final flood map at $t = 180 \text{ s}$. The velocity field of flood flow at $t = 180 \text{ s}$ is presented in Figure 4.6, in which (a) shows the velocity field in the whole computational domain and (b) presents the zoom-in view near the eastern end of the channel.

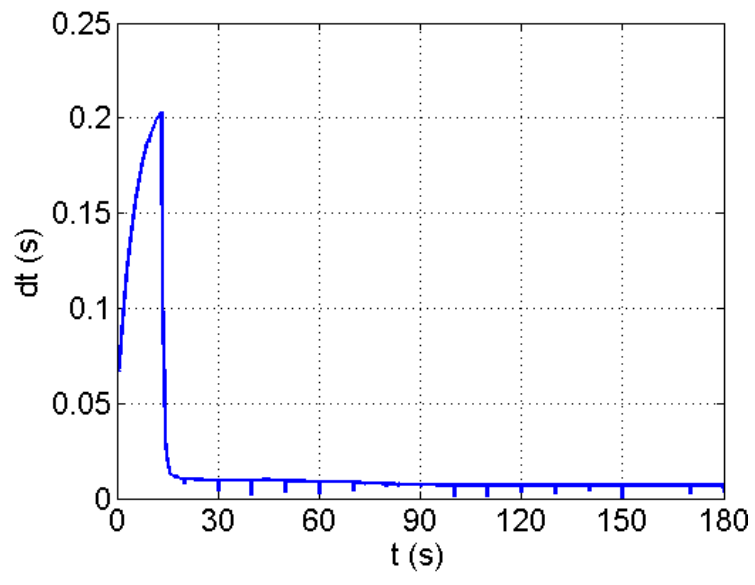
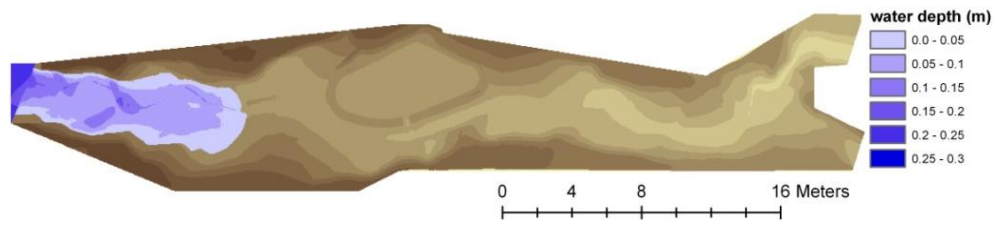
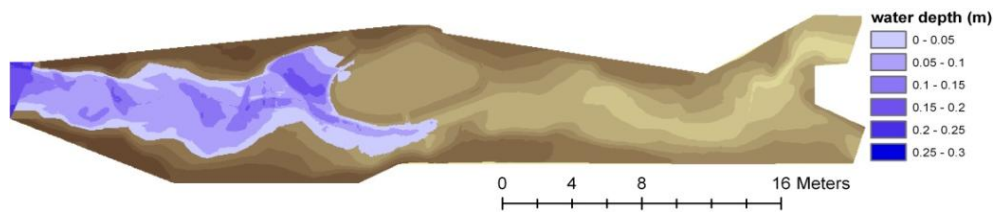


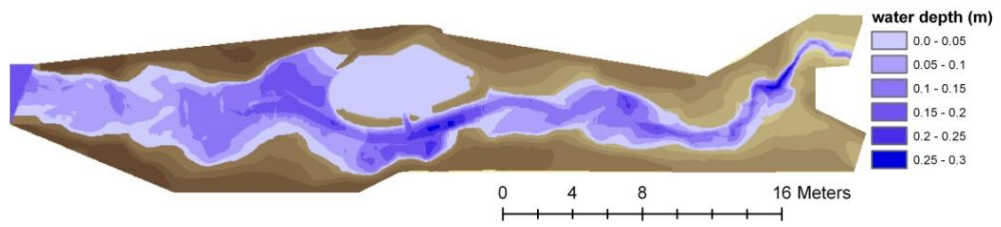
Figure 4.4 Toce River dam break: time history of the adaptive time step in 180 s.



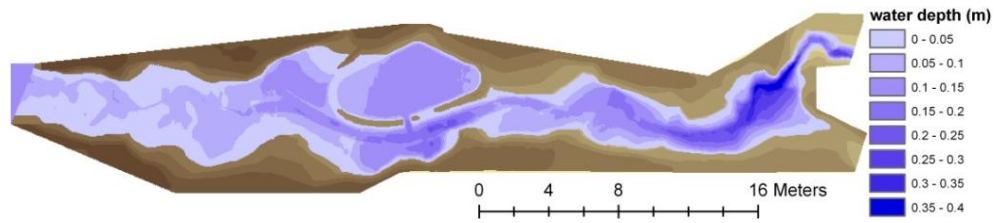
(a) $t = 25$ s



(b) $t = 35$ s

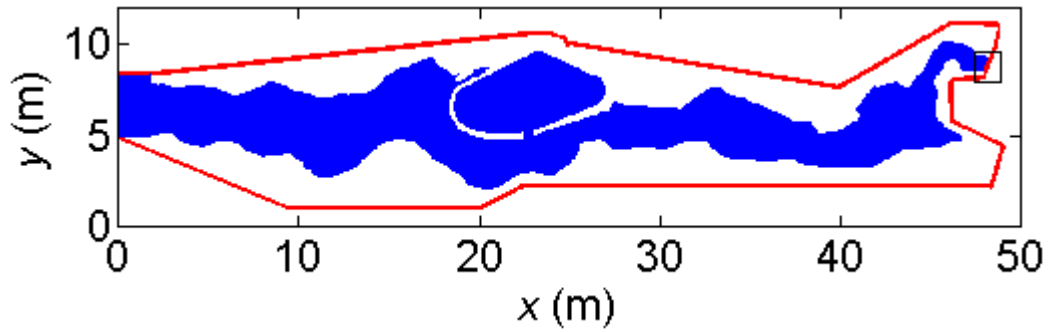


(c) $t = 65$ s

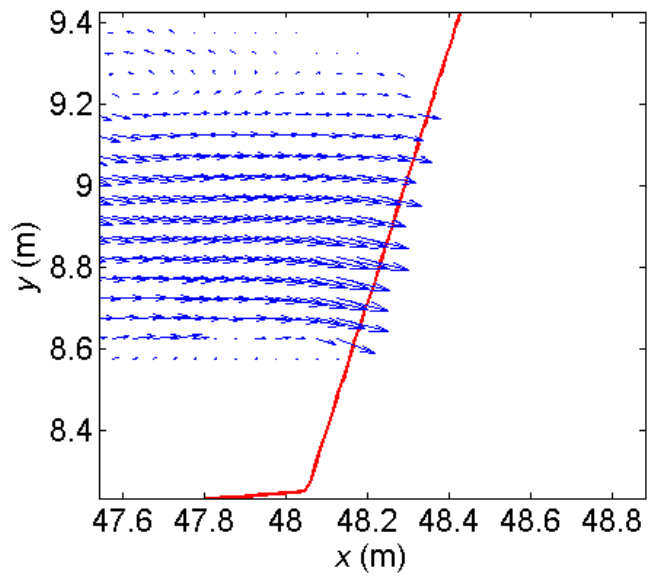


(d) $t = 180$ s

Figure 4.5 Toce River dam break: flood routing.

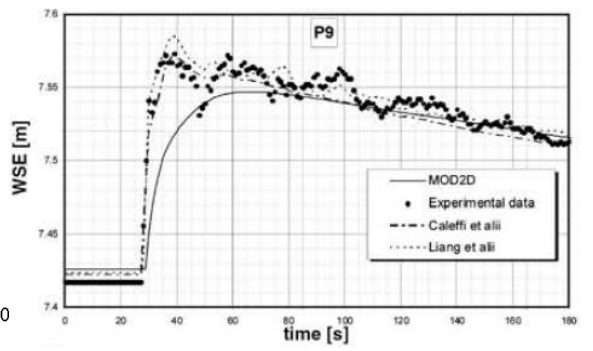
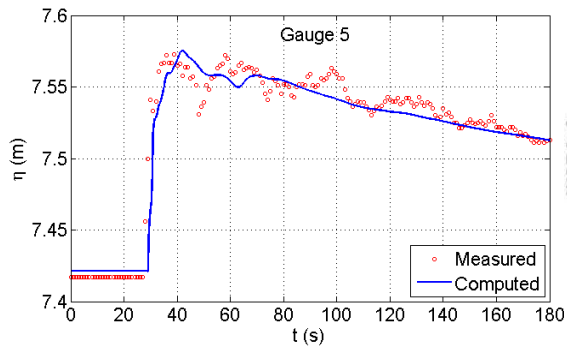
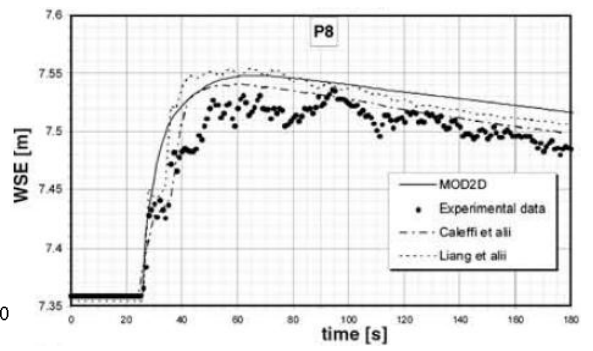
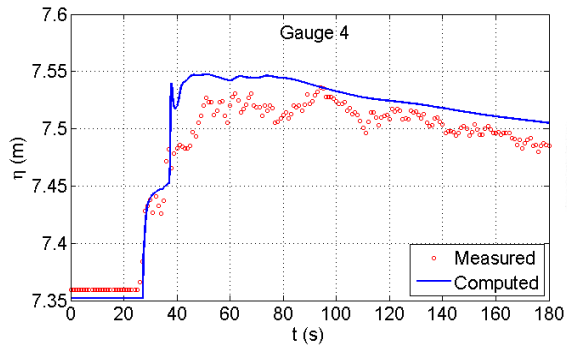
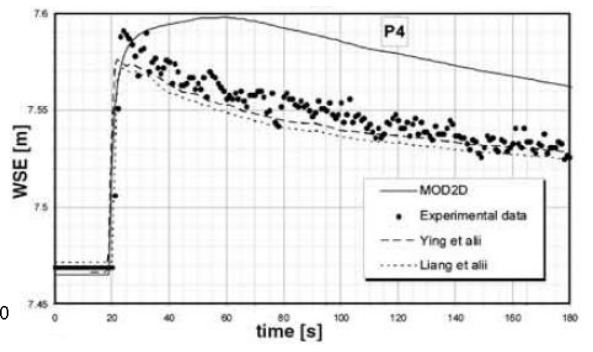
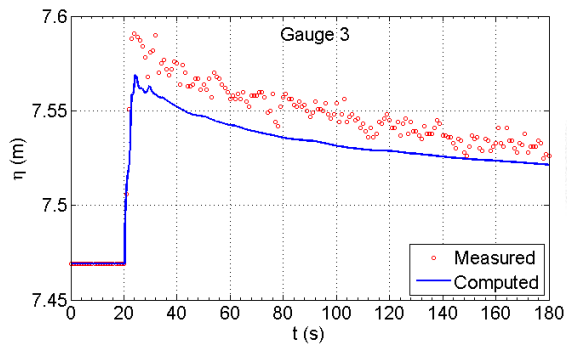
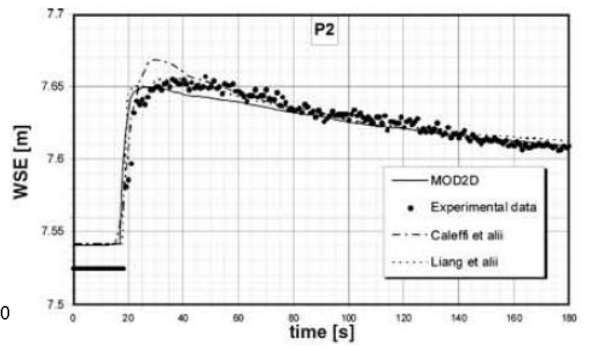
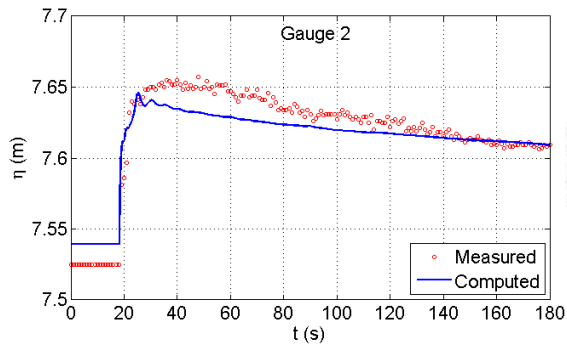
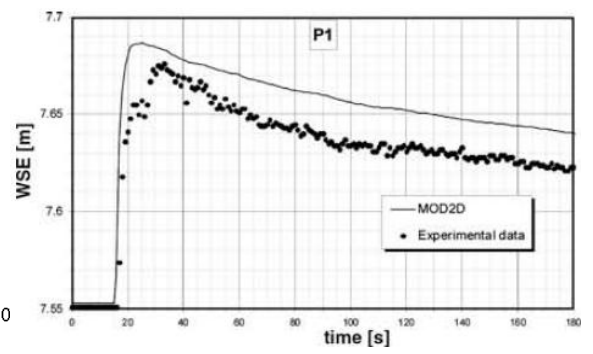
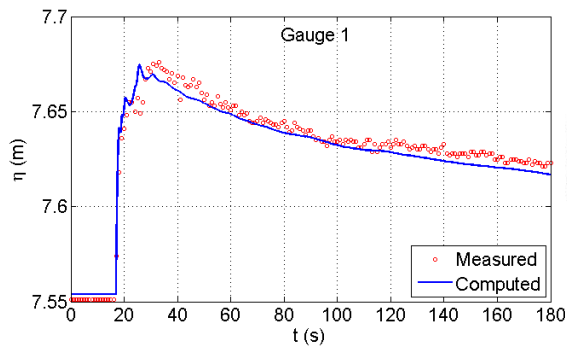


(a)



(b)

Figure 4.6 Toce River dam break: velocity field at $t = 180$ s (a) in the whole domain; (b) zoom-in view near the outlet.



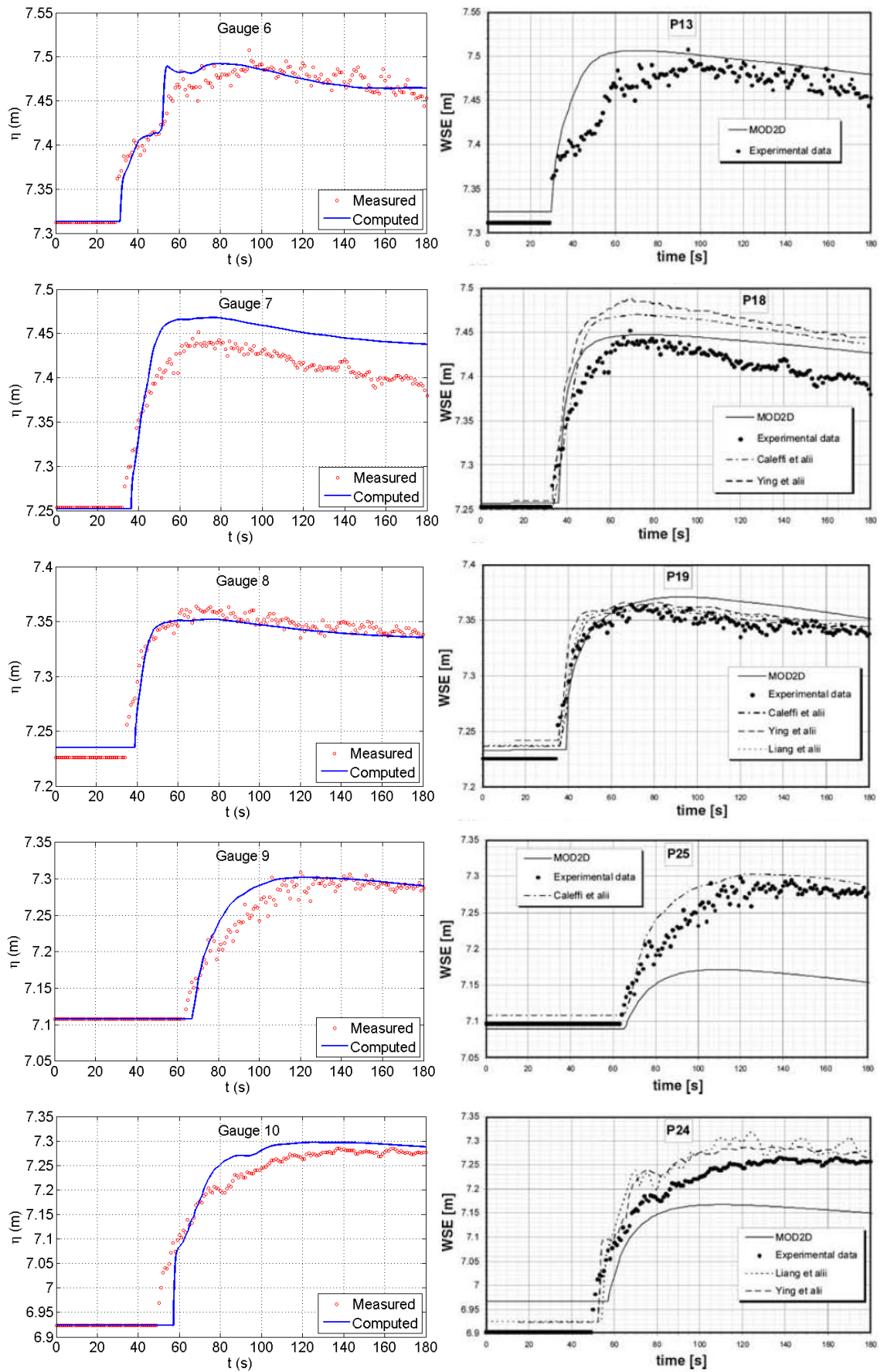


Figure 4.7 Toce River dam break: time history of water depth at different gauge points. (Left – by the present model; right – by Prestininzi (2008)).

Figure 4.7 compares the numerical predictions with the experimental measurements and other published numerical simulations by Prestininzi (2008), in terms of time history of water surface elevation. The predictions by the present model are obviously much closer to the experimental data than the numerical simulations provided by Prestininzi (2008). The numerical predictions compare reasonably well with the experimental measurements. Obvious deviation from the laboratory measurements is observed for the water surface elevation at certain gauge points, e.g. G7. G7 is located outside of the reservoir at the valley where the main flood wave passes through. Slightly upstream of the G7 a breach is created on the reservoir dam so that a jet of flow rushes out and joins the main flood wave right upstream of G7. The flow travelling through G7 is therefore highly complex and turbulent and may not be adequately described by the hydrostatic shallow water equations. A similar discrepancy at G7 was also simulated by Prestininzi (2008) and Caleffi *et al.* (2003) using alternative numerical schemes shown in Figure 4.7. Furthermore, measuring this highly turbulent flow may be associated with great uncertainty.

Overall, successful handling this experimental but realistic dam-break test indicates the capability of the current model in modelling natural extreme flood hydrodynamics induced by dam breaks.

4.1.3 Malpasset dam break

The Malpasset dam on the Reyran river valley and its associated floodplain in southern France are shown in Figure 4.8. The Malpasset dam was a two-way curved arch dam, with a 66.5 m maximum height and a 223 m crest length, on the Reyran river valley in southern France. In December 1959, the dam collapsed unexpectedly and the flood wave rushed along the valley and down to the plain in 20 minutes, where the city of Frejus is located. This flood event caused about \$ 68 million economic losses and 400 casualties. After the disastrous event, a police survey was undertaken to estimate the maximum water level at certain locations by tracing flow marks. Laboratory studies were carried out by Electricite de France (EDF) to measure the arrival time and maximum water level at gauge points near to those police surveying locations. In Figure 4.8, 'G' stands for the gauging points in the laboratory studies and 'P' represents the

police survey points. The experimental measurements were found to agree quite well with the field data.

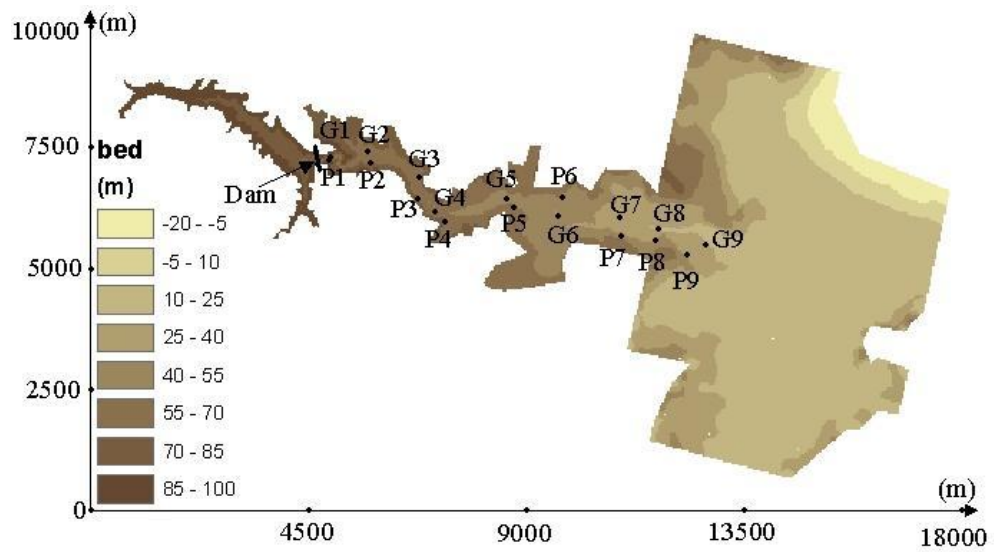


Figure 4.8 Malpasset dam break: floodplain and location of gauges (G) and police survey points (P).

This case has been used by many researchers as a case study to test their numerical models (e.g. Alcrudo and Gil 1999; Hervouet 2000; Valiani *et al.* 2002; Schwanenberg and Harms 2004; Liang *et al.* 2007). In this work, simulations are performed on an $18000 \text{ m} \times 10000 \text{ m}$ domain, which is approximated by a uniform mesh with 450×250 cells (but those cells outside the region shown in Figure 4.8 are excluded from the flow computation). The broken dam is idealised as a straight breach across the narrow throat of the valley. During the simulation, a constant water level of 100 m is assumed in the upstream reservoir and the Manning coefficient is set to $n = 0.033 \text{ s/m}^{1/3}$ in the whole computational domain, as suggested by CADAM. The downstream floodplain is initially dry. All of the boundaries are assumed to be transmissive. The simulation is carried out for 1800 s flood event. The running time is 258.58 s. The time history of the adaptive time step is recorded in Figure 4.9.

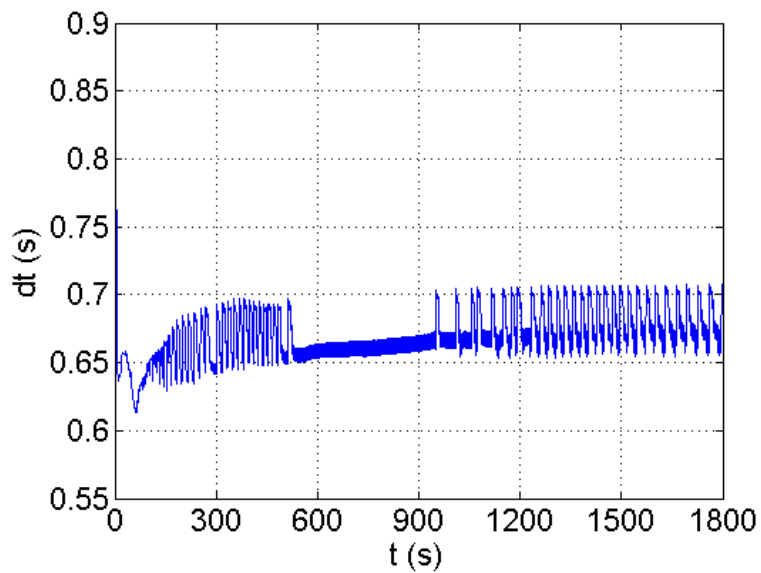
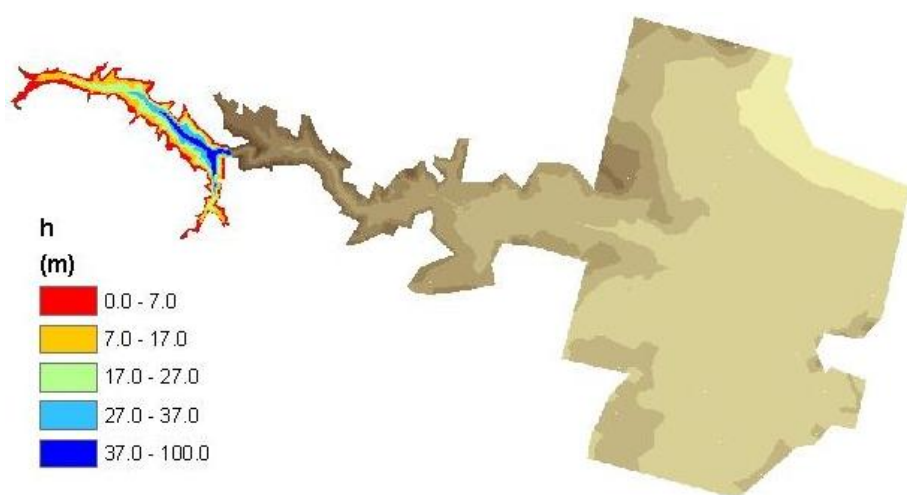
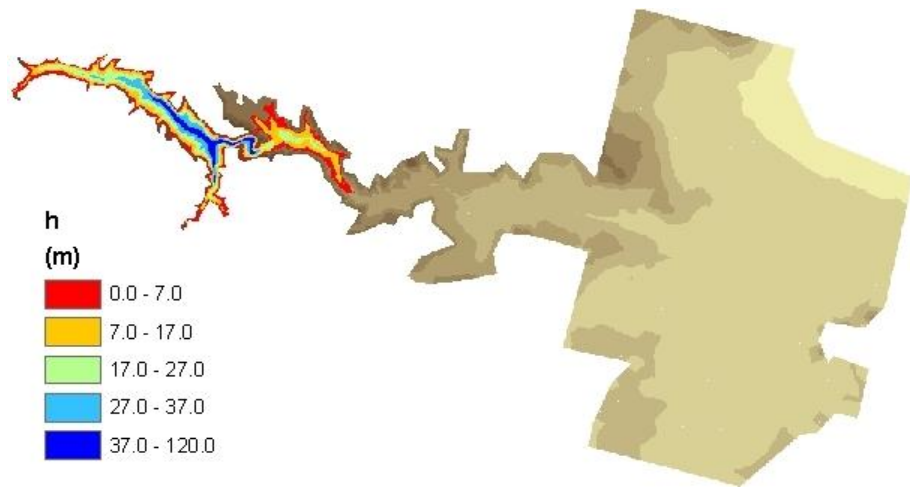


Figure 4.9 Malpasset dam break: time history of the adaptive time step in 1800 s.

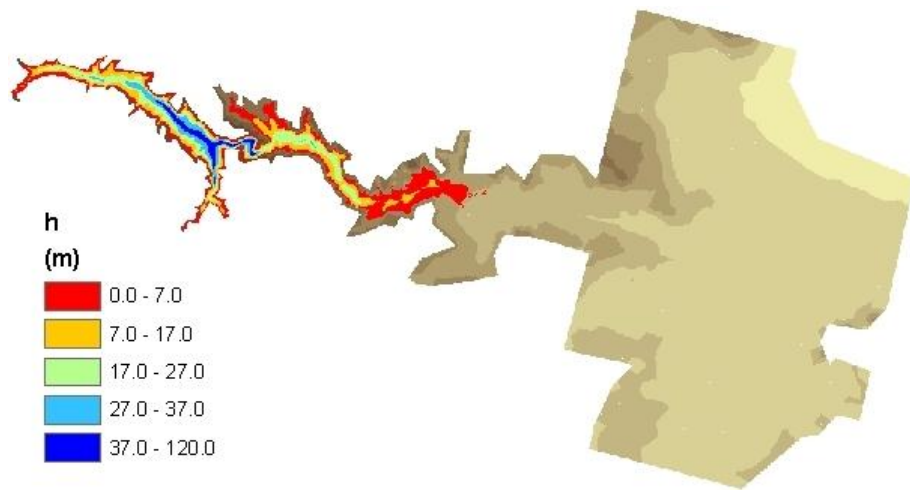
Figure 4.10 presents the flood depth and extent at different output times. At $t = 10$ min after the dam breaks, the violent flow is observed to rapidly travel downstream along the narrow Reyran river valley. The flood front has reached the valley's mouth at $t = 20$ min and is about to inundate the open-plan floodplain. At $t = 30$ min, the flood water has already inundated a wide area in the downstream floodplain and caused damages to the local villages. The velocity field at $t = 30$ min is presented in Figure 4.11, in which (a) is for the whole computational domain and (b) is the zoom-in view near the flood front.



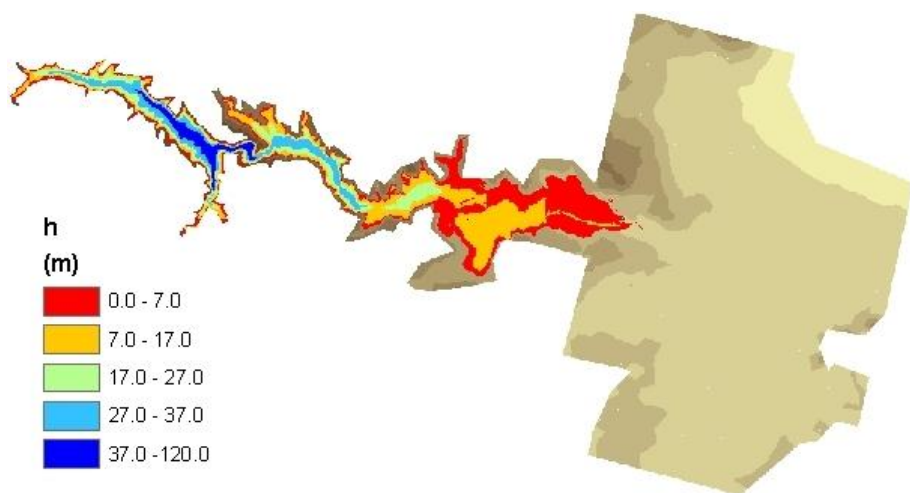
(a) at $t = 0$ min



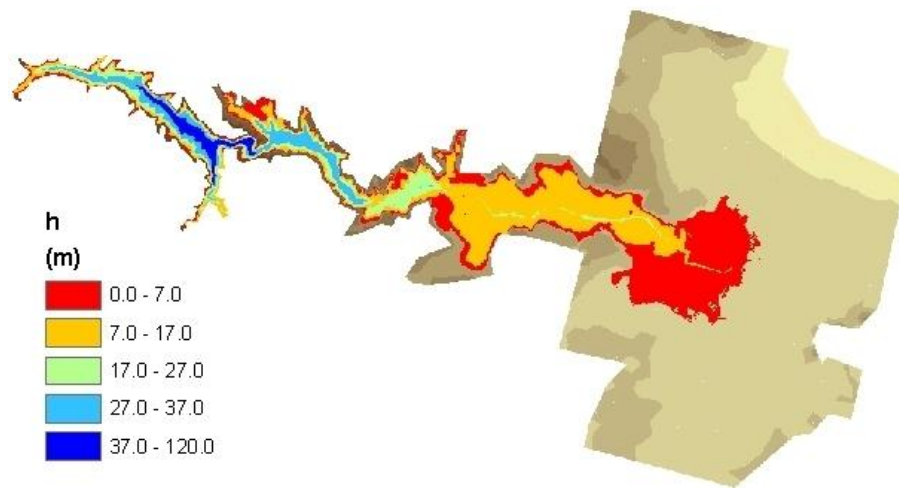
(b) at $t = 5$ min



(c) at $t = 10$ min

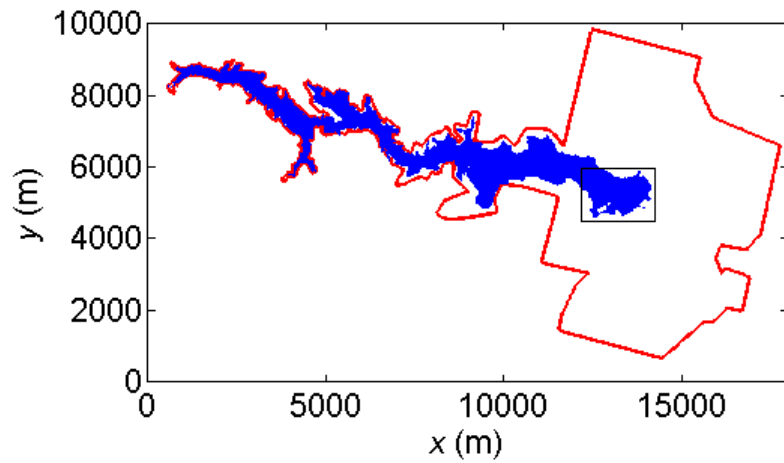


(d) at $t = 20$ min

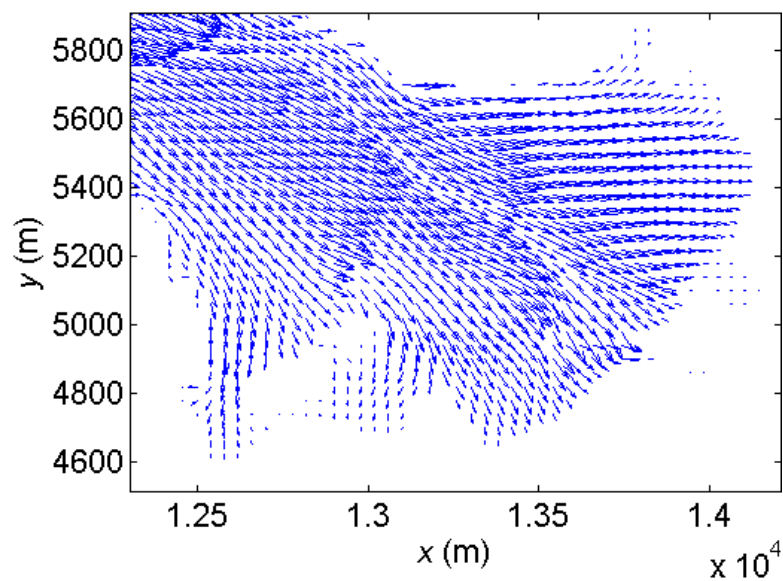


(e) at $t = 30$ min

Figure 4.10 Malpasset dam break: numerical inundation map at different output times.



(a) The whole domain



(b) Zoom-in view near the flood front

Figure 4.11 Malpasset dam break: velocity field at $t = 30$ min: (a) the whole domain; (b) zoom-in view near the flood front.

Figure 4.12 (left) compares the predicted maximum water depth with that obtained by police survey and close agreement is observed in all surveying points. The similar numerical simulations are predicted by Liang *et al.* (2007) shown in Figure 4.12 (right). Figure 4.13 and Figure 4.14 plot the numerical predictions and experimental measurements in terms of arriving time and maximum water depth in different gauge points. The arriving time is accurately predicted in all but the last gauge point. At Gauge 9, the predicted flood front is delayed more than 100 s compared with the measured one. The discrepancy is also predicted by Alcrudo and Gil (1999) presented in Figure 4.13 (right) using an alternative Godunov-type shallow flow model and the present prediction is observed to be slightly better. In terms of maximum water level, the numerical solutions compare reasonably well with those laboratory data in most of the gauge points. Small disagreements are found at Gauge 2 and Gauge 4 and again this is also predicted by Liang *et al.* (2007) illustrated in Figure 4.14 (right) and others (e.g. Alcrudo and Gil 1999; Hervouet 2000; Valiani *et al.* 2002). The present model generally predicts similar or better results than those reported in literature, due to the use of non-negative well-balanced algorithm. From the results, it confirms that the current shallow flow model is well-suited for practical dam-break modelling.

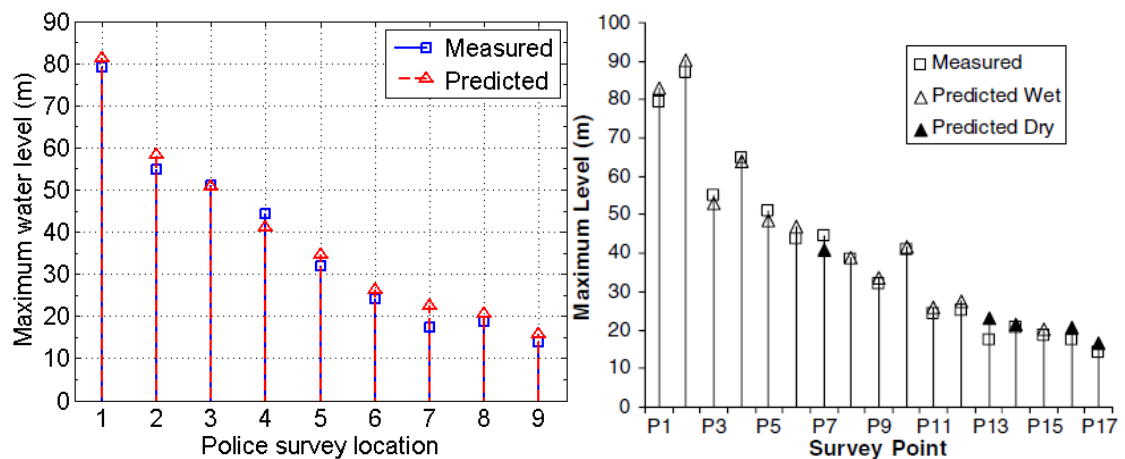


Figure 4.12 Malpasset dam break: comparison of numerical and surveyed maximum water depth (left – by the present model; right – by Liang *et al.* (2007)).

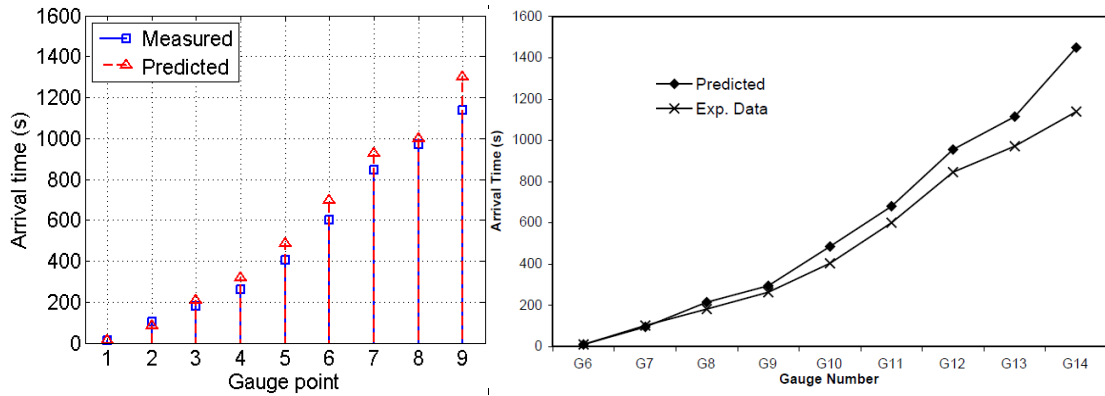


Figure 4.13 Malpasset dam break: comparison of numerical and measured arrival time at different gauge points (left – by the present model; right – by Alcrudo and Gil (1999)).

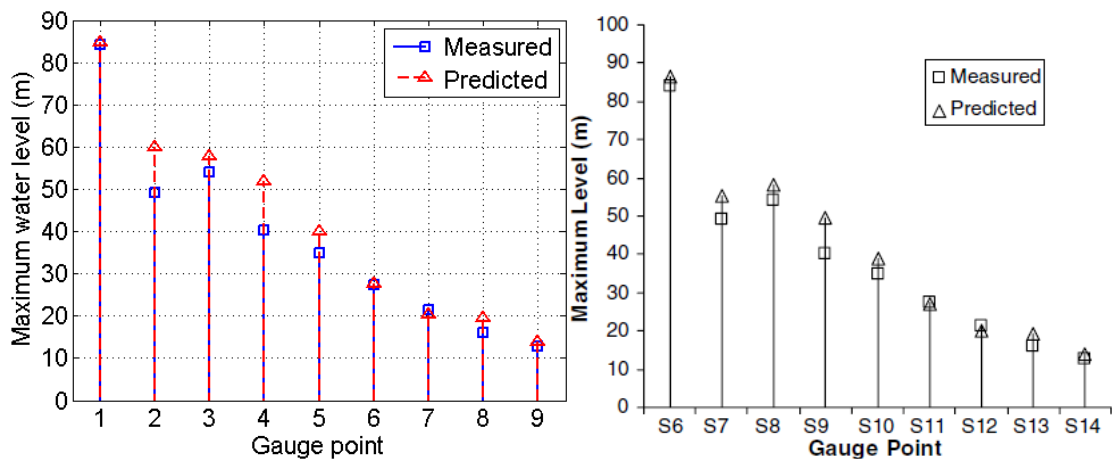


Figure 4.14 Malpasset dam break: comparison of numerical and experimental maximum water depth at different gauge points (left – by the present model; right – by Liang *et al.* (2007)).

4.2 Conclusions

In this chapter, the model has been tested against three benchmark dam-break cases suggested by CADAM, including the real-world case of Malpasset dam break. In all of the tests, the numerical predictions agree reasonably well with those experimental measurements or field data and are generally more accurate than those reported in the literature. This confirms the robustness of the model and its potential becoming a useful predictive tool in simulating dam breaks or other flood events, such as flash floods or

different types of flood inundation. Overall, the model has the following main advantages:

- Due to the use of a shock-capturing Godunov-type scheme, the model is suitable for simulations in all of the flow regimes including shock-like flow discontinuities that generally associated with dam-break waves;
- The model automatically provides well-balanced and non-negative (in terms of water depth) solutions for applications involving wetting and drying over complex domain topography and there is no need to modify any flow variable in order to maintain stability within the limit of the CFL criterion.

Chapter 5 Coastal Wave Run-up Applications

Objectives

- Improve and validate the fully 2D shallow flow model for application in coastal hydrodynamic modelling.

Introduction

Extreme coastal disasters, e.g. the storm surge, severe wind induced tidal wave or tsunami, may lead to damage of coastal defences, huge casualties and economic losses. In order to better manage coastal zones and protect human lives and properties, it is essential to accurately predict and better understand the coastal hydrodynamics and relevant processes, especially wave run-up as it may directly cause overtopping of flood defences.

Wave run-up over a sloping beach or coastal defence is a complex process including wave transformation, reflection, breaking, hydraulic jump, etc. The nonlinear shallow water equations have been widely used for the wave run-up prediction (e.g. Dodd 1998; Hu *et al.* 2000; Hubbard and Dodd 2002; Delis *et al.* 2008; Liang *et al.* 2010) and Brocchini and Dodd (2008) provides a useful review. In this chapter, the 2D well-balanced shallow flow model is improved for simulating the hydrodynamics associated with coastal wave run-ups and validated against several benchmark cases. For this purpose, fully transmissive (non-reflective) boundary conditions are investigated and implemented in the current model to take more accurate account of wave dynamics.

5.1 Non-reflective Boundary Condition

In hydrodynamic modelling, before a simulation is carried out, the first step is to define a problem domain where actual numerical computation takes place. Then an essential step is to correctly impose boundary conditions. In the coastal applications, the seaward

boundary conditions provide the inflow information and the incident wave propagates from the seaward boundary. When the incident wave arrives at the sloping beach or the coastal defence, the wave is reflected against the obstacle. The reflective wave propagates back to the seaward boundary. In this case, the reflective wave should be allowed to pass freely through the boundary or be absorbed. Otherwise, the reflective wave will interfere with the incident wave and introduce noises to the numerical solutions. Hence the seaward boundary must be able to generate the incident wave and meanwhile absorb the reflective wave. The aforementioned boundary conditions (refer to Chapter 3) cannot satisfy the requirements for the coastal applications and non-reflective boundary conditions have to be implemented to absorb the reflective waves from inside the computational domain to the inflow boundary. Herein the approach used by Cienfuegos *et al.* (2007) is investigated, where the solution of boundary flow information is based on the outgoing (β^-) and incoming (β^+) Riemann invariants as shown in Figure 5.1.

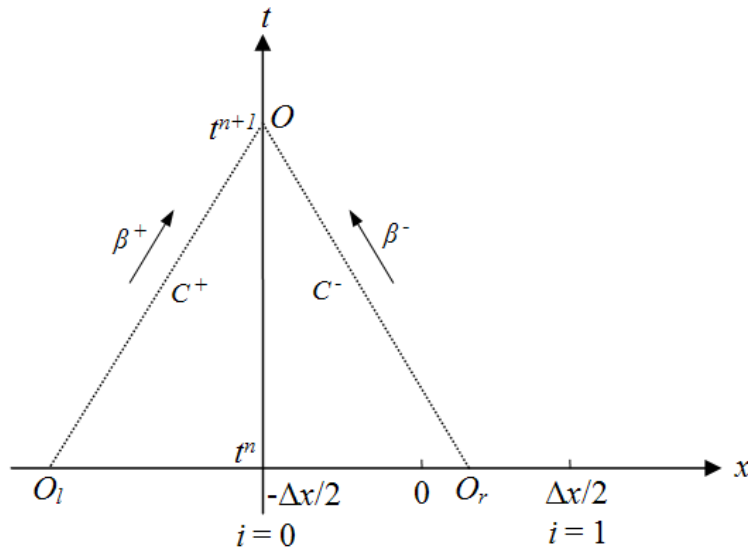


Figure 5.1 Non-reflective boundary conditions.

In Figure 5.1, the original point of the coordinate system is located at the central point of the ghost cell ($i = 0$), where $x = -\Delta x/2$. Herein Δx is the grid size. In this work, the seaward boundary is assumed to be at the western boundary, where the non-reflective boundary is implemented. The centre of the first inner cell locates at $x = \Delta x/2$ ($i = 1$). The incoming and outgoing Riemann invariants β^+ and β^- are respectively constant along the characteristic lines C^+ (defined with $dx/dt = u^+ + c$) and C^- (defined with $dx/dt = u^- - c$), respectively. In order to get the value of the outgoing Riemann

invariant β^- ($\beta^- = u^- - 2c$ with $c = \sqrt{gh^-}$), u^- and h^- must be calculated by linear interpolation and Newton's iteration method from the flow information at $x = \Delta x/2$. The incoming Riemann invariant β^+ can be calculated as

$$\beta^+ = 2\sqrt{g(z_{in} + h_0)} + z_{in}\sqrt{g/h_0}, \quad (5.1)$$

where z_{in} is the amplitude of the incident wave and h_0 is the mean water depth.

In this work, the assumption is that the seaward boundary is the western boundary along the y -direction. Hence the velocity component v is not under consideration. The boundary values of water depth h_b' and velocity u_b' are then calculated by

$$u_b' = 0.5(\beta^- + \beta^+), \quad (5.2)$$

$$h_b' = \frac{1}{16g}(\beta^- - \beta^+)^2, \quad (5.3)$$

which provides the boundary conditions for the Riemann solver.

5.2 Results

5.2.1 Sinusoidal wave reflected against a vertical wall

The first test is to validate the aforementioned non-reflective boundary conditions. This classic benchmark case is about a regular sinusoidal wave reflection at a vertical solid wall, which was also considered by Hu *et al.* (2000). The computational domain is a 1000 m long flat and frictionless uniform channel with a vertical wall at the eastern end. For 2D simulations, the width of the channel is set to be 25 m. A uniform mesh of 400×10 cells is employed in this computation. The western end of the channel is imposed as the non-reflective inflow boundary powered by a regular wave. The other two boundaries are assumed to be slip. The still water depth is 10 m. The inlet regular sinusoidal wave is defined as

$$z_{in} = 0.5H \sin\left(\frac{2\pi t}{T}\right), \quad (5.4)$$

where $H = 0.04$ m is the wave height and $T = 20.193$ s is the wave period.

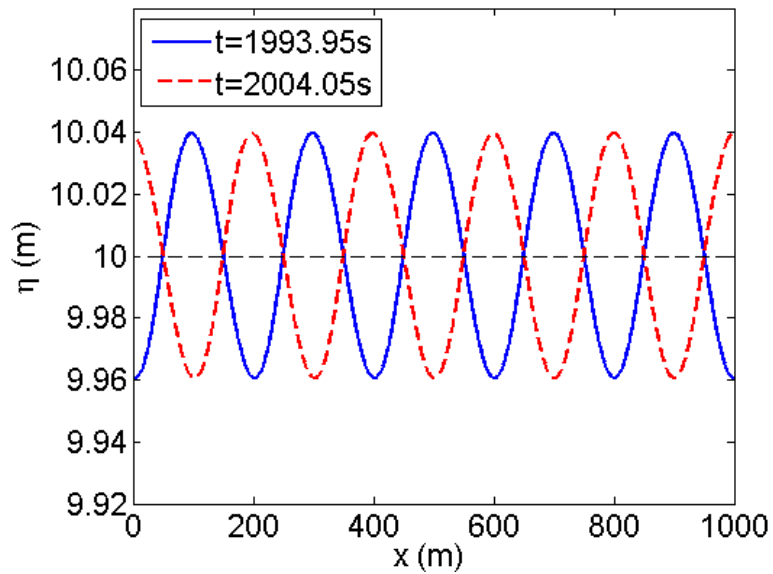


Figure 5.2 Sinusoidal wave reflected against a vertical wall: reflective waves at $t = 1993.95$ s and $t = 2004.05$ s.

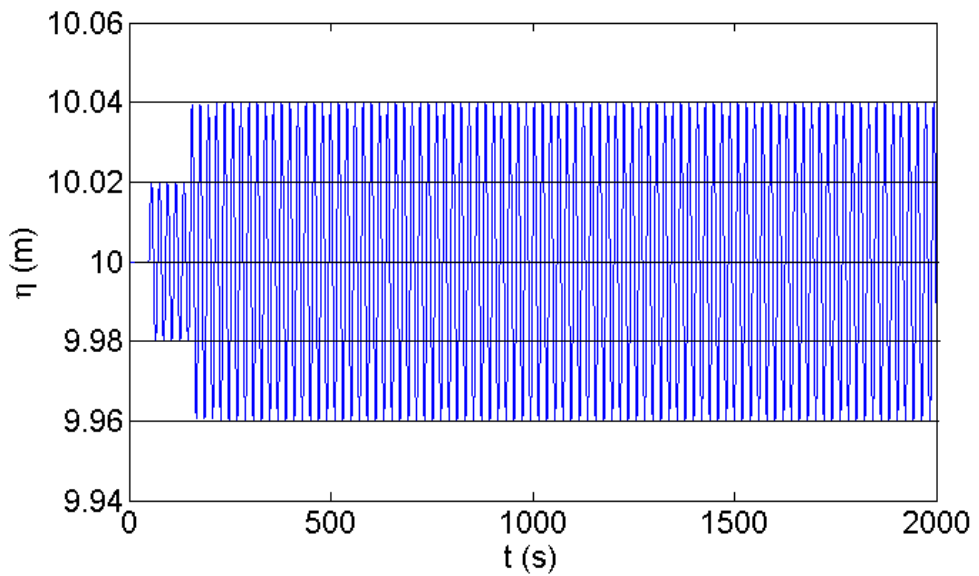


Figure 5.3 Sinusoidal wave reflected against a vertical wall: time history of water depth at $x = 500$ m.

The incident flow of the sinusoidal wave propagates along the channel. After it is reflected against the solid wall, the wave height is doubled to be 0.08 m, theoretically. The non-reflective boundary is implemented at the inlet boundary to absorb the reflective wave in order to avoid the spurious oscillations due to the re-reflective wave near the inlet boundary. Without the disturbance of the reflective wave, the regular wave is accurately reproduced at $t = 1993.95$ s and $t = 2004.05$ s as illustrated in Figure 5.2. The time history of the water surface elevation at $x = 500$ m is recorded in Figure

5.3, where amplitude of the reflected wave is maintained well without the spurious oscillation. Hence the effectiveness of the non-reflective boundary conditions is demonstrated.

5.2.2 Surge reflection

This test case is carried out along a flat and frictionless channel with a solid wall at the eastern end. In a channel of 10,000 m long and 250 m wide, a 10 m high surge wave propagates into the domain through the western inlet. Initially, the 5 m deep still water is assumed in the channel. A uniform grid with 400×10 cells is used in the computation. The analytical solution of this case is given by Chow (1959). Before the surge wave reaches the wall, the relationship between the water depth and velocity is given by the following equations.

$$u_1 h_1 = c_1 (h_1 - h_2), \quad (5.5)$$

$$c_1 = \sqrt{\frac{g h_1 (h_1 + h_2)}{2 h_2}}, \quad (5.6)$$

in which c_1 is the surge wave celerity; u_1 is the inlet flow velocity; h_1 is the water depth of the surge; $u_2 = 0$ is the initial water velocity; h_2 is the initial water depth. The surge wave with a height of 10 m travels along the channel before reaching the wall. In this idealized test, the front of the surge wave should keep vertical without dispersion. Figure 5.4 presents the numerical results $t = 200$ s in terms of water depth, where excellent agreement with the analytical solution is observed.

After the surge wave is reflected from the solid wall, the water depth and velocity of the associated flow become h_3 and u_3 and the analytical solution of h_3 and u_3 are given by (Chow 1959)

$$u_1 h_1 = c_2 (h_3 - h_1), \quad (5.7)$$

$$c_2 = \sqrt{\frac{g h_3 (h_1 + h_3)}{2 h_1}} - u_1, \quad (5.8)$$

where c_2 is the reflective wave celerity. After the reflection, the theoretical height of the reflected surge wave increases to 16.854 m. The predicted water depth at $t = 1000$ s is compared with the analytical solution in Figure 5.5. The numerical simulation is again

found to agree well with the exact solution. Figure 5.6 and Figure 5.7 show the time histories of water depth and flow velocity at $x = 5000$ m and both match well the analytical solutions.

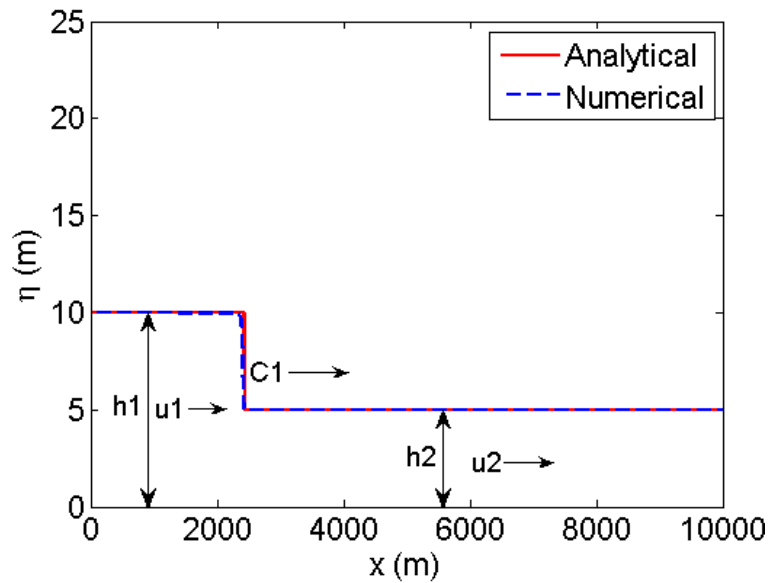


Figure 5.4 Surge reflection: comparison of the analytical and predicted water depth at $t = 200$ s.

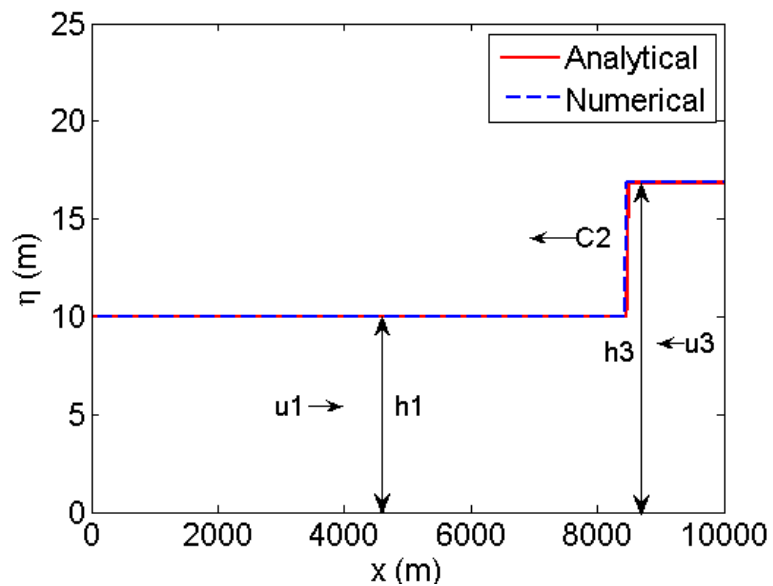


Figure 5.5 Surge reflection: comparison of the predicted and analytical water depth at $t = 1000$ s.

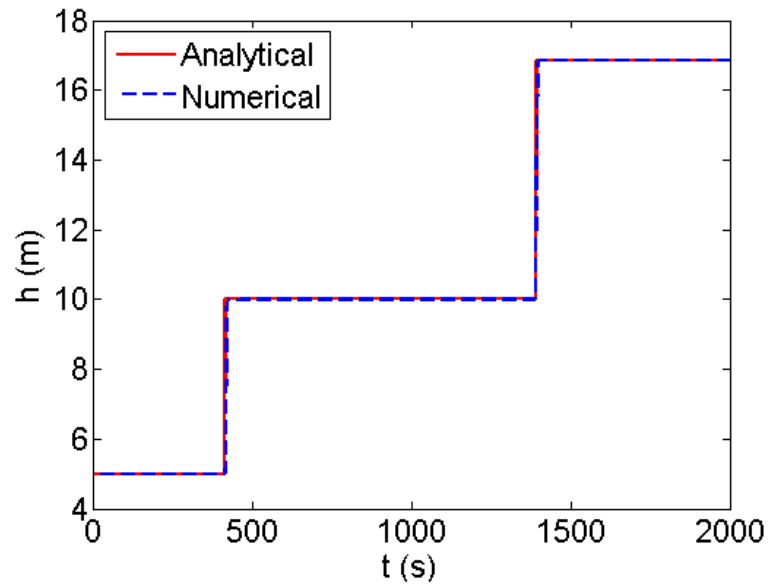


Figure 5.6 Surge reflection: time history of the water depth at $x = 5000$ m.

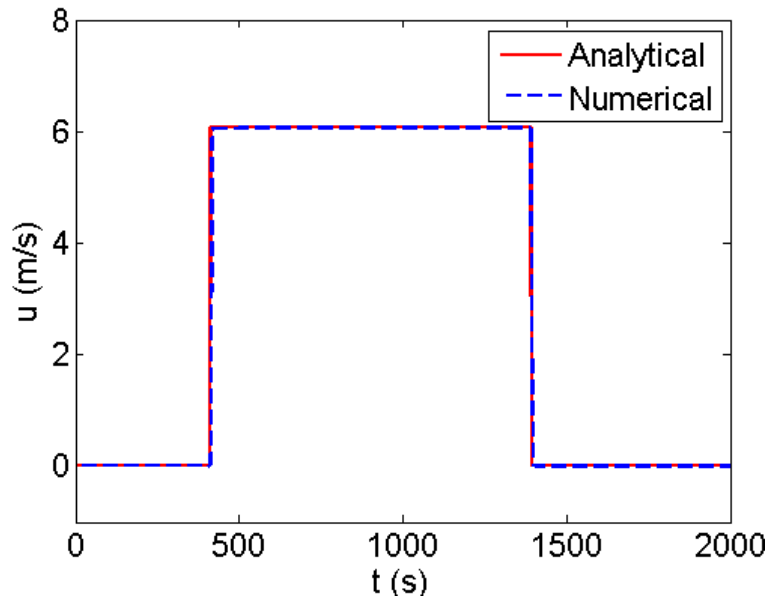


Figure 5.7 Surge reflection: time history of the flow velocity at $x = 5000$ m.

5.2.3 Tidal flow in a channel with non-uniform topography

This analytical test is to reproduce a tidal flow along a channel with varying topography, which was also studied by Zhou *et al.* (2001). The channel is 14 km long and 350 m wide with a frictionless bed defined by

$$z_b(x) = 10 + \frac{40x}{L} + 10 \sin \left[\pi \left(\frac{4x}{L} - 0.5 \right) \right], \quad (5.9)$$

The analytical solutions of water depth and velocity of the flow are given by Bermudez and Vazquez (1994):

$$h(x,t) = 64.5 - z_b(x) - 4 \sin \left[\pi \left(\frac{4t}{86400} + 0.5 \right) \right], \quad (5.10)$$

$$u(x,t) = \frac{(x-L)\pi}{5400h(x,t)} \cos \left[\pi \left(\frac{4t}{86400} + 0.5 \right) \right]. \quad (5.11)$$

A uniform computational mesh is created to contain 400×10 cells. $h(0, t)$ and $u(0, t)$ are given at the western end of the domain as the inflow boundary condition. While $u(L, t)$ is used to define the outflow boundary at the eastern end of the channel. The north and south boundaries are set to be slip.

The numerical predictions of the water level and velocity along the central line are recorded at $t = 7552.13$ s and compared with the analytical solutions in Figure 5.8 and Figure 5.9. The numerical predictions agree well with the analytical solutions and this demonstrates the capability of the present model on simulating flows over irregular bed topography.

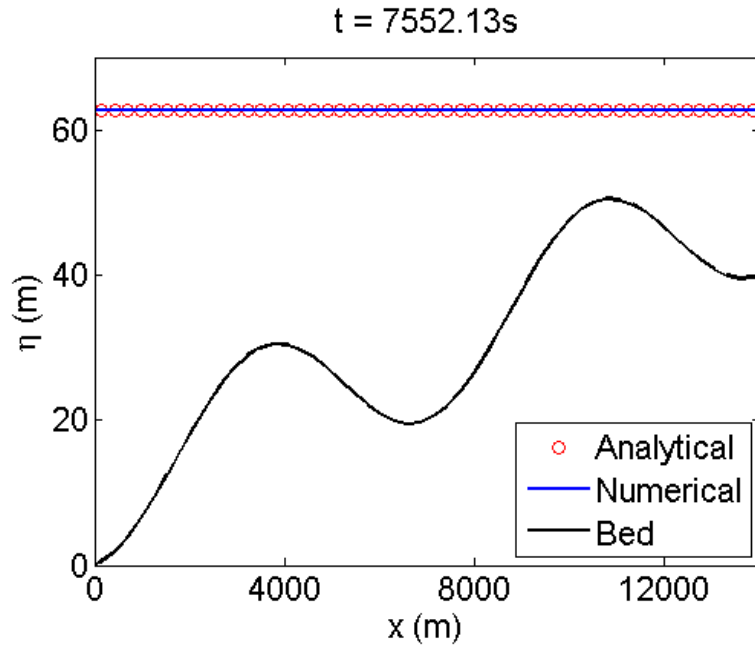


Figure 5.8 Tidal flow: comparing analytical and prediction water level at $t = 7552.13$ s.

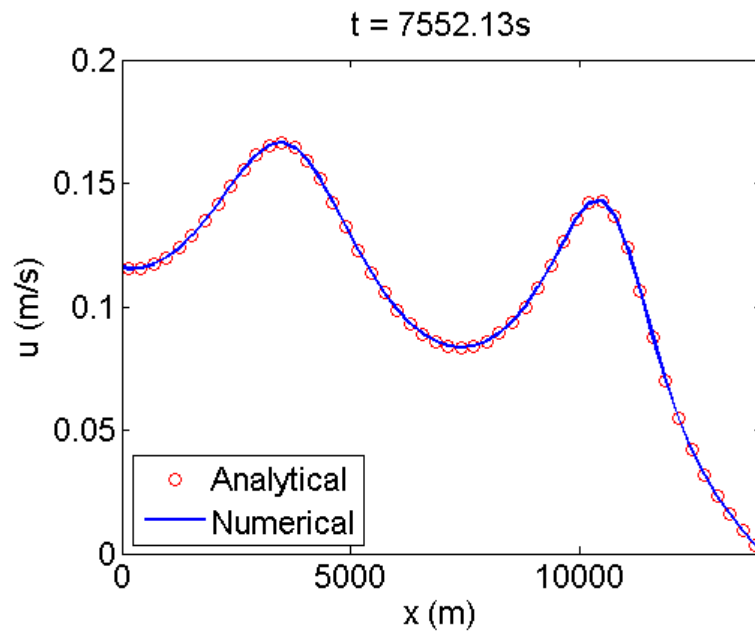


Figure 5.9 Tidal flow: comparing analytical and predicted velocity at $t = 7552.13$ s.

5.2.4 Shallow flow oscillation in a parabolic bowl

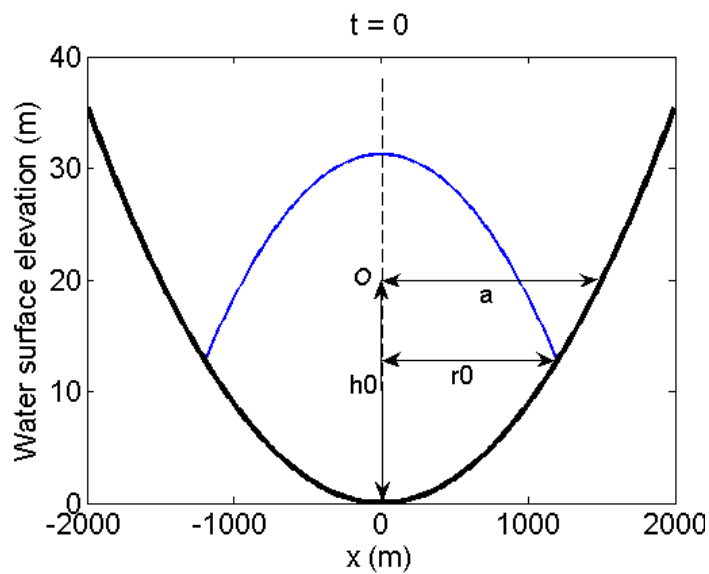


Figure 5.10 Shallow flow oscillation in a parabolic bowl: the bed profile and the initial water surface elevation.

This 2D analytical case is chosen to validate the capability of the fully 2D shallow flow model on capturing the moving shoreline. This case has been adopted by numerous researchers to validate their numerical models, including Balzano (1998). As shown in Figure 5.10, the topography of the parabolic bowl is defined by

$$z_b(x, y) = h_0 \frac{(x^2 + y^2)}{a^2}, \quad (5.12)$$

where the origin of the coordinate system is at the domain centre, O indicates the still water level at the domain centre, h_0 is the corresponding still water depth and a is the distance from O to the shoreline.

The analytical solution of the water surface elevation was derived by Thacker (1981) and is given as

$$\eta(x, y, t) = h_0 \left[\frac{(1 - A^2)^{1/2}}{1 - A \cos \omega t} - \frac{x^2 + y^2}{a^2} \left(\frac{1 - A^2}{(1 - A \cos \omega t)^2} - 1 \right) \right], \quad (5.13)$$

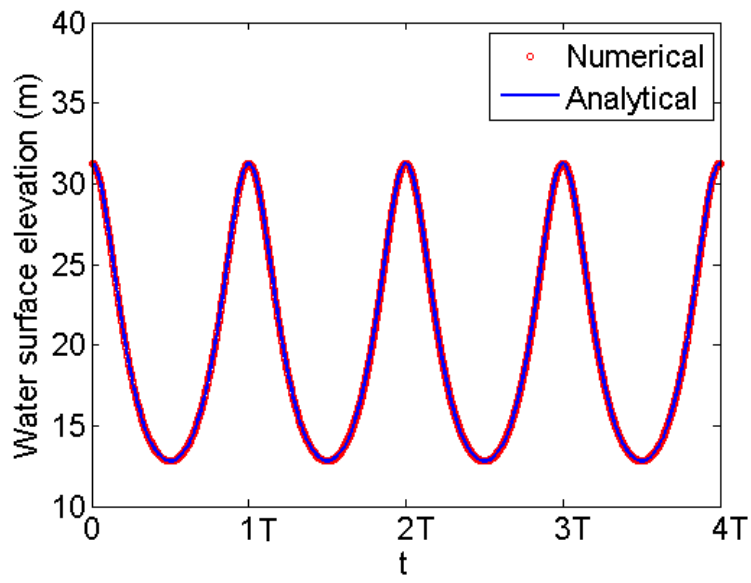
in which

$$A = \frac{a^4 - r_0^4}{a^4 + r_0^4}, \quad \omega = \sqrt{\frac{8gh_0}{a^2}}, \quad (5.14)$$

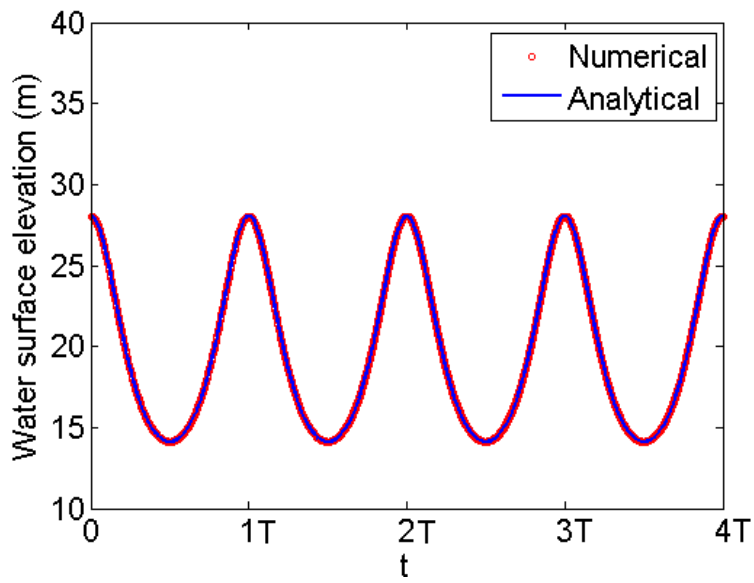
where r_0 is the distance from the initial location of the shoreline to the domain centre. In this case, $h_0 = 20$ m; $a = 1500$ m and $r_0 = 1200$ m.

The $4000 \text{ m} \times 4000 \text{ m}$ frictionless computational domain is approximated by a uniform mesh of 400×400 cells. The initial water surface elevation is defined by equation (5.13) and (5.14) at $t = 0$. Open boundary conditions are implemented but the boundary settings do not have any influence on the numerical solution as the flow cannot reach the edge of the parabolic bowl in this case. Simulation is run to reproduce the flow oscillation for $4T$ (T is a period). The time history of the water surface elevation is recorded at two gauging points, i.e. G1 (0, 0) and G2 (500, 0).

Figure 5.11 compares the numerical and analytical water level at two gauge points. The predictions match perfectly the analytical solutions. The central profiles along x -axis are presented in Figure 5.12 at $t = T/4, T/2, 3T/4, T, 5T/4, 3T/2, (2+3/4)T$ and $4T$. The moving shoreline has been almost exactly captured even after a four periods as shown in Figure 5.12 (h) for $t = 4T$. The capability of the current model in dealing with non-uniform bed topography and repeating wetting and drying process has been confirmed.

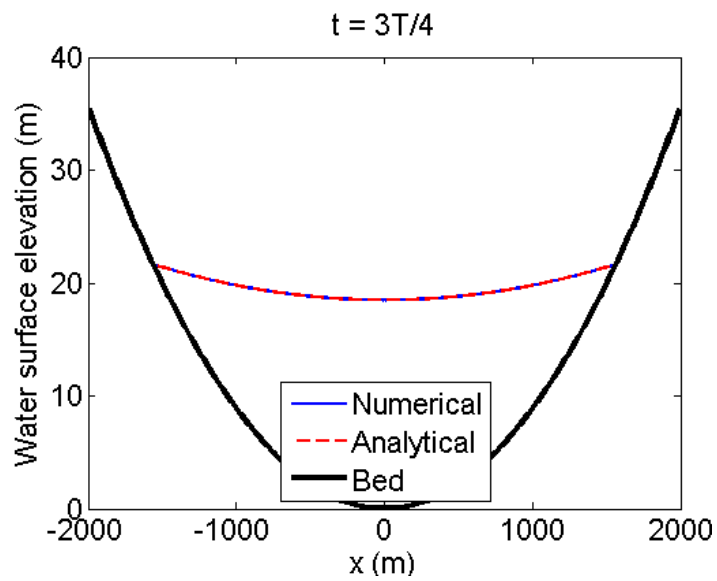
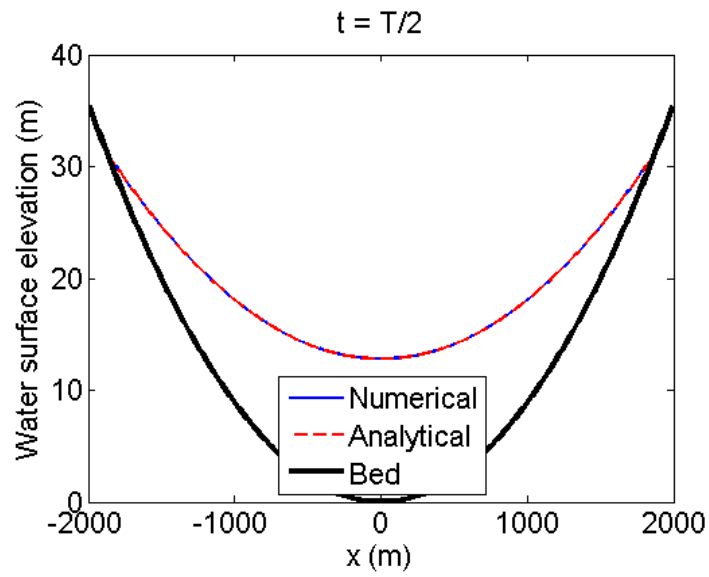
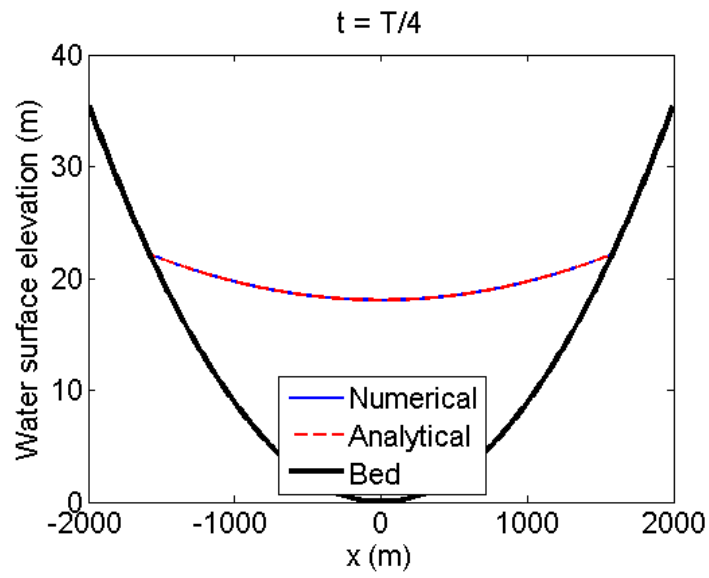


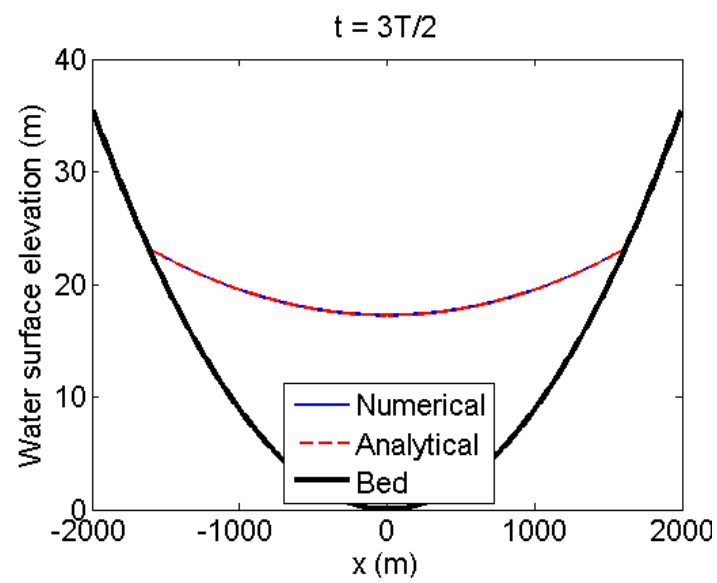
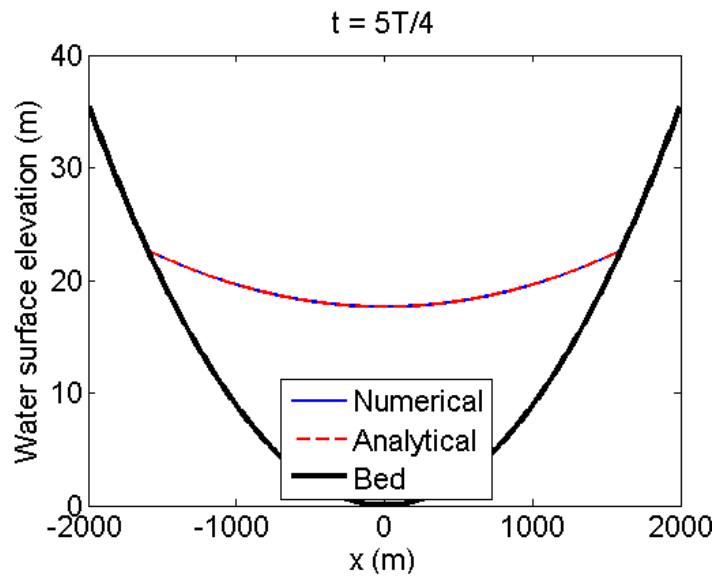
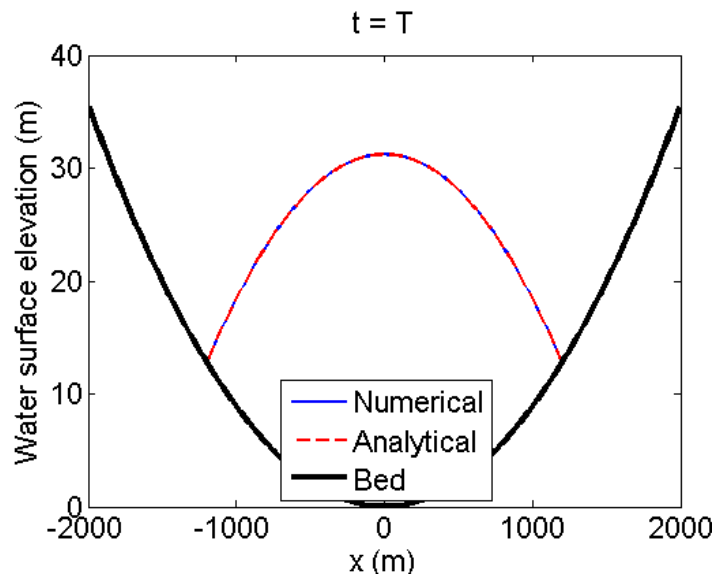
(a)



(b)

Figure 5.11 Shallow flow oscillation in a parabolic bowl: time histories of the water surface elevation (a) at $x = 0$ and (b) at $x = 500$ m.





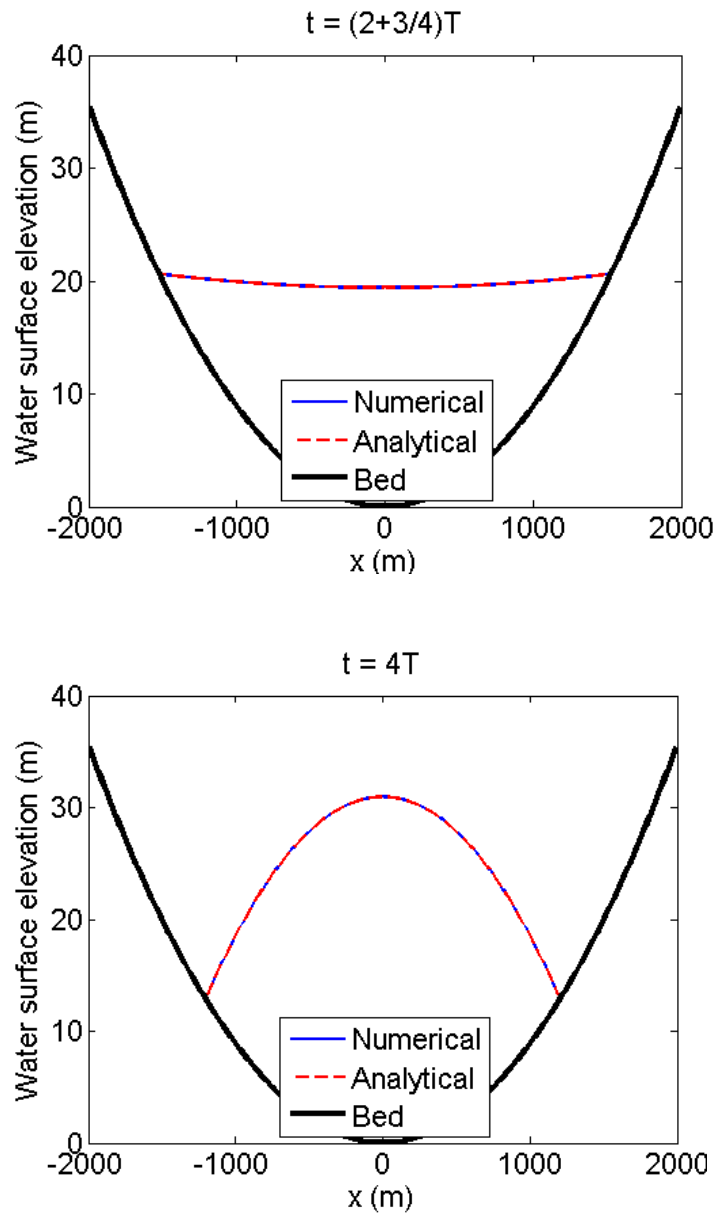


Figure 5.12 Shallow flow oscillation in a parabolic bowl: water surface profile at different output times.

5.2.5 Solitary wave run-up along a sloping beach

This classic benchmark test is about a solitary wave running up and down a sloping beach, which was experimentally and analytically studied by Synolakis (1987) and has been widely used as a benchmark to validate numerical models (e.g. Hu *et al.* 2000; Yamazaki *et al.* 2009). Both the analytical and experimental tests are considered in this work.

5.2.5.1 Analytical test

As shown in Figure 5.13, the computational domain starts from a flat sea bed, which is then followed by a sloping beach with a slope of 1: 19.85. The whole domain is 100 m long and 10 m wide. The still water level intersects the beach at O , which is located at $x = 80$ m. The distance from O to the left hand side of the domain is defined as ξ . The toe of the beach is 19.85 m away from O (X_o). The solitary wave centres at X_c with a height of $h_o = 0.019$ m. X_c can be calculated by

$$X_c = X_o + \sqrt{\frac{4H}{3h}} \operatorname{arccosh}(\sqrt{1/0.05}), \quad (5.15)$$

The mean water depth H is 1 m. The detailed analytical solutions for this test may be found in Synolakis (1987) and Hu *et al.* (2000). The initial water surface and velocity of the wave are given by

$$\eta(x) = h \operatorname{sech}^2 \left(\sqrt{\frac{3h}{4H^3}} (x - X_c) \right), \quad (5.16)$$

$$u(x) = \eta(x) \sqrt{\frac{g}{H}}, \quad (5.17)$$

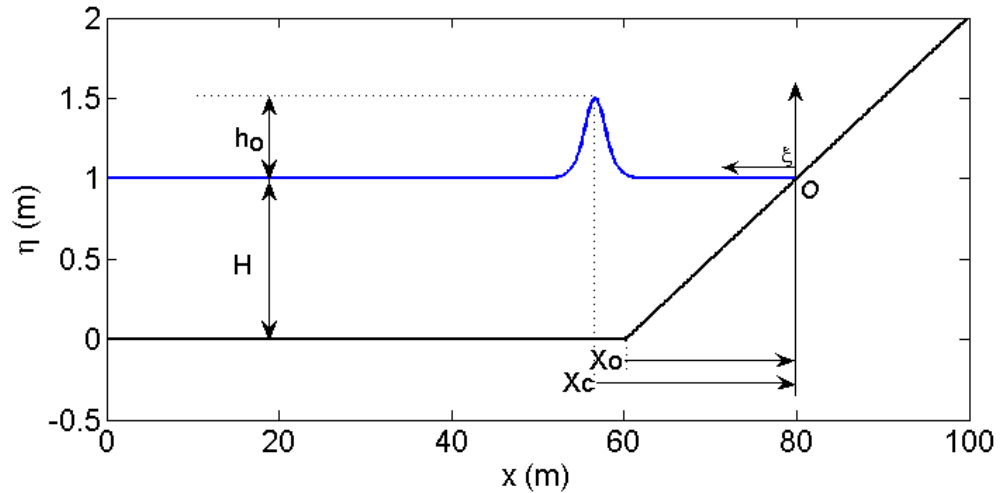
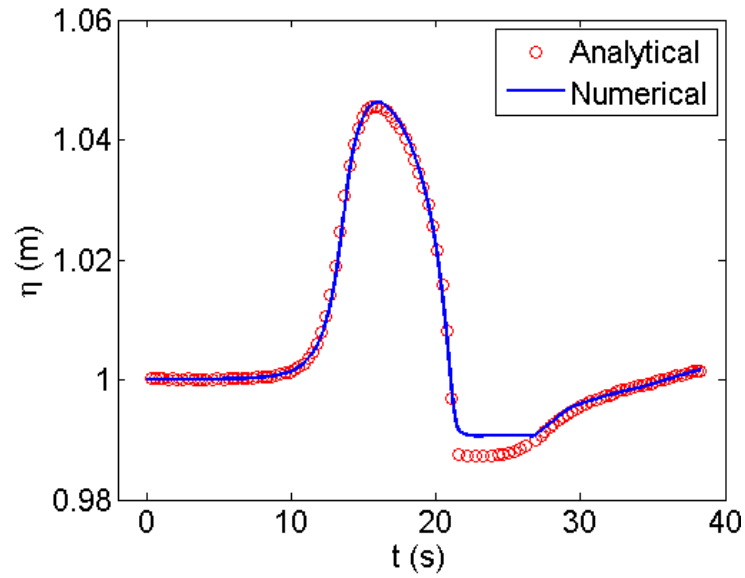


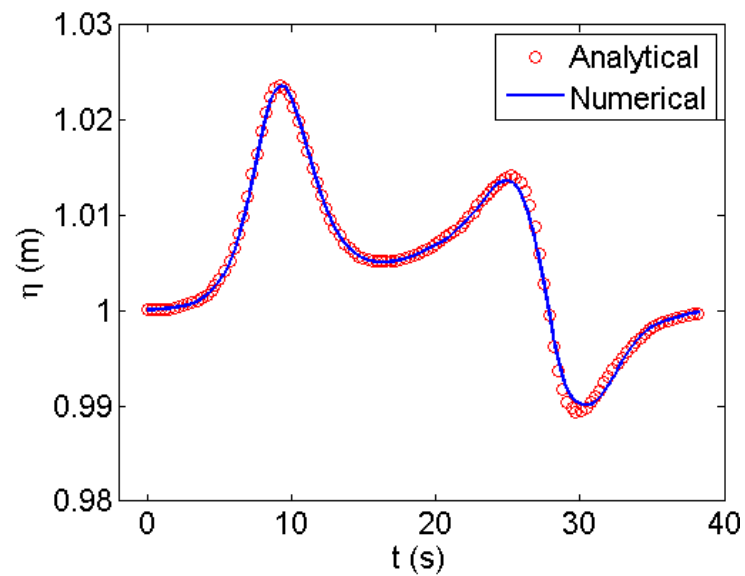
Figure 5.13 Analytical solitary wave run-up: definition of solitary wave and bed profile.

The solitary wave propagates from left to right and then climbs up the sloping beach. The non-reflective boundary conditions are implemented at the western end of the domain while open boundary is assumed at the opposite side. The other boundary walls

are assumed to be slip. The computational domain is decomposed by a uniform grid of 400×40 cells.



(a)

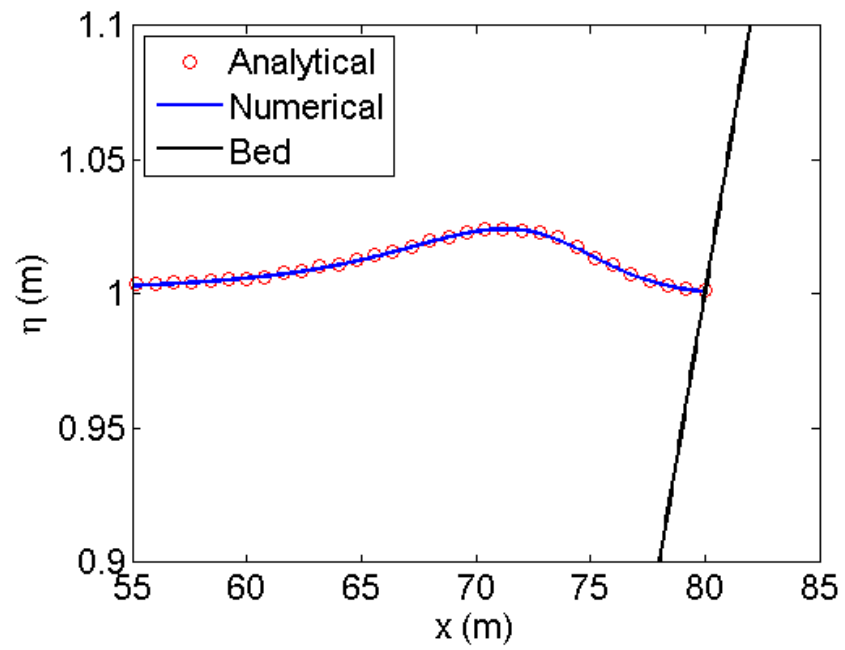


(b)

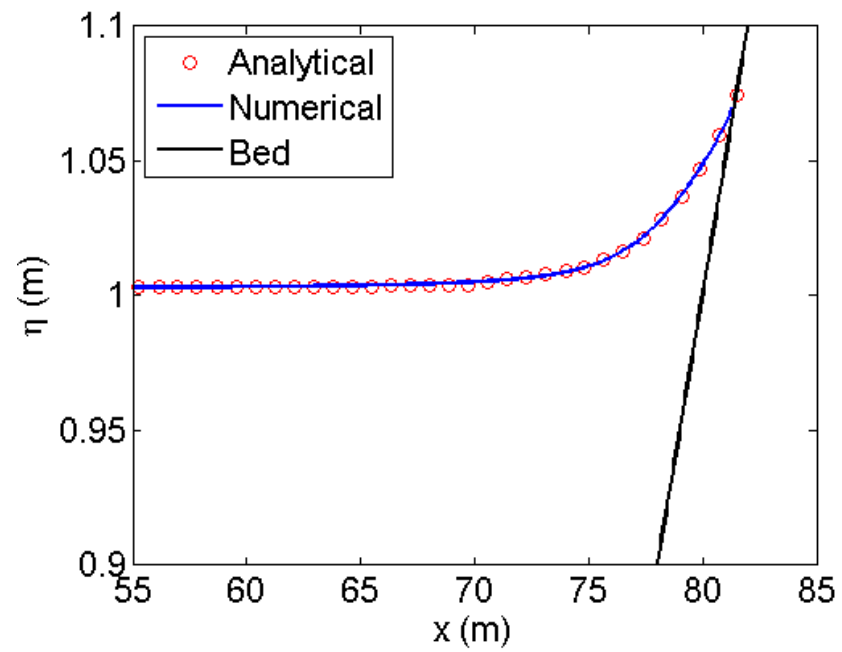
Figure 5.14 Analytical solitary wave run-up: time history of the water level at (a) $\xi = 0.25$ m and (b) $\xi = 9.95$ m.

Figure 5.14 illustrates the time histories of the water surface elevation at $\xi = 0.25$ m and $\xi = 9.95$ m for a duration of 40 s and the numerical predictions compare reasonable well with the analytical solutions. In Figure 5.15, snapshots of the solitary wave run-up are captured at different dimensionless times $t(g/H)^{1/2}=30$, $t(g/H)^{1/2}=50$ and $t(g/H)^{1/2}=70$.

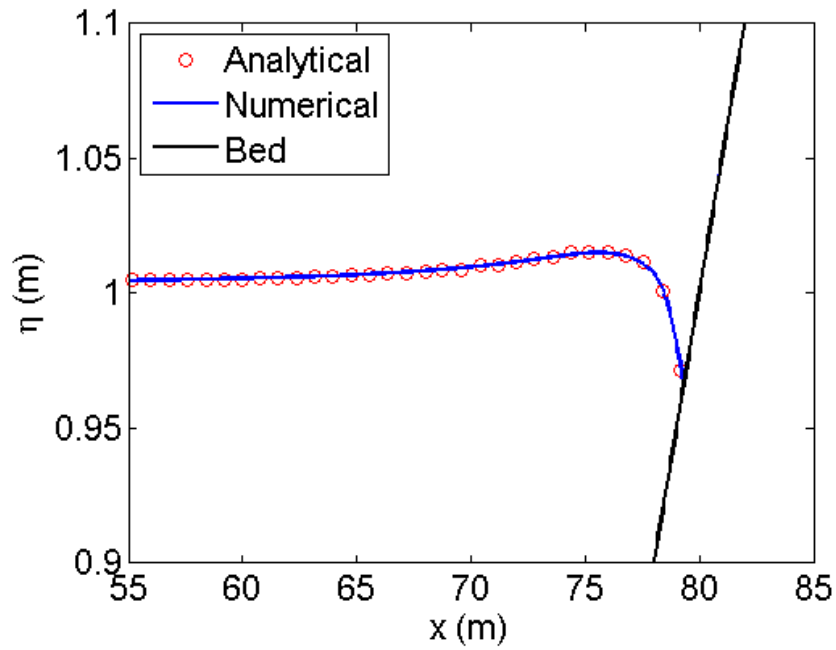
Again the predicted wave profiles are found to agree very well with the analytical solutions and no spurious oscillation is detected at the wet-dry interface.



(a)



(b)



(c)

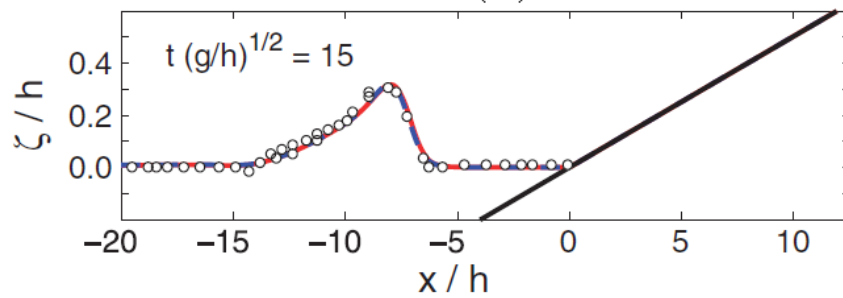
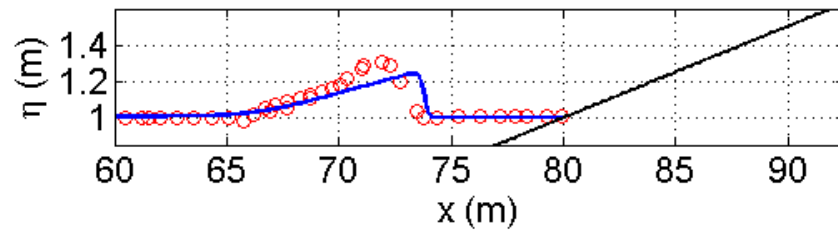
Figure 5.15 Analytical solitary wave run-up: wave profiles at (a) $t(g/h)^{1/2}=30$; (b) $t(g/h)^{1/2}=50$; (c) $t(g/h)^{1/2}=70$.

5.2.5.2 Experimental test

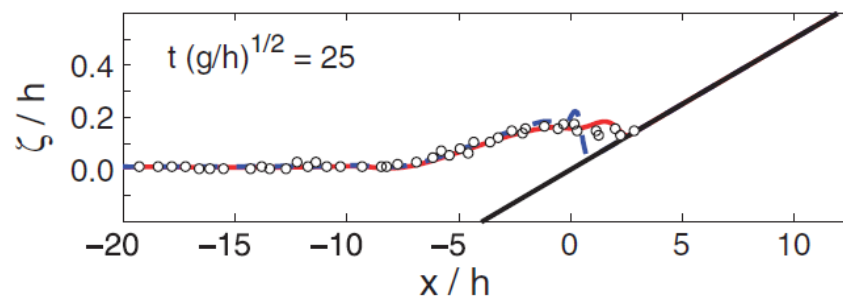
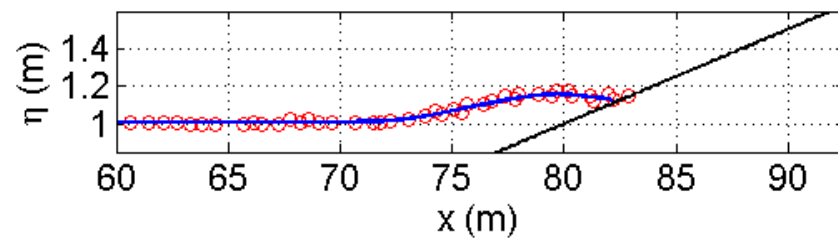
The experiment tests of solitary wave run-up on a sloping beach carried out by Synolakis (1987) have been adopted by numerous modellers to test their numerical models (e.g. Yamazaki *et al.* 2009). In this work, we consider a severe shallow wave event as Yamazaki *et al.* (2009) did, where the wave height is assumed to be 0.3 m. The Manning's n is set to be $0.01 \text{ s/m}^{1/3}$. Other settings are the same as those in the analytical test. A uniform grid of 800×20 cells is applied.

Figure 5.16 illustrates the predicted wave run-up profiles at $t(g/h)^{1/2} = 15, 25, 40, 50, 55, 65$, compared with the laboratory data and the predictions simulated by Yamazaki *et al.* (2009). The run-up process involves wave propagation, breaking, climbing, retreating and formation of a hydraulic jump. At the beginning, the solitary wave propagates from the original location to the sloping beach. The wave front arrives at the sloping beach about $t(g/h)^{1/2} = 15$. The wave becomes steeper when the wave begins to climb up the sloping beach. Then the solitary wave breaks due to the shallow water effect at around $t(g/h)^{1/2} = 25$. After breaking, the wave runs up along the sloping beach. At $t(g/h)^{1/2} = 40$, the wave run-up reaches the maximum height with the associated momentum becoming

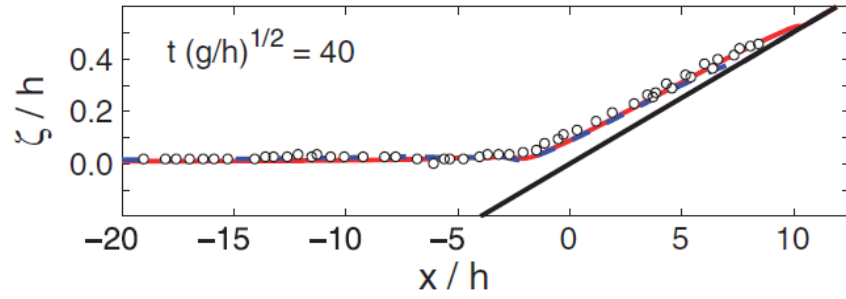
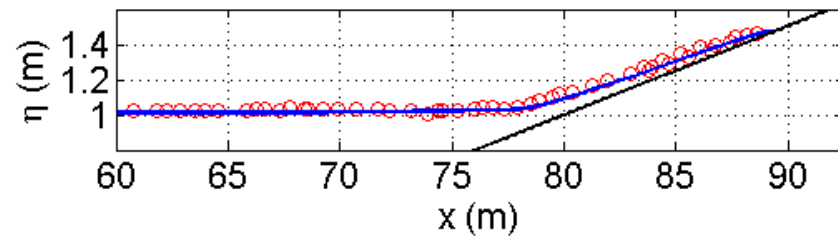
zero. After that, the wave begins to retreat at $t(g/h)^{1/2} = 50$. Supercritical flow is developed when the wave retreats from the slope. When the supercritical flow joins the slower subcritical flow near the toe, a hydraulic jump forms, as shown in Figure 5.16 (e-f) for $t(g/h)^{1/2} = 55$ and $t(g/h)^{1/2} = 65$. The numerical predictions generally agree very well with the experimental measurements. The present fully 2D shallow flow model accurately reproduces the important stages of wave run-up and run-down, e.g. wave breaking, wave running up and down and the formation of hydraulic jump. Both the analytical and experimental solitary wave run-up tests demonstrates that the current numerical scheme performs well in dealing with the complex coastal hydrodynamic phenomena, e.g. wave breaking, moving shoreline, hydraulic jump, etc.



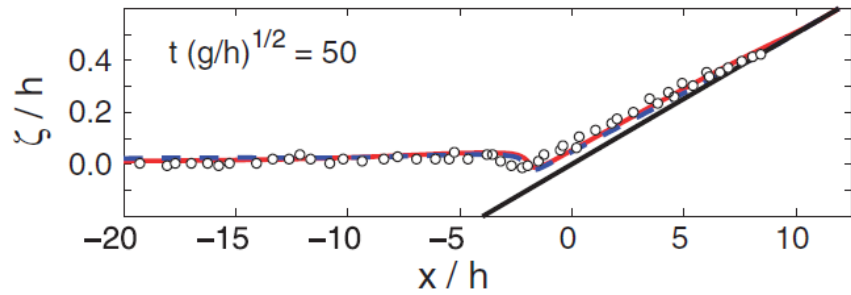
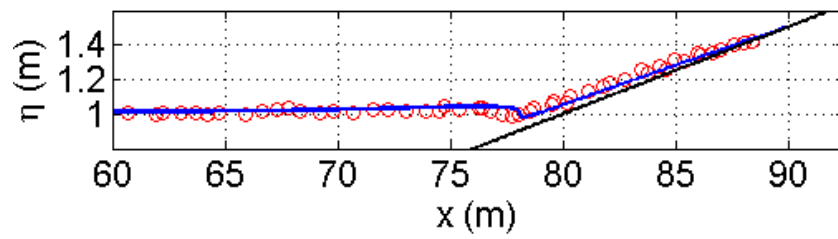
(a) $t(g/H)^{1/2} = 15$



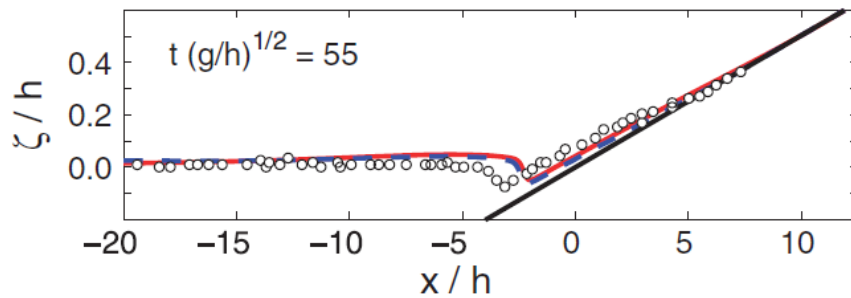
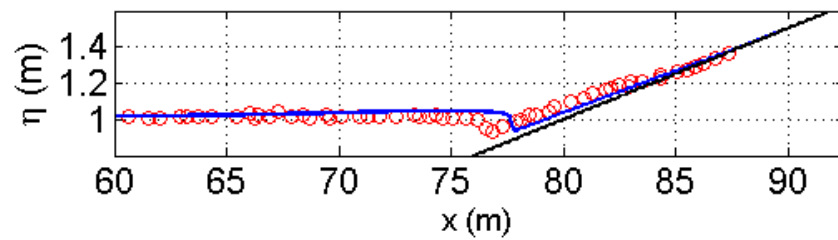
(b) $t(g/H)^{1/2} = 25$



(c) $t(g/H)^{1/2} = 40$



(d) $t(g/H)^{1/2} = 50$



(e) $t(g/H)^{1/2} = 55$

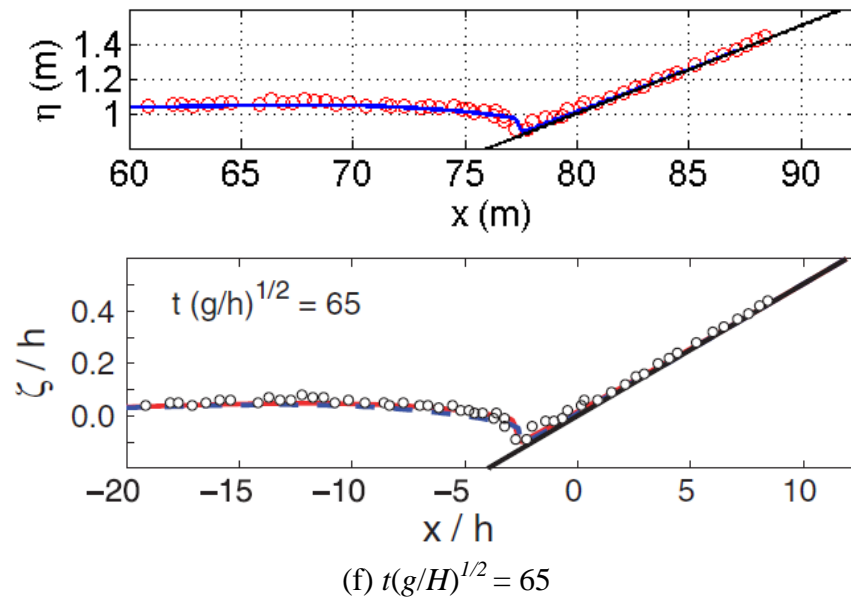


Figure 5.16 Experimental solitary wave run-up: wave profiles at different output times, (up – by the present model, where \circ (red) stands for experimental data, — (blue) represents numerical results and — (black) denotes sea bed; down – by Yamazaki *et al.* (2009), where \circ (black) stands for experimental data, — (blue and red) represents numerical results and — (black) denotes sea bed).

5.2.6 Experimental tsunami run-up with realistic domain features

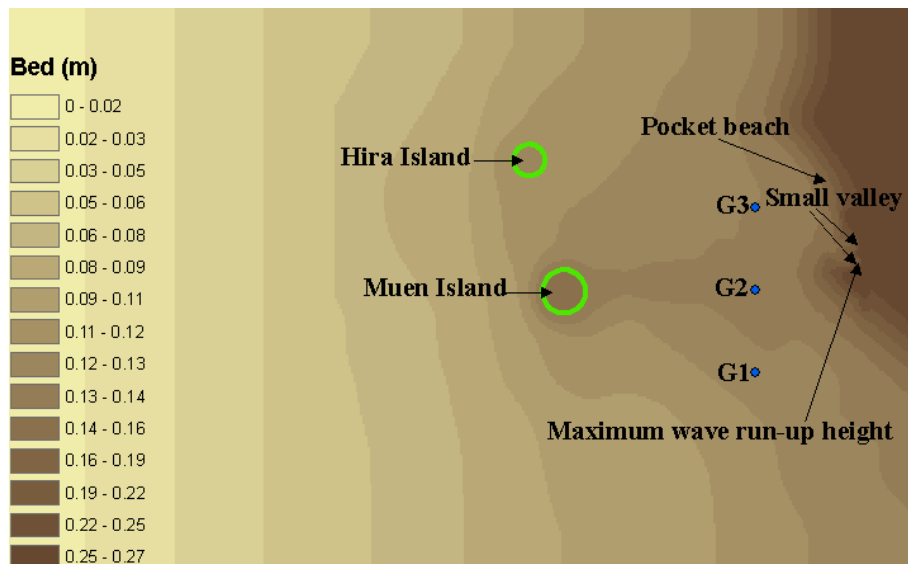
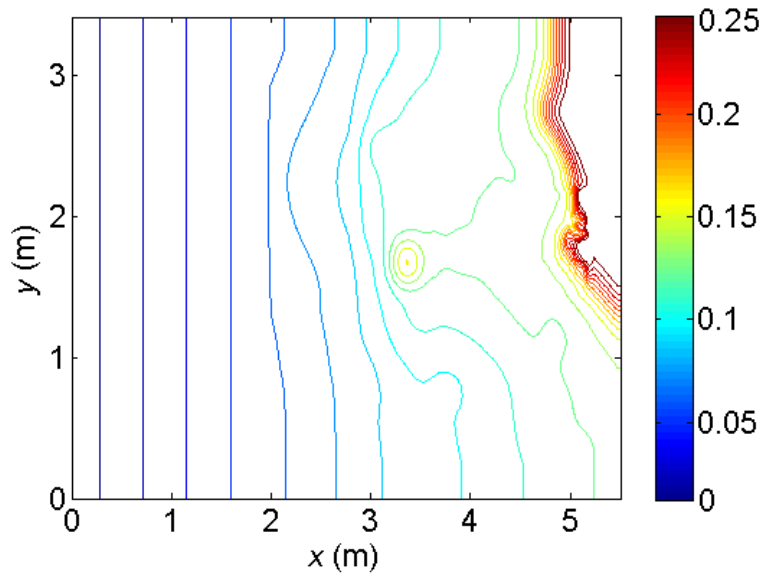


Figure 5.17 Tsunami run-up: domain topography.

A 7.8 magnitude of the earthquake took place at the offshore of the south-western Hokkaido Island, Japan, on 12 July 1993 triggered a tsunami disaster. In the event, the economic damage was recorded to be up to 600 million US dollars. 250 people were killed and more than half of the deaths were caused by the tsunami. The maximum wave run-up of 31.7 m in height at Monai Valley of Okushiri Island was one of the remarkable features associated with the event. A physical experiment of 1: 400 in scale was carried out by the Hydraulic Department of the Central Research Institute of Electric Power Industry in Abiko to reproduce the maximum tsunami run-up at the Monai area (Matsuyama and Tanaka 2001). The experimental case is also studied by Franchello (2010).

The laboratory model was built in a large wave flume of 3.4 m wide, 205 m long and 6 m deep. The selected 5.488 m \times 3.402 m computational domain focuses on the area with maximum observed run-up height, consisting of a pocket beach and two small valleys. The maximum run-up height happened at the south valley. The domain topography is presented in Figure 5.17 and Figure 5.18 where contours of the topography are plotted. Three gauge points located near to the small valley in the pocket beach are used to record the evolution of the water surface elevation and flow velocity around the pocket beach area.



(a)

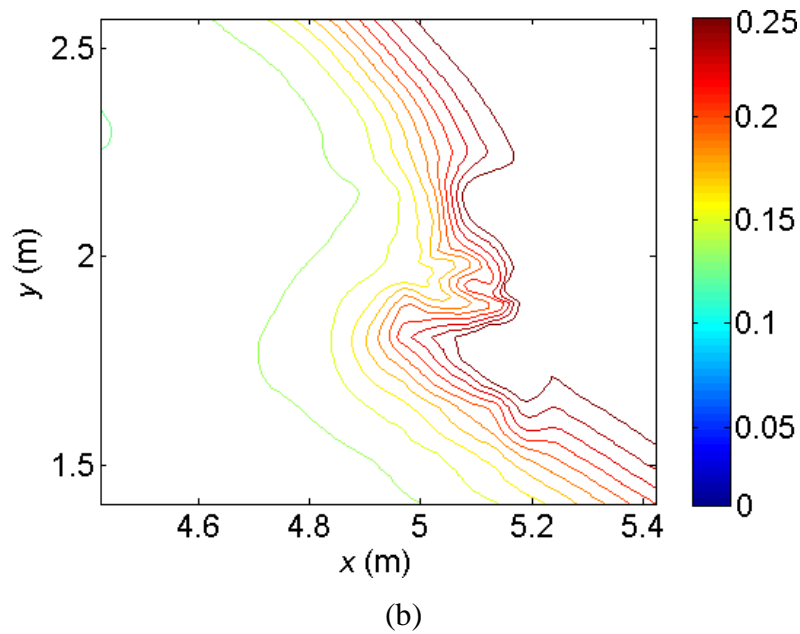


Figure 5.18 Tsunami run-up: contour lines of the bed topography of (a) the whole computational domain; (b) the pocket beach and two small valleys.

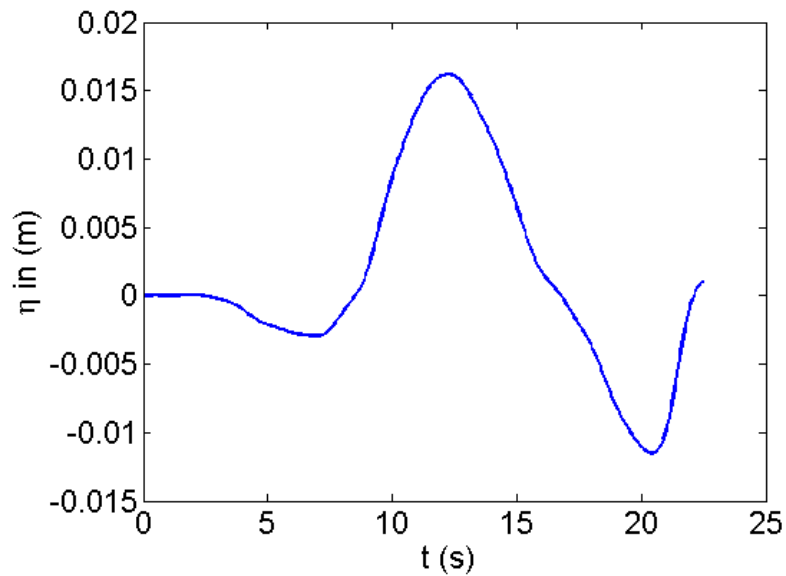
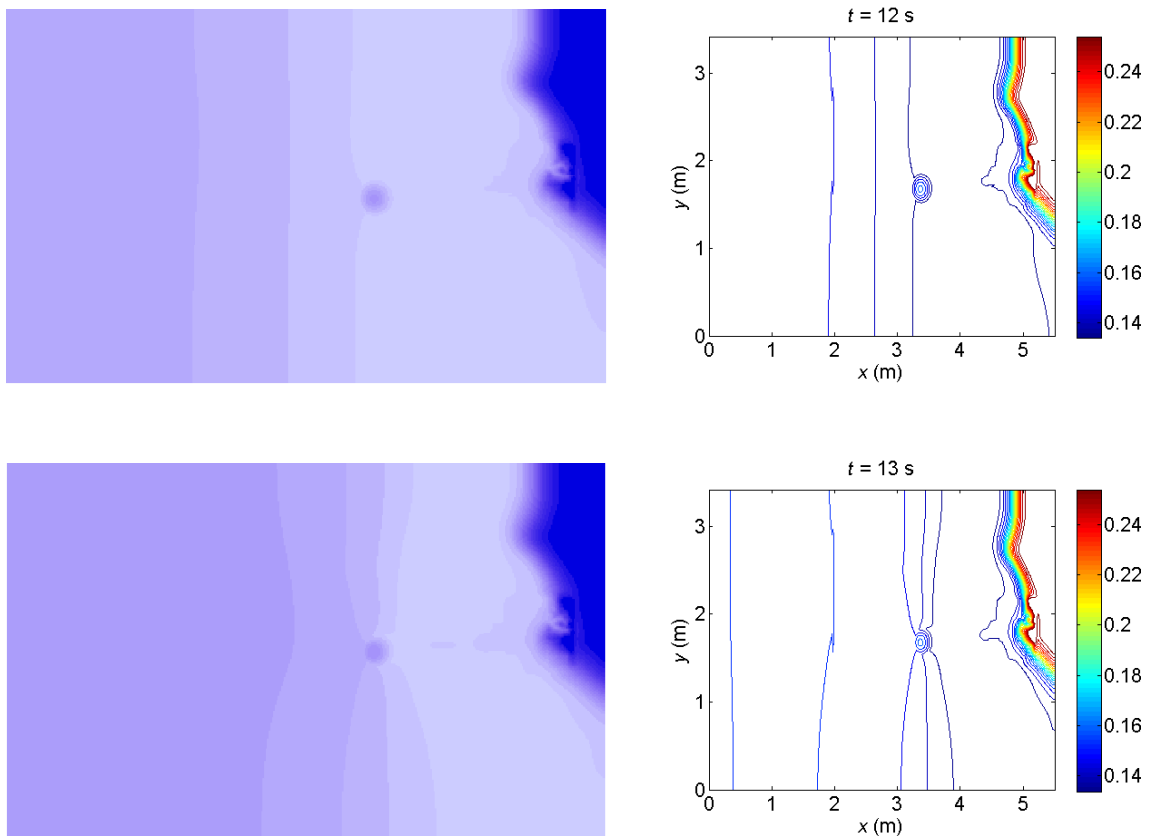


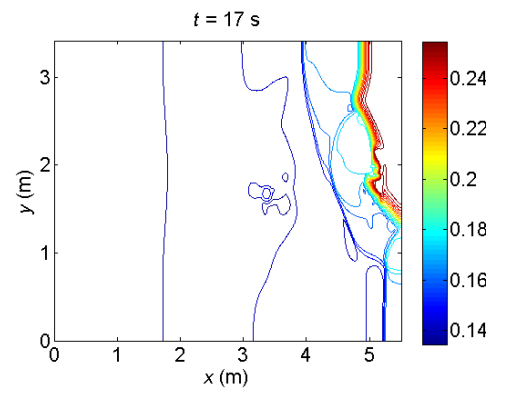
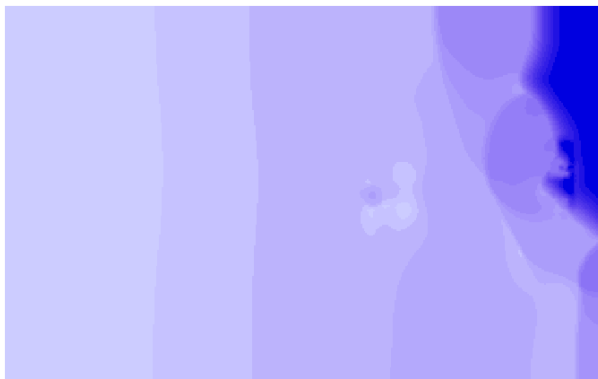
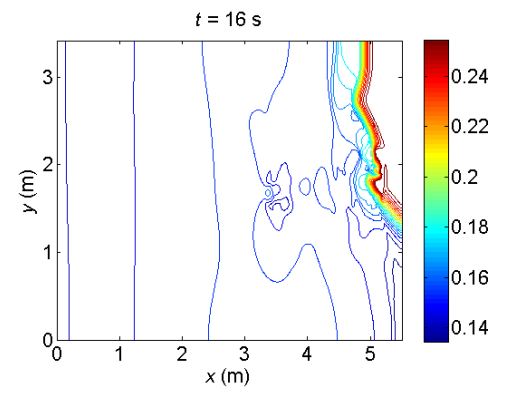
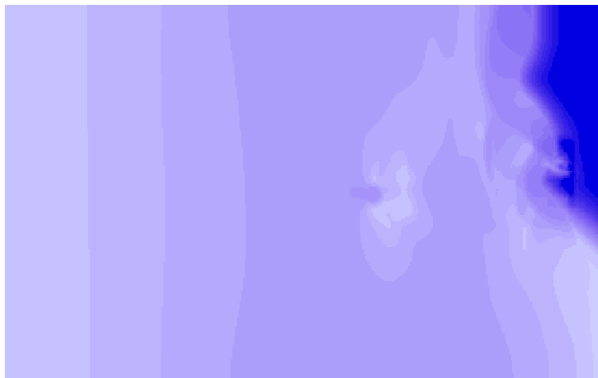
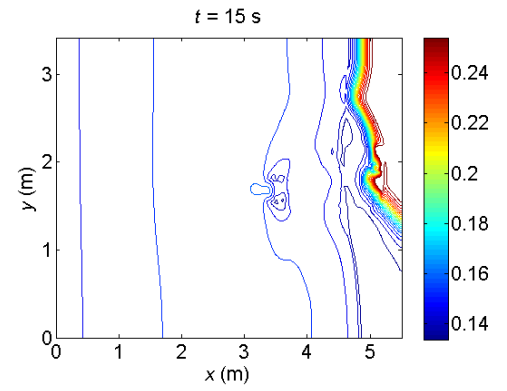
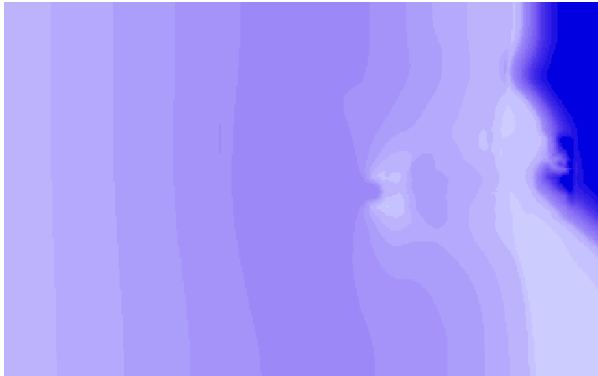
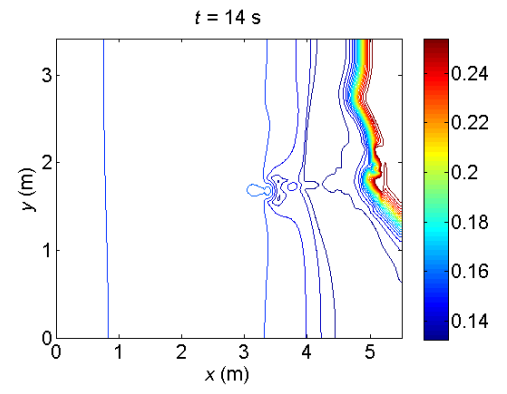
Figure 5.19 Tsunami run-up: the 22.5 s incident wave.

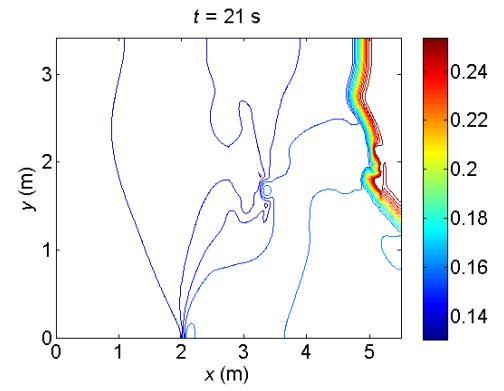
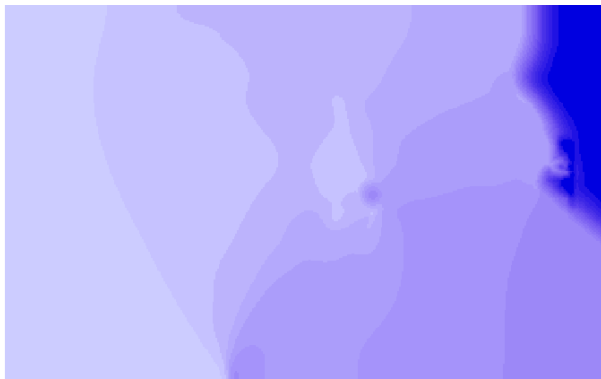
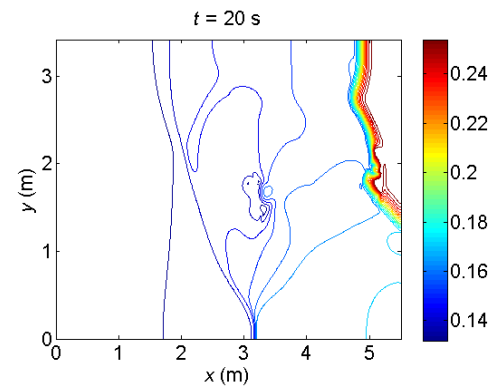
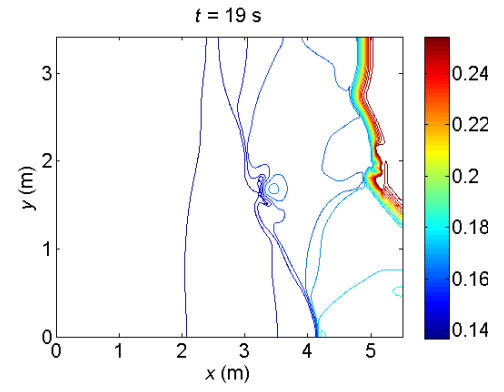
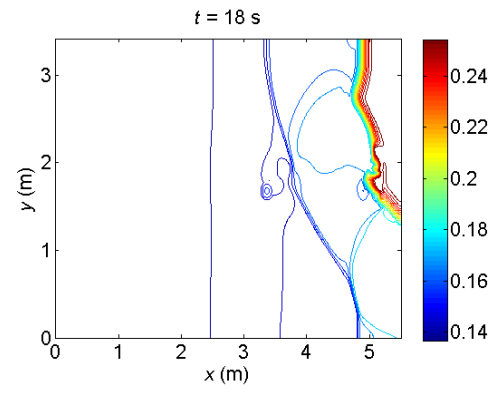
A uniform grid with a resolution of 0.014 m is used for the simulation. The Manning coefficient n is set to be 0.01. The western end of the computational domain is used as the inflow boundary and implemented with non-reflective boundary conditions. The other three boundaries are set to be solid wall boundaries. The 22.5 s incident tsunami wave, as illustrated in Figure 19, was produced by a wave generator and propagated from the western side of the computational domain. The mean water depth is set to be

0.13535 m. The duration of the numerical prediction is 30 s. The CFL number is set to be 0.5.

Figure 5.20 presents the evolution of the tsunami running-up and -down over the beach from $t = 12$ s to $t = 22$ s, in terms of water surface plots (left) and contours (right) at every second. The tsunami wave first hits the Muen Island, causes a shock wave to form and then propagates towards the beach. The wave front reaches the edge of the beach and runs up to the south valley. The maximum wave run-up height is recorded at about 16 s. This remarkable peak run-up height may be caused by the particular land feature formed by the pocket beach and two small valleys. Then the flood wave travels from the location with maximum run-up height to the north along the beach. After reaching the maximum height, the flow retreats from the beach. Reflected waves are observed to travel to the upstream and interacted with the incident wave and shock.







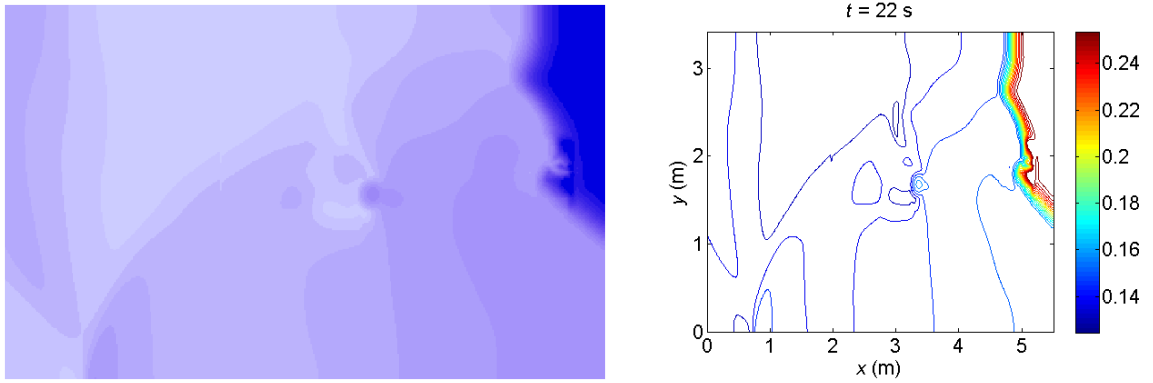
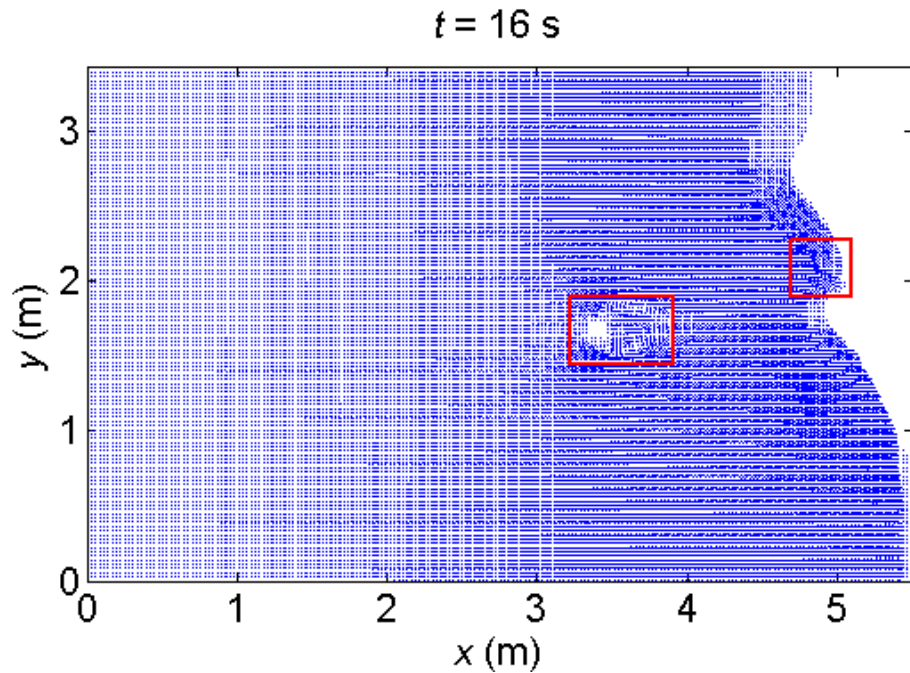


Figure 5.20 Tsunami run-up: flood maps (left) and water surface contours (right) at different output times.

The velocity field of the whole domain at $t = 16$ s when the maximum run-up height is achieved is presented in Figure 5.21 (a). The maximum wave run-up happens at the south valley. The velocity vectors near the two valleys are shown in Figure 5.21 (b), which implies the flow hydrodynamics of the propagating wave when the maximum wave run-up occurs. At $t = 16$ s, the wave front runs up along the south valley. After it reaches the maximum run-up height, the wave retreats from the south valley and travels to the north valley along the beach. The corresponding velocity field around the Muen Island is also illustrated at Figure 5.21(c).



(a) In the whole domain

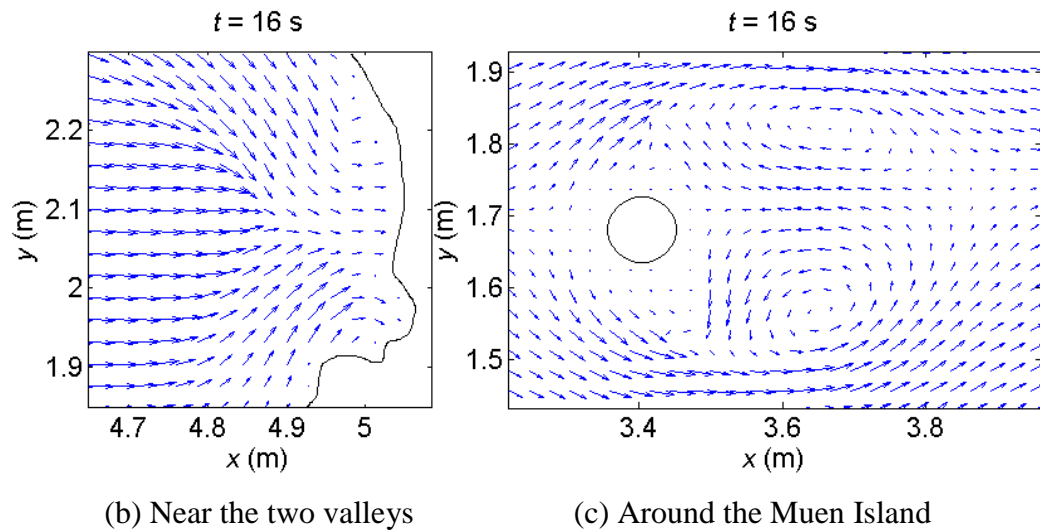
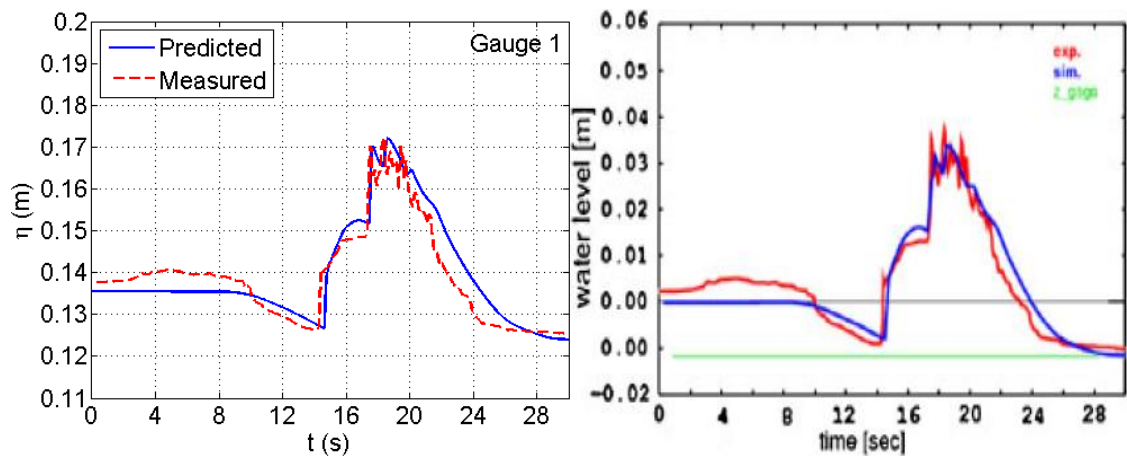


Figure 5.21 Tsunami run-up: predicted velocity field (a) in the whole domain; (b) near the two valleys; (c) around the Muen Island.

The predicted time histories of water surface elevation at the three gauging points are compared with the experimental measurements and the simulations predicted by Franchello (2010) in Figure 5.22. According to the inflow condition, the water surface elevation begins to decrease from 2.5 s. The experimental data presents a positive increase after 2.5 s. In contrast, the numerical prediction presents the smooth and still water surface until the tsunami wave arriving. The numerical arrival time and the peak water level agree closely with the experimental measurements. The peak water surface elevation simulated by the present model is much closer to the experimental data than the simulation provided by Franchello (2010). Successfully handling of this test case with extreme hydrodynamic conditions and realistic domain features reveals the capability of the present shallow flow model for practical coastal simulations.



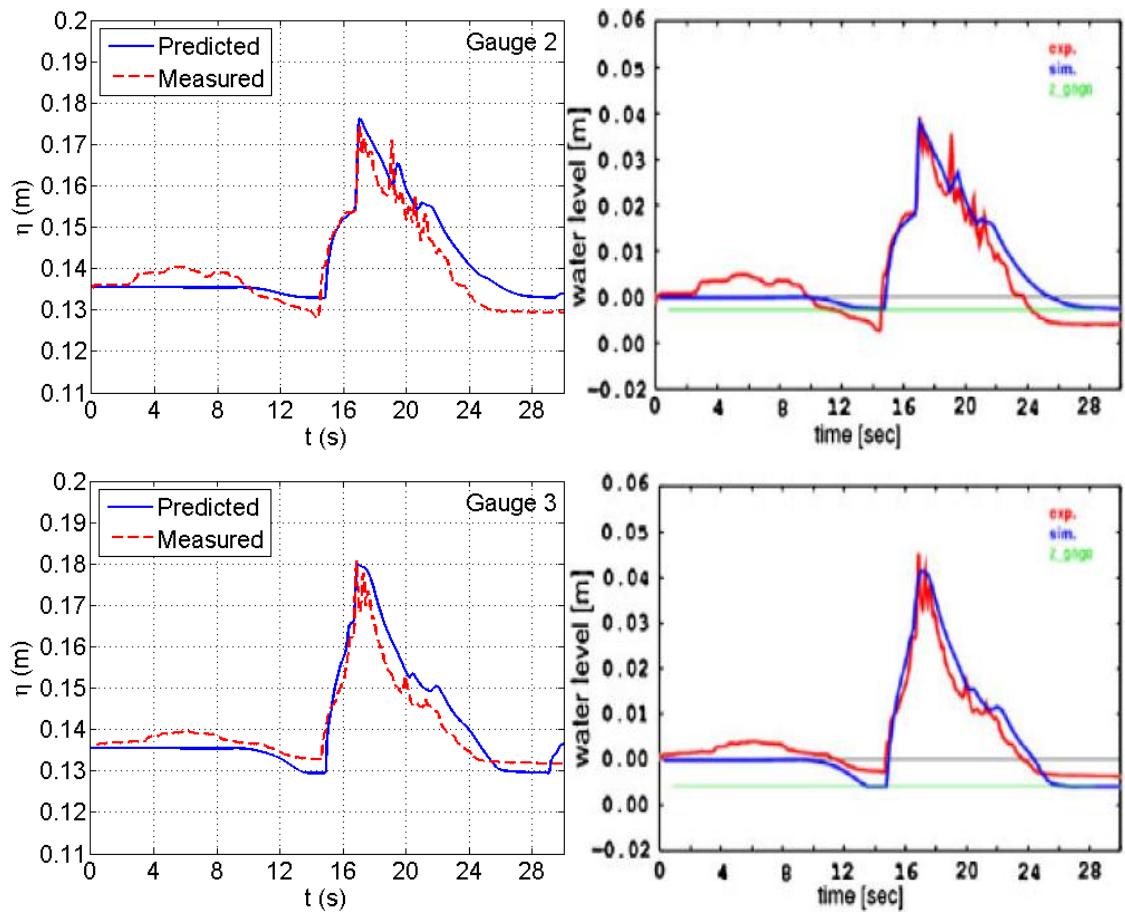


Figure 5.22 Tsunami run-up: time histories of water level at three gauge points (left – by the present model; right – by Franchello (2010)).

5.3 Conclusions

This chapter validates a robust numerical tool for coastal hydrodynamic simulations.

- Non-reflective boundary conditions have been used to improve the existing shallow flow model for coastal simulations. The non-reflective boundary may effectively absorb the wave reflected by the coastal defence, structure and sloping beach at the inlet boundary and ensures reliable predictions;
- The improved numerical scheme is validated against several benchmark tests. The current fully 2D shallow flow model, implemented with non-negative Riemann solver, has been proved to be a powerful tool for a wide range of realistic coastal simulations.

Chapter 6 Effect of Spatial Resolution and Numerical Accuracy

Objectives

- Quantitatively investigate the effects of the spatial resolution and the order of accuracy of the numerical scheme on shallow flow modelling;
- Advise the issues of optimum grid scale and numerical accuracy in providing reliable and efficient simulations.

Introduction

The grid scale and order of numerical accuracy may significantly influence the accuracy and efficiency in numerical computations. Different spatial resolutions could change the representation of the near-bank region of floodplain (e.g. Horritt and Bates 2001b). The induced change of bed topography could lead to significant impact on the computational accuracy of predicted water depth, water surface level, arriving time and flood extent. Theoretically, finer mesh resolution should provide better representation of the background topography and hence leads to more accurate numerical prediction. However, in large-scale real-world simulations, refined grid resolution increases significantly the number of computational nodes and may result in unbearable computational cost. Therefore, it is an important issue to investigate the effect of grid scale on computational accuracy and efficiency and hence to find out the optimum solution to the problem.

In the present fully 2D shallow flow model, higher order numerical accuracy is achieved by using 2nd-order Runge-Kutta method in time and MUSCL (Monotone Upstream-centred Schemes for Conservation Laws) slope limited linear reconstruction approach in space. The MUSCL scheme is adopted to reconstruct the face values of the flow variables at the interface, which also restricts the local slope of flow variables for stable simulations. Compared with a 1st-order scheme, a 2nd-order scheme demands higher computational time, especially for those realistic cases. Therefore the effect of numerical accuracy on the numerical predictions is also investigated, aiming to advise the balance between the computational efficiency and accuracy.

In this work, the quantitative methods of Root Mean Square Error (RMSE) and Fit Statistics (e.g. Aronica *et al.* 2002) are implemented to quantify the effects of grid scale and order of numerical accuracy. When assessing the scale effect, reference solutions are obtained on fine mesh and those coarse-mesh results are linearly interpolated into the fine mesh during the quantifying process.

Three test cases are presented in this chapter. The first case is used to investigate the scale effect, which is a laboratory-scale dam-break flow over a triangular structure. An analytical case of the 2D oscillating flow in a frictional parabolic basin is implemented to evaluate the balance between the numerical accuracy and efficiency. Finally, the realistic Malpasset dam-break case is implemented to investigate the effects of these two influencing factors on the reliability of the numerical solution and the computational efficiency.

6.1 Mathematical Methods

The mathematic methods of Root Mean Square Error (RMSE) and Fit Statistics (F^1 and F^2) (Aronica *et al.* 2002) are employed to assess the effects of the spatial resolution and numerical order on solution accuracy and computational efficiency. In this study, water depth ($h = \eta - z_b$) is taken as the considering factor. For the investigation of the scale effect, the prediction with the highest resolution is set to be the benchmark solution for the RMSE method and Fit statistics. In the computation, the lower resolution predictions are linearly interpolated into the higher resolution, in order to compare the predictions at the same grid size. In the study of the numerical order accuracy, the second order simulation or analytical solution is employed as a reference for the estimation of RMSE and Fit statistics (F^1 and F^2).

The RMSE is calculated as

$$RMSE(h, \hat{h}) = \sqrt{\frac{\sum_{i,j} (h_{i,j} - \hat{h}_{i,j})^2}{n}}, \quad (6.1)$$

where n is the number of grid cells in the computational domain. $h_{i,j}$ is the water depth at the considering cell (i, j) . $\hat{h}_{i,j}$ is the corresponding benchmark water depth.

When calculating fit statistics (F^1 and F^2), the critical water depth to define the wet-dry status is generally set to be 0.1 m (Aronica *et al.* 2002). The Fit Statistics F^1 is used to indicate the performance of the model on predicting the wet-dry front (e.g. Aronica *et al.* 2002). It presents the percentage of the cells, in the coincided wet-dry state with the benchmark.

$$F^1 = \frac{\sum_{i,j} P_{i,j}^{B_0C_0} + \sum_{i,j} P_{i,j}^{B_1C_1}}{n}, \quad (6.2)$$

where (i, j) is the index of the cells; B and C stand for the benchmark cell and the compared cell, respectively. The subscripts 0 means a cell is dry while 1 denotes a wet cell. In equation (6.2), $P_{i,j}^{B_0C_0}$ and $P_{i,j}^{B_1C_1}$ have two possible values 0 and 1. 1 is taken when the wet-dry state in B and C are matched. While 0 means the wet-dry state is opposite in B and C . F^1 ranges from 0 to 1, in which 0 means that there is no fitted cell in the present comparison and 1 indicates that the wet-dry state in all of the compared cells is exactly that same as those benchmark cells. The value of F^1 increases with the increase of the fit ratio. Hence, F^1 stands for the ratio of the fitted cells against the total number of the grid cells.

Another statistic method, F^2 , introduced by Horritt and Bates (2001b), is used to estimate the ratio between the numerical flooded area and the observed inundated area. Herein F^2 is used to estimate the percentage of the coincided flood extent between the current prediction and the benchmark, which can be described by,

$$F^2 = \frac{W_c \cap W_b}{W_c \cup W_b}, \quad (6.3)$$

in which W_c and W_b stand for the number of inundated cells given by the present simulation and the benchmark solution, respectively. F^2 can be specifically calculated using the following formula,

$$F^2 = \frac{\sum_{i,j} P_{i,j}^{B_1C_1}}{\sum_{i,j} P_{i,j}^{B_1C_1} + \sum_{i,j} P_{i,j}^{B_1C_0} + \sum_{i,j} P_{i,j}^{B_0C_1}}, \quad (6.4)$$

where $P_{i,j}^{B_1C_0}$ is 1 when the benchmark cell is wet and the present compared cell is dry; otherwise it is 0. $P_{i,j}^{B_0C_1}$ is 1 when the benchmark cell is dry and the compared cell is wet;

otherwise its value is 0. In equation (6.4), the numerator accounts for the coincided inundated area predicted by both sets of solutions. The denominator gives the sum of the flooding area defined by either the compared simulation or the benchmark. Therefore, F^2 is a variable between 0 and 1. 0 represents the wet-dry state in the compared solution is totally different from the benchmark lattices while 1 represents that the predicted flooding extent is absolutely the same as that in the benchmark lattices.

6.2 Case Studies and Discussions

In this section, the effects of the grid resolution and numerical order of accuracy on computational accuracy and efficiency are investigated based on three test cases, i.e. a laboratory dam break over a triangular hump, an oscillation wave in a parabolic bowl and the realistic Malpasset dam break inundation. These three cases have been used to validate the fully 2D shallow flow model (in Chapter 3 and 4). The numerical simulations are found to agree well with the experimental measurements, analytical solutions and field records, respectively. In this chapter, the effects of grid resolution and numerical order of the numerical scheme on the flood extent and prediction of water depth and water surface elevation are investigated intensively.

6.2.1 Dam-break flow over a triangular bump

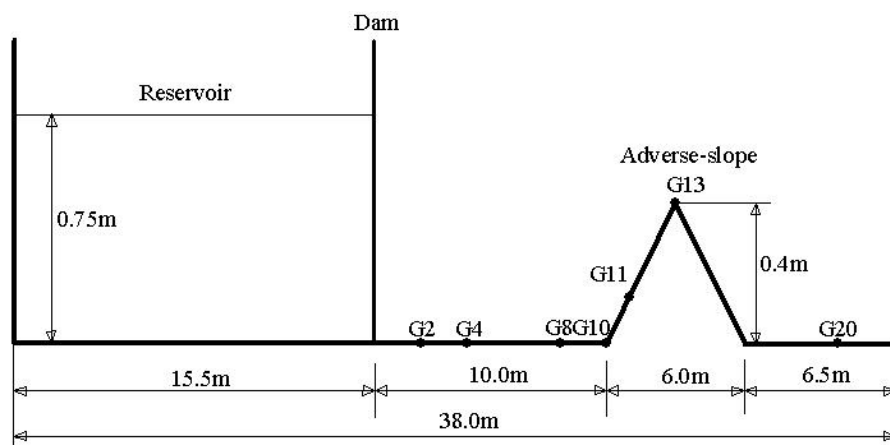
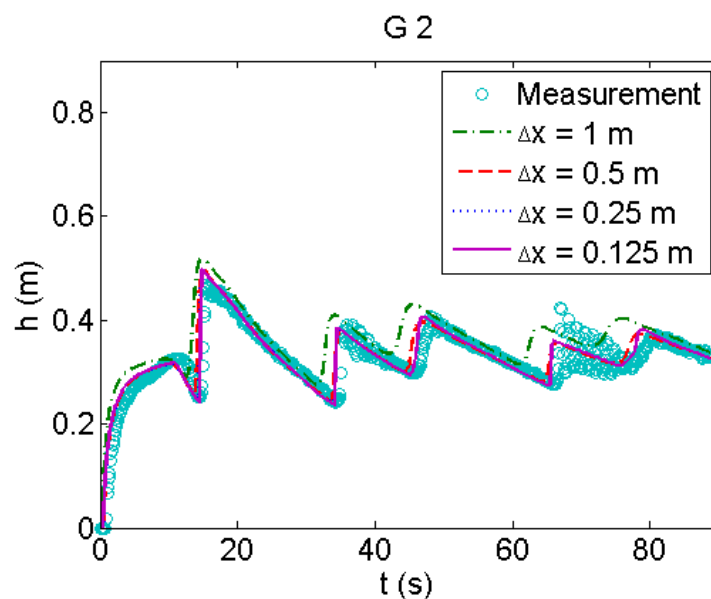


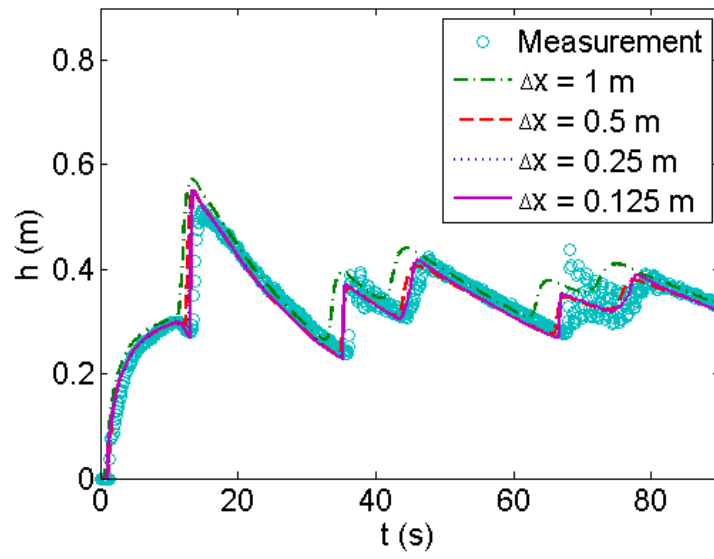
Figure 6.1 Dam-break flow over a triangular bump: bed profile.

This test case is adopted to estimate the scale effect on the simulation of a dam break flow over a triangular bump. The channel is 38 m long and 5 m wide with a reservoir at the upstream and the bed profile is given in Figure 6.1. Four grids with different resolution (level 1 $\Delta x = 1$ m, level 2 $\Delta x = 0.5$ m, level 3 $\Delta x = 0.25$ m, level 4 $\Delta x = 0.125$ m) are investigated in this work. The finest resolution ($\Delta x = 0.125$ m) is taken as the benchmark in the analysis using the RMSE method and the fit statistics approaches. Seven gauge points are located along the channel to record the time history of the water depth. Herein, for ‘G2’, ‘G’ stands for the gauge point and ‘2’ means the distance between the gauge point and the dam is 2 m. Other gauging points are defined in the same way.

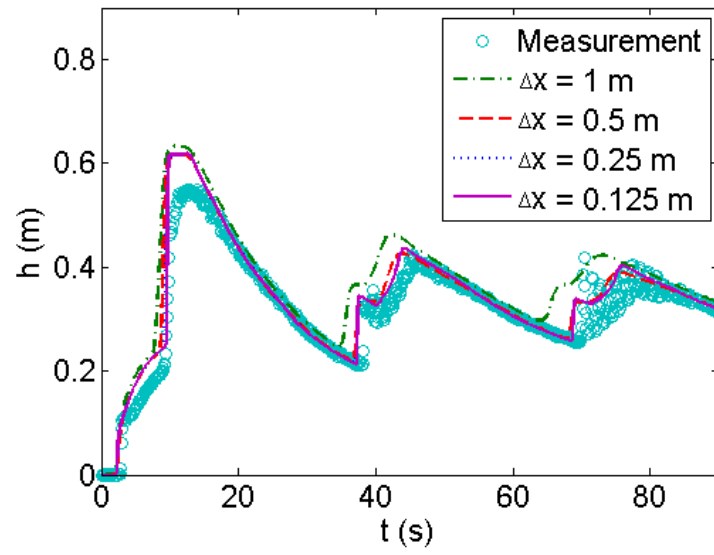
As shown in Figure 6.2 the time history of measured water depth are compared with the numerical predictions based on different grid resolutions at different gauges. Obviously, the numerical predictions diverge from the solution on the finest grid ($\Delta x = 0.125$ m) as the grid size increases, except Gauge 13. The different comparison at G13 is caused by the location of this gauge point. Gauge 13 is at the peak of the triangular hump. When the grid is 38×5 ($\Delta x = 1$ m), Gauge 13 is right located at the central point of the control volume. In the current finite volume scheme, the values of the flow variables are stored at the central point of cell. When the resolution is chosen from $\Delta x = 0.125$ m, $\Delta x = 0.25$ m and $\Delta x = 0.5$ m, the bed elevation of Gauge 13 is not right at the peak of the hump and lower than the real one. The recorded water depth is linearly interpolated by using the values in two neighbour cells, which may introduce extra source of error into the solution and hence lead to an inconsistent comparison.



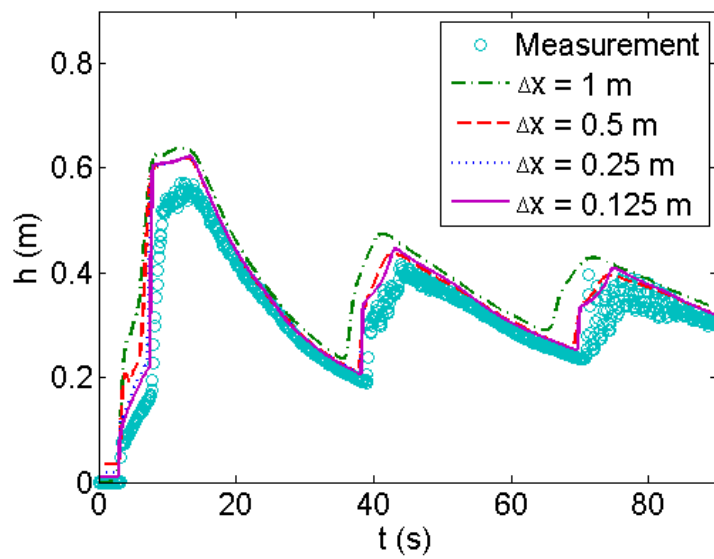
G 4



G 8



G 10



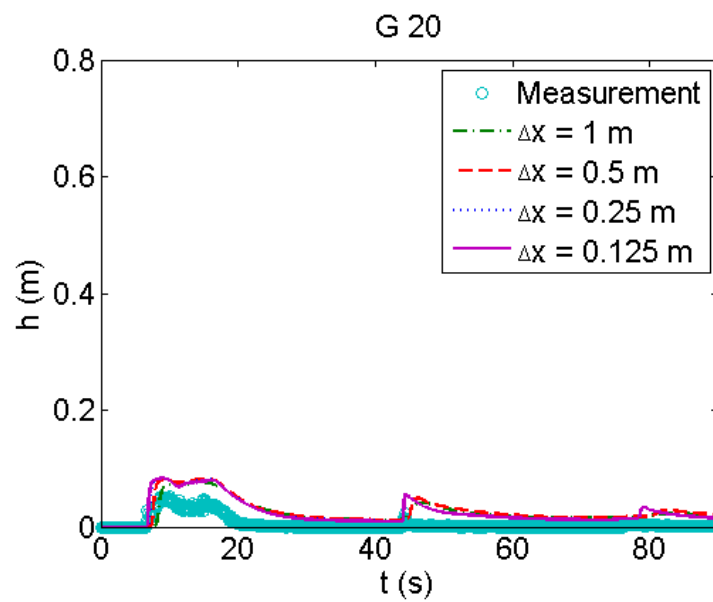
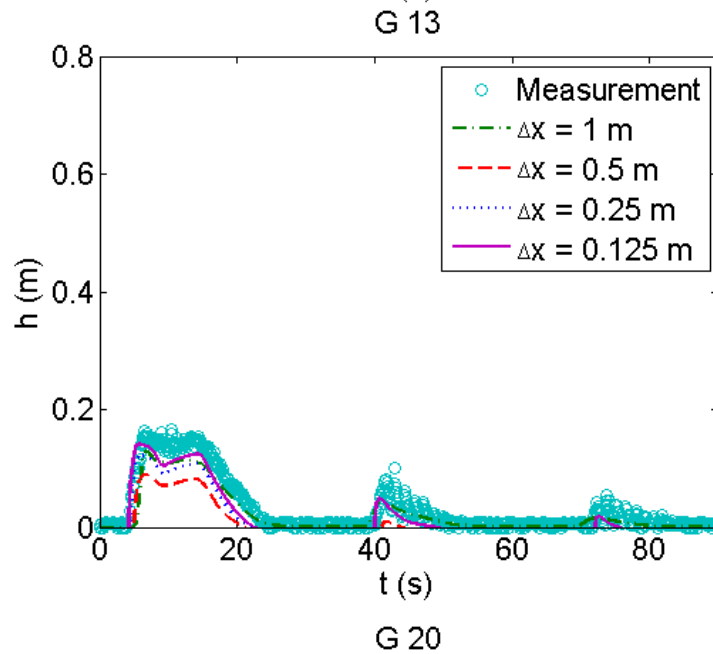
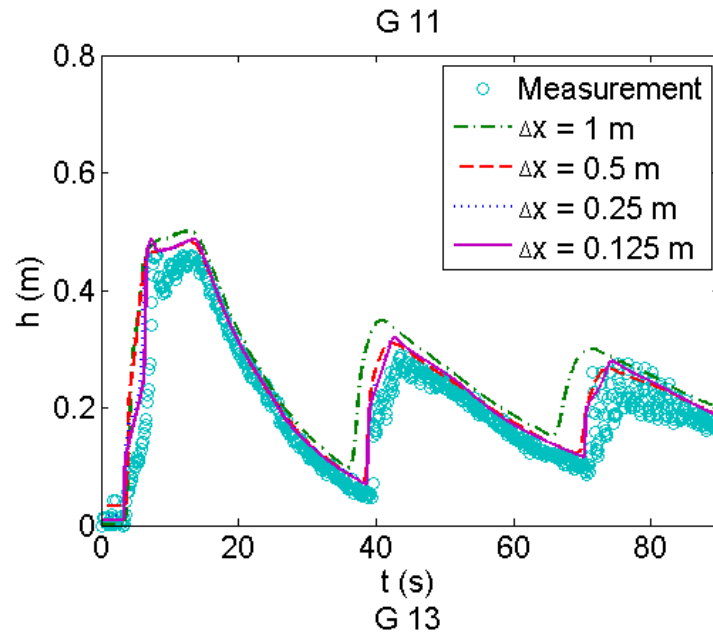


Figure 6.2 Dam-break flow over a triangular bump: time history of the water depth at different gauges.

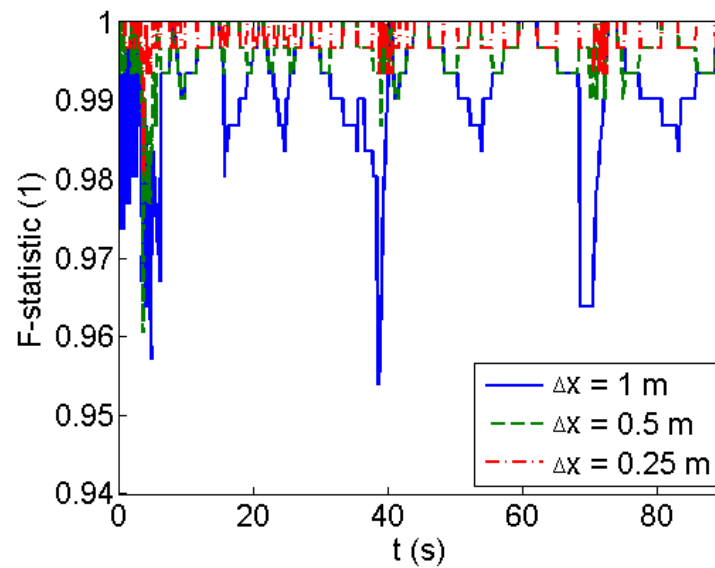


Figure 6.3 Dam-break flow over a triangular bump: time histories of Fit statistics (F^1) for 90 s.

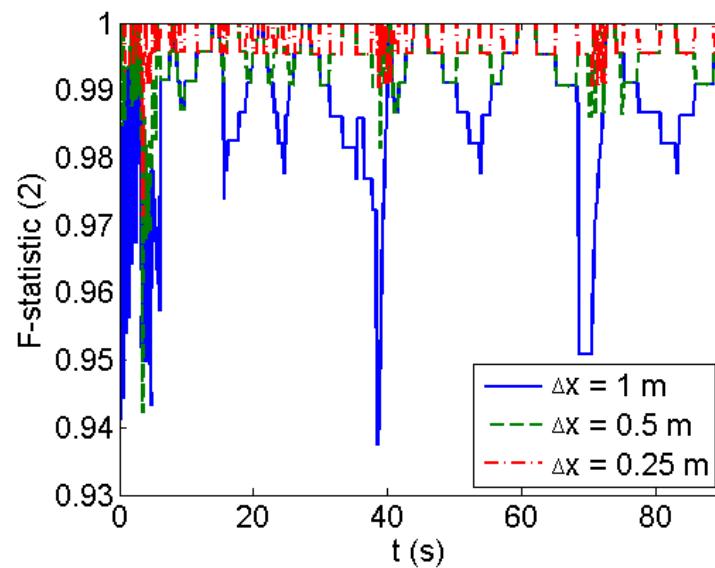


Figure 6.4 Dam-break flow over a triangular bump: time histories of fit statistics (F^2) for 90 s.

Further investigation of the flood extent and the water depth in the entire domain is carried out by using fit statistics and RMSE methods. The numerical solutions from the level 1-3 simulations are interpolated onto the finest level 4 grid, and then compared

with the benchmark prediction (level 4). Figure 6.3 illustrates the general performances of the present model on the matching rate based on different resolutions, compared with the benchmark resolution. F^1 is used to estimate the fitted percentage of the coincided wet-dry state cell in the whole grid. Figure 6.4 illustrates the fit rate (F^2) of the inundated area between the compared scales and the benchmark scale. Both sets of statistics confirm that the numerical solutions converge as the grid resolution increases.

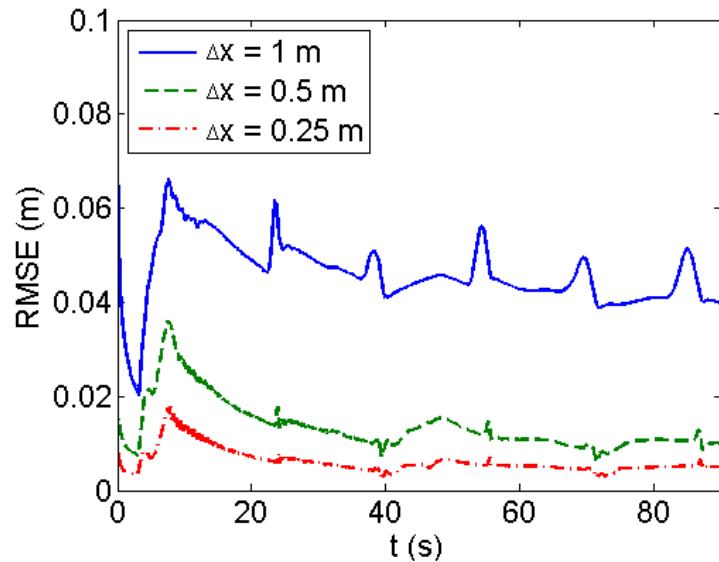


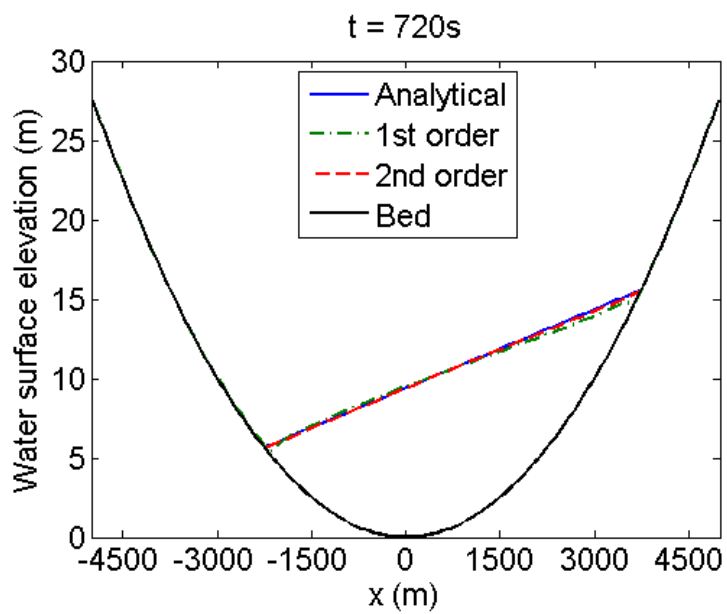
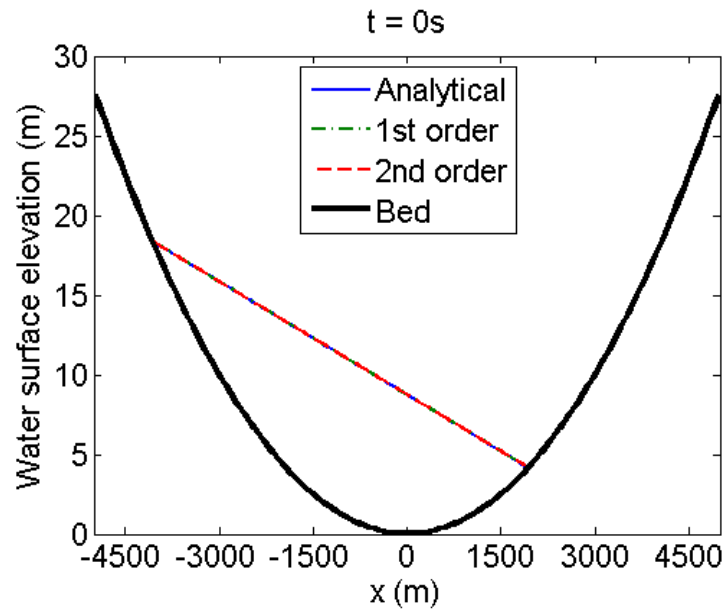
Figure 6.5 Dam-break flow over a triangular bump: time histories of the root mean square errors (RMSE) calculated against water depth for 90 s.

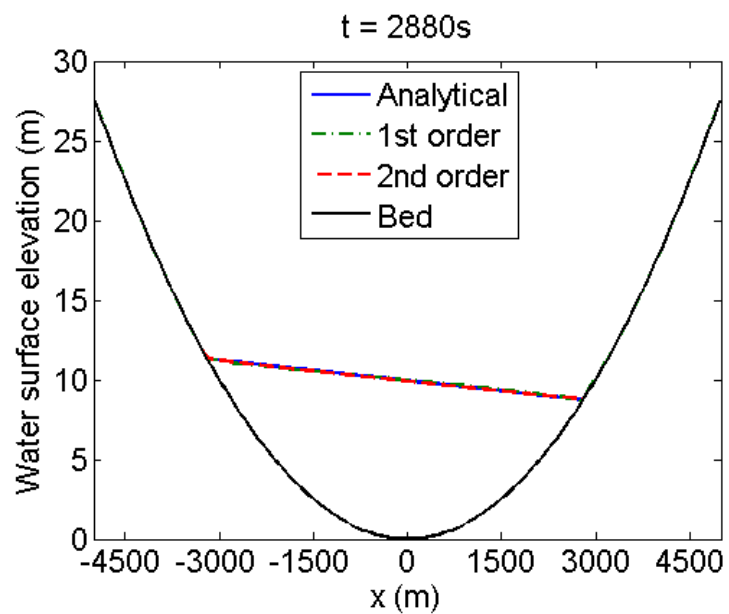
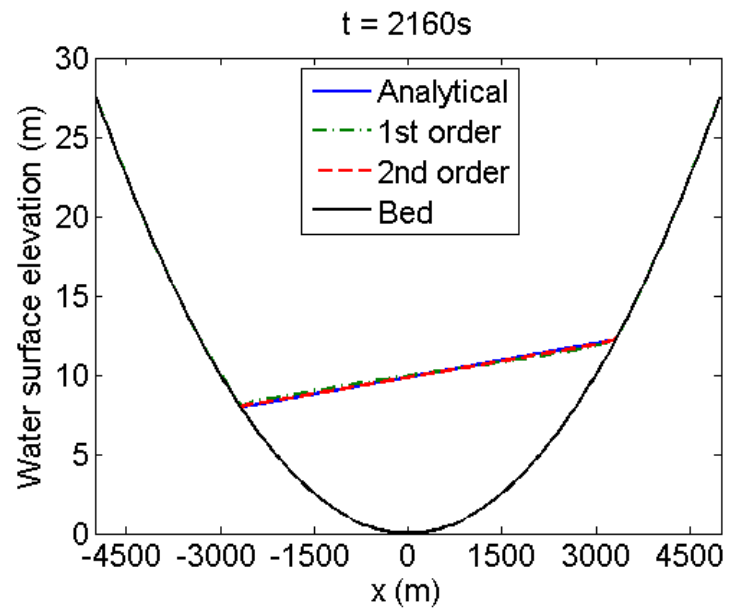
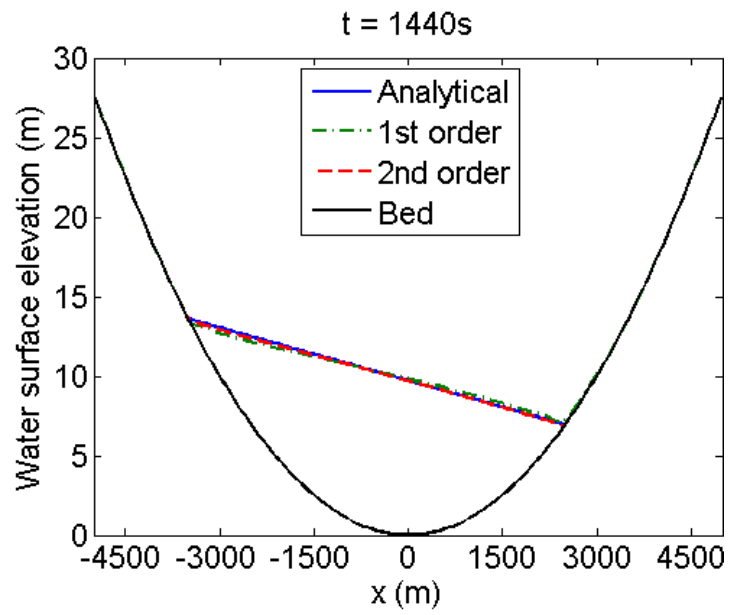
Figure 6.5 compares the root mean square error of the water depth for different grid scale levels throughout the simulation time of 90 s. Again, the RMSE appears to obvious decreases with increasing mesh resolution. The predicted water depth presents a consistent response to the change of the grid scale throughout the process of simulation.

6.2.2 Frictional flow in a parabolic bowl with planar surface

This 2D analytical case, which has been used in Chapter 3 to validate the fully 2D shallow flow model, is used to quantify the effect of the accuracy order of the numerical scheme. The same initial and boundary conditions are implemented. Here the simulation is carried out in 7200 s using both the 1st order and 2nd order accurate schemes, respectively. Figure 6.6 presents the central profile along the x -direction at $t = 0$ s, $t = 720$ s, $t = 1440$ s, $t = 2160$ s, $t = 2880$ s, $t = 3600$ s, $t = 7200$ s. The obvious deviation

from the analytical solutions happens in 1st order simulation in the first 1440 s. After that, both the 1st and 2nd order simulations provide a good agreement with the analytical solution.





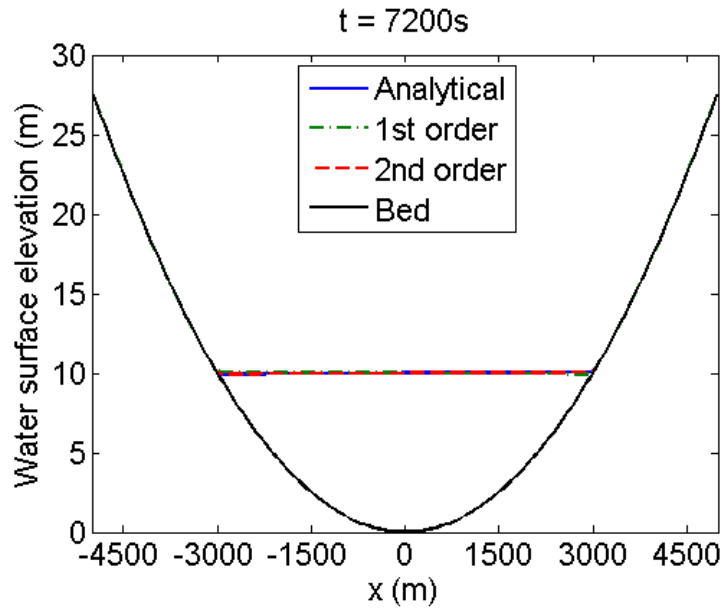
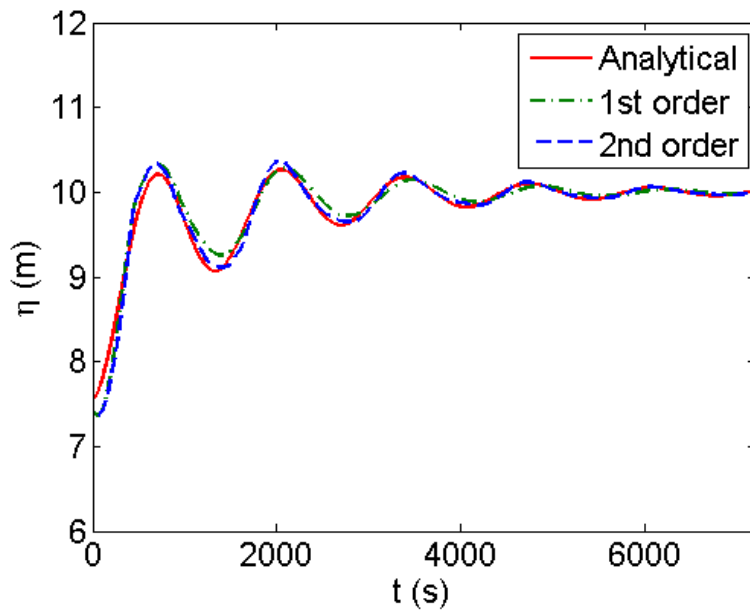
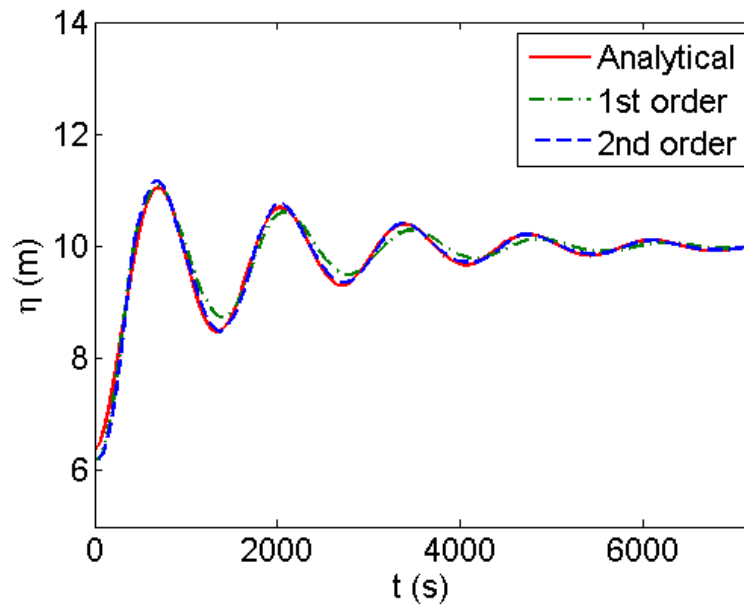


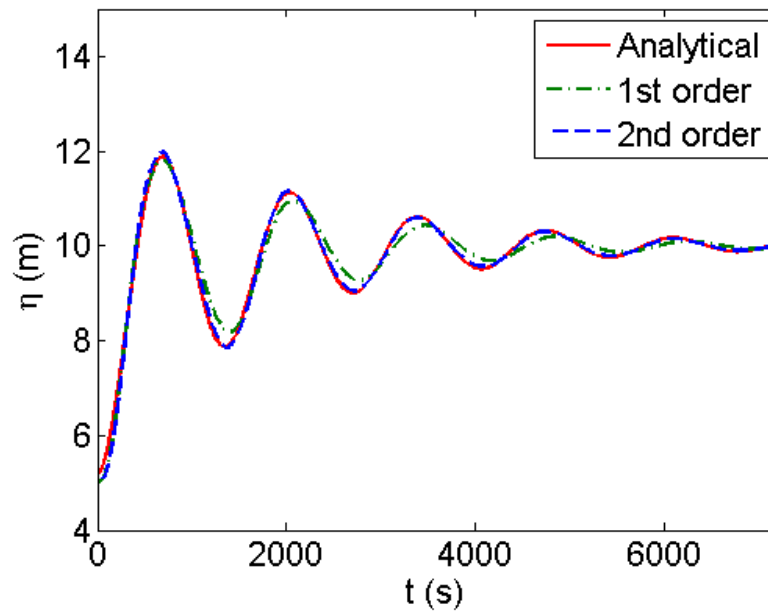
Figure 6.6 Frictional flow in a parabolic bowl with planar surface: central profiles of water surface along the x -axis at different times.



(a)



(b)



(c)

Figure 6.7 Frictional flow in a parabolic bowl with planar surface: time histories of the water surface elevation in 7200 s at (a) G1 ($x = 500$ m); (b) G2 ($x = 1000$ m); (c) G3 ($x = 1500$ m).

The comparisons are also made between the 1st and 2nd order predicted water surface elevation and the analytical solution at three gauges. The three gauge points are located at $x = 500$ m, $x = 1000$ m and $x = 1500$ m along the x -axis. The numerical time histories of water free surface level are plotted in Figure 6.7 and compared with the analytical solution. The 2nd order predictions are found to agree better with the analytical solution while the 1st order simulations present more obvious differences from the analytical

solution throughout the 7200 s. The difference between 1st and 2nd order simulations decreases with time as the flow approaches the motionless steady state due to the friction effect. Overall, the 2nd order scheme appears to provide better performance.

Further analysis is carried out using the fit statistics and the root mean square error method and the results are shown in Figure 6.8, Figure 6.9 and Figure 6.10, respectively. The 2nd order simulation is first taken as the benchmark in the analysis of fit statistics (F^1 and F^2). Figure 6.8 illustrates the fit ratio (F^1) between the 1st order and 2nd order in terms of wet-dry state in global cells. The lowest fit ratio is 92% at around $t = 1200$ s. The differences decrease with time when the motion of the flow is slowed down by the bed friction effect. Figure 6.9 shows the fit statistics F^2 of flood extent between the 1st order and the 2nd order throughout 7200 s. More than 87.9% of 1st order prediction presents the same inundated state as the 2nd order simulation. Obviously, the 2nd order scheme provides better performance. Furthermore, quantitative investigation should be taken.

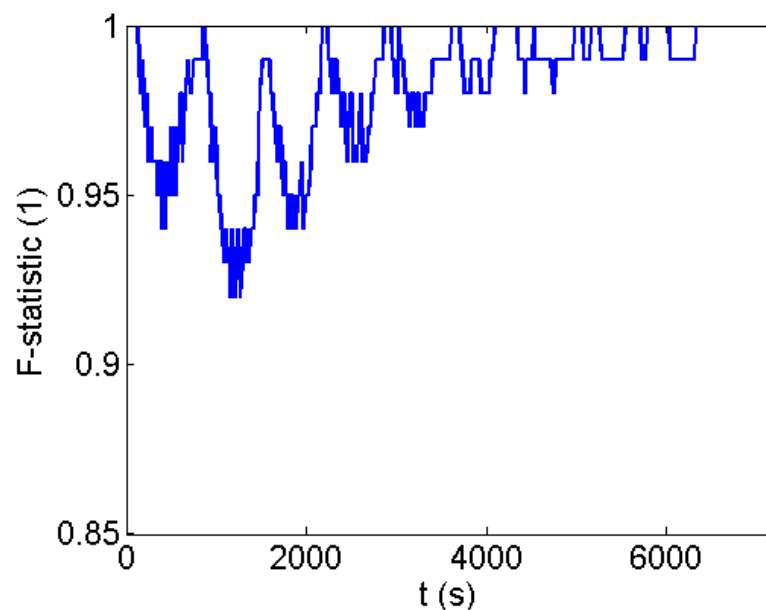


Figure 6.8 Frictional flow in a parabolic bowl with planar surface: time history of fit statistics (F^1) for 7200 s.

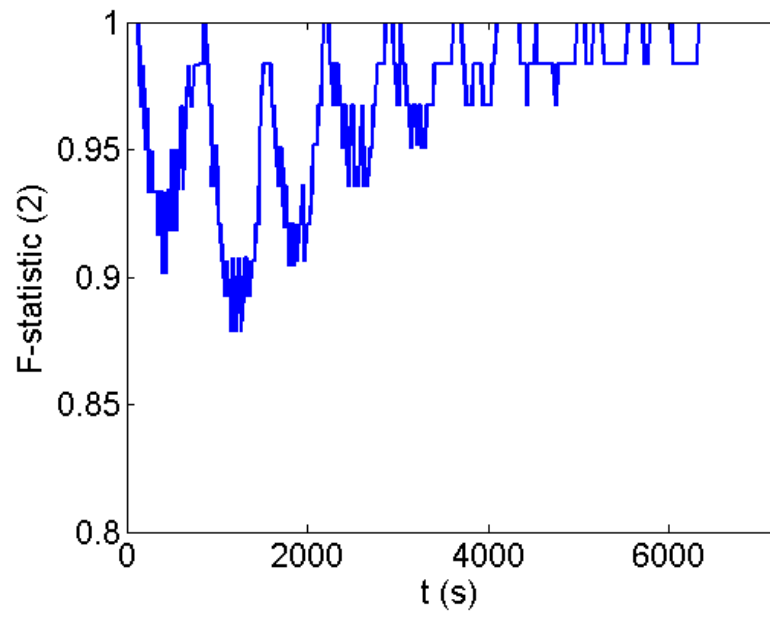
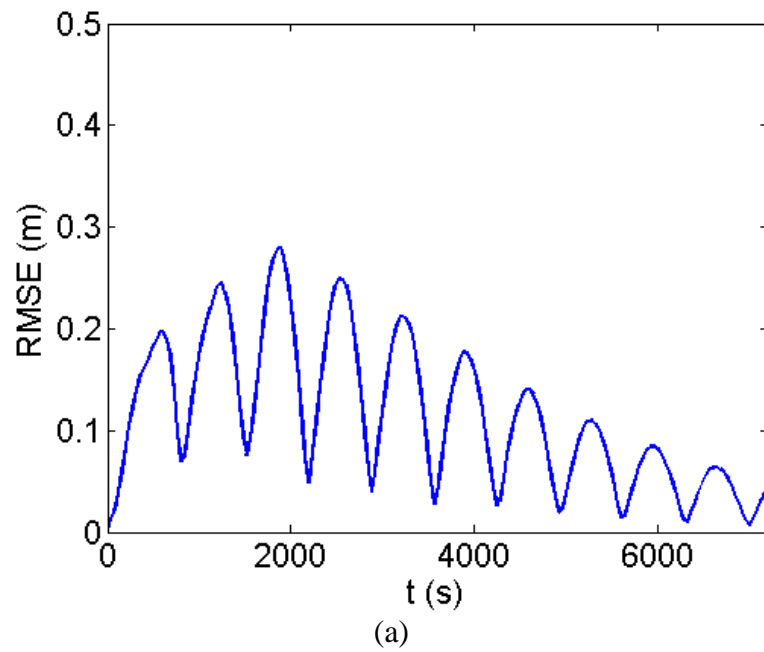


Figure 6.9 Frictional flow in a parabolic bowl with planar surface: time history of fit statistics (F^2) for 7200 s.



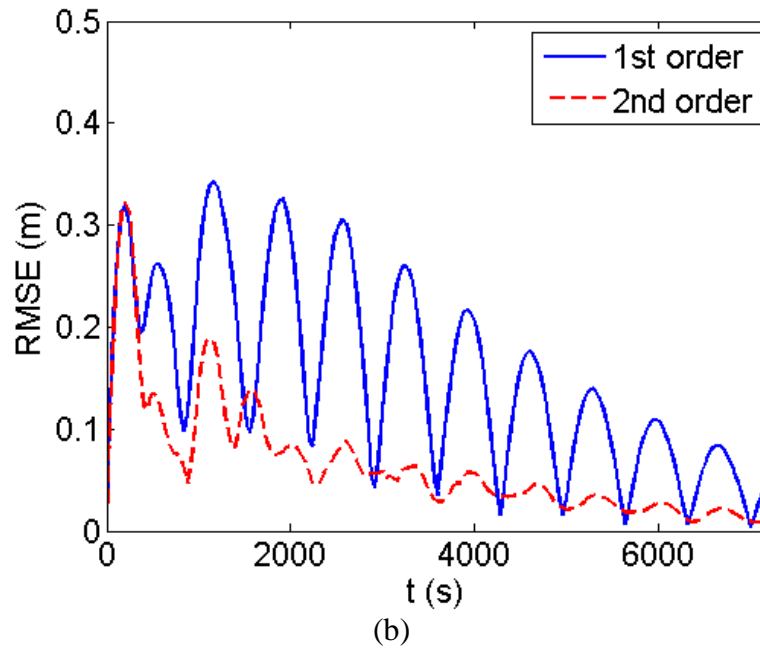


Figure 6.10 Frictional flow in a parabolic bowl with planar surface: time histories of RMSE in terms of water depth for 7200 s: (a) use the 2nd order prediction as the benchmark; (b) use the analytical solution as the benchmark.

The evolution of RMSE throughout the simulation time of 7200 s is described in Figure 6.10. The benchmark in Figure 6.10 (a) is the 2nd order numerical prediction. In (a), the maximum root mean square error is 0.28 m at $t = 1880$ s for this comparison. While the analytical solution is taken as the benchmark in Figure 6.10 (b), the RMSE at $t = 1880$ s is 0.324 m for the 1st order prediction and 0.08 m for the 2nd order prediction. The improvement of using 2nd order numerical scheme is evident. The comparison of the central profile shows obvious differences at $t = 720$ s and $t = 1440$ s in Figure 6.6, which are also obviously presented in Figure 6.8 - Figure 6.10. Furthermore, the computing time is 29.36 s for 1st order simulation and 134.78 s for 2nd order simulation. The 2nd order scheme does not consume too much computational time for this particular case. Therefore, for this type of theoretical cases with simple topography and flow set-up, higher-order scheme may produce more accurate numerical solutions under acceptable computational cost. However, whether this conclusion can be extended to large-scale simulations over realistic domain topographies is still not clear.

6.2.3 Malpasset dam break

The case of Malpasset dam break is implemented here to investigate the effect of grid scale and the numerical order of accuracy in the realistic domain with complicated bed topography and irregular boundary. This realistic case has been validated and investigated in Chapter 4. In this work, the experimental measurements and police survey records are used to verify the numerical simulation and study the effects of spatial resolution and numerical order of accuracy on the solution reliability and computational efficiency.

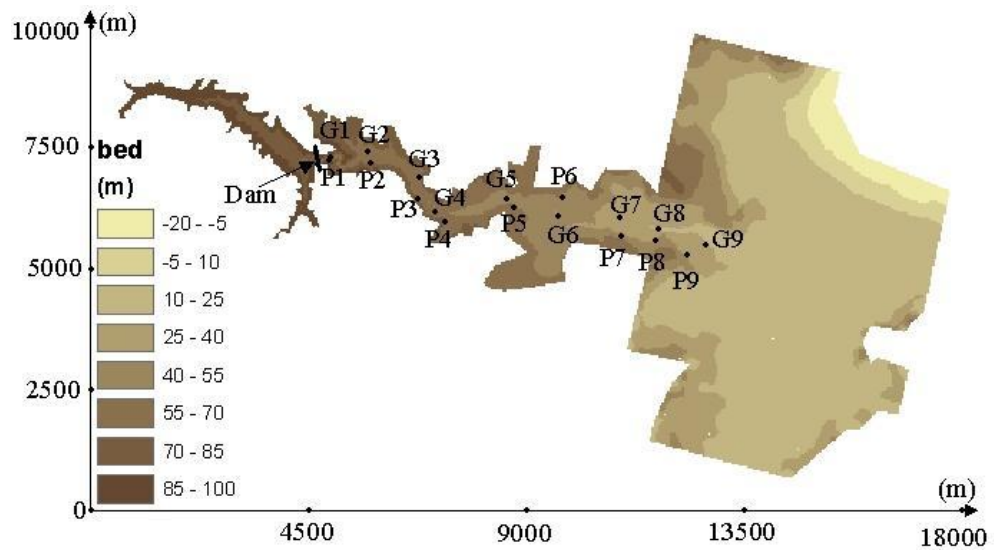


Figure 6.11 Malpasset dam break: plane view of the floodplain and location of Gauge points (G) and Police survey points (P).

The computational domain fits in an $18000 \text{ m} \times 10000 \text{ m}$ rectangle region as shown in Figure 6.11, where ‘G’ denotes the experimental gauge points and ‘P’ presents the police survey locations. In this simulation, five uniform grids of different resolution have been adopted, which contain 90×50 cells ($\Delta x = 200 \text{ m}$), 225×125 cells ($\Delta x = 80 \text{ m}$), 450×250 cells ($\Delta x = 40 \text{ m}$), 900×500 cells ($\Delta x = 20 \text{ m}$) and 1800×1000 cells ($\Delta x = 10 \text{ m}$), respectively.

The numerical predictions of the arrival time and the peak water surface elevation at gauges (G1 – G9) are firstly compared with the experimental measurements. Secondly, the maximum water level at gauging points (P1 – P9) is compared with the police survey records. When studying the scale effect, the numerical results are predicted using the 1st order scheme for more efficient simulations.

6.2.3.1 Investigation of scale effect

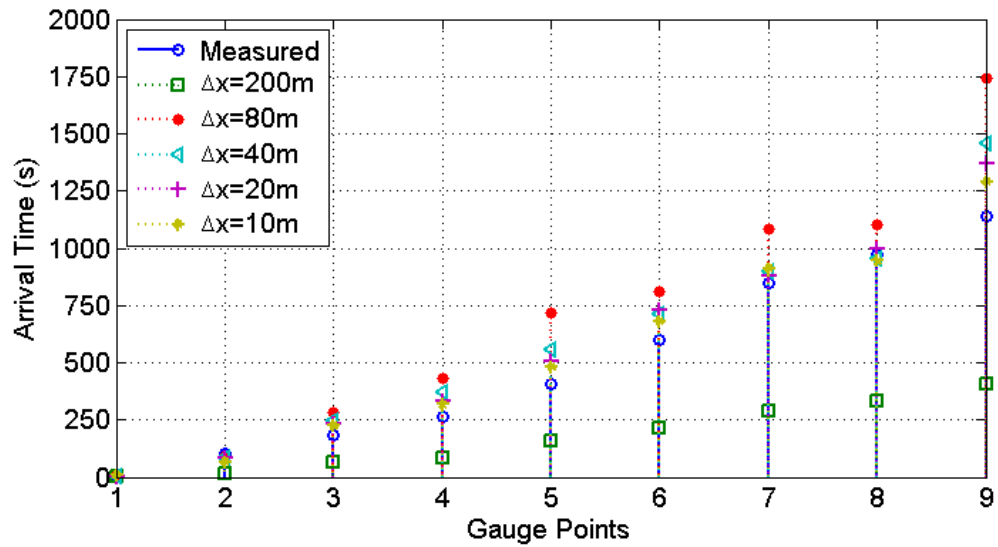


Figure 6.12 Malpasset dam break: the arrival time at different gauge points predicted on grids with different resolutions.

Figure 6.12 illustrates the comparison of the arrival time between the experimental data and the numerical predictions predicted on grids of different size at different gauge points. The largest discrepancies of arrival times are predicted by spatial resolution ($\Delta x = 200$ m), which is even earlier at G7 and G8 than at G6. The big discrepancy happens when the resolution reach $\Delta x = 80$ m. It means a low-limit of the spatial resolution exists in the accurate simulation. The predictions of higher resolution present better performance at most gauges. However, lower resolutions give better prediction at some gauges, e.g. G2 and G7. Hence, the response of the predicted arriving time is not consistent with the change of spatial resolution.

Figure 6.13 compares the maximum water levels predicted on different grids with the experimental data at different gauge points. The maximum errors still happens in the coarsest grid ($\Delta x = 200$ m), which reaches 43.75% of the experimental measurement happening at G9. The big error is not acceptable in the application. It means the numerical scheme cannot provide a right performance after the grid scale reaches a limit. The responses of predictions to the change of the grid resolution are not consistent at different gauging points. This finding means that higher resolution may not provide more accurate prediction in the real-world application. A similar conclusion is obtained

by comparing the predicted peak water levels with the police survey records at different gauges as shown in Figure 6.14.

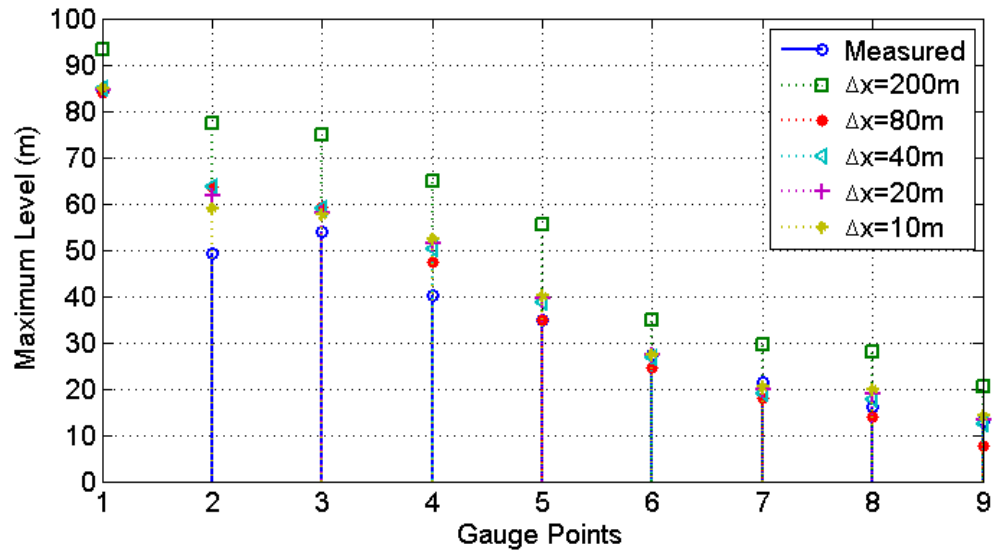


Figure 6.13 Malpasset dam break: the maximum water level at different gauge points predicted by grids with different resolutions.

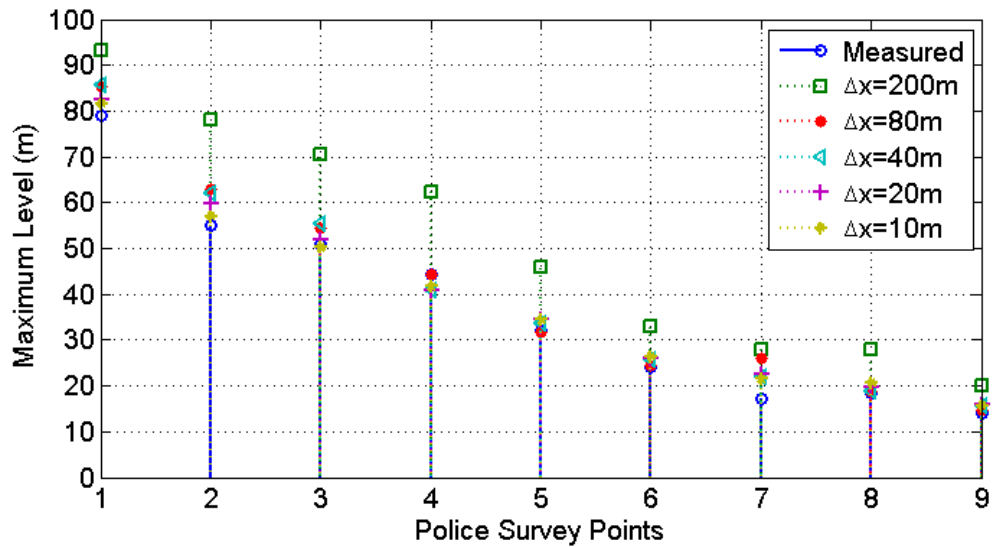
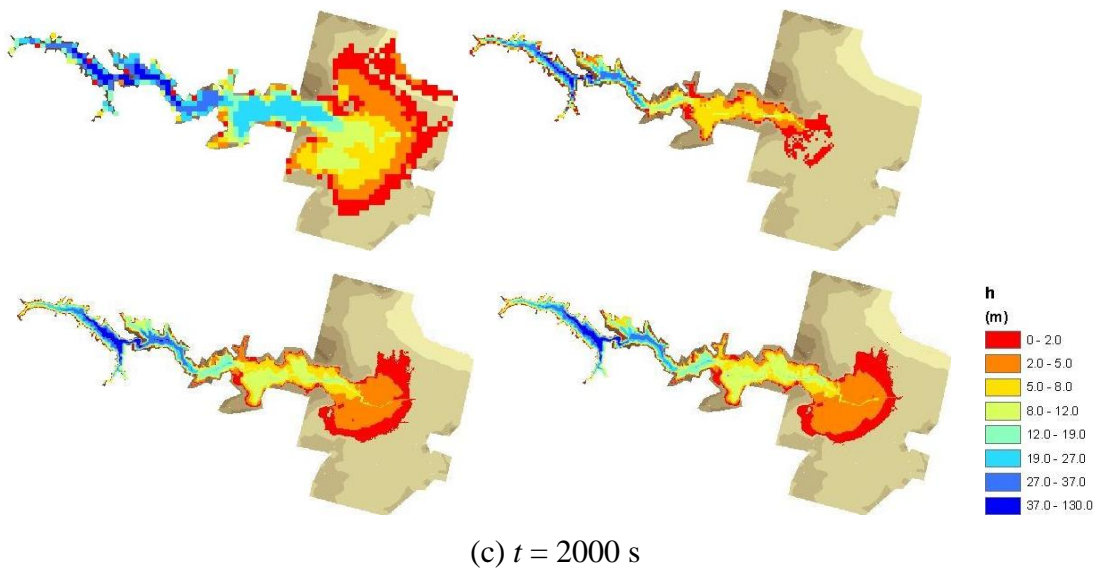
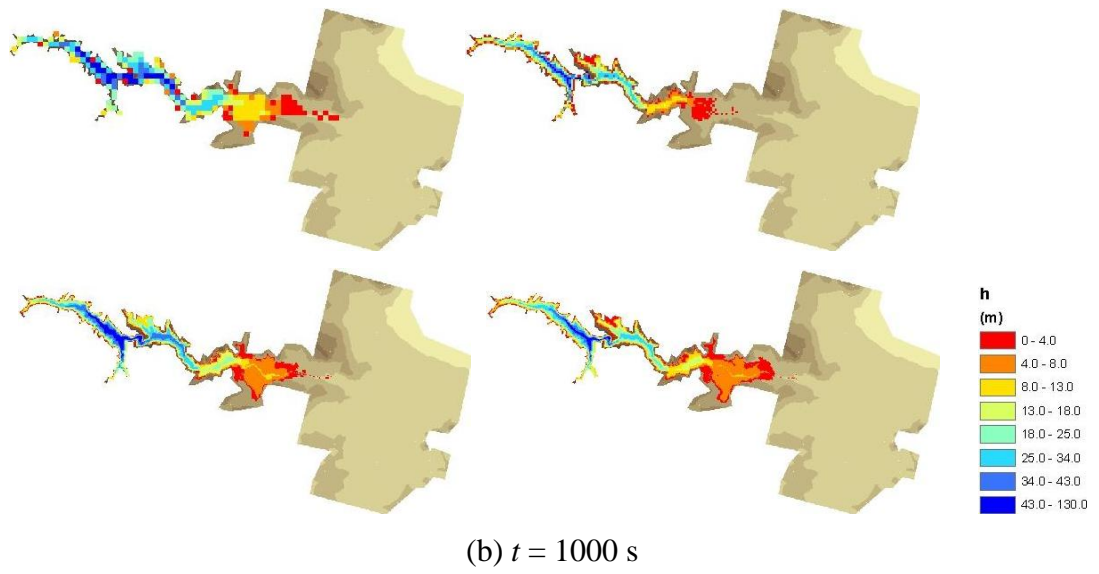
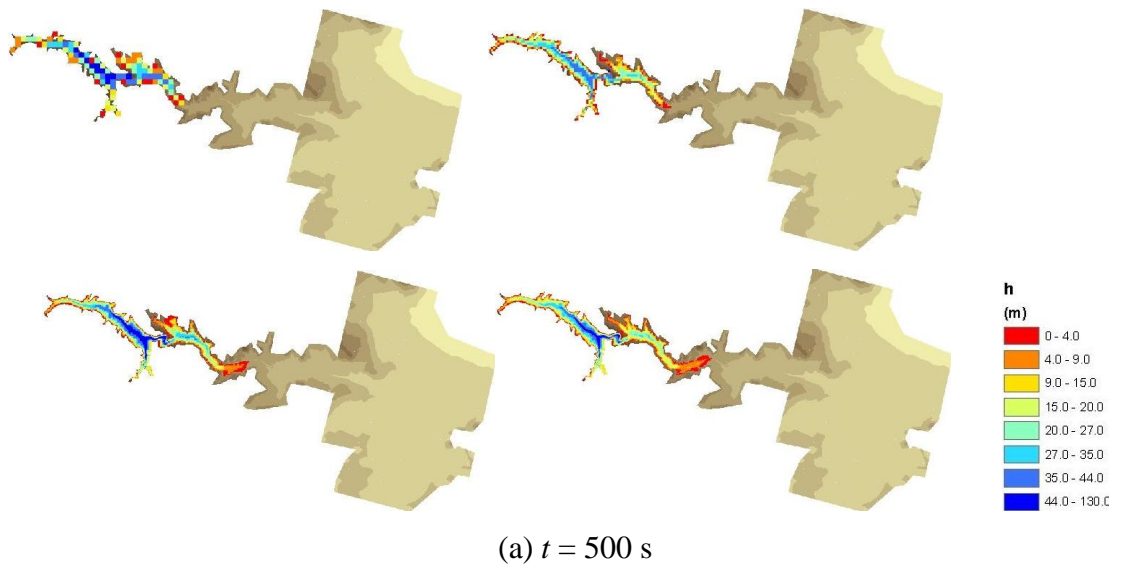


Figure 6.14 Malpasset dam break: the maximum water level predicted on different grid scales at the Police survey locations.



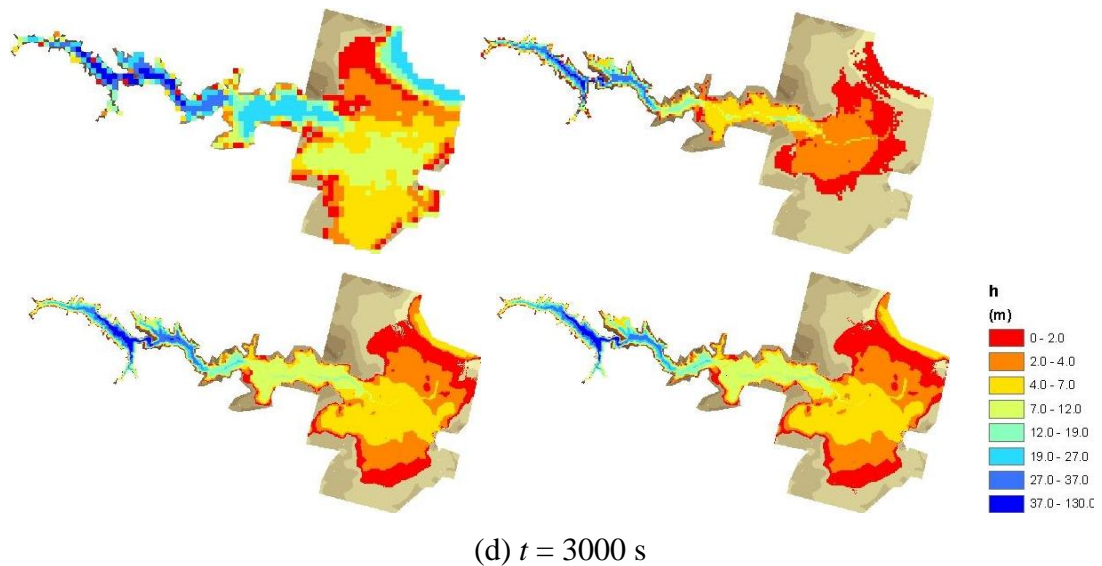


Figure 6.15 Malpasset dam break: the snapshots of flood map at different times predicted on different resolutions: $\Delta x = 200$ m (Northwest), $\Delta x = 80$ m (Northeast), $\Delta x = 40$ m (Southwest) and $\Delta x = 20$ m (Southeast).

The flood extent predicted on different grid scales is investigated in Figure 6.15, where the results are due to $\Delta x = 200$ m (Northwest), $\Delta x = 80$ m (Northeast), $\Delta x = 40$ m (Southwest) and $\Delta x = 20$ m (Southeast), respectively. The snapshots of inundated area are captured and compared in Figure 6.15 at (a) $t = 500$ s, (b) $t = 1000$ s, (c) $t = 2000$ s and (d) $t = 3000$ s. In (a), the snapshots present a regular decreased spread speed with the increasing grid size. In (b), the coarsest grid ($\Delta x = 200$ m) presents faster evolution of the flood front than the finest grid. For the other resolutions, higher resolution produces faster evolution of flood extent. At $t = 2000$ s (c), the 40 m resolution predicts a similar flood extent and water depth with the 20 m resolution. The 80 m model provides a lower spread speed of the flood extent while the 200 m scale shows different prediction with a much larger flood extent reaching the seaside. In (d) $t = 3000$ s, the flood front arrives at the seaside. The 20 m and 40 m resolution predictions present the similar flood extent and water depth with slight difference. Compared with higher resolution predictions, the 80 m resolution prediction shows a slower propagation of flood extent and big discrepancy of water depth. Overall, the present model shows good performance on the grids ($\Delta x = 40$ m and $\Delta x = 20$ m). A slower evolution of the flood front is shown in the 80 m prediction. The 200 m simulation presents different predictions of flood extent and water depth. The above comparisons reveal that the predicted flood extent and water depth has regular response to the changing grid

resolution with a low-limit. Furthermore, the improvement of computational accuracy by increasing the resolution is regularly decreased.

Further investigation of the scale effect is carried out by using the fit statistics and the root mean square error methods. The numerical results on grids (coarse 80 m, medium 40 m, fine 20 m) are evaluated against the benchmark prediction on grid 10 m. In order to estimate the evolution of the fit statistics and the RMSE until the convergent time, a tolerance error is set to be 1.0×10^{-6} . For this case, the results cannot converge until 533734.98 s. The reason might be the complex bed topography and irregular computational domain. Considering the convergent time, the simulation in the first 5000 s is estimated by fit statistics and RMSE method. In 5000 s, the trend of the changes of three curves has been shown clearly.

The fit rate (F^1) of the wet-dry state in the global cells is compared based on different scales in Figure 6.16. Figure 6.17 presents the fit ratio (F^2) of flood extent between the comparing resolutions and the benchmark resolution. Obviously, the increasing resolution improves the fit rate with the benchmark prediction. The minimum fit ratio occurs on the 80 m simulation. It shows a regular response of predicted results to the increasing grid resolution.

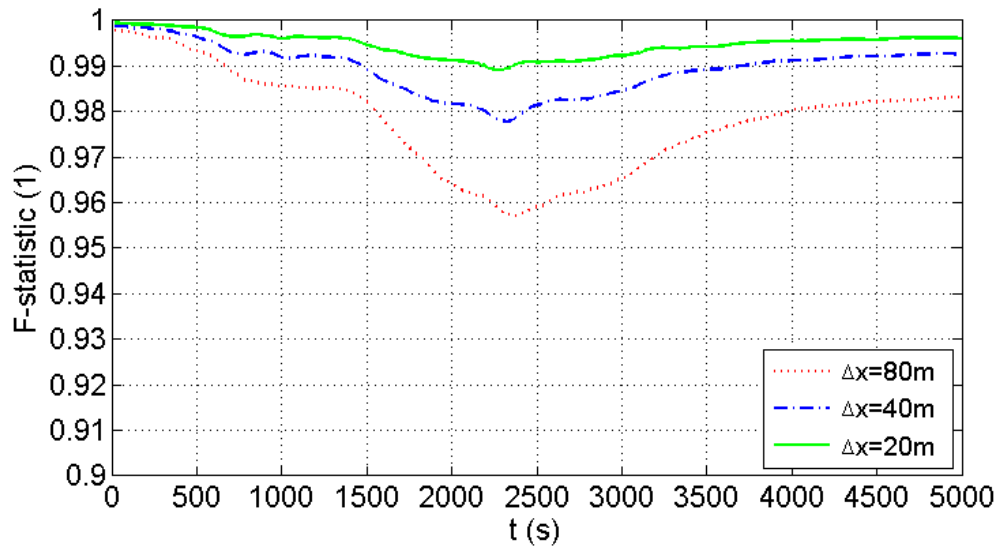


Figure 6.16 Malpasset dam break: Fit statistics (F^1) history in 5000 s based on different grid scales.

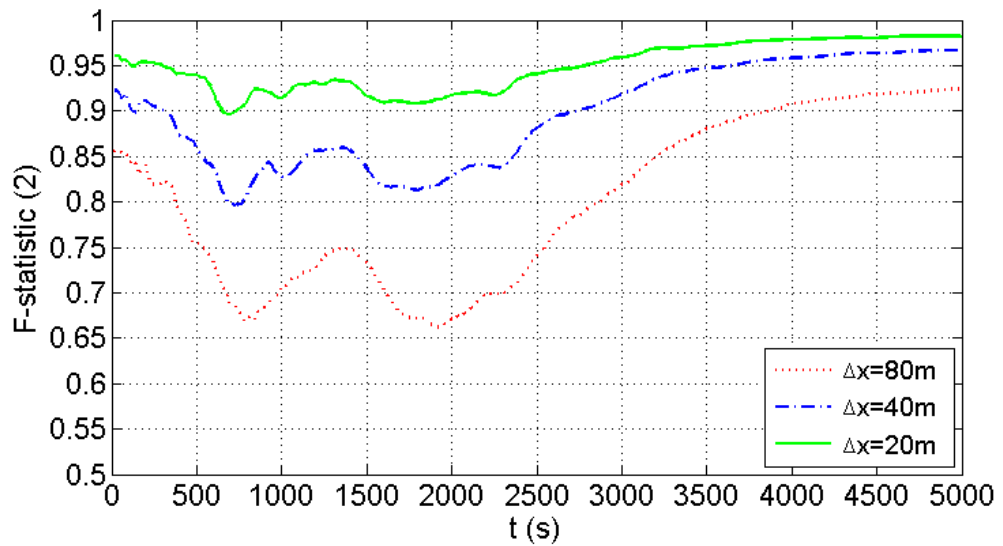


Figure 6.17 Malpasset dam break: Fit statistics (F^2) history in 5000 s based on different grid scales.

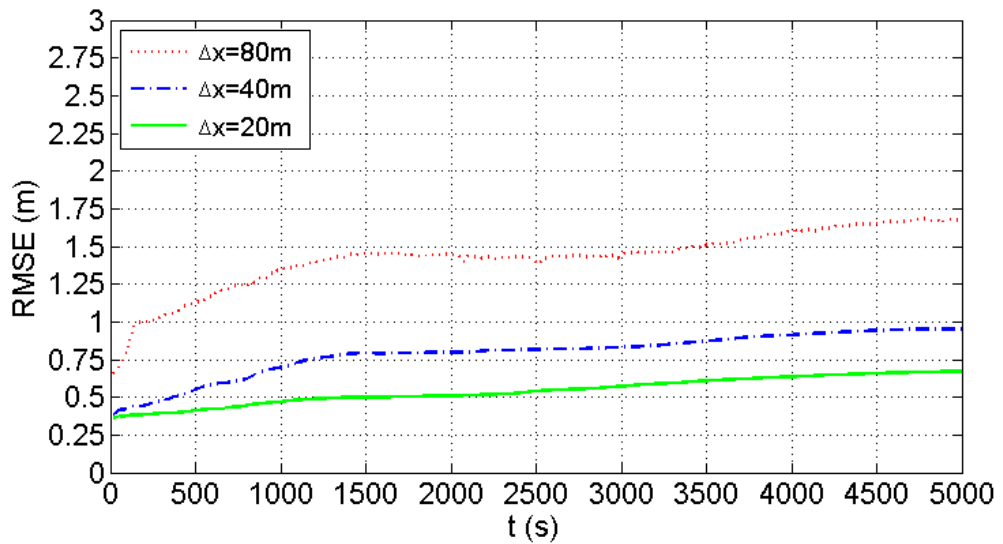


Figure 6.18 Malpasset dam break: Root Mean Square Error (RMSE) history of the water depth in 5000 s based on different grid scales.

RMSE of water depth is studied to examine the response of computed water depth to the changing grid scales illustrated in Figure 6.18. A regular change of RMSE corresponds to the increased grid resolution. Table 6.1 presents the corresponding computational expenses and RMSEs at 5000 s to different resolutions. As shown in Table 6.1, the optimum resolution is 40 m for the particular case in this study, which maintains both computational accuracy and efficiency. However, the balance between numerical accuracy and computational cost is still a big issue in the application of the realistic

flood simulation. It is difficult to decide a common criterion of the optimum grid resolution.

Resolution	RMSE at 5000 s	Computational Time
80 m	1.6875 m	105.2435 s
40 m	0.9585 m	778.5783 s
20 m	0.6805 m	6475.1264 s

Table 6.1 The corresponding RMSE and computational time to different grid scales.

6.2.3.2 Investigation of numerical order accuracy

The investigation of the numerical order accuracy is studied by using fit statistics and RMSE method for the realistic flooding inundation case. In this work, the simulations are performed on 40 m grid resolution. The 2nd order prediction is set to be benchmark. F^1 keeps as a constant 1 with time throughout 5000 s simulation. The result means that the wet-dry state in the global cell of the 1st order simulation is absolutely the same as that of the 2nd order prediction. The fit rate F^2 of the flood extent is also a constant as 1, which means that the performance of 1st order scheme on predicting flood extent is the same as the 2nd order scheme.

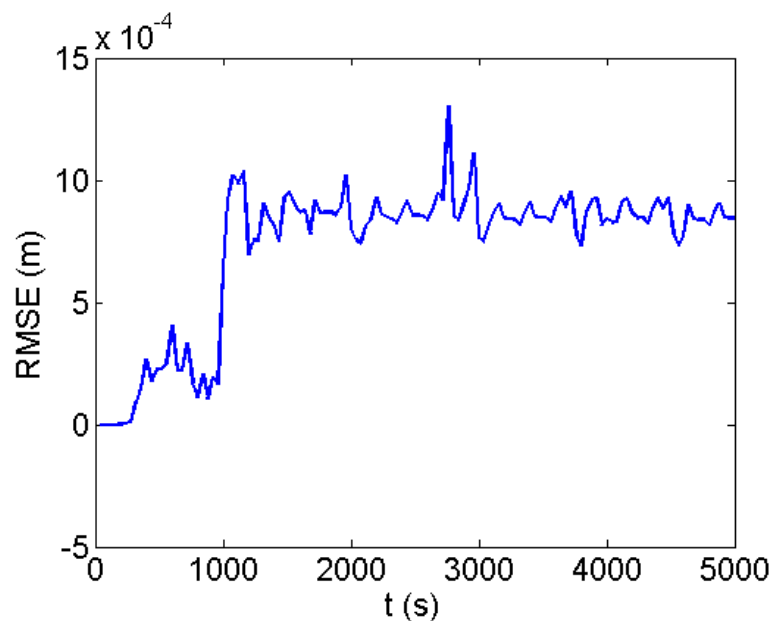


Figure 6.19 Malpasset dam break: Root Mean Square Error (RMSE) history of the water depth in 5000 s.

Further investigation focus on the root mean square error of the predicted water depth illustrated in Figure 6.19. The maximum RMSE of the simulated water depth is less than 1.4×10^{-3} m. The RMSE can be neglected in the application of the realistic large-scale flood simulation, in which the maximum water depth is up to 20 m. Furthermore, the computing times are 778.5783 s for 1st order accuracy and 1659.4531 s for 2nd order accuracy. From above comparisons, it is found that the 1st order scheme can provide the same level of computational accuracy as the 2nd order scheme, and is much more efficient than the 2nd order prediction. Hence, the 1st order scheme is more suitable for the realistic flooding inundation application.

6.3 Conclusions

The investigation of the effects of spatial resolution and the numerical order based on the aforementioned fully 2D shallow flow model in Chapter 3 has been presented. Three test cases are adopted to study the effect of the spatial resolution and the numerical order. Root Mean Square Error method and Fit statistics are implemented to evaluate the response of water depth and flood extent to the change of grid resolution and numerical order. The comparisons demonstrate that:

- The numerical simulations of water depth, arriving time and flood extent are sensitive to the change of spatial resolution in the experimental and realistic cases. However, the responses of water depth, maximum water surface level and arriving time are not consistent with the change of grid resolution at some gauging points. The coarse mesh may provide better prediction at some gauges. In the realistic case, the effect of grid resolution on the numerical accuracy reaches a high-limit with increasing resolution. Furthermore, an unreliable result could be reproduced when the grid resolution decreases to a low-limit. However, a common criterion of a optimum grid resolution is difficult to be decided in the realistic applications;
- The numerical order has different effects on the different applications. The numerical predictions of water depth and flood extent are sensitive to the numerical order in the analytical case, but not in the realistic case. For the

analytical case, the effect of 2nd order scheme is significant in improving the numerical accuracy. And the 2nd order scheme consumes an acceptable computational expense of 105.42 s. For the particular analytical case, the 2nd order scheme is a better choice. For the realistic flood simulation, the 1st order model predicts the same flood extent as the 2nd order code does. The peak RMSE of water depth is less than 1.4×10^{-3} m. And the running time of the 2nd order scheme is 2.13 times of the 1st order model. The advantage of the numerical accuracy cannot justify the loss of the numerical efficiency. Hence, the 1st order scheme is recommended for the particular realistic flood simulation.

Chapter 7 Zero-inertia Model

Objectives

- Developed and validate a new zero-inertia model (simplified 2D shallow flow model);
- Compared the performance of the new zero-inertia model with that of the aforementioned fully 2D shallow flow model in flood simulations.

Introduction

Flood modelling has, in the last decade, gone through a fruitful period of development, fostered by the availability of new datasets (including high resolution topographic data) and faster computing resources. Numerous computational tools suitable for realistic simulations have been reported (e.g. Hunter *et al.* 2005; Bates and De Roo 2000; Horritt and Bates 2002; Bradbrook *et al.* 2004; Yu and Lane 2006a; Liang *et al.* 2008). Among these, the models based on solution to the fully 2D shallow water equations represent the state-of-the-art in flood modelling and have begun to gain popularity (e.g. Mignot *et al.* 2006; Liang *et al.* 2008). However, due to the high computational cost associated with the fully 2D simulations, substantial efforts have been made to develop computationally more efficient flood models. One of the strategies is to simplify the governing equations and meanwhile endeavour to maintain a reasonable physical representation of flood waves. The zero-inertia models (ZIMs), or diffusion-wave models (DWMs), fall in this category. Based on the assumption of slow-varying flood waves, the ZIM governing equation can be derived from the fully 2D shallow water equations by neglecting the momentum dynamic terms (the three shallow water equations are simplified and finally combined into a single zero-inertia equation). Less violent flow and substantially simplified governing equation essentially mean that ZIMs can normally adopt simpler numerical methods and may have potential in providing more efficient numerical computation.

After it was introduced by Cunge *et al.* (1976), the diffusion-wave concept has been used by many researchers to develop over-land flow models and a number of successful

ZIMs or DWMs for flood simulations have also been reported and become popular in literature. Bates and De Roo (2000) adopted the diffusion-wave approach to develop their raster-based flood model (LISFLOOD-FP), whose performance has been compared with a 1D model (HEC-RAS) by Horritt and Bates (2002) and a 2D finite element shallow flow model (TELEMAC-2D) by Horritt and Bates (2001) and (2002). They demonstrated that LISFLOOD-FP can reproduce flood extent to a reasonable high accuracy, despite the use of highly simplified equation and simple numerical method. Later on, Bradbrook *et al.* (2004) introduced another explicit model based on the diffusion-wave concept for the flood inundation simulations. Application of ZIM/DWM in urban flood prediction was exploited in Yu and Lane (2006a). Common to these models, flux limiters are often required in order to combat numerical instability and save computational time. However, as showed in Hunter *et al.* (2005) and Bates *et al.* (2010), a flux limiter may have an adverse effect on the solution quality.

Therefore, this work presents an alternative ZIM for flood modelling based on a depth-positivity-preserving condition that (a) does not require a flux-limiter to maintain stable numerical results and (b) facilitates simulations with wetting and drying over natural floodplains. After demonstrating its performance via two analytical test cases, the new model is applied to reproduce a flood inundation event in the 36 km² Thamesmead floodplain near London, England. The numerical results are also compared with the aforementioned fully 2D shallow flow model.

7.1 Zero-inertial Model

ZIMs only consider the continuity equation from the depth-averaged shallow water system of equations, i.e.

$$\frac{\partial \eta}{\partial t} + \frac{\partial Q^x}{\partial x} + \frac{\partial Q^y}{\partial y} = 0, \quad (7.1)$$

where t denotes time, x and y are the Cartesian coordinates, η is the water level, $h = \eta - z_b$ gives the water depth with z_b being the bed level, Q^x and Q^y (m²/s) are the x and y components of the momentum flux, which are herein accounted using the Manning stage-discharge relationship, i.e.

$$Q^x = h^{5/3} n^{-1} \left(\frac{\partial \eta}{\partial x} \right)^{1/2} \quad \text{and} \quad Q^y = h^{5/3} n^{-1} \left(\frac{\partial \eta}{\partial y} \right)^{1/2}, \quad (7.2)$$

where n is the Manning roughness coefficient.

In this work, the zero inertia equation given by (7.1) is solved by an explicit finite volume method and the following formula is used to update the water level at cell (i, j) to a new time step:

$$\eta_{i,j}^{k+1} = \eta_{i,j}^k + \Delta t \left(\frac{Q_{i+1/2,j}^x - Q_{i-1/2,j}^x}{\Delta x} + \frac{Q_{i,j+1/2}^y - Q_{i,j-1/2}^y}{\Delta y} \right), \quad (7.3)$$

where the superscript k indicates time level, Δt denotes the time step, $Q_{i+1/2,j}^x$, $Q_{i-1/2,j}^x$, $Q_{i,j+1/2}^y$ and $Q_{i,j-1/2}^y$ respectively represent the fluxes across the four cell interfaces. It is well-known that the finite volume method facilitates excellent mass conservation, which is an important property a numerical code should have for flood modelling.

7.1.1 Depth-positivity-preserving condition

At a cell interface $(i+1/2, j)$ shared by cells (i, j) and $(i+1, j)$, a single value for the bed elevation is defined as

$$\hat{z}_b = \max(z_{bi+1,j}, z_{bi,j}), \quad (7.4)$$

based on which the non-negative water depth is reconstructed, i.e.

$$\hat{h}_{i,j} = \max(0, \eta_{i,j} - \hat{z}_b) \quad \text{and} \quad \hat{h}_{i+1,j} = \max(0, \eta_{i+1,j} - \hat{z}_b), \quad (7.5)$$

The free-surface elevations at (i, j) and $(i+1, j)$ are then accordingly reconstructed to be

$$\hat{\eta}_{i,j} = \hat{h}_{i,j} + \hat{z}_b \quad \text{and} \quad \hat{\eta}_{i+1,j} = \hat{h}_{i+1,j} + \hat{z}_b, \quad (7.6)$$

The corresponding value of the water depth at the interface $(i+1/2, j)$ is obtained by averaging those central values given in (7.5)

$$h_{i+1/2,j} = (\hat{h}_{i,j} + \hat{h}_{i+1,j})/2, \quad (7.7)$$

Similar treatment can be done for the faces $(i-1/2, j)$, $(i, j+1/2)$, $(i, j-1/2)$. It should be noted that local amendments (7.4)-(7.7) apply locally and temporary at the stage of interface flux calculation and does not produce violation in the mass conservation.

7.1.2 Flux calculation

Across the interface $(i+1/2, j)$, the momentum flux is estimated by approximating (7.2) using the reconstructed the free-surface elevation (7.6) and non-negative water depth (7.7), namely

$$Q_{i+1/2,j}^x = h_{i+1/2,j}^{5/3} n^{-1} \left| \frac{\hat{\eta}_{i+1,j} - \hat{\eta}_{i,j}}{\Delta x} \right|^{1/2}, \quad (7.8)$$

The fluxes $Q_{i-1/2,j}^x$, $Q_{i,j+1/2}^y$ and $Q_{i,j-1/2}^y$ across the other interfaces $(i-1/2, j)$, $(i, j+1/2)$ and $(i, j-1/2)$ are estimated in a similar way, i.e.

$$Q_{i-1/2,j}^x = h_{i-1/2,j}^{5/3} n^{-1} \left| \frac{\hat{\eta}_{i,j} - \hat{\eta}_{i-1,j}}{\Delta x} \right|^{1/2}, \quad (7.9)$$

$$Q_{i,j+1/2}^y = h_{i,j+1/2}^{5/3} n^{-1} \left| \frac{\hat{\eta}_{i,j+1} - \hat{\eta}_{i,j}}{\Delta y} \right|^{1/2}, \quad (7.10)$$

$$Q_{i,j-1/2}^y = h_{i,j-1/2}^{5/3} n^{-1} \left| \frac{\hat{\eta}_{i,j} - \hat{\eta}_{i,j-1}}{\Delta y} \right|^{1/2}, \quad (7.11)$$

Then the water level at cell (i, j) can then be updated to the next time step using (7.3).

7.1.3 Time stepping and boundary conditions

In the present ZIM, a fixed time step is employed. For the test cases considered in this work, two types of boundary conditions, *i.e.* open (transmissive) and closed (slip), are used. For open (transmissive) boundary conditions, the flow information at those ghost points is simply provided to give zero gradients of water surface and velocities across the boundary. Closed (slip) boundary conditions require zero normal velocity/flux at the boundary.

7.2 Results

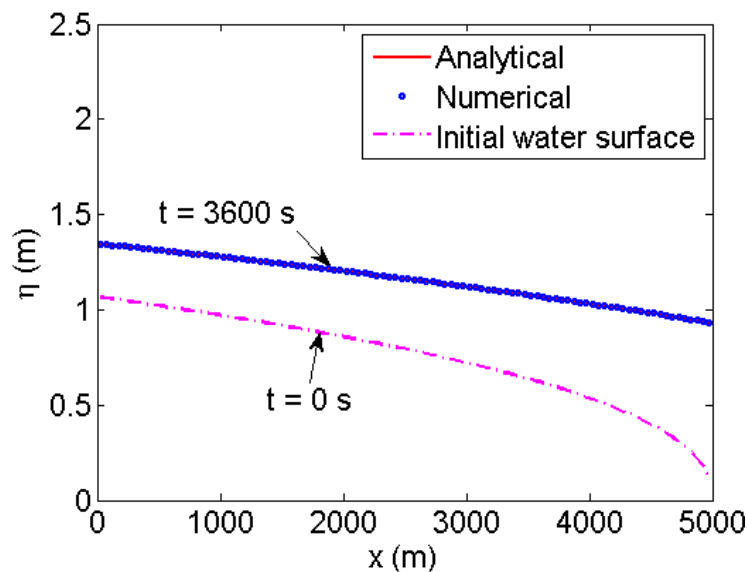
The current ZIM is first validated using two analytical benchmarks. And then the ZIM is finally used in forecasting a hypothetical flood inundation event. Results are compared with either analytical solutions or alternative numerical predictions produced by the aforementioned fully 2D shallow flow model in Chapter 3. All the simulations are run on a standard Pentium desktop PC.

7.2.1 Open channel flow with flat bed

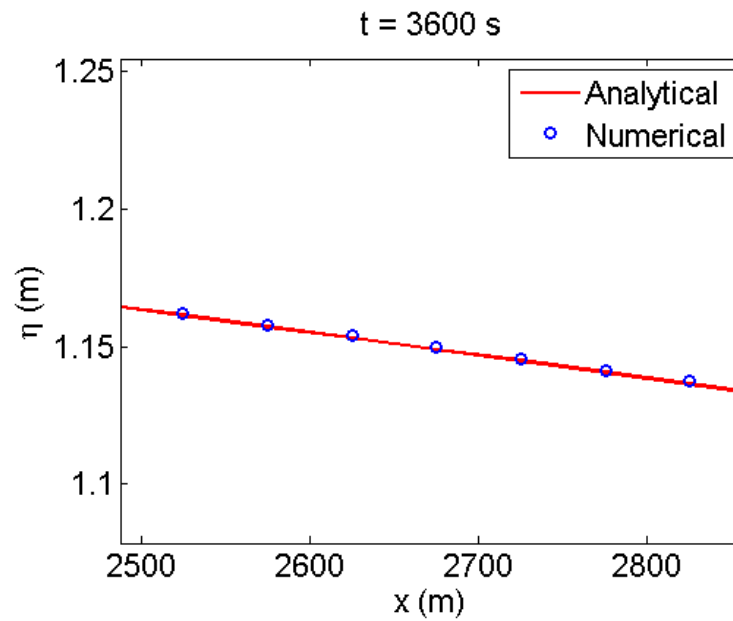
This is a 1D analytical test case that has been investigated in Hunter *et al.* (2005) and Bates *et al.* (2010). With the assumption of a constant flow velocity and planar bed without slope, the analytical solution of water depth can be found by Hunter *et al.* (2005),

$$h(x,t) = \left[\frac{7}{3} (A - n^2 u^3 (x - ut)) \right]^{3/7}, \quad (7.14)$$

Herein, $u = 1$ m/s is the flow velocity; $n = 0.01$ m^{-1/3}s is Manning coefficient; $A = 0.5$ is a constant. The computational domain is assumed to be 5000 m long and 200 m wide and is discretized by a uniform grid with 100×4 cells. The initial condition and the inflow boundary condition can be directly calculated from (7.14), i.e. $h(x,0)$ and $h(0,t)$. Simulations are run up to $t = 3600$ s.



(a)



(b)

Figure 7.1 Open channel flow with flat bed: (a) initial flow condition and the final free-surface profile predicted by the ZIM; (b) a zoomed part of the solution.

Simulations are performed with a fixed time step of 0.035 s. Figure 7.1 (a) presents the predicted results in terms of free-surface profiles, which match very well with the analytical solution (as show the zoomed portion in Figure 7.1 (b)). This can be also noted in Figure 7.2 showing the associated RMSEs of the predicted water depth and the analytical solution.

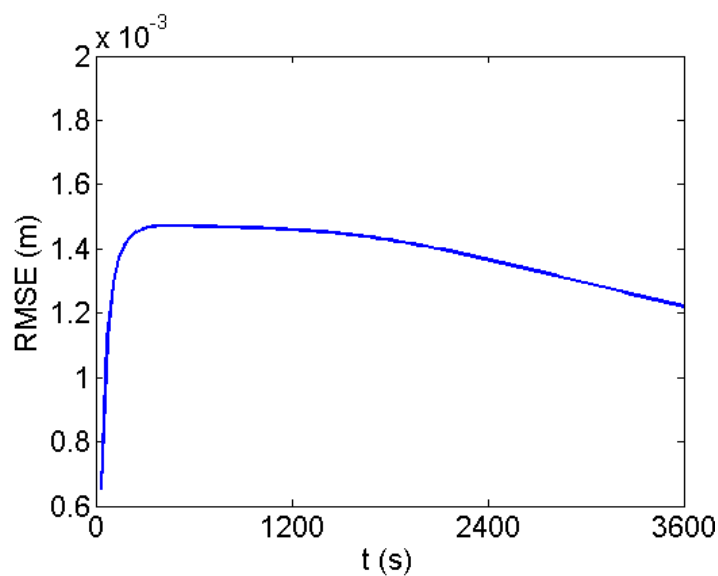
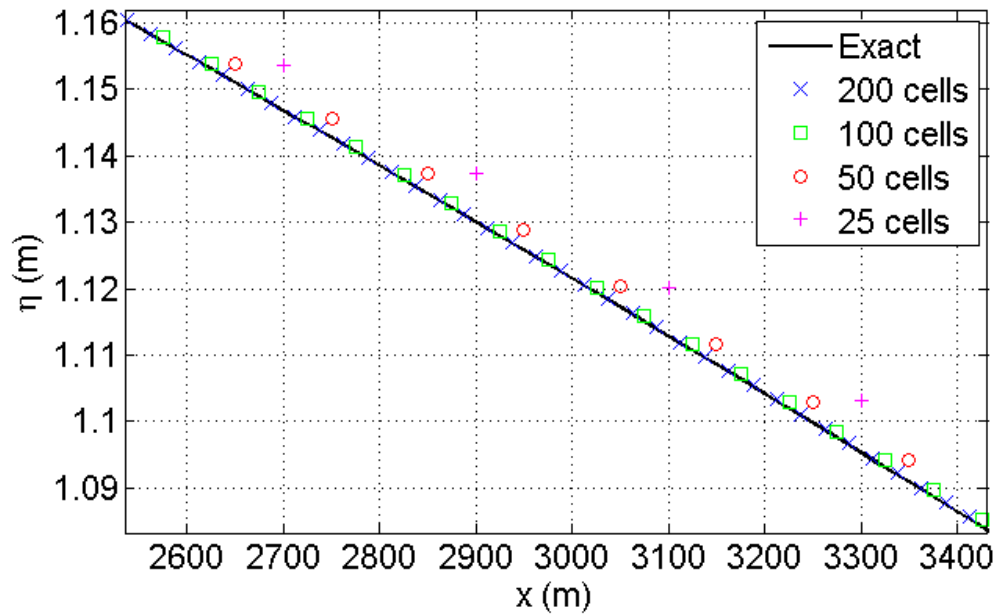
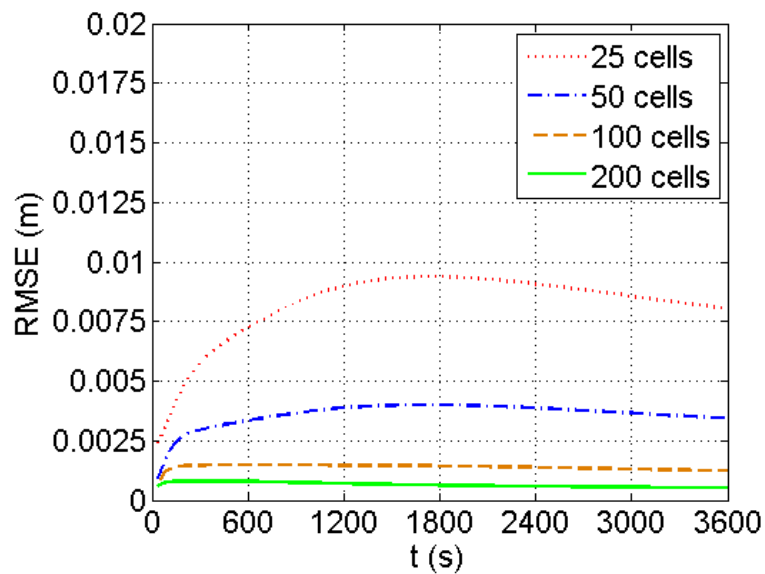


Figure 7.2 Open channel flow with flat bed: the time history of the RMSE.

Finally, a grid convergence study is carried out with a fixed time step $\Delta t = 0.035$ s. Calculations are performed using respectively 200, 100, 50 and 25 computational cells in the flow direction. The longitudinal free-surface profiles (zoom-in view in Figure 7.3 (a)) and their associated time history of RMSE (i.e. Figure 7.3 (b)) on different grids are plotted in Figure 7.3. The resolution of the current ZIM model is seen to improve with grid refinement in proportion with a reduction in the RMSE.



(a)



(b)

Figure 7.3 Open channel flow with flat bed: a grid convergence study for the ZIM model: (a) the final free-surface; (b) the associated time histories of the RMSE.

7.2.2 Tidal flow over a beach with varying slope

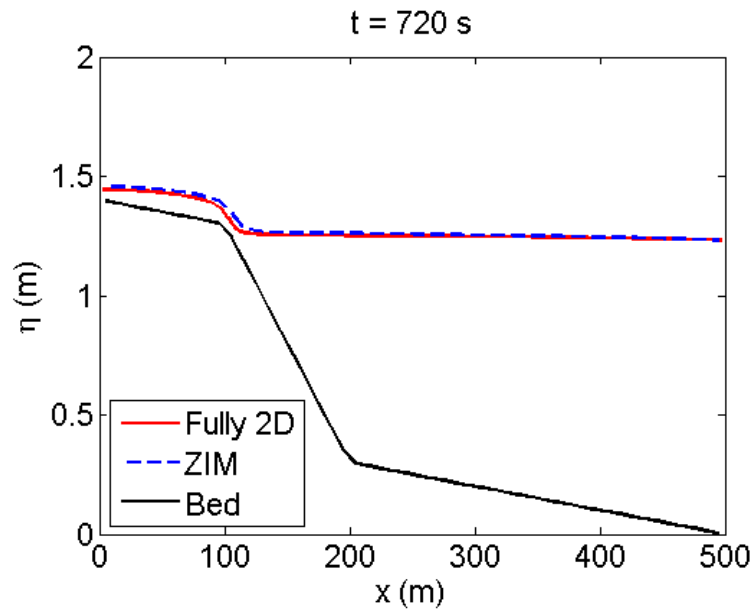
This test case is about a tidal flow moving over a beach with varying bed slope defined as

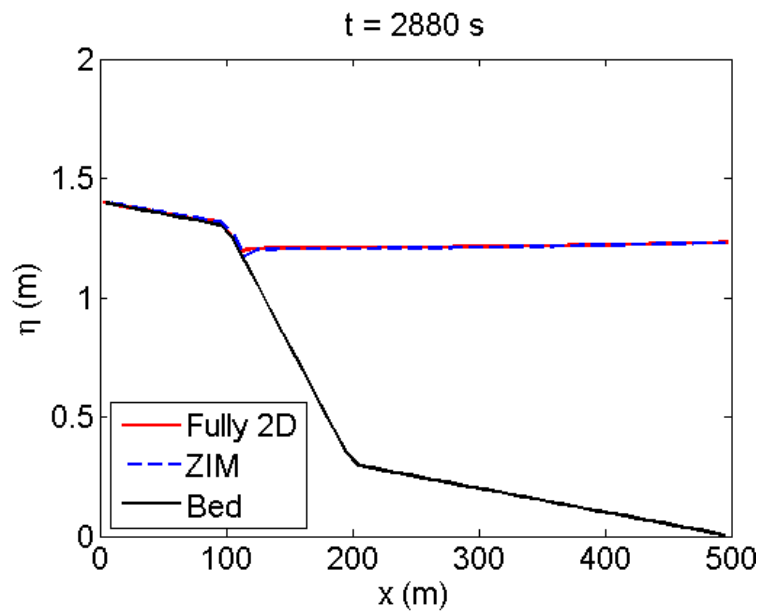
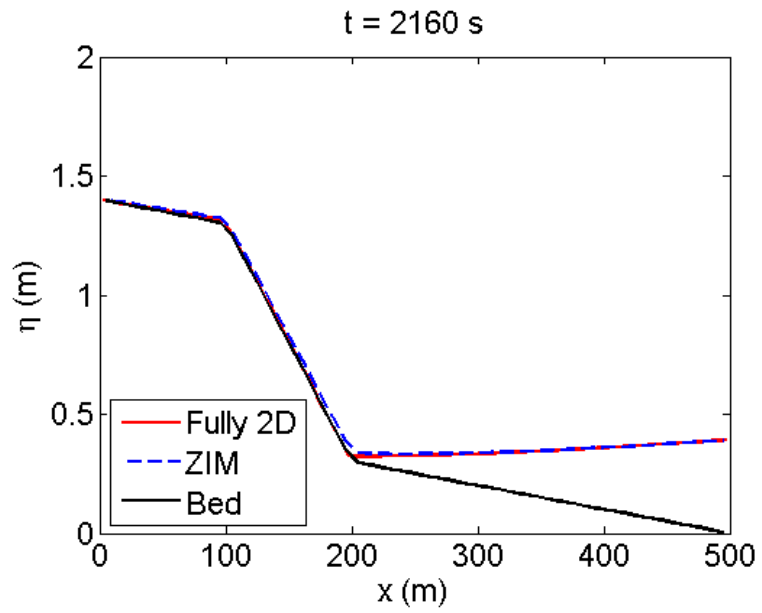
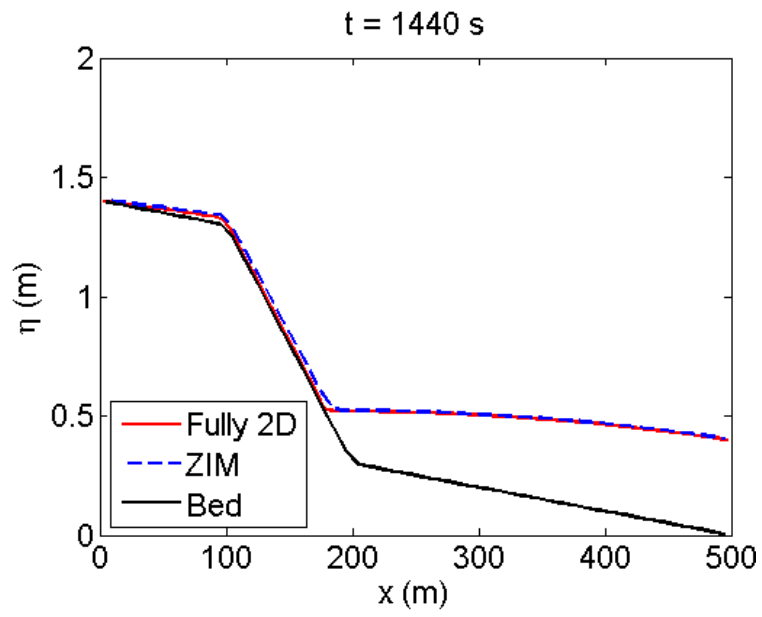
$$z_b(x) = \begin{cases} -0.001x + 1.4 & \text{if } x \leq 100\text{m} \\ -0.01x + 2.3 & \text{if } 100\text{m} < x < 200\text{m} \\ -0.001x + 0.5 & \text{if } x \geq 200\text{m} \end{cases}, \quad (7.15)$$

Assuming a period of $T = 3600$ s, the flow mimicking a tidal cycle is provided through

$$h(t) = 1.0 + 0.75 \cos\left(2\pi \frac{t}{T}\right), \quad (7.16)$$

which is imposed at the eastern end of the domain as the inlet flow condition. The $500 \text{ m} \times 50 \text{ m}$ computational domain is approximated by a 50×5 uniform grid. Initially, the water body inside the domain is motionless with a surface elevation of 1.75 m . While the western boundary is closed, the southern and northern lateral walls are transmissive. A constant Manning coefficient of 0.03 is used for the entire domain.





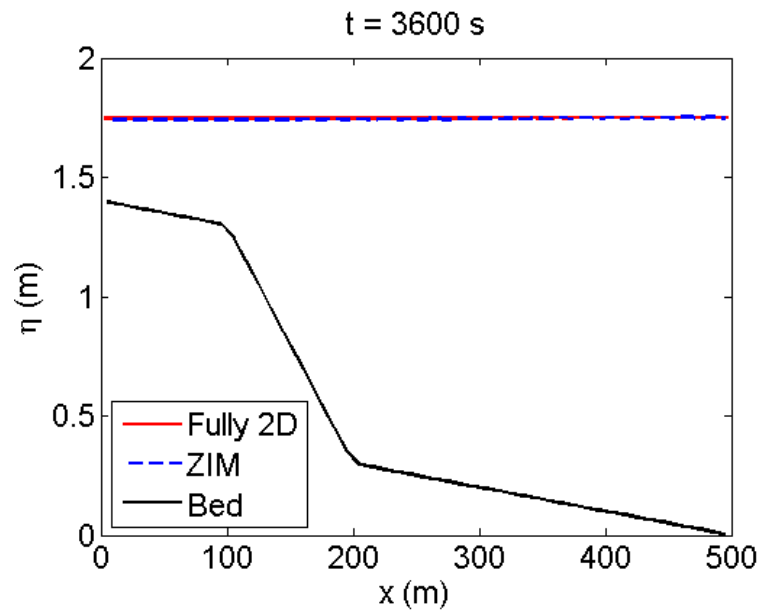


Figure 7.4 Tidal flow over a beach with varying slope: free-surface profiles predicted by the ZIM and fully 2D shallow flow model (using a fixed time step of 0.0075 s) at different output times.

A simulation is performed using the ZIM with a “fixed-time-step” of 0.0075 s. The associated free-surface profiles at several output times up to one period cycle are depicted in Figure 7.4 indicating very good agreement with the results provided by the aforementioned fully 2D finite volume Godunov-type shallow water model in Chapter 3. Figure 7.5 presents the associated time history of the RMSE of water depth predicted by the ZIM and the fully 2D shallow flow model. For now, it is worth bearing in mind that the required CPU time for the simulations is 185 s.

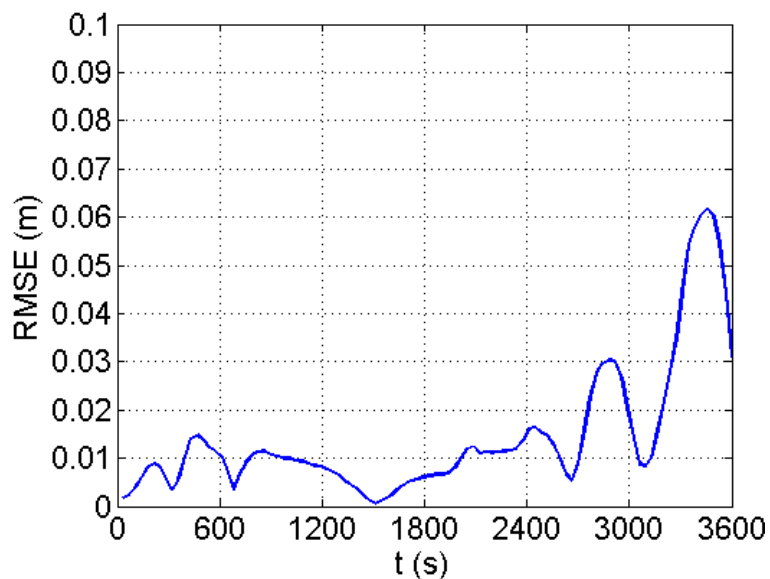


Figure 7.5 Tidal flow over a beach with varying slope: the time history of the RMSE.

7.2.3 Thamesmead flood inundation

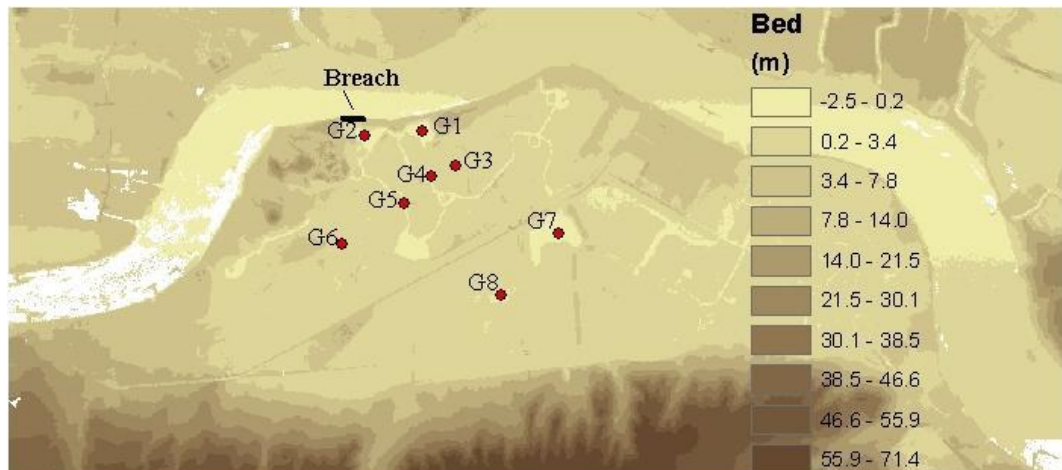


Figure 7.6 Thamesmead flood inundation: floodplain (also being illustrated are the locations of the breach and 8 gauge points for recording time history of water surface elevation).

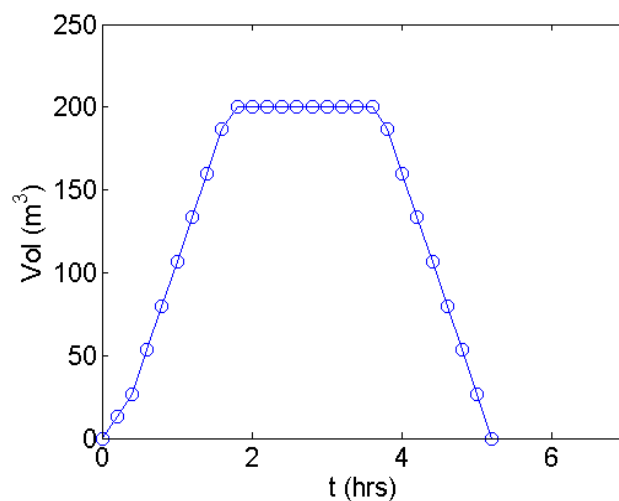


Figure 7.7 Thamesmead flood inundation: inflow hydrograph.

The limiter-free ZIM is applied to predict an idealised inundation event at Thamesmead, which is part of the Thames floodplain at the south bank of the River Thames in England. The selected 9000 m × 4000 m floodplain is represented by a processed 10 m bare-earth DTM shown in Figure 7.6. As shown in Figure 7.6, a 150 m long breach of the flood defence is centred at (545855 m, 181040 m) with the coordinates of the bottom left corner given as (543000 m, 178000 m). Also indicated in Figure 7.6 are eight gauge points for recording time histories of water surface elevation during the

simulation. The idealised hydrograph shown in Figure 7.7 is imposed at the breach to drive the flood event. The originally dry computational domain is discretized by a 450×200 uniform grid and the roughness coefficient $n = 0.035$ is assumed to be constant in the whole computational domain. Transmissive boundary conditions are used for this simulation. A fixed time step is set to be 0.05 s.

The simulation is carried out for a 10-hour flood event. Figure 7.8 shows the inundation maps at $t = 1.5$ hrs and $t = 10$ hrs produced by the current ZIM, compared with those predicted by the fully 2D Godunov-type shallow water model introduced in Chapter 3. The time histories of the water surface level at the eight selected gauging points are plotted in Figure 7.9 compared with those fully 2D results. The ZIM prediction follows closely with the fully 2D calculation, which is confirmed quantitatively by the RMSE illustrated in Figure 7.10, calculated against the two sets of solutions. The RMSE goes stable after $t = 6$ hrs which is smaller than 0.05 m.

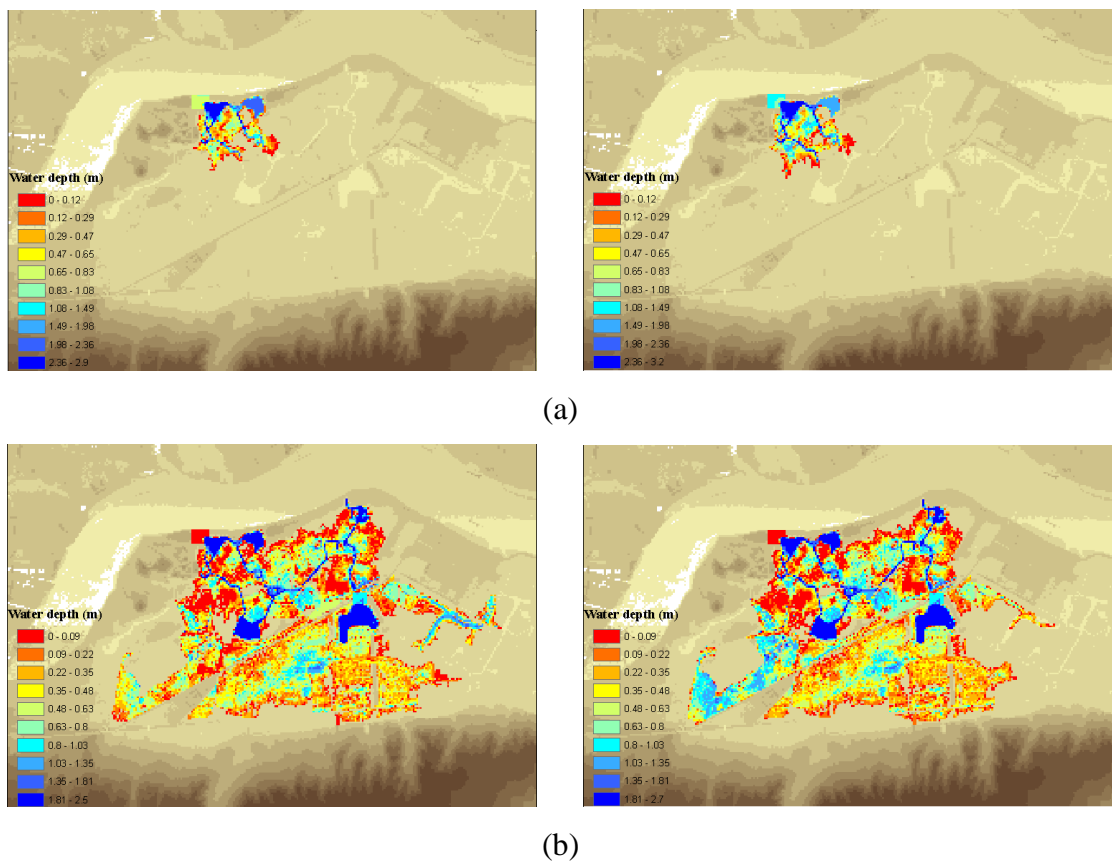
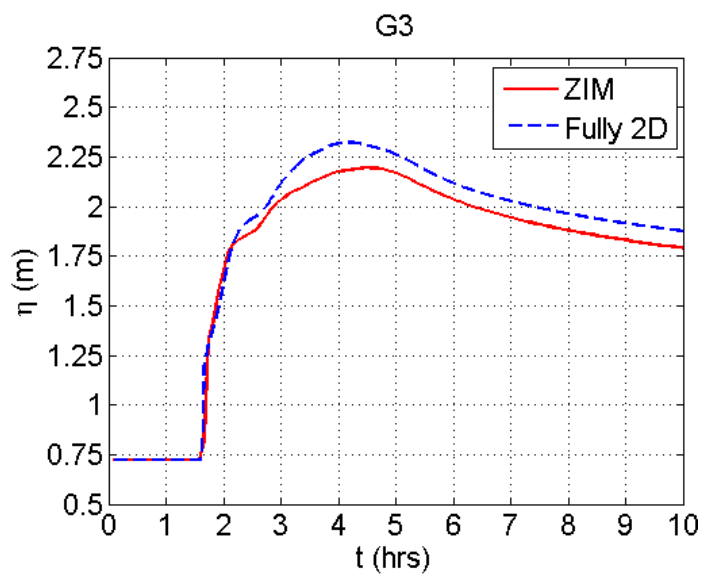
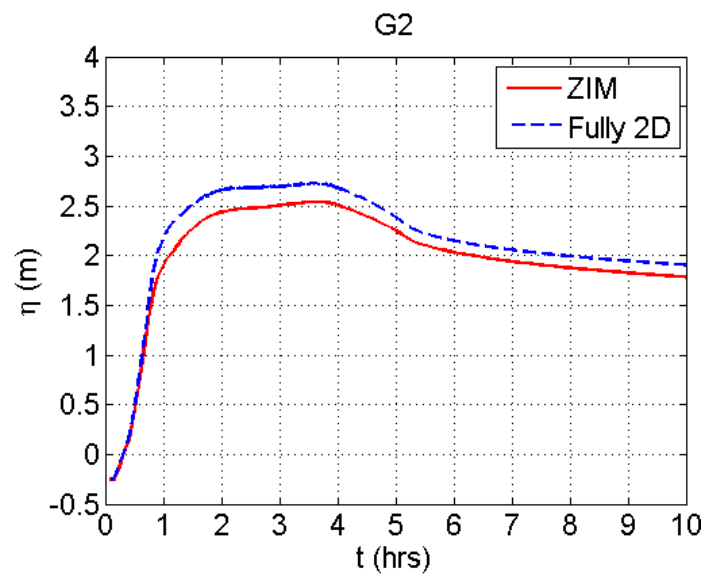
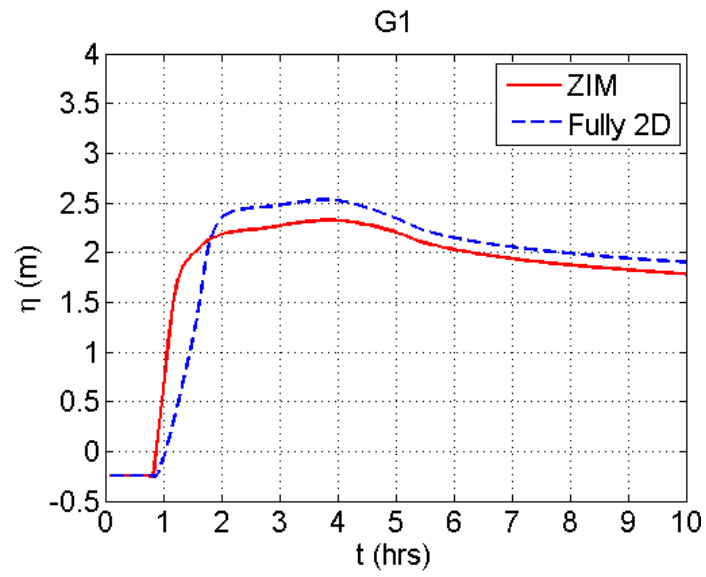
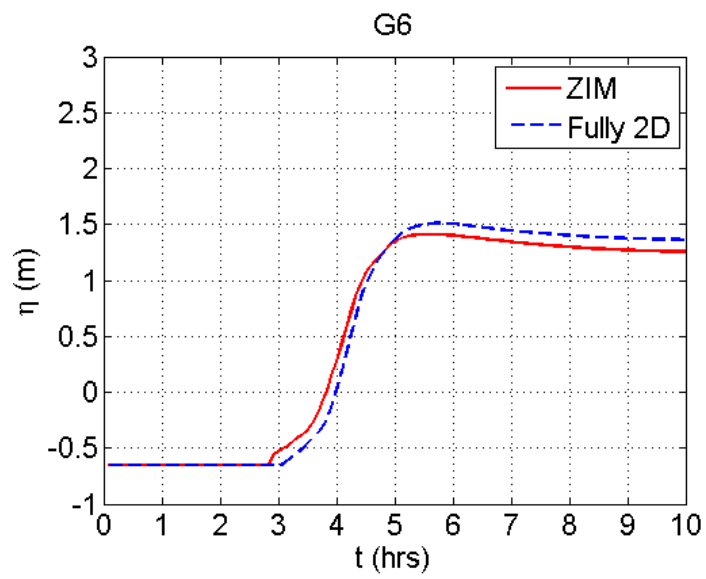
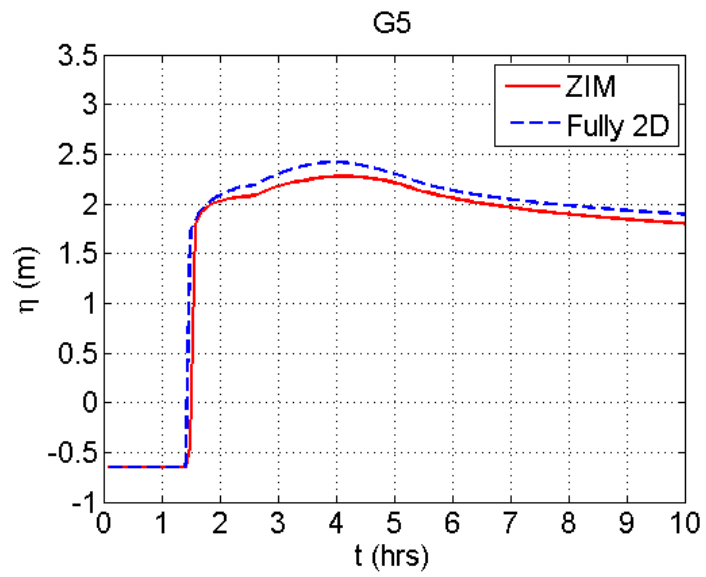
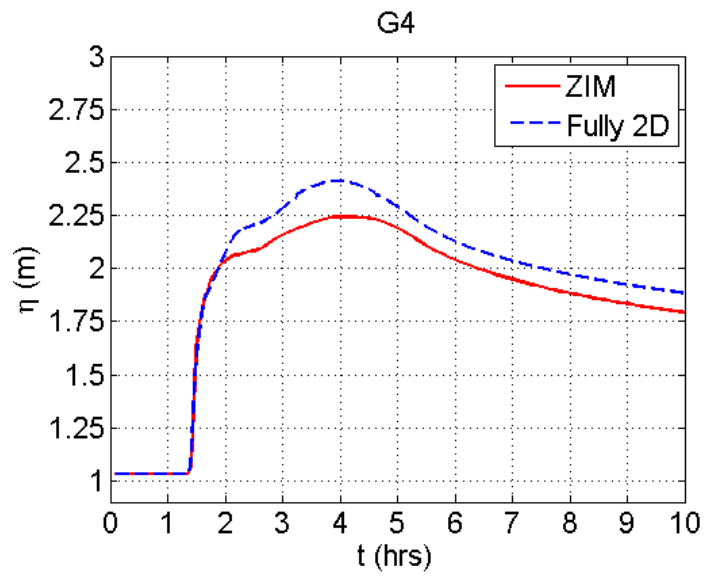


Figure 7.8 Thamesmead flood inundation: flood maps of the Thamesmead flood inundation predicted by the ZIM model (left) and the fully 2D model (right): (a) $t = 1.5$ hrs; (b) $t = 10$ hrs.





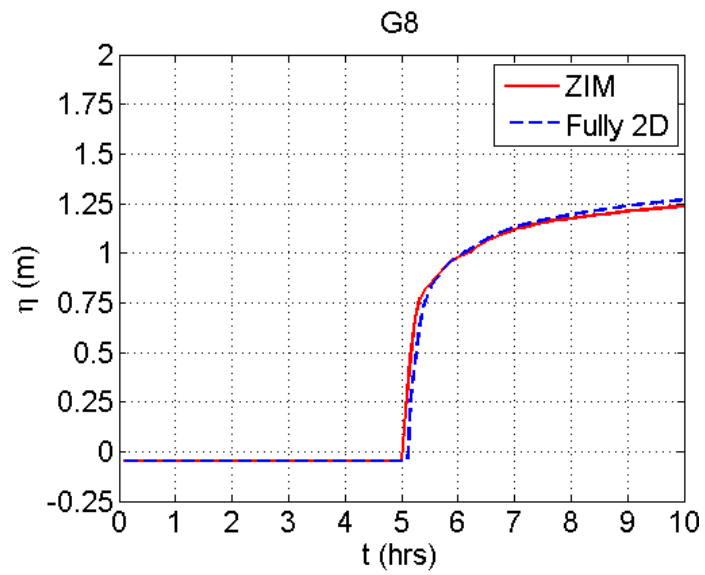
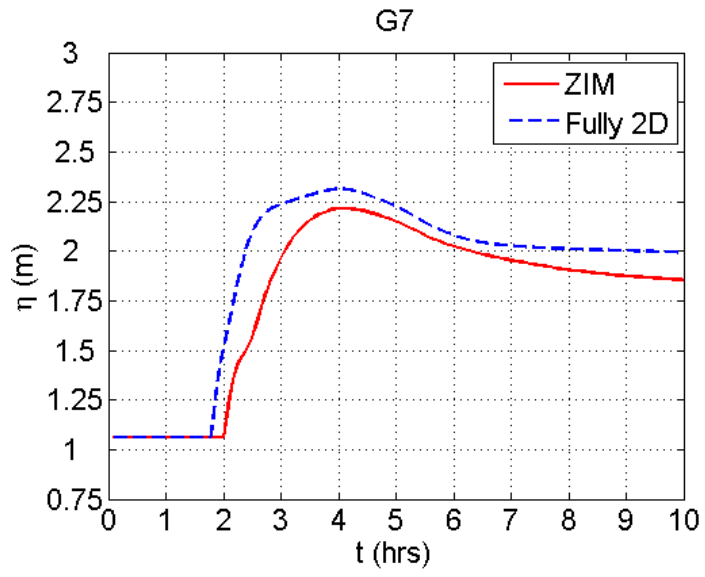


Figure 7.9 Thamesmead flood inundation: time histories of water depth at eight different gauge points.

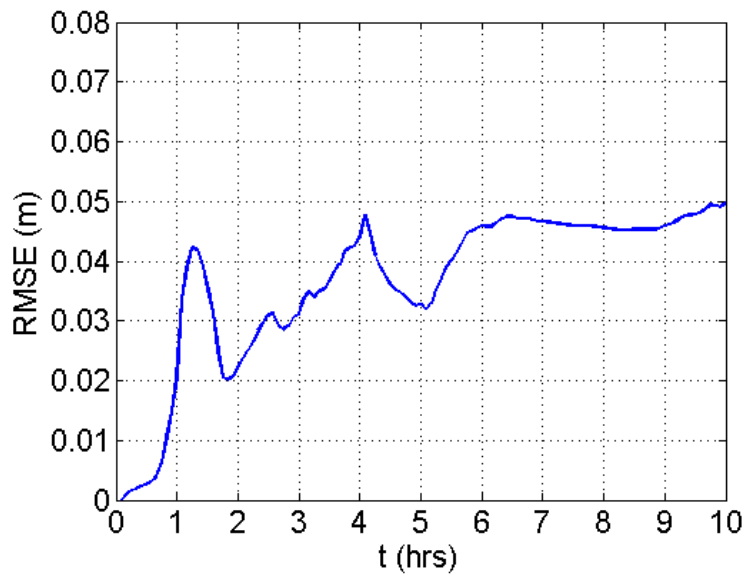


Figure 7.10 Thamesmead flood inundation: time history of RMSE calculated against the fully 2D solution.

In order to confirm the mass conservation of the current finite volume ZIM, the total volume of water inside the computational domain is measured and plotted against the total volume of mass through the breach in Figure 7.11. For this case, since no outflow is induced, the inflow mass should be the same as those accumulated inside the domain. Evidently, excellent mass conservation property of the finite volume model is confirmed.

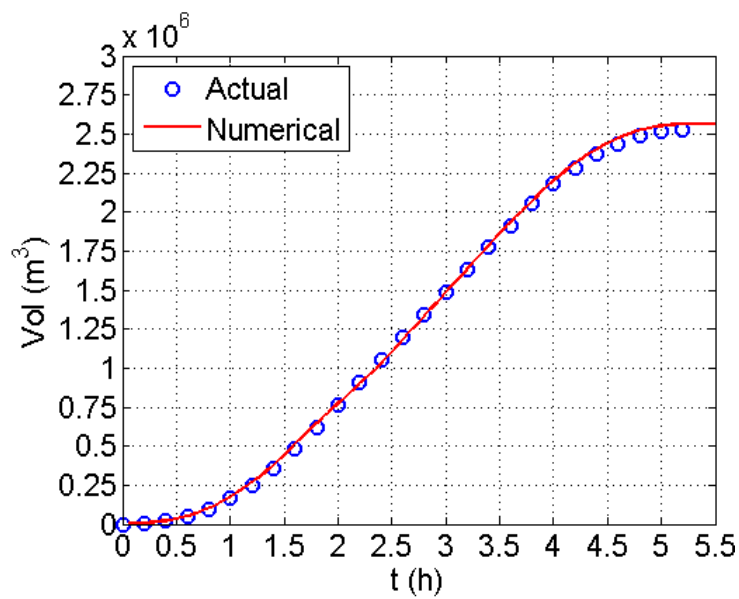


Figure 7.11 Thamesmead flood inundation: mass conservation.

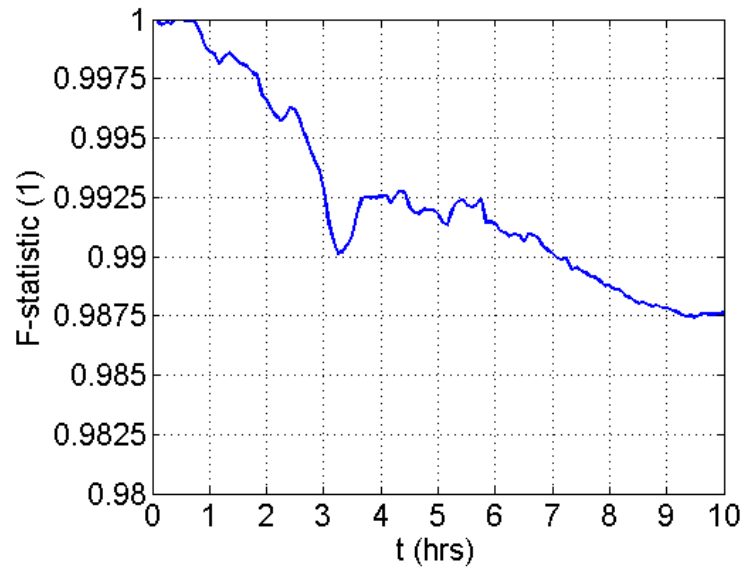


Figure 7.12 Thamesmead flood inundation: Fit-statistic (F^1).

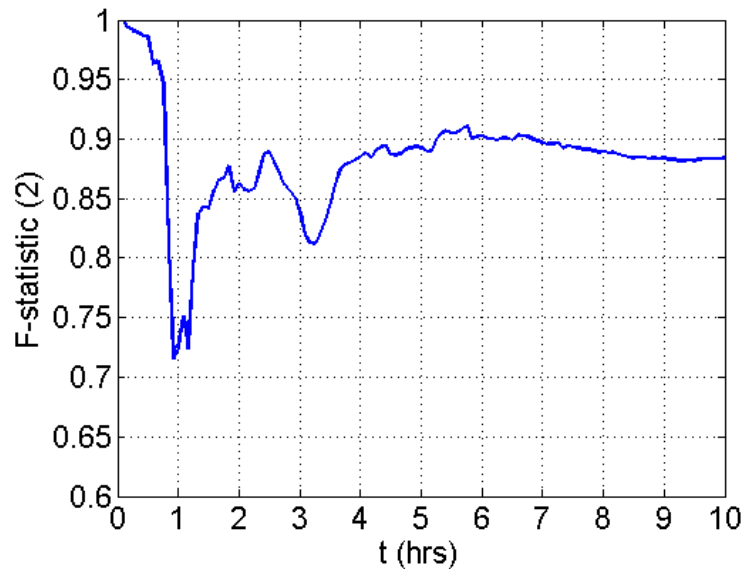


Figure 7.13 Thamesmead flood inundation: Fit-statistic (F^2).

The Fit-Statistic (F^1 and F^2) method (refer to Chapter 6 for details) are employed here to further investigate the performance of the present zero-inertia model. F^1 presents the fitted rate of cells with the same wet-dry state. F^2 shows the percentage of matched flood extent predicted by the ZIM and the fully 2D shallow flow model. Herein the computed results of the fully 2D shallow flow model are taken as the benchmark. As shown in Figure 7.12 and Figure 7.13, F^1 and F^2 both convergence from $t = 5.5$ hrs. At $t = 10$ hrs, over 98.75% of the global cells predicted by ZIM presents the same wet-dry state as the fully 2D simulation. And the percentage of the matched flood extent is

nearly 88.75%. It also proves that the accuracy of ZIM converges to the fully 2D shallow flow model.

In terms of computational time, the ZIM code necessitates around 8 hrs for this simulation while the fully 2D model only requires 16.4 min. This coincides with the findings reported in Hunter *et al.* (2008) and confirms that, for complex real-world flood simulations, a ZIM could be more expensive than a fully 2D shallow flow model. Hunter *et al.* (2008) compared the performance of six different models on simulating urban flood event, including fully 2D shallow flow model and zero-inertia model, in which the zero-inertia model took several times longer computational time than the fully 2D shallow flow model. As mentioned in Hunter *et al.* (2005), due to the lack of the inertia terms, careful time step has to be operated to avoid large inter-cell flux and spurious oscillations for the explicit zero-inertia model. This resulted in the increase of the computational cost. In order to maintain the computational stability, Hunter *et al.* (2005) investigated the governing equations and then developed an optimal time step for the explicit diffusion wave model (i.e. zero-inertia model), which is a quadratic function of grid size. However, the drawback of this approach is that the time step may tend to zero when the free surface gradient tends to zero. Hence, a water depth threshold has to be operated to avoid this particular situation. In order to obtain computational efficiency, Bates *et al.* (2010) included an inertia term to control flow velocities and inter-cell fluxes. Hence, the governing equation was changed from parabolic to hyperbolic, which has different stability condition. Therefore, a new adaptive time step was developed to control the computational stability and reduce the computational cost.

7.3 Conclusions

This work presents a zero-inertia model (ZIM) featured by a spatial depth-positivity-preserving reconstruction for flux calculation, which is based on a finite volume formulation. After the two theoretical test cases of mono-directional flow over horizontal or varying-sloping bed, the following conclusions can be drawn. The ZIM produces a solution that agrees well analytical solution without needing a flux limiter.

Based on the above findings, the present limiter-free ZIM is set up to simulate a realistic inundation event in the Thamesmead floodplain near London, UK. The numerical

predictions are compared very well with those produced by a fully 2D Godunov-type shallow flow model. Furthermore, mass conservation is monitored and confirmed in this case for the current finite volume ZIM. However, the ZIM is found to be computationally much more demanding than the fully 2D model and hence the potential of more efficient simulations is not justified for this type of simplified models. This confirms the conclusion indicated in Hunter *et al.* (2008).

Chapter 8 Conclusion and Future Work

This thesis has presented a novel fully 2D shallow flow model to successfully solve different flow regimes, i.e. transcritical, subcritical, supercritical flow and shock-like flow, and also accurately predict the wet-dry interface over the complex domain topography. A zero-inertia equation, which is simplified from the fully 2D shallow water equations, has been solved by using a limiter-free explicit finite volume scheme, incorporated with the non-negative water depth reconstructed method, and validated against an idealised dam-break flooding inundation case. In this chapter, the conclusions of this study are presented including the advantages and limitations of the presented numerical models and the proposed future work based on the present research.

8.1 Conclusions

8.1.1 Fully 2D shallow flow model

The well-balanced fully 2D shallow water equations have been solved by using a finite volume Godunov-type scheme. The HLLC Riemann solver is adopted to solve the interface fluxes. The second order accuracy is achieved by using Runge-Kutta time integration method and the MUSCL slope limiter in space. A non-negative water depth reconstruction approach is implemented here to deal with the wetting and drying interfaces, incorporated with a local bed elevation modification method. A limited implicit scheme is implemented to discretise the friction source term to avoid the spurious oscillation. For the explicit numerical scheme, the Courant-Friedrichs-Lewy (CFL) criterion is adopted to limit the time step in order to maintain the computational stability. A local boundary modification method is applied to deal with the non-aligned domain boundary or the obstacles and structures in the computational domain.

The numerical model has been validated against several benchmark cases. The numerical model has presented accurate simulation of the tidal wave over the complex bed topography. Hydraulic jump corresponds closely to the theoretical solution, in which the velocity field is also predicted accurately. The numerical model is found to be

able to correctly simulate the different flow regimes, e.g. transcritical flow and shock-like flow, and accurately capture the wet-dry interfaces over the complex bed topography. The reflection, interaction and transaction of the shock wave have been accurately reproduced in the applications. The numerical scheme is proved to be second order accurate based on an analytical solution. The fully 2D shallow flow model has been verified to be a reliable numerical tool for the flooding simulation of different flow regimes over complex domain topography.

8.1.2 Dam-break simulation

The realistic dam-break flood has been successfully predicted by the present model. For the dam-break violent flow, violent hydrodynamics features have been accurately captured in the experimental case and real-world case. The shock-like discontinuity has been correctly simulated by implementing the Godunov-type scheme, incorporated with the approximate HLLC Riemann solver. The well-balanced model has presented good performance on reproducing the dam-break flow over complex domain topography with repeatedly the wetting-drying problem. The unphysical oscillation at the wet-dry front has been avoided due to the application of the non-negative water depth reconstruction approach. The arriving time, water depth and flood velocity have been accurately simulated in the experimental and realistic dam-break cases.

8.1.3 Coastal wave run-up simulation

A non-reflective boundary condition is adopted here to absorb the reflective wave and let the incident wave in, in order to avoid the unphysical oscillations. The present model has been validated against analytical and experimental benchmark cases. The numerical prediction shows that complicated coastal phenomena, e.g. hydraulic jump, wave run-up, surge wave, have been correctly simulated. And moving shoreline and wave run-up have been accurately captured, compared with the analytical solution and the experimental measurement.

8.1.4 Effect of grid scale and numerical order

The mesh resolution is an important influencing factor of the computational accuracy and efficiency. In this work, an experimental dam-beak case and a realistic Malpasset dam-break case are studied to investigate the effect of grid scale. The predictions of water depth, maximum water surface level, arriving time and flood extent are sensitive to the change of grid resolution. The results demonstrate that the mesh refinement improves the computational accuracy by sacrificing the numerical efficiency. However, the coarser mesh could provide better predictions at some gauges. The effect of mesh refinement reaches to a high-limit with increasing resolution. Therefore, it is hard to find a general standard for an optimum grid scale to balance accuracy and efficiency for complex real-world applications.

The numerical order is proved to be an important factor influencing the computational efficiency and accuracy. For the particular analytical case, oscillation flow in the parabolic basin, the second order scheme improves computational accuracy and consumes acceptable computing time of 105.42 s. However, for the realistic Malpasset dam-break case, the first order scheme seems to be a better option. The 1st order scheme provides the same prediction of the flood extent as that of the 2nd order scheme. RMSE of water depth is less than 1.4×10^{-3} m, which can be neglected in the real-world flood event. However, the 2nd order scheme cost much more computational expense as 2.13 times of that of the 1st order scheme. It implies that 1st order scheme may provide a good and efficient performance in reproducing the real-world flood event over complex domain topography.

8.1.5 Zero-inertia model

The zero-inertia equation is derived from the fully 2D shallow water equations. Herein, the governing equation is simply solved by an explicit limiter-free finite volume method. The interface flux is calculated by the Manning's equation. A non-negative reconstruction method (in terms of water depth) is implemented to capture the wet-dry front and avoid the negative water depth.

Two theoretical cases are employed here to validate the present zero-inertia model. Due to the implementation of the positive-water-depth-preserving reconstructed method, wet-dry front is accurately captured without unphysical oscillation and negative water depth. Then the present positivity-preserving zero-inertia model is validated against a realistic flooding inundation event at Thamesmead, UK. The performance of ZIM is compared with the aforementioned fully 2D shallow flow model. The dam-break flow is successfully reproduced with correctly prediction of wetting and drying process without spurious oscillations. The mass conservation is confirmed due to the finite volume method, and proved by comparing the summation of inflow volume with the predicted water volume in the whole domain. The predicted arrival time and water depth of ZIM are close to those of the fully 2D shallow flow model at gauging points. The comparison between ZIM and fully 2D shallow flow model is also quantified using Root Mean Square Error (RMSE) mathematical method and Fit statistic approach (introduced in Chapter 6) in terms of water depth. The RMSE converges to 0.05 m after the cessation of inflow while the fit statistics of flood extent converges to 88.75%. However, ZIM is much more computational expensive than the fully 2D shallow flow model. Hunter *et al.* (2008) also found a similar conclusion that a ZIM/DWM could consume more computational cost than a fully 2D shallow flow solver, which may be caused by the lack of the dynamic terms. Therefore, the problem related to the computational efficiency could be an inherent problem of the zero-inertia model.

8.2 Future Work and Recommendation

8.2.1 Fully 2D shallow flow model

This fully 2D shallow flow model has been verified to be a robust tool for reproducing complex shallow flow hydrodynamics features of the realistic flood events in rivers, lakes, reservoirs and coastal areas. In the real-world application, the flood flow can wash away bridges, embankments, coastal defences and dams causing landslide and dam/dyke-break, and also sweep off the sediment along river bed and floodplain. Hence the present flood model is proposed to combine with the sediment transport formulas in the future, in order to simulate the motion of the sediment in the flood flow. Then the numerical model can be implemented to predict arrival time, flood water depth, velocity,

flood route, inundated extent and sediment transport in the real-world flood event, e.g. flood in the Songhua River in Jilin province of China.

The natural disaster, e.g. severe storm, extreme tidal wave and Tsunami, may happen in the coastal area, inducing huge economic loss and heavy casualties. The present novel numerical tool can be implemented to provide accurate prediction of arrival time, wave run-up and moving shoreline, and also to reproduce complex coastal phenomena, such as surge wave and hydraulic jump, etc. The numerical prediction can be used in coastal defence designing, Tsunami warning systems and coastal risk analysis to build a safe living environment in the coastal area.

The present model is performed on a uniform Cartesian grid, in which the numerical schemes can be easily operated. The uniform-grid based model has been verified to be able to provide good performance in predicting realistic flooding inundation events over the complex domain topography. However, according to the investigation of the scale effect, the finer mesh could provide better prediction but is computational expensive. Further study can be carried out focusing on the sensitivity of input variables to the grid scale, in order to investigate the optimum spatial resolution for the realistic flood simulation.

In order to obtain further computational efficiency, an adaptive Quadtree grid (e.g. Rogers *et al.* 2001; Liang *et al.* 2004) is proposed to be implemented on the present model in the future, which could save up to 6 times computing time compared with the uniform Cartesian grid. The adaptive Quadtree grid is a particular type of unstructured grid, which has the advantages of cheap computational cost, automatic generation, simple hierarchical data structure for mesh information storage and easy grid adaptation.

8.2.2 Zero-inertia model

In this work, the zero-inertia equation has been successfully solved and validated against the flooding inundation event at Thamesmead area. The numerical prediction has been compared well with the simulation of the fully 2D shallow flow model. However, the zero-inertia scheme is not as efficient as expected. In order to maintain the computational stability, a small time step is required for this explicit zero-inertia model

while it also causes increased numbers of iteration. Hunter *et al.* (2005) and Bates *et al.* (2010) reveal that the reason of less efficiency is the lack of the dynamic terms in the zero-inertia equation. And this problem has been solved by implementing an inertia formulation of the shallow water equations in Bates *et al.* (2010). The efficient performance of the modified zero-inertia model has been proved. To improve the computational efficiency, this new method is proposed to be adopted on the present zero-inertia model. However, the proposed model may still cost more computational expenses than the fully 2D shallow flow model.

References

- Akanbi, A.A. and Katopodes, N.D. (1988) 'Model for flood propagation on initially dry land', *Journal of Hydraulic Engineering*, 114, (7), pp. 689-706.
- Alcrudo, F. and García-Navarro, P. (1993) 'A high-resolution Godunov-type scheme in finite volumes for the 2D shallow-water equations', *International Journal for Numerical Methods in Fluids*, 16, (6), pp. 489-505.
- Alcrudo, F. and Gil, E. (1999) 'The Malpasset dam break case study', *CADAM, Concerted Action on Dam Break Modelling, Proceedings of Zaragoza Meeting, Zaragoza, Spain, November 18 – 19*. Office for Official Publications of the European Communities, Luxembourg.
- Anastasiou, K. and Chan, C.T. (1997) 'Solution of the 2D shallow water equations using the finite volume method on unstructured triangular meshes', *International Journal for Numerical Methods in Fluids*, 24, (11), pp. 1225-1245.
- Aronica, G., Bates, P.D. and Horritt, M.S. (2002) 'Assessing the uncertainty in distributed model predictions using observed binary pattern information with GLUE', *Hydrological Processes*, 16, (10), pp. 2001-2016.
- Audusse, E., Bouchut, F., Bristeau, M.-O., Klein, R. and Perthame, B. (2004) 'A fast and stable well-balanced scheme with hydrostatic reconstruction for shallow water flows', *SIAM Journal on Scientific Computing*, 25, (6), pp. 2050-2065.
- Audusse, E. and Bristeau, M.-O. (2005) 'A well-balanced positivity preserving "second-order" scheme for shallow water flows on unstructured meshes', *Journal of Computational Physics*, 206, (1), pp. 311-333.
- Balzano, A. (1998) 'Evaluation of methods for numerical simulation of wetting and drying in shallow water flow models', *Coastal Engineering*, 34, (1-2), pp. 83-107.

- Bates, P.D. and de Roo, A.P.J. (2000) 'A simple raster-based model for flood inundation simulation', *Journal of Hydrology*, 236, (1-2), pp. 54-77.
- Bates, P.D., Horritt, M.S. and Fewtrell, T.J. (2010) 'A simple inertial formulation of the shallow water equations for efficient two-dimensional flood inundation modelling', *Journal of Hydrology*, 387, (1-2), pp. 33-45.
- Bellos, C. V., Soulis, J. V. and Sakkas, J. G. (1991) 'Computation of two-dimensional dam-break induced flows', *Advances in Water Resources*, 14, (1), pp. 31-41.
- Bermúdez, A. and Vázquez, M.E. (1994) 'Upwind methods for hyperbolic conservation laws with source terms', *Computers & Fluids*, 23, (8), pp. 1049-1071.
- Bermúdez, A., Dervieux, A., Desideri, J.A. and Vázquez, M.E. (1998) 'Upwind schemes for the two-dimensional shallow water equations with variable depth using unstructured meshes', *Computer Methods in Applied Mechanics and Engineering*, 155, (1-2), pp. 49-72.
- Bradbrook, K.F., Lane, S.N., Waller, S.G. and Bates, P.D. (2004) 'Two dimensional diffusion wave modelling of flood inundation using a simplified channel representation', *International Journal of River Basin Management*, 3, pp. 211-223.
- Brissette, F.P., Leconte, R., Marche, C. and Rousselle, J. (2003) 'Historical evolution of flooding damage on a USA/Quebec River Basin', *Journal of the American Water Resources Association*, 39, (6), pp. 1385-1396.
- Brocchini, M. and Dodd, N. (2008) 'Nonlinear shallow water equation modelling for coastal engineering', *Journal of Waterway, Port, Coastal and Ocean Engineering*, 134, (2), pp. 104-120.
- Brufau, P., Vázquez-Cendón, M.E. and García-Navarro, P. (2002) 'A numerical model for the flooding and drying of irregular domains', *International Journal for Numerical Methods in Fluids*, 39, (3), pp. 247-275.

- Brufau, P., García-Navarro, P. and Vázquez-Cendón, M.E. (2004) 'Zero mass error using unsteady wetting-drying conditions in shallow flows over dry irregular topography', *International Journal for Numerical Methods in Fluids*, 45, (10), pp. 1047-1082.
- Burg, C.O.E., Huddleston, D.H. and Berger, R.C. (2001) 'Efficient, robust design tool for open-channel flow', *Journal of Hydraulic Engineering*, 127, (1), pp. 62-70.
- Burguete, J., García-Navarro, P., Murillo, J. and Garcia-Palacin, I. (2007) 'Analysis of the friction term in the one-dimensional shallow water model: application to open channel and river flow', *Journal of Hydraulic Engineering*, 133, (9), pp. 1048-1063.
- Burguete, J., García-Navarro, P. and Murillo, J. (2008) 'Friction term discretization and limitation to preserve stability and conservation in the 1D shallow-water model: Application to unsteady irrigation and river flow', *International Journal for Numerical Methods in Fluids*, 58, (4), pp. 403-425.
- Bussing, T.R.A. and Murman, E.M. (1988) 'Finite-volume method for the calculation of compressible chemically reacting flows', *AIAA Journal*, 26, (9), pp. 1070-1078.
- Caleffi, V., Valiani, A. and Zanni, A. (2003) 'Finite volume method for simulating extreme flood events in natural channels', *Journal of Hydraulic Research*, 41, (2), pp. 167-177.
- Casulli V. (1990) 'Semi-implicit finite difference methods for the two-dimensional shallow water equations', *Journal of Computational Physics*, 86, (1), pp. 56-74.
- Casulli V. (2009) 'A high-resolution wetting and drying algorithm for free-surface hydrodynamics', *International Journal for Numerical Methods in Fluids*, 60, (4), pp. 391-408.
- Causon, D.M., Ingram, D.M., Mingham, C.G., Yang, G. and Pearson, R.V. (2000) 'Calculation of shallow water flows using a Cartesian cut cell approach', *Advances in Water Resources*, 23, (5), pp. 545-562.

- Chang, H. Franczyk, J. and Kim, C. (2009) 'What is responsible for increasing flood risks? The case of Gangwon Province, Korea', *Natural Hazards*, 48, (3), pp. 339-354.
- Chow, V.T. (1959) 'Open-channel Hydraulics', New York, McGraw-Hill.
- Cienfuegos, R., Barthélemy, E. and Bonneton, P. (2007) 'A fourth-order compact finite volume scheme for fully nonlinear and weakly dispersive Boussinesq-type equations. Part II: boundary conditions and validation', *International Journal for Numerical Methods in Fluids*, 53, (9), pp. 1423-1455.
- Cunge, J.A., Holly, F.M. and Verwey, A. (1976) 'Practical aspects of computational river hydraulics', Pitman, London.
- De Roo, A.P.L., Price, D.A. and Schmuck, G. (1999) 'Simulating the Meuse and Oder floods using the LISFLOOD model', *Proceedings of the Giessen Meeting, November, Kassel University Press*, pp. 41-50.
- Delis, A.I., Kazolea, M. and Kampanis, N.A. (2008) 'A robust high-resolution finite volume scheme for the simulation of long waves over complex domains', *International Journal for Numerical Methods in Fluids*, 56, (4), pp. 419-452.
- Dodd, N. (1998) 'Numerical model of wave run-up, overtopping, and regeneration', *ASCE Journal of Waterway, Port, Coastal and Ocean Engineering*, 124, (2), pp. 73-81.
- Dressler, R.F. (1952) 'Hydraulic resistance effect upon the dam-break functions', *Journal of Research of the National Bureau of Standards*, 49, (3), pp. 217-225.
- Erduran, K.S., Kutija, V. and Hewett, C.J.M. (2002) 'Performance of finite volume solutions to the shallow water equations with shock-capturing schemes', *International Journal for Numerical Methods in Fluids*, 40, (10), pp. 1237-1273.

- Fennema, R. T. and Chaudhry, M. H. (1990) 'Explicit methods for 2D transient free-surface flows', *Journal of Hydraulic Engineering*, 116, (11), pp. 1013-1014.
- Ferziger, J.H. and Peric, M. (1999) 'Computational methods for fluid dynamics', Berlin; New York; Springer. ISBN 3-540-65373-2.
- Fiedler, F.R. and Ramirez, J.A. (2000) 'A numerical method for simulating discontinuous shallow flow over an infiltrating surface', *International Journal for Numerical Methods in Fluids*, 32, (2), pp. 219-240.
- Fraccarollo, L. and Toro, E.F. (1995) 'Experimental and numerical assessment of the shallow water model for two dimensional dam-break type problems', *Journal of Hydraulic Research*, 33, (6), pp. 843-864.
- Franchello, G. (2010) 'Shoreline tracking and implicit source terms for a well balanced inundation model', *International Journal for Numerical Methods in Fluids*, 63, (10), pp. 1123-1146.
- Galland, J.C., Goutal, N. and Hervouet, J.-M., (1991) 'TELEMAC: a new numerical model for solving shallow water equations', *Advances in Water Resources*, 14, (3), pp. 138-148.
- Gallegos, H.A., Schubert, J.E. and Sanders, B.F. (2009) 'Two-dimensional, high-resolution modelling of urban dam-break flooding: A case study of Baldwin Hills, California', *Advances in Water Resources*, 32, (8), pp. 1323-1335.
- García-Navarro, P. and Vázquez-Cendón, M.E. (2000) 'On numerical treatment of the source terms in the shallow water equations', *Computers & Fluids*, 29, (8), pp. 951-979.
- Godunov, S.K. (1959) 'A difference scheme for numerical solution of discontinuous solution of hydrodynamic equations', *Matematicheskii Sbornik*, 47, pp. 271-306.

- Goutal, N. and Maurel, F. (1997) 'Proceedings of the 2nd workshop on dam-break wave simulation', HE 43/97/016/B, Département Laboratoire National d'Hydraulique, Groupe Hydraulique Fluviale Electricité de France, France.
- Greenberg, J.M. and Leroux, A.Y. (1996) 'A well-balanced scheme for the numerical processing of source terms in hyperbolic equations', *SIAM Journal on Numerical Analysis*, 33, (1), pp. 1-16.
- Haider, S., Paquier, A., Morel, R. and Champagne, J.Y. (2003) 'Urban flood modelling using computational fluid dynamics', *Proceedings of the ICE - Water and Maritime Engineering*, 156, (2), pp. 129-135.
- Harten, A., Lax, P.D. and van Leer, B. (1983) 'On upstream differencing and Godunov-type schemes for hyperbolic conservation laws', *SIAM Review*, 25, (1), pp. 35-61.
- Hervouet, J.-M. and Van Haren, L. (1996) 'Recent advances in numerical methods for fluid flows', In: Anderson, M.G., Walling, D.E. and Bates, P.D. (Eds.), *Floodplain Processes*, Wiley, Chichester, pp. 183-214.
- Hervouet, J.-M. and Petitjean, A. (1999) 'Malpasset dam-break revisited with two-dimensional computation', *Journal of Hydraulic Research*, 37, (6), pp. 777-788.
- Hervouet, J.-M. (2000) 'A high resolution 2-D dam-break model using parallelization', *Hydrological Processes*, 14, (13), pp. 2211-2230.
- Hirsch, C. (1990) 'Numerical computation of internal and external flows', Volume 2, *Computational methods for inviscid and viscous flows*. New York: Wiley.
- Horritt, M.S. and Bates, P.D. (2001a) 'Predicting floodplain inundation: raster-based modelling versus the finite-element approach', *Hydrological Processes*, 15, (5), pp. 825-842.
- Horritt, M.S. and Bates, P.D. (2001b) 'Effects of spatial resolution on a raster based model of flood flow', *Journal of Hydrology*, 253, (1-4), pp. 239-249.

- Horritt, M.S. and Bates, P.D. (2002) 'Evaluation of 1D and 2D numerical models for predicting river flood inundation', *Journal of Hydrology*, 268, (1-4), pp. 87-99.
- Horritt, M. (2004) 'Development and testing of a simple 2D finite volume model of sub-critical shallow water flow', *International Journal for Numerical Methods in Fluids*, 44, (11), pp. 1231-1255.
- Hubbard, M.E. and Dodd, N. (2002) 'A 2D numerical model of wave run-up and overtopping', *Coastal Engineering*, 47, (1), pp. 1-26.
- Hu, K., Mingham, C.G. and Causon, D.M. (1998) 'A bore-capturing finite volume method for open-channel flows', *International Journal for Numerical Methods in Fluids*, 28, (8), pp. 1241-1261.
- Hu, K., Mingham, C.G. and Causon, D.M. (2000) 'Numerical simulation of wave overtopping of coastal structures using the non-linear shallow water equations', *Coastal Engineering*, 41, (4), pp. 433-465.
- Hunter, N.M., Horritt, M.S., Bates, P.D., Wilson M.D. and Werner, M.G.F., (2005) 'An adaptive time step solution for raster-based storage cell modelling of floodplain inundation', *Advances in Water Resources*, 28, (9), pp. 975-991.
- Hunter, N. M., Bates, P.D., Horritt, M.S. and Wilson M.D. (2006) 'Improved simulation of flood flows using storage cell models', *Proceedings of the ICE - Water Management*, 159, (1), pp. 9-18.
- Hunter, N.M., Bates, P.D., Neelz, S., Pender, G., Villanueva, I., Wright, N.G., Liang, D., Falconer, R.A., Lin, B., Waller, S., Crossley, A.J. and Mason, D. (2008) 'Benchmarking 2D hydraulic models for urban flooding', *Proceedings of ICE, Water Management*, 161, (1), pp. 13-30.
- Jha, A.K., Akiyama, J. and Ura, M. (2000) 'Flux-difference splitting schemes for 2D flood flows', *Journal of Hydraulic Engineering*, 126, (1), pp. 33-42.

- Kesserwani, G. and Liang, Q. (2010) 'Well-balanced RKDG2 solutions to the shallow water equations over irregular domains with wetting and drying', *Computers & Fluids*, 39, (10), pp. 2040-2050.
- Kutija, V. (1993) 'On the numerical modelling of supercritical flow', *Journal of Hydraulic Research*, 31, (6), pp. 841-858.
- Kundzewicz, Z.W., Ulbrich, U., Brücher, T., Graczyk, D., Krüger, A., Leckebusch, G.C., Menzel, L., Pinskiwar, I., Radziejewski, M. and Szwed, M. (2005) 'Summer floods in Central Europe - Climate change track?', *Natural Hazards*, 36, (1-2), pp. 165-189.
- Lai, J.-S., Lin, G.-F. and Guo, W.-D. (2005) 'An upstream flux-splitting finite-volume scheme for 2D shallow water equations', *International Journal for Numerical Methods in Fluids*, 48, (10), pp. 1149-1174.
- Lai, J.-S., Guo, W.-D., Lin, G.-F. and Tan, Y.-C. (2010) 'A well-balanced upstream flux-splitting finite-volume scheme for shallow-water flow simulations with irregular bed topography', *International Journal for Numerical Methods in Fluids*, 62, (8), pp. 927-944.
- Leclerc, M., Bellemare, J.-F., Dumas, G. and Dhatt, G. (1990) 'A finite element model of estuarian and river flows with moving boundaries', *Advances in Water Resources*, 13, (4), pp. 158-168.
- Lee, S.-H. and Wright, N.G. (2010) 'Simple and efficient solution of the shallow water equations with source terms', *International Journal for Numerical Methods in Fluids*, 63, (3), pp. 313-340.
- LeVeque, R. J. (1998) 'Balancing Source Terms and Flux Gradients in High-Resolution Godunov Methods: The Quasi-Steady Wave-Propagation Algorithm', *Journal of Computational Physics*, 146, (1), pp. 346-365.

- Liang, D., Lin, B. and Falconer, R.A. (2007) 'A boundary-fitted numerical model for flood routing with shock-capturing capability', *Journal of Hydrology*, 332, (3-4), pp. 477-486.
- Liang, Q., Borthwick, A.G.L. and Stelling, G. (2004) 'Simulation of dam- and dyke-break hydrodynamics on dynamically adaptive quadtree grids', *International Journal for Numerical Methods in Fluids*, 46, (2), pp. 127-162.
- Liang, Q., Du, G., Hall, J.W. and Borthwick, A.G.L. (2008) 'Flood inundation modelling with an adaptive quadtree grid shallow water equation solver', *Journal of Hydraulic Engineering*, 134, (11), pp. 1603-1610.
- Liang, Q. and Borthwick, A.G.L. (2008) 'Simple treatment of non-aligned boundaries in a Cartesian grid shallow flow model', *International Journal for Numerical Methods in Fluids*, 56, (11), pp. 2091-2110.
- Liang, Q. and Borthwick, A.G.L. (2009) 'Adaptive quadtree simulation of shallow flows with wet-dry fronts over complex topography', *Computers and Fluids*, 38, (2), pp. 221-234.
- Liang, Q. and Marche, F. (2009) 'Numerical resolution of well-balanced shallow water equations with complex source terms', *Advances in Water Resources*, 32, (6), pp. 873-884.
- Liang, Q. (2010) 'Flood simulation using a well-balanced shallow flow model', *Journal of Hydraulic Engineering*, 136, (9), pp. 669-675.
- Liang, Q., Wang, Y. and Archetti, R. (2010) 'A well-balanced shallow flow solver for coastal simulations', *International Journal of Offshore and Polar Engineering*, 20, (1), pp. 41-47.
- Lin, G.F., Lai, J.S. and Guo, W.D. (2003) 'Finite volume component-wise TVD scheme for 2D shallow water equations', *Advances in Water Resources*, 26, (8), pp. 861-873.

- Matsuyama, M. and Tanaka H. (2001) 'An experimental study of the highest run-up height in the 1993 Hokkaido Nansei-oki earthquake tsunami', *ITS 2001 Proceedings*, session 7, Number 7-21.
- Marche, F., Bonneton, P., Fabrie, P. and Seguin, N. (2007) 'Evaluation of well-balanced bore-capturing schemes for 2D wetting and drying processes', *International Journal for Numerical Methods in Fluids*, 53, (5), pp. 867-894.
- Milly, P.C.D., Wetherald, R.T., Dunne, K.A. and Delworth, T.L. (2002) 'Increasing risk of great floods in a changing climate', *Nature*, 415, (6871), pp. 514-517.
- Mingham, C.G. and Causon, D.M. (1998) 'High resolution finite volume method for the shallow water equations', *Journal of Hydraulic Engineering*, 124, (6), pp. 605-614.
- Mignot, E., Paquier, A. and Haider, S. (2006) 'Modelling floods in a dense urban area using 2D shallow water equations', *Journal of Hydrology*, 327, (1-2), pp. 186-199.
- Miyata, H. (1986) 'Finite-difference simulation of breaking waves', *Journal of Computational Physics*, 65, (1), pp. 179-214.
- Murillo, J., García-Navarro, P. and Burguete, J. (2009) 'Time step restrictions for well-balanced shallow water solutions in non-zero velocity steady states', *International Journal for Numerical Methods in Fluids*, 60, (12), pp. 1351-1377.
- Nguyen, D.K., Shi, Y.-E., Wang, S.S.Y. and Nguyen, T.H. (2006) '2D shallow-water model using unstructured finite-volumes methods', *Journal of Hydraulic Engineering*, 132, (3), pp. 258-269.
- Noelle, S., Pankratz, N., Puppo, G. and Natvig, J.R. (2006) 'Well-balanced finite volume schemes of arbitrary order of accuracy for shallow water flows', *Journal of Computational Physics*, 213, (2), pp. 474-499.

- Osher, S. (1981) 'Numerical solution of singular perturbation problems and hyperbolic systems of conservation laws', In: Axelsson, O. *et al.* (Editors), *Mathematical Studies*, North Holland: Amsterdam, 47, pp. 179-204.
- Pan, C.-h., Dai, S.-q. and Chen, S.-m. (2006) 'Numerical simulation for 2D shallow water equations by using Godunov-type scheme with unstructured mesh', *Journal of Hydrodynamics*, 18, (4), pp. 475-480.
- Prestininzi, P. (2008) 'Suitability of the diffusive model for dam break simulation: Application to a CADAM experiment', *Journal of Hydrology*, 361, (1-2), pp. 172-185.
- Pitt, M. (2007) 'The Pitt Review: lessons learned from the 2007 floods', United Kingdom – Government.
- Ritter, A. (1892) 'The propagation of water waves', *Ver Deutsch Ingenieur Zeitschr*, 36, Pt. 3, (33), pp. 947-954.
- Roe, P.L. (1981) 'Approximate Riemann solvers, parameter vectors, and difference schemes', *Journal of Computational Physics*, 43, (2), pp. 357-372.
- Rogers, B.D., Fujihara, M. and Borthwick, A.G.L. (2001) 'Adaptive Q-tree Godunov-type scheme for shallow water equations', *International Journal for Numerical Methods in Fluids*, 35, (3), pp. 247-280.
- Rogers, B.D., Borthwick, A.G.L. and Taylor, P.H., (2003) 'Mathematical balancing of flux gradient and source terms prior to using Roe's approximate Riemann solver', *Journal of Computational Physics*, 192, (2), pp. 422-451.
- Sampson, J., Easton, A. and Singh, M. (2006) 'Moving boundary shallow water flow above parabolic bottom topography', *ANZIAM J.*, 47, (EMAC2005), pp. 373-387.
- Sanders, B.F. (2008) 'Integration of a shallow water model with a local time step', *Journal of Hydraulic Research*, 46, (4), pp. 466-475.

- Schwanenberg, D. and Harms, M. (2004) 'Discontinuous Galerkin finite-element method for transcritical two-dimensional shallow water flows', *Journal of Hydraulic Engineering*, 130, (5), pp. 412-421.
- Sheu, T.W.H. and Fang, C.C. (2001) 'High resolution finite-element analysis of shallow water equations in two dimensions', *Computer Methods in Applied Mechanics and Engineering*, 190, (20-21), pp. 2581-2601.
- Sleigh, P.A., Gaskell, P.H., Berzins, M. and Wright, N.G. (1998) 'An unstructured finite-volume algorithm for predicting flow in rivers and estuaries', *Computers & Fluids*, 27, (4), pp. 479-508.
- Soares-Frazão, S. (2007) 'Experiments of dam-break wave over a triangular bottom sill', *Journal of Hydraulic Research*, 45, (6 supp 1), pp. 19-26.
- Synolakis, C.E. (1987) 'The run-up of solitary waves', *Journal of Fluid Mechanics*, 185, pp. 523-545.
- Tan, W. (1992) 'Shallow water hydrodynamics', Elsevier Oceanography Series, 55, Elsevier Science Publishers BV, Amsterdam, The Netherlands.
- Tchamen, G.W. and Kahawita, R.A. (1998) 'Modelling wetting and drying effects over complex topography', *Hydrological Processes*, 12, (8), pp. 1151-1182.
- Teng, W.H., Hsu, M.H., Wu, C.H. and Chen, A.S. (2006) 'Impact of flood disasters on Taiwan in the last quarter century', *Natural Hazards*, 37, (1-2), pp. 191-207.
- Thacker, W.C. (1981) 'Some exact solutions to the nonlinear shallow-water wave equations', *Journal of Fluid Mechanics*, 107, pp. 499-508.
- Tisdale, T.S., Scarlatos, P.D. and Hamrick, J.M. (1998) 'Streamline upwind finite-element method for overland flow', *Journal of Hydraulic Engineering*, 124, (4), pp. 350-357.

- Toro, E.F. (1994) 'Experimental and computational analysis for two-dimensional dam-break type problems', Internal Report (IDR 2), Dipartimento di Ingegneria Civile ed Ambientale, Università Degli studi di Trento.
- Toro, E.F., Spruce, M. and Speares, W. (1994) 'Restoration of the contact surface in the HLL-Riemann solver', *Shock Waves*, 4, (1), pp. 25-34.
- Toro, E.F. (1997) 'Riemann solvers and numerical methods for fluid dynamics', Springer-Verlag, Berlin/Heidelberg.
- Toro, E.F. (2001) 'Shock-capturing methods for free-surface shallow flows', Chichester: John Wiley & Sons.
- Tucciarelli, T. and Termini, D. (2000) 'Finite-element modelling of floodplain flow', *Journal of Hydraulic Engineering*, 126, (6), pp. 416-424.
- US Army Corps of Hydraulic Engineers, HEC-RAS. <http://www.hec.usace.army.mil>
- Valiani, A., Caleffi, V., and Zanni, A. (2002) 'Case study: Malpasset dam-break simulation using a two-dimensional finite volume method', *Journal of Hydraulic Engineering*, 128, (5), pp. 460-472.
- van Leer, B. (1979) 'Towards the ultimate conservative difference scheme. V. A second-order sequel to Godunov's method', *Journal of Computational Physics*, 32 (1), 101-136.
- Vázquez-Cendón, M. E. (1994) 'Estudio de esquemas descentrados para su aplicación a las leyes de conservación hiperbólicas con términos fuente', Ph.D. thesis, Universidad de Santiago de Compostela.
- Vázquez-Cendón, M. E. (1999) 'Improved treatment of source terms in upwind schemes for shallow water equations in channels with irregular geometry', *Journal of Computational Physics*, 148, (2), pp. 497-526.

- Vincent, S., Caltagirone, J.-P. and Bonneton, P. (2001) 'Numerical modelling of bore propagation and run-up on sloping beaches using a MacCormack TVD scheme', *Journal of Hydraulic Research*, 39, (1), pp. 41-49.
- Wang, L.X. (1987) 'Composite-model of 1D and 2D flows', *Advanced course and workshop on mathematical modelling of alluvial river*, IRTCES-Beijing, China.
- Wang, J.S., Ni, H.G. and He, Y.S. (2000) 'Finite-difference TVD scheme for computation of dam-break problems', *Journal of Hydraulic Engineering*, 126, (4), pp. 253-262.
- Wang, J., He, Y. and Ni, H. (2003) 'Two-dimensional free surface flow in branch channels by a finite-volume TVD scheme', *Advances in Water Resources*, 26, (6), pp. 623-633.
- Whitham, G.B. (1955) 'The effects of hydraulic resistance in the dam-break problem', *Proceedings of the Royal Society of London. Series A, Mathematical and Physical Sciences*, 227, (1170), pp. 399-407.
- Wright, N.G., Villanueva, I., Bates, P.D., Mason, D.C., Wilson, M.D., Pender, G. and Neelz, S. (2008) 'Case Study of the Use of Remotely Sensed Data for Modeling Flood Inundation on the River Severn, U.K', *Journal of Hydraulic Engineering*, 134, (5), pp. 533-540.
- Yamazaki, Y., Kowalik, Z. and Cheung, K.F. (2009) 'Depth-integrated, non-hydrostatic model for wave breaking and run-up', *International Journal for Numerical Methods in Fluids*, 61, (5), pp. 473-497.
- Yang, J.Y., Liu, Y. and Lomax, H. (1987) 'Computation of shock wave reflection by circular cylinders', *AIAA journal*, 25, (5), pp. 683-689.
- Yoon, T.H. and Kang, S.K. (2004) 'Finite volume model for two-dimensional shallow water flows on unstructured grids', *Journal of Hydraulic Engineering*, 130, (7), pp. 678-688.

- Yu, D. and Lane, S.N. (2006a) 'Urban fluvial flood modelling using a two-dimensional diffusion-wave treatment, part 1: mesh resolution effects', *Hydrological Processes*, 20, (7), pp. 1541-1565.
- Yu, D. and Lane, S.N. (2006b) 'Urban fluvial flood modelling using a two-dimensional diffusion-wave treatment, part 2: development of a sub-grid-scale treatment', *Hydrological Processes*, 20, pp. 1567-1583.
- Zhang, X., Long, W., Xie, H., Zhu, J. and Wang, J. (2007) 'Numerical simulation of flood inundation processes by 2D shallow water equations', *Frontiers of Architecture and Civil Engineering in China*, 1, (1), pp. 107-113.
- Zhao, D.H., Shen, H.W., Tabios III, G.Q., Lai, S.J. and Tan, W.Y. (1994) 'Finite-volume two-dimensional unsteady-flow model for river basins', *Journal of Hydraulic Engineering*, 120, (7), pp. 863-883.
- Zhao, D.H., Shen, H.W., Lai, J.S. and Tabios III, G.Q. (1996) 'Approximate Riemann solvers in FVM for 2D hydraulic shock wave modeling', *Journal of Hydraulic Engineering*, 122, (12), pp. 692-702.
- Zhou, J. G. and Stansby, P. K. (1999) '2D shallow water flow model for the hydraulic jump', *International Journal for Numerical Methods in Fluids*, 29, (4), pp. 375-387.
- Zhou, J.G., Causon, D.M., Mingham, C.G. and Ingram, D.M. (2001) 'The surface gradient method for the treatment of source terms in the shallow-water equations', *Journal of Computational Physics*, 168, (1), pp. 1-25.
- Zhou, J.G., Causon, D.M., Ingram, D.M. and Mingham, C.G. (2002) 'Numerical solutions of the shallow water equations with discontinuous bed topography', *International Journal for Numerical Methods in Fluids*, 38, (8), pp. 769-788.
- Zhou, J.G., Causon, D.M., Mingham, C.G. and Ingram, D.M. (2004) 'Numerical prediction of dam-break flows in general geometries with complex bed topography', *Journal of Hydraulic Engineering*, 130, (4), pp. 332-340.

Zoppou, C. and Roberts, S. (2000) 'Numerical solution of the two-dimensional unsteady dam break', *Applied Mathematical Modelling*, 24, (7), pp. 457-475.

Zoppou, C. and Roberts, S. (2003) 'Explicit schemes for dam-break simulations', *Journal of Hydraulic Engineering*, 129, (1), pp. 11-34.